The effect of deformation on mechanical properties of bulk metallic glasses

Inaugural-Dissertation

zur Erlangung des Doktorgrades

der Mathematisch-Naturwissenschaftlichen Fakultät

der Heinrich-Heine-Universität Düsseldorf

vorgelegt von

Mehrdad Golkia

aus Teheran

Düsseldorf, April 2020

Aus dem Institut für Theoretische Physik II: Weiche Materie
der Heinrich-Heine-Universität Düsseldorf

Gedruckt mit der Genehmigung der
Mathematisch-Naturwissenschaftlichen Fakultät der
Heinrich-Heine-Universität Düsseldorf

Referent: Prof. Dr. Jürgen Horbach
Korreferent: Prof. Dr. Stefan U. Egelhaaf

Tag der mündlichen Prüfung: 09.06.2020

This thesis is dedicated to a question,
“What is consciousness?”

Acknowledgements

I want to thank Prof. Dr. Jürgen Horbach for his patient and support during my Ph.D. I was lucky to have a supervisor who is always ready to share his boundless knowledge and is open to scientific and non-scientific discussions.

I would also like to thank my second supervisor Prof. Dr. Stefan U. Egelhaaf and also, Prof. Dr. Hartmut Löwen for our helpful and practical discussions during institute seminars.

I also appreciate our tranquil and peaceful working environment while finishing up my thesis. This would not have been possible without the help of Coronavirus (COVID-19). Due to the unexpected pandemic situation of Coronavirus outbreak, my Ph.D. defense will not be public. Therefore, in the end, I would like to call some names, including family, friends, and colleagues.

"wish you were all here!"

Shahin, Amir, Mahnaz and
Pejman, Leila, Ashkan, Padide, Milad, Reza, Afsane, Dariush, Armin, Saba, Siavash, Mohammad, Ali, Ulrike, Omid, Soheil, Elnaz, Siamak, Golsoo, Kiawash, Gilava, Farzane, Raha, Ina, Pegah, Mojtaba, Elham, Emad, Farnaz, Steffen, Sara, Amin, Anahita, Maziar, Sourena, Ario, Nima, Gaurav, Pinaki, Saswati, Nicolas, Oliver, Michael, Laura, Bastian, Stephan, Guo, Joachim, Stefanie, Benjamin, Niklas, Paul, Konstantin, René, Claudia, Soudeh.

Summary

Bulk metallic glasses (BMGs), compared to their crystalline counterparts, show remarkable mechanical properties like high strength, high wear, and corrosion resistance, very high resilience, etc., within the elastic limit for very small deformations. Despite all these promising mechanical properties, the response of BMGs to an external load beyond the elastic limit for large deformations often results in a catastrophic failure due to brittleness and limited ductility. Therefore, the mechanical properties of BMGs, especially when subjected to an external load, has been a topic of many research groups during the last decades.

We investigate the effects of deformation on mechanical properties of a $Ni_{80}P_{20}$ model metallic glass former, using non-equilibrium molecular dynamics computer simulations. Using a Lennard-Jones model, samples are equilibrated in the super-cooled liquid (SCL) state from which the glass state is obtained via a fast quench. The response of the prepared samples in the SCL and glass state is studied by subjecting them to shear via a simple planar Couette flow geometry. These responses are reflected in the stress-strain curve in which, for the SCLs, a cross over from a Newtonian to non-Newtonian response, marked by the occurrence of an overshoot, is observed.

Within the elasticity limit, a linear response is observed in the elastic regime of the stress-strain curve of the SCLs and glasses. The effect of deformation on elastic properties of the samples in the glass state is studied by applying a stress-fluctuation formalism and calculating the elastic constant tensor. The elastic constants of the undeformed states are then compared to those of the deformed states, after switch-off the shear load. The latter samples are in a new glass state with residual stresses. Also, as the elastic properties are reflected in the low-frequency spectrum of the vibrational modes, the density of states is calculated for both undeformed and deformed states. The vibrational properties of the samples, before and after deformation, are also studied in terms of current correlation functions and the Boson peak. After the overshoot, while short-lived in-homogeneous flow patterns are observed in SCLs, in glasses, these inhomogeneities appear to be more persistent and often result in the formation of shear bands. We characterize the formation and evolution of these in-homogeneous flow pasterns both in SCLs and glasses, as they play a crucial role in a better understanding of yielding and plastic deformation. Further, we adjust the ductility of our model by introducing a minor micro-alloying in the system such that while, the elastic properties of the system remain similar to the original model the plasticity is enhanced.

Zusammenfassung

Massive metallische Gläser zeigen im Vergleich zu ihren kristallinen Pendants bemerkenswerte mechanische Eigenschaften, wie zum Beispiel eine hohe Festigkeit, eine hohe Verschleiß- und Korrosionsbeständigkeit und eine sehr hohe Elastizität innerhalb des Elastizitätsbereiches bei sehr kleinen Verformungen. Trotz all dieser vielversprechenden mechanischen Eigenschaften führt die Antwort metallischer Gläser auf eine äußere Belastung jenseits der Elastizitätsgrenze, d.h. bei großen Verformungen, häufig zu einem katastrophalen Materialversagen aufgrund von Sprödigkeit und begrenzter Duktilität. Daher hat sich in den letzten zwanzig Jahren die Forschung intensiv den mechanischen Eigenschaften metallischer Gläser gewidmet.

Wir untersuchen die Auswirkungen der Verformung auf die mechanischen Eigenschaften des metallischen Glasbildners $Ni_{80}P_{20}$ mithilfe von Nichtgleichgewichtsmolekulardynamikcomputersimulationen. Unter Verwendung eines Lennard-Jones-Modells werden unterkühlte Flüssigkeiten (engl.: super-cooled liquids, SCL) äquilibriert und aus diesen Glassamples über ein schnelles Abkühlen generiert. Die so erhaltenen Gläser werden dann in einer ebenen Couetteströmungsgeometrie geschert. Für die unterkühlten Flüssigkeiten zeigen die Spannungs-Dehnungskurven mit zunehmender Scherrate einen Übergang von einer newtonschen zu einer nichtnewtonschen Flüssigkeit, wobei in letzterem Fall ein Überschwinger bei einer Dehnung von etwa 10% in der Spannungs-Dehnungskurve auftritt.

Unterhalb der Elastizitätsgrenze wird eine lineare Antwort in der Spannungs-Dehnungs-Kurve der unterkühlten Flüssigkeiten und Gläser beobachtet. Der Einfluss der Verformung auf die elastischen Eigenschaften der Proben im Glaszustand wird untersucht, indem ein Formalismus zur Beschreibung der Spannungsfluktuationen angewendet und der Elastizitätstensor berechnet wird. Die elastischen Konstanten der unverformten Zustände werden dann mit denen der verformten Zustände nach dem Abschalten der Scherbelastung verglichen. Letztere Proben befinden sich in einem neuen Glaszustand, der Restspannungen aufweist. Da sich die elastischen Eigenschaften im Niederfrequenzspektrum der Schwingungsmoden widerspiegeln, wird die Zustandsdichte sowohl für unverformte als auch für verformte Zustände berechnet. Die Schwingungseigenschaften der Proben vor und nach der Verformung werden mit Stromkorrelationsfunktionen analysiert, insbesondere im Hinblick auf die Untersuchung des Bosonenpeaks. Während in unterkühlten Flüssigkeiten kurzlebige inhomogene Strömungsmuster beobachtet werden, sind in Gläsern solche Inhomogenitäten beständiger und es zeigt sich häufig (insbesondere bei genügend kleinen Scher-

raten) die Bildung von Scherbändern. Wir charakterisieren die Bildung und Entwicklung dieser inhomogenen Fließmuster sowohl in unterkühlten Flüssigkeiten als auch in Gläsern, da sie eine entscheidende Rolle für ein besseres Verständnis der Fließgrenze und der plastischen Verformung spielen. Darüberhinaus passen wir die Duktilität unseres Modells an, indem wir eine kleine Menge einer dritten Komponente einführen ("micro-alloying"), was zu einer besseren Duktilität des Systems führt, während seine elastischen Eigenschaften nahezu unverändert bleiben.

Contents

1 Introduction

The synthesis of a metallic glass, by quenching a Gold-Silicon alloy ($Au_{75}Si_{25}$) from the melt, was first reported by [Klement, Willens, and Duwez (1960)][1]. A glass state is obtained by extremely fast cooling of a melted glass-forming alloy below its melting temperature. Generally, the cooling rate should be fast enough to bypass crystallization, and therefore, in a small temperature window above T_g (the glass transition temperature), the viscosity increases by several orders of magnitude and the glass-forming liquid forms an *amorphous solid*. At this stage, the structural relaxation times exceed experimentally accessible timescales and the so-called *glass transition* happens [Binder and Kob (2011)]. Due to technical difficulties in production, mainly achieving sufficiently fast cooling rates; initially, metallic glasses were only produced as narrow ribbons or wires and only by a few research groups. Metallic glasses were produced in bulk[2] after some development

[1] This had happened as part of a research program "*whose purpose was far remote from metallic glasses*" said by P. Duwez in a report twenty-one years later [Duwez (1981)]. The purpose of the latter research program was to obtain a solid solution in binary alloys of Cu and Ag. In this report, the author describes: "*The phase diagram of* CuAg *is a eutectic type, which is in contradiction to the generally accepted Hume-Rothery rules. Since the separation of the homogeneous liquid into* Cu*-rich and* Ag*-rich phases during cooling is a rate process, I thought that by cooling the melt very rapidly, the* Cu *and* Ag *atoms would not have time to cluster and would be forced into a nonequilibrium solid solution*". Successfully designing a piece of simple equipment which is now referred to as "gun technique", they quenched small pieces of single-phase, face-centered solid solution of CuAg. The author continues that: "*The next alloy to be quenched could have been another system in which complete solubility would be predicted but does not occur under normal conditions. I was more interested, however, in finding out what would happen in a system in which the two components cannot form a solid solution under any circumstances because, for example, they have different crystal structures and very different valences*". Surprisingly, an unexpected result occurs when a $Ag-Ge$ alloy with 23 at.%Ge concentration was quenched and found to be in a hexagonal close-packed phase, which does not exist in equilibrium. This was the first nonequilibrium crystalline phase obtained by liquid quenching. The author continues: "*The next move was a lucky one leading to the first metallic glass. The alloy system* $Au-Si$ *is very similar to* $Ag-Ge$*, and it was expected that a hexagonal close-packed phase would also be obtained in* $Au-Si$ *alloys. Instead, the x-ray diffraction pattern of the quenched* $Au-20$ *at.%*Si *alloy indicated the absence of crystallinity. But was the alloy really amorphous, or were we overenthusiastic about some rather questionable results ?*".

[2] Hereafter, Bulk metallic glasses are referred to as BMGs in this thesis.

was made in the cooling methods, e.g., fast-spinning wheel method [Liebermann and Graham (1976)].

On the other hand, the amorphous state and the glass transition phenomenon, as one of "*the deepest and most interesting unsolved problems in solid-state theory*" said by the Nobel laureate Philip W. Anderson [Anderson (1995)], had always been a puzzling problem among theoretical physicists. In parallel to experimental developments, there have been many theoretical approaches towards a fundamental understanding of the glass transition phenomenon. Among them, the only microscopic approach is the mode-coupling theory (MCT) of the glass transition, proposed by [Bengtzelius, Götze, and Sjölander (1984) and Leutheusser (1984)], which made many predictions about features of glassy dynamics [Janssen (2018)]. During late 1980s and beginning of 1990s, also particle-based computer simulation [Allen and Tildesley (2017)] were used to model glass-forming systems. An important issue of the early simulation methods was to test the predictions of MCT. A model for $Ni_{80}P_{20}$ metallic glass former was introduced by [Kob and Andersen (1994)] with the aim of testing MCT predictions [Kob and Andersen (1995a) and Kob and Andersen (1995b)]. The so-called *Kob-Andersen binary mixture*, consists of two types of particles which are interacting via a *Lennard-Jones* [Lennard-Jones (1924)] potential. Kob-Andersen binary Lennard-Jones mixture is a good glass former system that can bypass crystallization without showing any phase separation. Using short-range pairwise additive Lennard-Jones interaction, without any orientations degrees of freedom, this model is a significantly reliable and simple (in comparison to organic systems, polymers, silicates, and other network makers systems) model which has been extensively used during the last decades and made a significant increase in the number of publications during the last decades (check Fig. 1.1).

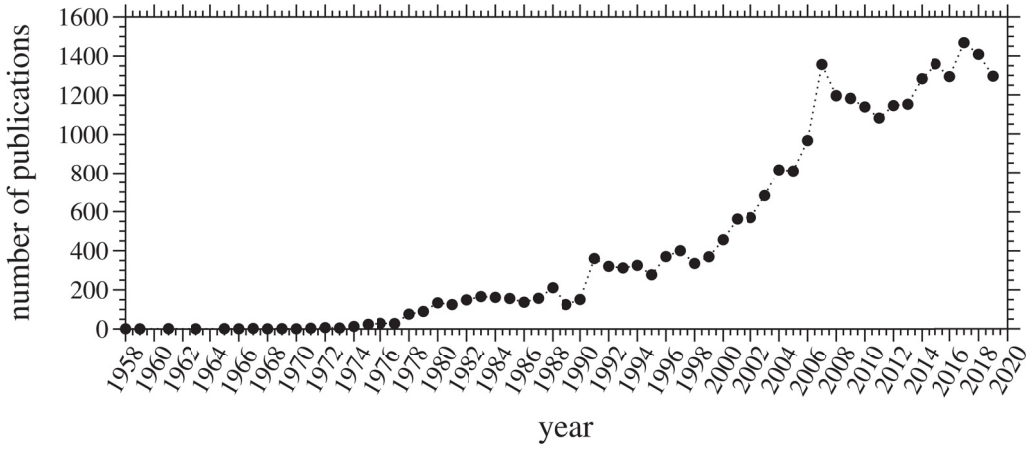

Figure 1.1: Number of publications by keyword *"metallic glasses"* per year. Data source: the Clarivate Analytics (following the acquisition of Thomson Reuters) Web of Science.

Rather than testing the theoretical predictions, another primary focus of the latter simulation methods was to try to investigate the poorly understood mechan-

ical responses of BMGs when subjected to an external load. BMGs have unique mechanical properties (high strength, high wear, and corrosion resistance, etc.) compared to their crystalline counterparts. Therefore, they are of great technological interest [Wang, Dong, and Shek (2004)]. The possibility of controlling the viscosity of BMGs over a wide range, such that one can form them into different shapes, made commercial use of these materials possible, e.g., golfing putters and tennis racquets were designed by *Liquidmetal Technologies*[3] and electric guitars made of amorphous metal by *Heraeus*[4]. BMGs were used in creating NASA's Genesis spacecraft solar wind collectors[5]. Possible medical applications of these materials also have been studied during the last years [Schroers, Kumar, et al. (2009) and Zberg, Uggowitzer, and Löffler (2009)]. Nevertheless, a significant drawback in the mechanical properties of these materials is their limited ductility and catastrophic failures in tension after reaching the elastic limit [Ashby and Greer (2006)]. Many research groups (both in theory and experiment) have investigated and studied the rheological properties of bulk metallic glasses being subjected to an external load [Inoue (2000) and Schuh, Hufnagel, and Ramamurty (2007)].

A reference state (in equilibrium) in order to study the rheological properties appears slightly above the glass transition temperature T_g where the system enters a metastable regime, the so-called *super-cooled liquid* (SCL) state [Öttinger (2006)]. The macroscopic response of SCLs and glasses when subjected to an external load can be studied via the so-called *stress-strain curve* [Larson (1999)] which, represents the evolution of stresses in a system as a function of strain. A typical stress-strain curve for glasses consists of three regimes: namely an elastic, a transient, and a steady-state regime. Beyond the elastic regime of the stress-strain curve, the cross-over response to a non-Newtonian liquid is marked by the occurrence of an overshoot in the transient regime, while the stress-strain curve of the glasses always represents a non-Newtonian response, the super-cooled liquids show a cross-over response from a Newtonian (for low strain rates) to a non-Newtonian liquid (for high strain rates). Initially, in the elastic regime, both SCLs and glasses behave as Hookean materials [Hooke (2016)], showing a linear response between the stresses and the applied external force. To obtain the elastic properties of glasses in computer simulations, applying a stress-fluctuation formalism [Lutsko (1989)], one can directly calculate the elastic moduli of a system. The elastic properties of a system can also be characterized in the low-frequency regime of the vibrational density of states [Sólyom (2007)]. A characteristic feature of amorphous solids in the low-frequency range of the spectrum ($\approx$ 1THz) is the occurrence of the Boson peak [Wang (2012a)]. In the

[3] www.liquidmetal.com
[4] www.heraeus.com
[5] http://genesismission.jpl.nasa.gov

limit of low frequencies, acoustic sound waves reflect the elastic features of the system and can be studied via the current correlation functions [Boon and Yip (1991)].

In the case of the super-cooled liquids, right after the overshoot, short-lived inhomogeneous flow patterns appear in the system, which span the whole system in a tiny strain window. On the other hand, in glasses, the inhomogeneities appear to be more persistent and often result in the formation of *shear bands* [Hays, Kim, and Johnson (2000) and Varnik, Bocquet, Barrat, and Berthier (2003)]. The shear bands are band-like structures with a higher strain or mobility than in other regions of the system, and play an essential role in understanding the phenomenon of yielding in glasses under external load [Hofmann, Suh, et al. (2008)]. Studying the effects of shear bands on mechanical properties of BMGs, and understanding the underlying processes which result in the formation and evolution of these inhomogeneities in the system, plays a crucial role in better understanding the phenomenon of yielding and plastic deformation in glasses.

Micro-alloying, as a method to adjust the mechanical properties of BMGs beyond the elastic limit, has been used in experiments by adding a tiny amount ($\approx 1\%$) of an alloying element to the glass-forming system [Hubek, Seleznev, et al. (2018) and Nollmann, Binkowski, et al. (2016)]. As a result of adding 1% of Co in a $Pd_{40}Ni_{40}P_{20}$ glass former in the latter references, minor changes are reported in the elastic response of the materials but, the significant effect of micro-alloying is for large deformations where the samples appeared to be more ductile concerning the original material without micro-alloying.

In this thesis, we study the effect of a simple planar Couette flow shear deformation (in which, the upper and lower planes of the samples are moving in the opposite direction with a constant velocity) on mechanical properties of a $Ni_{80}P_{20}$ metallic glass former, using non-equilibrium atomistic molecular dynamics computer simulation [Alder and Wainwright (1959) and Rahman (1964)]. In order to model the $Ni_{80}P_{20}$ metallic glass former, we used the Kob-Andersen binary Lennard-Jones mixture [Kob and Andersen (1994)] which consist of 80% A-type particles and 20% B-type particles, interacting via a Lennard-Jones [Lennard-Jones (1924)] potential. The samples are equilibrated in the super-cooled liquid state, and from there, we obtain the glass state via a sudden quench. The response of the samples in the super-cooled liquid and glass state to an external load is studied by subjecting them to a shear deformation using Lees-Edwards boundary conditions [Lees and Edwards (1972)]. The main focus of the current study is to try to characterize the effects of deformation on the mechanical properties of the model metallic glass former. Therefore, throughout this thesis, we make a comparison between the mechanical properties of the samples in the quiescent undeformed states, as a reference, and the deformed states. The latter state is obtained after switching off the shear load at a certain strain point

in the steady-state regime and allowing the stresses to relax for a certain time. A characteristic feature of BMGs are the remaining stresses in the system after switching off the external load, the so-called *residual stresses* [Ballauff, Brader, et al. (2013)]. After switching off the external load, the stresses show a decay towards a finite value, and a new deformed glass state with residual stresses is obtained. Therefore, another key focus of our study is to try to investigate the effects of residual stresses on the mechanical properties of our model glass former.

The elastic properties of the samples in the quiescence undeformed state are obtained by calculating the elastic moduli (shear modulus, Young's modulus, Poisson's ratio, and bulk modulus) with which later we compare the results of the deformed states. Further, as the elastic properties are reflected in the low-frequency spectrum of the vibrational modes, we characterize the effects of deformation on the vibrational modes in the low-frequency regime by means of current correlation functions and the Boson peak.

Beyond the elastic limit, we characterize the formation of inhomogeneous flow patterns (both in SCLs and glasses) that appear as a transient response to the external shear. For the super-cooled liquids, we analyze the crossover from Newtonian to non-Newtonian behavior. We show that, while in SCLs, the in-homogeneous flow patterns are short-lived, in glasses, these inhomogeneities are long-lived and form shear bands. Further, we will show that in glasses, shear bands can form in the flow direction as horizontal bands or perpendicular to the flow direction as vertical bands. We characterize the latter shear bands in terms of mobility maps, stress-strain relations, mean-squared displacements, and (local) potential energies.

The mechanical properties of a BMG, at large deformation, can be adjusted by making a minimal change in the alloy composition of the material. Therefore, in this work, we propose a model for micro-alloying in $Ni_{80}P_{20}$ metallic glass former, based on the original Kob-Andersen binary Lennard-Jones mixture. This has been done by introducing a third species type C, therefore, turning the binary mixture into a ternary system. We characterize the effects of micro-alloying on the mechanical properties of the new model by applying deformation on the system and comparing the macroscopic response of the system to the original model.

In the following, this thesis is organized into five main chapters. After the introduction, in **chapter 2** we discuss about the response of liquid and glasses under mechanical load. The chapter will begin with a brief introduction to the phenomenon of glass transition, including an overview of the changes occurring in the glass-forming liquid, in terms of dynamics and microscopic structure. Different regimes in the stress-strain curve (including the crossover response of the SCLs from a Newtonian to a non-Newtonian liquid) are also

discussed for SCLs and glasses. In **chapter 3**, we will give a theoretical description of the quantities which we have calculated in this work. This includes an overview of the elastic constant tensor definition and calculation of different elastic moduli, and the Lamé coefficients. Then, we will give a brief description of the vibrational properties of solids. This includes a brief description of the density of phonon states within the harmonic approximation and the corresponding Einstein and Debye descriptions. Furthermore, we will discuss the Boson peak as a characteristic feature in glasses, and introduce the dynamic correlation functions with which we study the propagation of acoustic sound waves in the system. In **chapter 4**, we will introduce the computational methods which we have used in our study. This consists of an overview of Molecular Dynamics simulations, including the requirements needed to perform non-equilibrium simulations in micro-canonical and canonical ensembles (numerical integration methods, thermostating, boundary conditions, etc.). The last subsection of this chapter describes the simulation details. In **chapter 5** we will present the results of our study. We will begin this chapter by discussing the response of SCLs and glass samples when subjected to a shear deformation. The formation and evolution of inhomogeneities in both SCLs and glass samples will be discussed in detail. Then, the effects of deformation on the elastic moduli of the glass samples, with respect to their initial undeformed states, will be presented. Furthermore, we investigate the effects of deformation on vibrational properties and the Boson peak of the glass samples. In the final section, we will present the results for a new micro-alloyed model, which we have proposed and make a detailed comparison to the original model.

2 Liquids and glasses under mechanical load

2.1 Liquids and the glass transition

"*If you have a glass full of liquid, you can discourse forever on its qualities, discuss whether it is cold, warm, whether it is really and truly composed of H-2-O, or even mineral water, or saki. Meditation is Drinking it!*"
Taisen Deshimaru

Simple liquids, crystalline solids, and the corresponding liquid-to-crystal transition have been studied for a long time, and their properties have been properly understood but, on the other hand, what makes glasses and the glass transition a puzzling phenomenon, relies on several un-answered rather poorly understood questions which have been addressed to these materials. Why does glass transition happen, and what are the underlying mechanism (or mechanisms)!? Why do the properties of the material depend on the history of their production and are time-dependent? What are the mechanical responses of these materials when subjected to an external load, and how does deformation change these responses? Etc. We will try to address these questions in detail. In this chapter, we will discuss the phenomenology of the glass transition, including an overview of the changes occurring during this transition in terms of dynamics and atomic correlations, from a simple to a super-cooled liquid and also in glasses. We will also discuss the glass transition temperature and discuss different glass-forming systems. Further, as the main focus of this thesis, we will make a comparison between the response of super-cooled liquids and glasses when subjected to an external load, including the cross-over response of super-cooled liquids from a Newtonian to a non-Newtonian liquid.

2.1.1 *The onset of slow dynamics and the glass transition*

When a liquid is cooled down slowly below its melting temperature T_m, the nucleation of crystalline nuclei, starts in the liquid. The nucleation is activated in the cooled liquid (in the metastable regime) with a small perturbation like a change in pressure. The nucleation process (homogeneous or heterogeneous nucleation) then follows by the formation of nuclei, which can grow in the system in a crystallization process [Mullin (2001)]. Therefore, the liquid will undergo a phase transition and become a crystalline solid. The process is schematically illustrated in Fig. 2.1. By slowly cooling a liquid, its volume will decrease as a function of temperature and shows a discontinuity at T_m. This discontinuity, is by definition, the signature of a first-order phase transition, as volume $V = (\partial G/\partial P)_T$, is the first derivative of Gibbs free energy G with respect to its thermodynamic conjugate variable pressure, P [Binder (1987) and Stanley (1971)]. If the cooling process is very fast, the story becomes very different. When a multi-component liquid (later in this chapter, we will discuss glass-forming liquids in more details) is quenched to temperatures below its melting temperature, there will be no discontinuity in the $V-T$ phase diagram and the liquid will undergo a gradual, continuous transition (the so-called "*glass transition*") and become an amorphous solid. A key remark here is that the crystallization process has to be bypassed during the glass transition in order to obtain an amorphous phase (later in this chapter, we will discuss this in more detail). In contrast to the liquid/crystal transition, the glass transition is not a thermodynamic transition. There is no phase coexistence between the two phases, and extensive variables (in this case volume) do not show any discontinuity. The liquid-to-glass transition is a kinetically driven phenomenon during which, the dynamics of the system shows a tremendous slowing down in a small temperature window around the *glass transition temperature* (T_g). Therefore, the glass transition can be considered as a "*kinetic phase transition*" [Debenedetti and Stillinger (2001)]. During the quench process (as illustrated in Fig. 2.1), the liquid will experience a metastable state in the super-cooled liquid regime [Öttinger (2006)] and show a glass transition at T_g.

In order to understand the glass transition phenomenon and the underlying processes during this transition, we need to have a clear picture of different aspects of this transition, e.g., what happens when a liquid is quenched to low temperatures? What kind of fluids shows a glass transition? What are the underlying processes resulting in the slowing down of the dynamics? Etc. Here, we try to give a brief and clear answer to these questions.

"How does fast cooling bypass the crystallization process?"

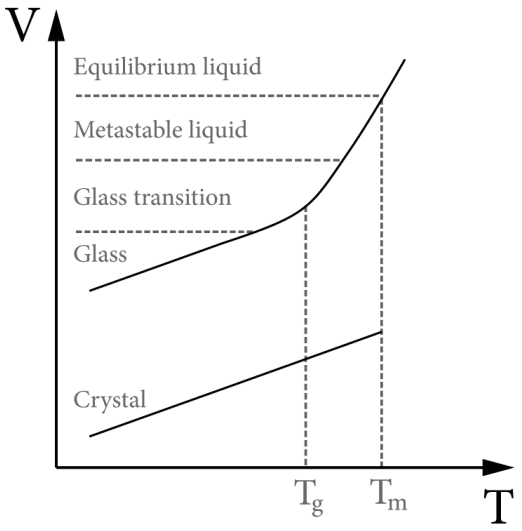

Figure 2.1: Schematic phase diagram of liquid to solid transition, showing different paths which will lead to crystalline or a glass phase.

By quenching a liquid with a sufficiently high cooling rate, the system will be driven out of equilibrium, and the liquid structure gets arrested in an amorphous state. The term "*sufficient*" here means that the cooling rate is much faster than the typical time needed for structural rearrangements. Therefore, the crystallization process is avoided as the system does not find the time to undergo a first-order liquid-to-crystal phase transition. This is due to the fact that, in a liquid-to-crystal transition, the activated nucleation processes in the metastable temperature regime will be followed by a crystallization process, but, at high cooling rates the system bypasses all these processes, and liquid structure gets frozen in a solid-state [Zallen (2008)].

"Do all liquids show glass transition by quenching?"

Even though in principle, by quenching any liquid, one can obtain a glass [Zallen (2008)], in a more realistic picture, one has to distinguish between *glass-forming liquids* and *non-glass-forming liquids* (which can be only driven to an amorphous state under special laboratory conditions). Glass-forming liquids are multi-component liquids in which, this multi-component nature bypasses the crystallization process. On the other hand, non-glass-forming liquids are mostly one-component liquids. This does not mean that one-component glass-forming liquids do not exist at all. Selenium (*Se*) [Pang, Wang, and Ding (1989) and Stephens (1976)] as an example, is a one-component glass-former. Obtaining a glass state is a matter of *"how fast"* and *"how far"* the liquid is quenched from the melting temperature. Therefore, glass transition in one-component liquids (also many multi-component fluids) is very difficult as bypassing the crystallization process needs special quench treatments, e.g., for the case of *Se* the crystalliza-

tion is suppressed kinetically, similar for polymer glass. Bulk metallic glasses (BMGs), being the subject of this study, are good glass-formers which are usually multi-component. Some examples are, $Zn_{20}Ca_{20}Sr_{20}Yb_{20}Li_{11}Mg_9$, $Ni_{80}P_{20}$, $Fe_{41}Co_7Cr_{15}Mo_{14}C_{15}B_6Y_2$ [Wang (2012b)], etc. BMGs have many applications [Inoue, Wang, and Zhang (2008) and Louzguine-Luzgin and Inoue (2013)], and therefore, have been the subject of many studies during the last decades.

The typical structural relaxation time in normal liquids are in the range of a few picoseconds[1]. As a result of lowering the temperature, there will be an increase in relaxation times of the liquid, which is a direct result of slowing down in the liquid's dynamics (check Fig. 2.2). This means relaxation times in liquids are strongly temperature-dependent [Binder and Kob (2011)]. Experimental studies have shown this strong temperature dependence such that a small change in temperature results in an increase in relaxation times by several orders of magnitude [Angell, Poole, and Shao (1994)]. Figure 2.2 is an Arrhenius plot (i.e. $\log(\eta)$ vs. $1/T$) of the temperature dependence of the viscosity. Viscosity shows a very similar temperature dependence behavior to structural relaxation times. However, experimentally $\eta(T)$ is a much easier quantity to measure (depending on the system) rather than relaxation times. As it is shown in Fig. 2.2, for some glass-formers, a change of the order of $1-2\%$ in temperature results in a change by several orders of magnitude in viscosity. For example, if one takes CKN in Fig. 2.2 where, $\log(\text{viscosity})$ is plotted as a function of inverse temperature KT^{-1} with large open circles, a small change from 1 to 3 in inverse temperature results in an increase in viscosity by 14 orders of magnitude. Different glass-forming

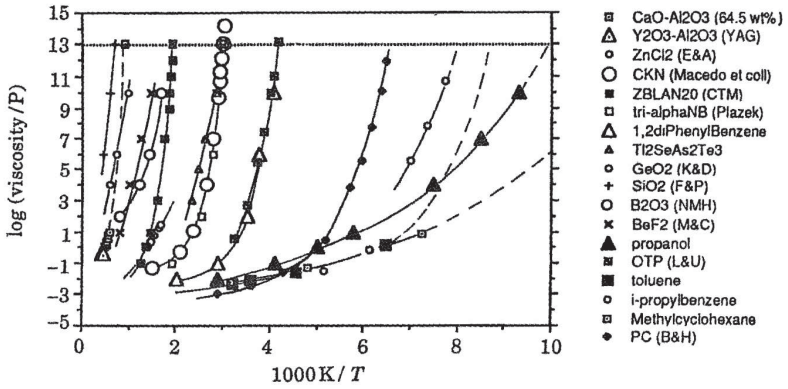

Figure 2.2: Arrhenius plot of temperature dependence of viscosity for several glass-forming liquids. *Image source:* [Angell, Poole, and Shao (1994)]

liquids show different tendency (with respect to different T_g's) towards glass transition. This has been shown in an Arrhenius plot ($\log(\eta)$ vs. T^{-1}) in Fig. 2.2. This makes the comparison between the curves in Fig. 2.2 very difficult. In order

[1]Rather than structural relaxation time, the bulk relaxation time $\tau = \eta/G_\infty$ in which, η is the viscosity, and G_∞ is the instantaneous shear modulus [Dyre (2006)], was first introduced by [Maxwell (1867)] (although Maxwell's description does not explain the non-exponential relaxation behaviors in glasses, nevertheless, it gives some reliable estimates).

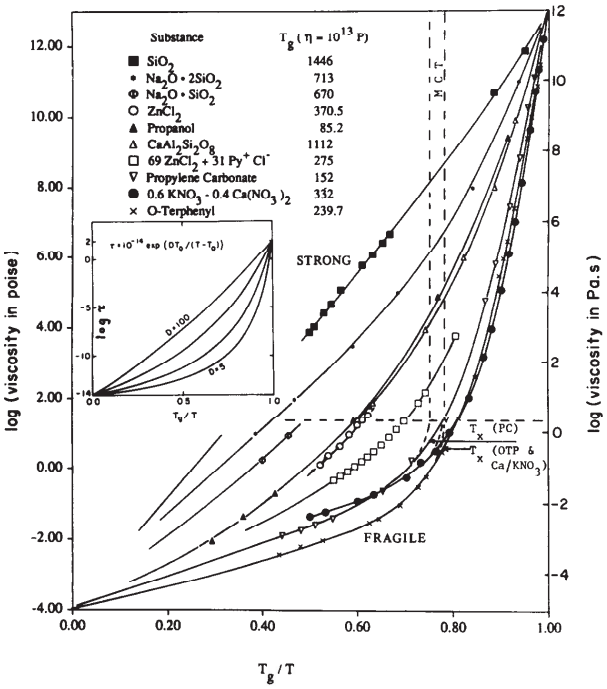

Figure 2.3: Arrhenius plot of temperature dependence of viscosity for different glass-forming liquids, scaled with glass transition temperature T_g. *Image source:* [Angell (1988)]

to overcome this problem, [Angell (1988)] suggested a classification in which, the glass-forming liquids are divided into two branches of *strong* and *fragile* (which does not refer to mechanical properties of the material). The Arrhenius plot of viscosities as a function of scaled temperature (T_g/T with $T_g = T\left(\eta = 10^{13}P\right)$), shown in Fig. 2.3, is called *Angell plot*[2]. With this representation one can clearly distinguish between a strong glass-former like SiO_2 (the linear line with close black squares, showing an Arrhenius increase) and a fragile glass-former like O-Terphenyl (the curved line with crosses, showing a non-Arrhenius increase). In a more quantitative way the so-called "*fragility*" of a glass-former is characterized with fragility index:

$$m = \left.\frac{d\log_{10}\eta}{dT_g/T}\right|_{T=T_g}, \tag{2.1}$$

with m being the slope of the curve in Angell plot in Fig. 2.3 at T_g, and ranges from 15 for strong glass-formers up to 200 for fragile glass-formers. Here it should be mentioned that, with this classification, the meaning of strong and fragile in Angell plot (shown in Fig. 2.3) is to show the temperature dependence of the increase in viscosity for different glass-forming liquids. Therefore, with this representation, the strong glass-former follows an Arrhenius law and the fragile glass-formers shows a non-Arrhenius behavior which can be fitted by the so-called *Vogel-Fulcher-Tammann* [Vogel (1921), Fulcher (1925) and Tammann and

[2]It should be mentioned that the choice of 10^{13}P is arbitrary and reflects a relaxation time of about one-two minutes ($\approx$ 100s) for a system at this viscosity. [Binder and Kob (2011)]

Hesse (1926)] function as:

$$\eta(T) = \eta_0 exp\left(\frac{B}{T - T_0}\right) \tag{2.2}$$

which shows a divergence at the so-called "*Vogel-temperature*", $T = T_0$ and a super Arrhenius increase of viscosity close to T_0. Here, the parameter B/T_0 determines the strong glass-formers when its very large and the fragile glass-formers for small values.

"What is T_g?"

In Fig. 2.1 we showed that, while quenching a glass-forming liquid, the volume shows a decrease down to the glass transition temperature T_g. At this point, the structural relaxation times increase by several orders of magnitude. Therefore, the system runs out of equilibrium and shows a glass transition. The temperature at which this transition happens, the glass transition temperature T_g, is not an intrinsic property of the system and it is highly dependent on the average cooling rate $\dot{T} = -\overline{dT/dt}$ with which the temperature is lowered [Aklonis and Kovacs (1979) and Zallen (2008)]. Figure 2.4 shows schematically how T_g changes with different $\dot{T}$. For $\dot{T}_3 < \dot{T}_2 < \dot{T}_1$ one obtains three different glass transition temperatures as: $T_{g_3} < T_{g_2} < T_{g_1}$. The lower the cooling rate, the lower the glass transition temperature. T_g shows a weak temperature dependence, i.e., a change of the order of one order of magnitude in cooling rate results in a shift of a few Kelvin in glass transition temperature. The shift in T_g towards the lower temperatures by extending the cooling process arises from the temperature dependence of relaxation times in the system. Close to glass transition temperature, the relaxation time increases by several orders of magnitude as a result of slow dynamics. Therefore, understanding the changes in the system dynamics during this transition will give us a more clear picture of the underlying processes which change the glass transition temperature.

"What are the underlying processes leading to slow dynamics?"

So far, we have seen that, by lowering the temperature in a glass-forming liquid, the relaxation times (typical time needed for structural re-arrangements) increase rapidly. As a result, the particle motion becomes slower and instead of a diffusive motion[3], the particles become trapped by the cages of their surrounding particles and become more and more correlated to their neighboring particles. In order to

[3]In terms of time-scales, diffusive motion corresponds to the linear regime at long times ($t \to \infty$) of the mean squared displacements where, MSD $\propto t$ (check Fig. 2.5). In terms of length scales, the diffusive regime corresponds to displacements larger than a particle radius (check Fig. 2.6).

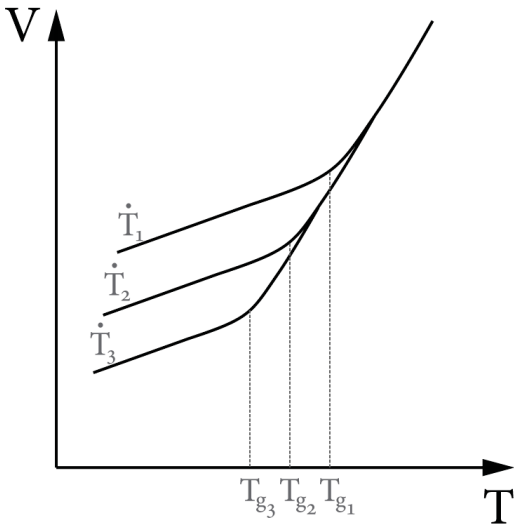

Figure 2.4: Schematic plot of cooling rate dependence of glass transition temperature.

investigate the underlying processes happening in the system dynamics while lowering the temperature, one can study the so-called "*mean-squared displacement*" (MSD)[4]. The MSD of a tagged particle i (in an N particle system) is defined as [Hansen and McDonald (2013)]:

$$\left\langle \Delta r^2(t) \right\rangle = \frac{1}{N} \sum_{i=1}^{N} \left\langle |\vec{r}_i(t) - \vec{r}_i(0)|^2 \right\rangle, \tag{2.3}$$

with $\vec{r}_i(t)$ the position of particle i at time t. The brackets denote an ensemble or time average. In the limit of $t \to \infty$; one expects that the Einstein relation holds, which is given by:

$$\left\langle \Delta r^2(t) \right\rangle = 2dDt, \tag{2.4}$$

with d the dimension and D the self-diffusion coefficient. Understanding the temperature dependence of MSD helps us to give a furthermore clear picture of the changes occurring in the system dynamics while lowering the temperature from a simple liquid to a super-cooled liquid just above the glass transition temperature and finally in a glass. This is shown in Fig. 2.5 (The presented results are obtained from a molecular dynamics computer simulation of Kob-Andersen binary Lennard-Jones mixture [Kob and Andersen (1994)] and are presented in reduced units. The details about the model and how it is implemented in computer simulation will be shown in chapter 4).

At short times, the MSD shows a quadratic behavior in time, for all temperatures (the purple dashed line in Fig. 2.5 is a quadratic function plotted next to

[4]Mean-squared displacement is the 2nd moment of a time-dependent correlation function $G_s(\vec{r}, t) = \frac{1}{N} \sum_j \langle \delta(\vec{r} - (\vec{r}_j(t) - \vec{r}_j(0))) \rangle$, the so-called *self-part of the van Hove function*. $G_s(\vec{r}, t)$ is the probability that a particle at time t has made a displacement $\vec{r}$ from its reference position $\vec{r}(0)$. [Harp and Berne (1970)]

the MSDs to show the t^2 dependence at short times). In this short-time regime, the tagged particle shows a ballistic motion and does not see the interactions with the other particles ("*ballistic regime*"). This quadratic behavior can be shown by a Taylor expansion of the trajectories in time: $\vec{r}_i(t) = \vec{r}_i(0) + \vec{v}_i(0)t + O\left(t^2\right)$ and therefore, $\left\langle \Delta r^2(t) \right\rangle = \left\langle |\vec{v}_i(0)|^2 \right\rangle t^2 + O\left(t^4\right)$. Considering velocities are given from a Maxwell-Boltzmann distribution one can easily show the temperature dependence of squared thermal velocities on temperature as $\left\langle |\vec{v}_i(0)|^2 \right\rangle = 3k_B T/2m$ [Binder and Kob (2011)]. The temperature dependence of MSD is shown in Fig. 2.5 where we clearly see that by lowering the temperature, the particle motion becomes slower and slower. For the liquid at high temperature one can distinguish between two different regimes. The ballistic regime at early times ($t \to 0$) and non-ballistic motion at later times ($t \to \infty$) where, the tagged particle sees the surrounding particles and interacts with them. As a consequence of these particle interactions at later times, the particles start to have random diffusive motion and MSD becomes a linear function of time (the linear regime is illustrated with gray dashed lines in Fig. 2.5). This is called the "*diffusive regime*".

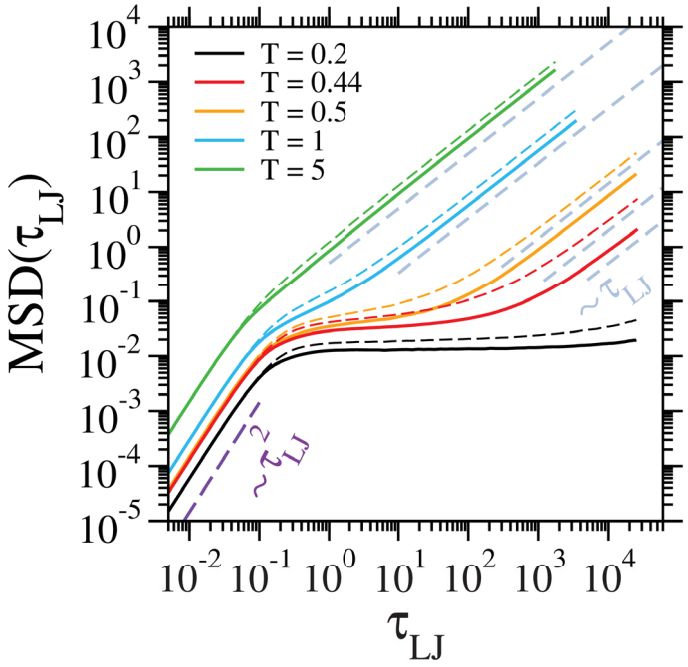

Figure 2.5: Mean squared displacement (solid lines correspond to particle type A and dashed lines with similar color correspond to particle type B), obtained from molecular dynamics computer simulation of Kob-Anderson binary Lennard-Jones mixture [Kob and Andersen (1994)] (the details about the model and how it is implemented in computer simulation will be shown in chapter 4), plotted at different temperatures (the values are in Lennard-Jones reduced units (check table 4.2)). The gray dashed lines are linear functions with slope = 1 and the purple dashed line is a quadratic function with slope = 2.

But, the difference between liquid dynamics at high and low temperatures arises from a third regime which, appears at low temperatures between the short-time regime and the diffusive regime at long times. As the temperature decreases and after the particles leave the ballistic regime and start to interact

with each other, they become trapped in the cages of their neighboring particles. This is called the "*caging regime*". At this stage, the particles are not moving that much, and MSD stays at a finite value. During this temporary time, the particles are only able to move within their cages, and it is only at relatively long times that they can leave their cages and show diffusive motion. This cage breaking behavior corresponds to the bending of the MSD at later times before reaching the diffusive regime. The importance of the caging regime comes from the fact that, as it is shown in Fig. 2.5, the caging regime is temperature-dependent, and it becomes broader at lower temperatures. Such that, in the glass state (black curve in Fig. 2.5), the particles need infinite time to break their cages and show diffusion motion. Another significance of the plateau regime in the super-cooled liquid is the occurrence of the so-called β-relaxations modes, which are due to the rattling of the particles within their cages. Therefore, the regime around the plateau in the MSD is called the β-relaxation regime. The β-relaxations are then followed, at later times, by the α-relaxation towards the diffusive regime [Binder and Kob (2011)]. The importance of the β-relaxation regime becomes even more significant at lower temperatures in the glass state (in the absence of α-relaxation) in which, the β-relaxation regime plays an important role in the mechanical properties, yielding, diffusion, aging, etc. of the material [Yu, Wang, and Samwer (2013)]. An extensive theoretical work has been done on the β-relaxation regime in terms of the mode-coupling-theory (MCT) [Bengtzelius, Götze, and Sjölander (1984) and Leutheusser (1984)]. The MCT predicts a dynamic singularity in the super-cooled liquids when the temperature is lowered below a certain critical temperature of T_c [Kob and Andersen (1994)]. Another prediction by the MCT, regarding the β-relaxation regime, is the existence of a von Schweidler law [Schweidler (1907)] in the plateau regime. The $\mathrm{MSD}(t)$ (in the latter regime) can be written as:

$$\mathrm{MSD}\,(t) = r_c^2 + A\left(\frac{t}{\tau_\beta}\right)^b , \tag{2.5}$$

with r_c a constant, A an amplitude, τ_β the temperature-dependent relaxation time of the β-relaxation and b a critical exponent.

"What makes a liquid, solid, at microscopic level?"

Up to now, we have seen that, by quenching a glass-forming liquid, the viscosity increases by several orders of magnitude, and the particles become trapped within the cages of their nearest neighbors. As a result, the liquid gets frozen in an amorphous solid state. What does this mean? By looking at a snapshot of atomic configurations solely, one cannot distinguish between a liquid and an amorphous solid. This is because, in a similar manner, in amorphous solids, there is no long-range structural order in the system. Meaning, in a crystalline solid where we have long-range order, by knowing the position of a single particle and the

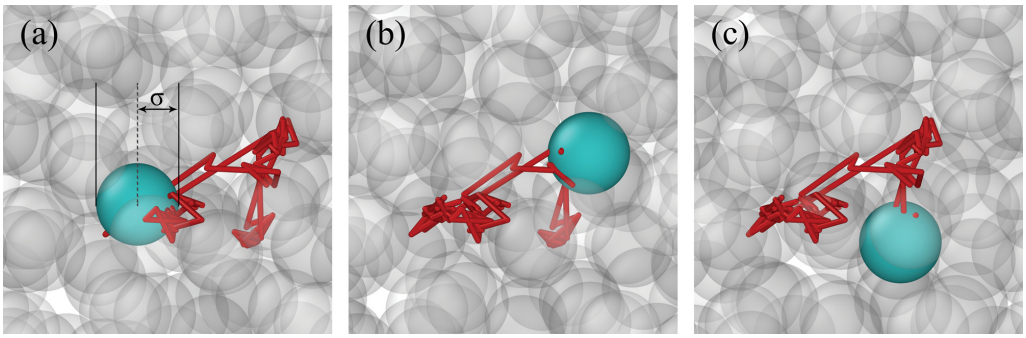

Figure 2.6: Schematic representation of particles motion in the super-cooled liquid state (at $T = 0.44$). Particle trajectory (in red) shows the distance that particle has traveled by hopping from one cage to another one. Figures (a), (b) and (c) correspond to $t_1 < t_2 < t_3$ respectively. In figure (c) the particle has reached the diffusive regime in Fig. 2.5

lattice constant, one can predict the average position of all the other atoms in any arbitrary direction [Kittel (1968) and Sólyom (2007)]. This is due to periodicity in crystalline solids. But, in amorphous solids and liquids, there are no periodicities and long-range order (this has been schematically shown in Fig. 2.7). What differs between an amorphous solid and a liquid are the short-range order and particle correlations with their nearest neighbors. The short-range orders in amorphous solids, allows us to study the physical quantities which are dependent on such a short-range correlation (interaction of particles with their nearest neighbors), like vibrational modes and propagation of sound waves. We will discuss this in more detail in the section (2.2.3).

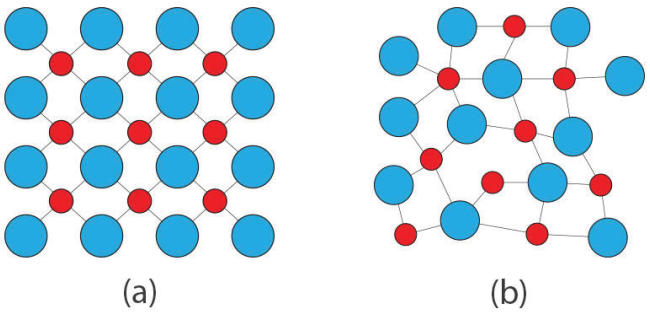

Figure 2.7: Schematic representation of a crystalline solid (a) and an amorphous solid (b).

Short and long-range correlations can be studied via spatial correlation functions. Here, we will introduce the *"radial distribution function"* ($g(r)$) as a tool to investigate the changes happening in particle correlations while lowering the temperature from a liquid state to obtain a glassy state eventually.

The radial distribution function measures to what extent the structure of a system is deviating from a random structure. This means, for an ideal gas, we expect the function to be 1, as the structure is completely random, and the possibility of finding a particle at a given distance in an arbitrary direction is 1. Considering particle i at position $\vec{r}_i$ the probability of finding other particles at

a given distance r, away from particle i can be obtained from the normalized pair correlation function as follows [Binder and Kob (2011) and Hansen and McDonald (2013)]:

$$g(r) = \frac{V}{N^2} \left\langle \sum_i \sum_{j \neq i} \delta\left(r - \left|\vec{r}_{ij}\right|\right) \right\rangle, \tag{2.6}$$

in which, V is the volume, N is the number of particles and $\left|\vec{r}_{ij}\right| = \left|\vec{r}_i - \vec{r}_j\right|$ is the relative distance between particle i and j. The role of the delta function in equation (2.6) is to count the number of particles which can be found within a shell of size r and $r + dr$ from the pinned particle. This is shown schematically in Fig. 2.8.

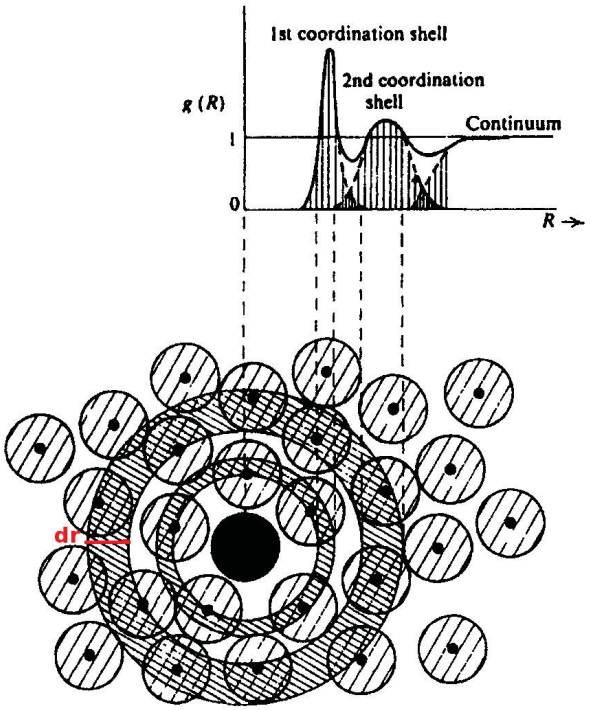

Figure 2.8: Schematic plot of $g(r)$, showing the position of first and second peak with respect to the first and second nearest neighbors. *Image source:* [Ziman and Ziman (1979)]

In Fig. 2.9, radial distribution functions are shown for four different temperatures (The presented results are obtained from a molecular dynamics computer simulation of Kob-Anderson binary Lennard-Jones mixture [Kob and Andersen (1994)] and are presented in reduced units. The details about the model and how it is implemented in computer simulation will be shown in chapter 4). These results are for three different states, namely liquid, a super-cooled liquid, and glass. The overall shape of all curves, as expected, shows a peak at distances relative to the shell of the first nearest neighbors. Here, we can see the increase in correlations between the first nearest neighbors (short-range order) with decreasing temperature. Before that, the function is just zero, as the particles cannot overlap.

The short-range order (the first peak in Fig. 2.9) shows an increase by lowering the temperature until in the glass state (black curve in Fig. 2.9) it shows the highest peak (it will further increase with decreasing T). The correlations eventually disappear at long distances and saturate at a value of 1, as there is no long-range order in the system. Here, rather than the increase in short-range correlations, another important observation can be made. In Fig. 2.9, we can see a significant change occurring in the second peak (corresponding to the second layer of nearest neighbors) as the temperature decreases from $T = 1$ to $T = 0.2$ (in reduced units see chapter 4). This split of the second peak (camel shaped black curve) is a characteristic behavior of metallic glasses. This splitting (often called medium-range order in the literature) already starts to appear in the super-cooled liquid state at $T = 0.44$ but gets very pronounced in the glass. There are several approaches in understanding the splitting of the second peak. For example, [Binder and Kob (2011)] explain this feature using *random close packing* structure and show that there are two layers of typical second nearest neighbors. Some other studies [Sheng, Luo, et al. (2006) and Wen, Cheng, Wang, and Ma (2009)] show that this splitting is due to the ordering of quasi-equivalent clusters, i.e., a minority of the particles in the system shows ordering. Despite being a topic of several studies, this phenomenon is still under a lot of debate!

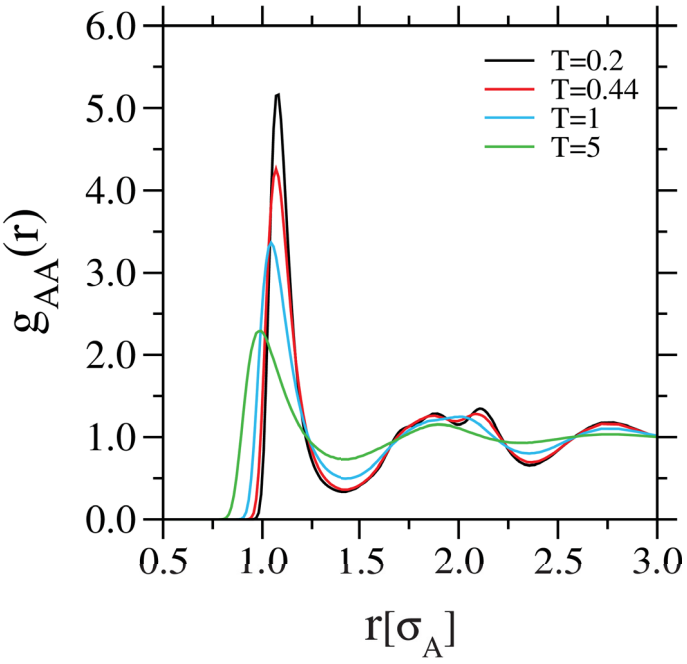

Figure 2.9: Radial distribution function calculated for correlations between A type particles ($g_{AA}(r)$) obtained from Molecular Dynamics computer simulation of Kob-Anderson binary Lennard-Jones mixture [Kob and Andersen (1994)] (the details about the model and how it is implemented in computer simulation will be shown in chapter 4). $g_{AA}(r)$ is shown for four different temperatures at three different states, from liquid to super-cooled liquids and the glass.

2.2 Rheology

In the previous section, we gave a brief overview of the changes occurring while lowering the temperature in a glass-forming liquid and different states which the fluid experiences before showing a glass transition. We saw that by quenching the liquid to temperatures well below the glass transition temperature, the viscosity increases rapidly. Finally, instead of a viscous liquid in the super-cooled liquid state, we obtain an amorphous solid. The rheological behavior of these materials is of great technological and scientific importance [Larson (1999)]. In this section, we will try to give a brief overview of the responses of glass-forming liquids to shear deformation in super-cooled liquid and glassy state.

2.2.1 From Newtonian liquids to glasses

To begin with, let's consider a fluid being subjected to a shear deformation using a simple planar Couette flow geometry [Batchelor and Batchelor (2000)]. The shear protocol is illustrated in Fig. 2.10. The flow is imposed to the system with constant shear rate $\dot{\gamma}$ in x-direction with a gradient in z-direction, such that the velocity profile will be given by $v_x(z) = \dot{\gamma} z$. For the *Newtonian fluids*, linear response holds such that, the steady-state stress, σ_{ss}, shows a linear increase with respect to the applied shear rate $\dot{\gamma}$, i.e. $\sigma = \eta\dot{\gamma}$ with η the zero shear viscosity [Binder and Kob (2011)]. The conditions under which this linearity holds and how one can distinguish between Newtonian and non-Newtonian liquids, strongly depends on the choice of shear rates and how far the fluid is from the glass transition temperature. As we discussed in the previous section, as the system reaches the glass transition temperature T_g, the viscosity increases by several orders of magnitude. Therefore, the linear response does not hold anymore even for very small $\dot{\gamma}$, as η decreases with increasing $\dot{\gamma}$ [Varnik (2006)], which is a characteristic property of glasses called *shear thinning*. This is shown in Fig. 2.11 where we present the shear rate dependence of viscosity for super-cooled liquids and glasses. From Fig. 2.11, we can see the decrease in viscosity with increasing shear rate. The only difference between the two appears at very low shear rates where the viscosity remains constant in the super-cooled liquids as they respond as a Newtonian liquid (we will discuss Newtonian and non-Newtonian liquids in more details in the next section). The time scale at which shear-thinning happens can be understood from the *Weissenberg number*, $We = \dot{\gamma}\tau$ (τ being the relaxation time of the un-sheared liquid) [Larson (1999)]. For $We > 1$ shear-thinning happens, the flow pattern will be non-linear, and the fluid behaves as a non-Newtonian fluid, and vice versa. This means, by a proper choice of shear rates, one can study different regimes in a super-cooled liquid where the system behavior changes from Newtonian to non-Newtonian (check Fig. 2.15) [Golkia,

Shrivastav, Chaudhuri, and Horbach (2020)]. Therefore, studying the response of glasses and super-cooled liquids to external load is of great importance in a deeper understanding of the properties of glasses [Lu, Ravichandran, and Johnson (2003)].

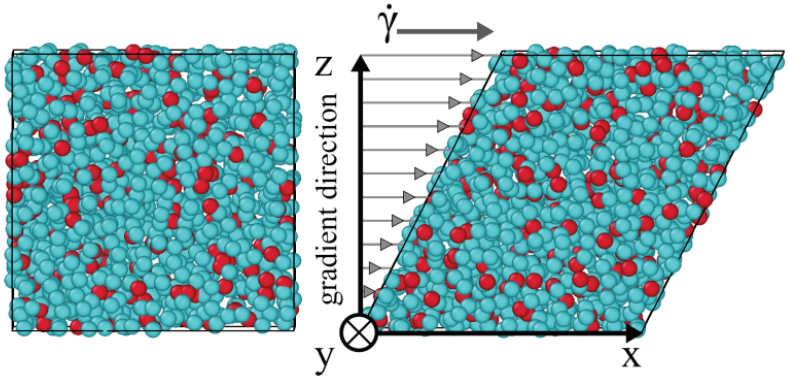

Figure 2.10: Schematic representation of shear protocol with a planar Couette flow geometry. The shear load is imposed in x-direction with a constant shear rate $\dot{\gamma}$ such that, the velocity profile shows a gradient in z-direction. The xz plane is being deformed and the corresponding component of the stress tensor will be σ_{xz}.

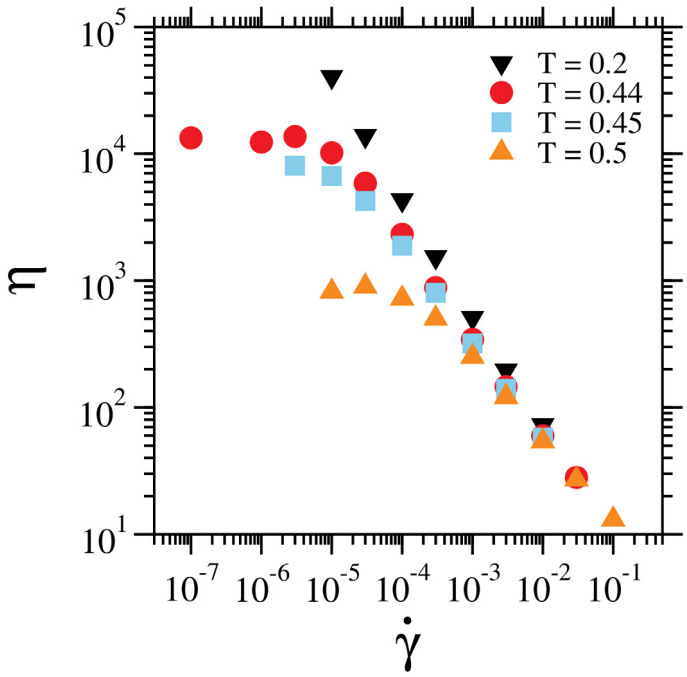

Figure 2.11: Viscosity as a function of shear rate for super-cooled liquids at T = 0.44, 0.45, 0.5 and glass at T = 0.2. At low shear rates (in the Newtonian regime) the viscosity remains constant for super-cooled liquids. But, by increasing shear rate (in the non-Newtonian regime) both super-cooled liquids and the glass show a decrease in viscosity.

2.2.2 *Affine vs. non-affine deformation*

In the previous section, we discussed the factors affecting the material's response to shear deformation from a Newtonian to a non-Newtonian flow. As it was mentioned earlier, in normal liquids, the relaxation times are in the range of a few picoseconds. Therefore, these materials have very low viscosities (e.g. compare viscosity of water $= 1.0016$ mPa.s at $T = 20^{\circ}C$ [Rumble (2017)] with viscosity of honey $\approx 2 \times 10^3 - 10^4$ mPa.s at $T = 20^{\circ}C$ [Yanniotis, Skaltsi, and Karaburnioti (2006)]) and even for very high shear rates, show a fast response to external load by a Newtonian flow. But, this is not the case for viscous liquids and glasses. When a viscous liquid in the super-cooled regime or glass is subjected to an external load (in this study shear deformation), the stresses start to build up in the system. The macroscopic response of the system and the increase of stresses as a function of applied strain rate, can be studied via the so-called *stress-strain curve* [Shrivastav, Chaudhuri, and Horbach (2016), Varnik, Bocquet, and Barrat (2004), and Zausch and Horbach (2009)]. Figure 2.12 shows a typical stress-strain curve obtained from a computer simulation of a metallic glass-former (the details of the simulation and the model which has been used will be discussed in chapter 4), being imposed to a shear deformation with a constant shear rate $\dot{\gamma} = 10^{-4}$ (stress-strain curves have been studied for different systems being imposed to shear deformation, e.g. [Zausch, Horbach, et al. (2008)] is a comparison between the results from Molecular Dynamics simulation, Mode Coupling Theory and confocal microscopy experiments on a colloidal system).

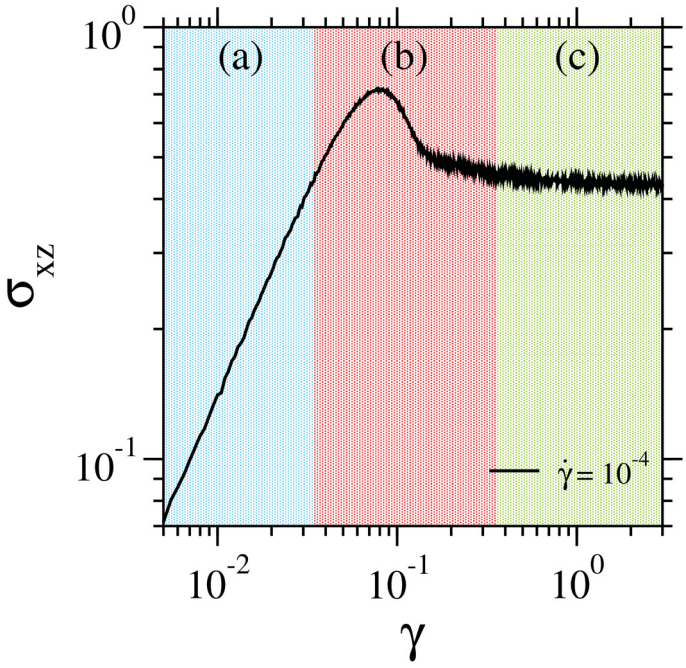

Figure 2.12: Stress-strain curve obtained from Molecular Dynamics simulations of metallic glass model (the simulation details will be shown in chapter 4), being imposed to a shear deformation with a constant shear rate $\dot{\gamma} = 10^{-4}$.

In Fig. 2.12 we see that, as a result of the applied deformation, initially the stresses (σ_{xz}) increase as a linear function of strain rate $\gamma = \dot{\gamma}t$ until it reaches a maximum (called *overshoot*). Then, after the overshoot, there is a small stress drop, and it continues gradually until the stresses remain at a finite value. Therefore, one can talk about three different regimes in stress-strain curve [Larson (1999)]. In Fig. 2.12, these three regimes (a, b and c) are shown with different colors. Initially, there is a linear relation between σ_{xz} and γ. This is called the *elastic regime*.

In the elastic regime (blue regime (a) in Fig. 2.12), the system responds elastically to an applied deformation (Hooke's law) [Landau, Lifshitz, et al. (1986)] and undergoes an affine deformation. This means by canceling the external load, the system can recover its original undeformed state, and the particle rearrangements are reversible. But, as the stresses are reaching a maximum, the stress-strain relation begins to deviate from a linear relation, the particle rearrangements are no longer reversible, and the system undergoes a non-affine (plastic) deformation [Falk and Langer (1998)]. This is called the *transient regime*.

Considering particle i being subjected to an external load (check Fig. 2.13), the displacement vector can be written as $\vec{u}_i = \vec{r}_i - \vec{R}_i$. Here, $\vec{R}_i$ is the reference position and $\vec{r}_i$ is the new displaced position. If the particle displacement $\vec{u}_i$ can be expressed as: $\vec{u}_i = D\vec{R}_i$, in which, $D = C^{-1}_{\alpha\beta\chi\kappa}\sigma_{\alpha\beta}$ is the deformation tensor, $C^{-1}_{\alpha\beta\chi\kappa}$ is the inverse elastic constant tensor and $\sigma_{\alpha\beta}$ the stress tensor (will be discussed in details in chapter 3. $\alpha\beta\chi\kappa$ are Cartesian coordinates.), the deformation is considered as an *affine* deformation (Fig. 2.12(a)). When the linear relation between displacements and the reference position does not hold anymore, the deformation is considered as *non-affine* (Fig. 2.12(b)) [Ganguly, Sengupta, Sollich, and Rao (2013) and Ogden (1997)].

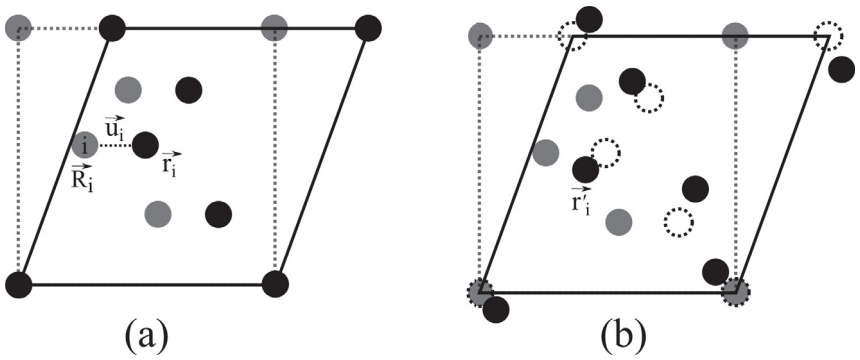

Figure 2.13: Schematic representation of affine deformation (a) and non-affine deformation (b) being imposed to a shear deformation. The gray circles represent the reference positions and the black circles show the displaced final position of particles. The dashed circles in (b) represent the expected position for an affine deformation.

In the transient regime (red regime (b) in Fig. 2.12), the stresses reach a maximum, and after crossing an overshoot, they decay and saturate at a finite

value. This is the regime in which the *yielding* occurs in the system [Shrivastav, Chaudhuri, and Horbach (2016) and Varnik, Bocquet, Barrat, and Berthier (2003)]. When a shear deformation is subjected to a system with a constant shear rate of $\dot{\gamma}$, a new time scale is introduced in the system as $1/\dot{\gamma}$. The occurrence of the overshoot, exhibiting a non-Newtonian response to the applied shear load, is a result of the latter time scale when its much smaller than the time scale for structural relaxation, i.e., $\dot{\gamma}\tau > 1$. The stresses show a compressed exponential decay towards the steady-state from the overshoot maximum, which occurs in a tiny strain window such that it often results in the formation of inhomogeneous flow patterns in the system. These band-like inhomogeneities, called *shear bands* (being another characteristic behavior of metallic glasses imposed on shear deformation, see section 2.2.4) appear to be a result of locally mobile regions in contrasts to regions with lower mobilities [Binkowski, Shrivastav, et al. (2016) and Shrivastav, Chaudhuri, and Horbach (2016)]. The shear bands tend to appear in metallic glasses under shear deformation after the overshoot (it should be mentioned here that the shear bands do not always appear in the system. "*How, why and when do the shear bands form?*" are open questions which are still under a lot of debates. [Golkia, Shrivastav, Chaudhuri, and Horbach (2020)]). Here, we should draw the readers attention to the fact that the response of the material in the transient regime and formation of in-homogeneous flow patterns, is high temperature and shear-rate dependent [Shrivastav, Chaudhuri, and Horbach (2016) and Varnik and Henrich (2006)] (This will be discussed in more details in chapter 5, where, we make a comparison between the mobility maps of the systems in the super-cooled liquid state and glass). In Fig. 2.14 we show the temperature dependence of the transient regime, for a system being imposed to a constant shear rate $\dot{\gamma} = 10^{-4}$ at three different temperatures $T = 0.5, 0.44, 0.2$. The first two temperatures are in the super-cooled liquid state, and the last temperature is well below the glass transition temperature.

It is clear from Fig. 2.14 that the transient regime becomes less pronounced with increasing temperature, such that, for $T = 0.5$, we do not observe an overshoot anymore. The stress-strain curve only shows a shoulder type increase and saturates at a finite value. But in an opposite manner, by decreasing temperature the overshoot and the transient regime become more and more pronounced until in the glass state, we observe a well-pronounced overshoot (more details on the shear rate dependence of the in-homogeneous flow patterns and the shear bands, can be found in [Shrivastav, Chaudhuri, and Horbach (2016)]. The temperature dependence has been studied in [Golkia, Shrivastav, Chaudhuri, and Horbach (2020)]). In the super-cooled liquids, the shoulder becomes even less pronounced in the limit of low shear rates. This is due to the fact that at low shear rates, the whole system starts to flow homogeneously but, at lower temperatures and higher shear rates, the in-homogeneities start to grow in the system, which results

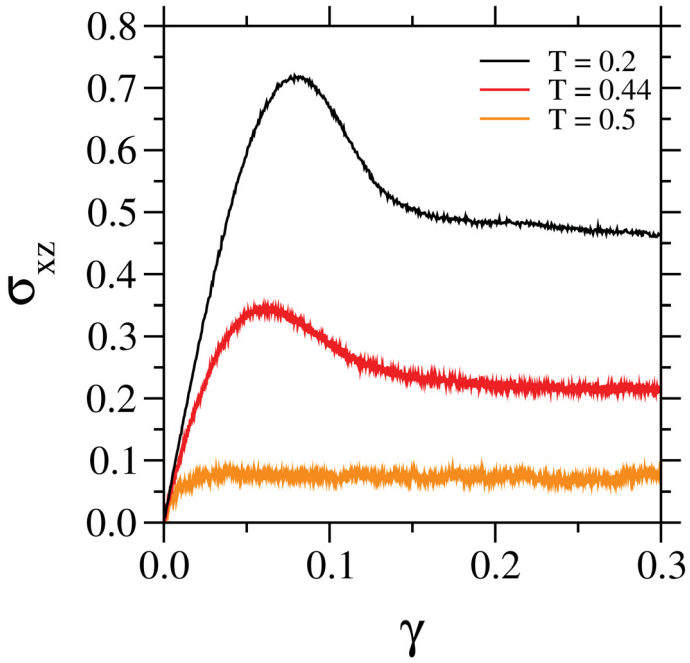

Figure 2.14: Stress-strain curves obtained from Molecular Dynamics simulations of metallic glass model (the simulation details will be shown in chapter 4) at three different temperatures. $T = 0.5$, 0.44 in the super-cooled liquid state and $T = 0.2$ in glass state. The systems are imposed to a shear deformation with a constant shear rate $\dot{\gamma} = 10^{-4}$.

in an overshoot in the stress-strain curve.

The third regime (c) in Fig. 2.12 is called the *steady-state regime*. In this regime, there are no shear bands and the non-mobile regions of the system also become mobile, the system fluidizes, and the whole system starts to show a steady flow with a linear velocity profile. These flow patterns can be studied in terms of the so-called *flow curve* which is the evolution of the steady-state stress σ_{ss} as a function of shear rate $\dot{\gamma}$. This is shown in Fig. 2.15 (The presented results are obtained from a molecular dynamics computer simulation of Kob-Anderson binary Lennard-Jones mixture [Kob and Andersen (1994)] and are presented in reduced units. The details about the model and how it is implemented in computer simulation will be shown in chapter 4. In Fig. 2.15, as it was discussed earlier, we can clearly see a crossover from a Newtonian (linear increase of σ_{ss} as a function of $\dot{\gamma}$, dashed gray lines in panel (a)) to a non-Newtonian (non-linear increase of σ_{ss} as a function of $\dot{\gamma}$, dashed gray lines in panel (b)) response in super-cooled liquids at the temperatures $T = 0.44$, 0.45, 0.5. This is not the case for the system in the glass state. Even at low shear rates, the flow pattern remains non-Newtonian and shows a typical Herschel–Bulkley behavior [Shrivastav, Chaudhuri, and Horbach (2016) and Varnik, Bocquet, and Barrat (2004)]. Herschel–Bulkley [Herschel and Bulkley (1926)] response of a fluid to an applied strain is associated to the non-Newtonian fluids where, the stress and strain do not have linear relation and the stress formation has a more complex relation with the applied strain as: $\sigma = \sigma_0 + \kappa\dot{\gamma}^n$, with σ_0 the yield stress, κ a

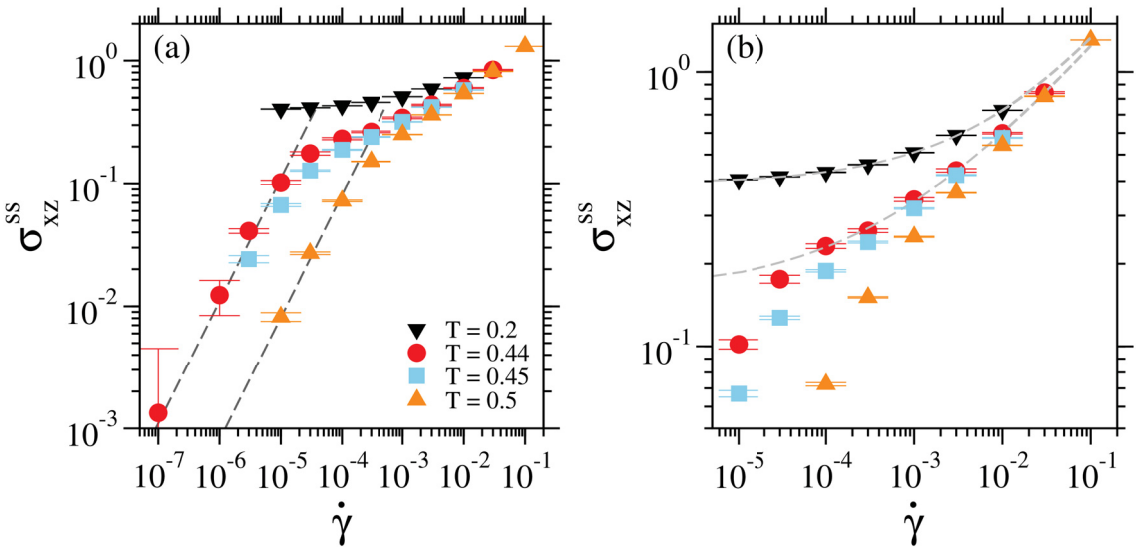

Figure 2.15: (a) Flow patterns for systems in the super-cooled liquid state at T = 0.44, 0.45, 0.5 and glass at T = 0.2. (dashed gray lines are linear fits in the limit $\dot{\gamma} \to 0$). (b) Herschel–Bulkley behavior of non-Newtonian fluid in the glass state (dashed gray lines).

constant and n the flow index (for $n < 1$ the fluid is shear-thinning and for $n > 1$ the fluid is shear-thickening. $n = 1$ and $\sigma_0 = 0$ corresponds to a Newtonian fluid). In Fig. 2.15(b) the data for system in glass state at temperature T = 0.2 has been fitted with the latter function (dashed gray lines. The fit values for the glass at T = 0.2 are $\sigma_0 = 0.389395$, $\kappa = 2.63875$ and $n = 0.446392$. The fit values for the super-cooled liquid at T = 0.44 are $\sigma_0 = 0.154735$, $\kappa = 2.6597$ and $n = 0.386652$). An important message here is, as the system reaches the temperatures close to glass transition temperature in the super-cooled liquid state, the Herschel–Bulkley behavior gets more pronounced. This is shown in Fig. 2.15(b), where, we also fitted the super-cooled liquid data at T = 0.44 with a Herschel–Bulkley function. But, eventually at low shear rates ($\dot{\gamma} \to 0$) the data starts to deviate from the fit function and becomes linear. This response is clearly less pronounced at higher temperatures in Fig. 2.15(b).

Up to now, we showed how the stresses build up in a metallic glass being imposed to shear deformation, which results in different responses in the system against the applied external load. But, another phenomenological behavior of metallic glasses appears when the external load is canceled, and the stresses are allowed to relax in the system. When the shear load is switched off from a metallic glass, not only the stresses, do not drop to zero, but they remain at a finite value in the system. These remaining stresses in the system are called *residual stresses* [Ballauff, Brader, et al. (2013)]. When a system is imposed to a shear deformation with a constant shear rate $\dot{\gamma}$, the stress relaxation in the system, is in the time-scale of $1/\dot{\gamma}$. But, as the system has been deformed in the time-scales of multiples of $1/\dot{\gamma}$ when the shear load is switched off, the stresses don't find the time needed to relax and remain as residual stresses in the system

(check Fig. 2.16).

Fig. 2.16 shows stress relaxation as a function of time (the shear load is switched off at strain $\gamma = 3$ in the steady-state regime of the stress-strain curve shown in Fig. 2.12, and the stresses are allowed to relax). We can see that the stresses tend to saturate at a finite value after a sharp stress drop from the switch-off point. Understanding the nature of these residual stresses and their effect on the mechanical properties of the material is of great importance [Withers (2007)]. Therefore, in this study, we tried to characterize the effect of deformation and the residual stresses on the mechanical properties of the metallic glasses by making a comparison between the undeformed (as reference) and deformed states.

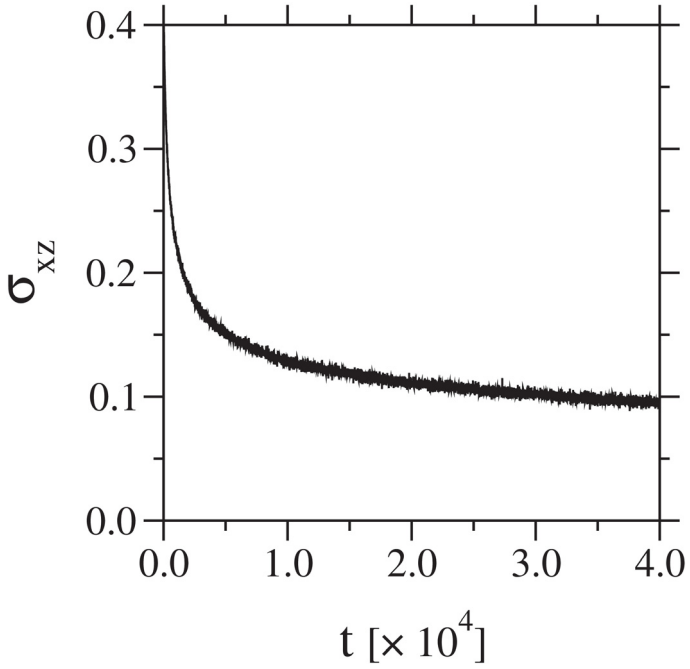

Figure 2.16: Stress relaxation as a function of time, obtained from Molecular Dynamics simulations of a metallic glass model (the simulation details will be shown in chapter 4), after switching off the shear load at $\gamma = 3$ in the steady state regime shown in Fig. 2.12.

2.2.3 *Vibrational properties of metallic glasses*

In the previous sections, we showed that, by lowering the temperature in a glass-forming liquid, the viscosity increases, and eventually below the glass transition, the viscous fluid behaves like an (amorphous) solid. We also discussed the fact that, during these transitions, the short-range order increase in the system, which results in higher correlations between the nearest neighbors. As a result of these short-range order, one can study some collective properties, similarly as for the crystalline solids, like vibrational excitations and propagation of sound waves for glasses within the classical harmonic approximation [Horbach, Kob, and Binder (1999) and Tanguy (2015)]. Of course, the challenge in the case of glasses and super-cooled liquids arises from the fact that there is no long-range

order in the system. Therefore, there is a limit in continuum responses of these materials beyond which the disorder changes the elastic responses of the system [Horbach, Kob, and Binder (2001) and Leonforte, Boissiere, et al. (2005)]. The interference of the collective excitations of the system with the disorder (in the time and length-scales at which the vibrational modes cannot be expressed in terms of plane waves anymore), results in another characteristic behavior of amorphous solids, the *Boson peak* (more details will be discussed in chapter 3.) [Grigera, Martin-Mayor, Parisi, and Verrocchio (2003) and Horbach, Kob, and Binder (1999)].

In this study, we tried to investigate the vibrational modes in metallic glasses in terms of some dynamic correlation functions, which will be discussed in the next chapter (3). We also investigate the effect of deformation and the residual stresses on vibrational excitations in metallic glasses, which will be discussed in detail in chapter 5.

2.2.4 *Shear banding in BMGs*

As it was discussed earlier in section 2.2.1, we showed that, while the steady-state shear stress (σ_{ss}) has a linear dependence on the applied shear rate ($\dot{\gamma}$) in a Newtonian fluid ($\sigma_{ss} = \eta\dot{\gamma}$ with η the shear viscosity), a non-Newtonian fluid shows a nonlinear response to an applied shear load and the shear viscosity decreases by increasing shear rate (check Fig. 2.11). This crossover from a Newtonian to a non-Newtonian liquid was shown in Fig. 2.15(a) where the linear response of the flow curve for the SCLs in the limit of $\dot{\gamma} \to 0$ changes to a non-linear response around a critical shear rate $\dot{\gamma}_c$ (we will discuss this in more details in chapter 5). In glasses reaching a linear response regime is not accessible, and the glass, under applied shear deformation, follows a Herschel-Bulkley law (as it was discussed in section 2.2.2 and shown in Fig. 2.15).

Going back to BMGs (as the main focus of this study), another characteristic behavior of the BMGs is the occurrence of long-lived in-homogeneous flow patterns, in the form of *shear bands* [Greer, Cheng, and Ma (2013) and Schuh, Hufnagel, and Ramamurty (2007)], after the overshoot on the stress-strain curve. These band-like structures are the regions with local higher mobilities to the rest of the system. Shear bands have been studied both in experiments as well as simulations [Binkowski, Shrivastav, et al. (2016) and Shrivastav, Chaudhuri, and Horbach (2016)]. In this work, we investigate and characterize the formation of different types of shear bands (horizontal or vertical). Also, we make a systematic comparison between the properties of the system (in terms of potential energy, dynamics, etc.) inside and outside of the shear band zones. All this has been done by making a comparison with the response of a super-cooled liquid to shear deformation as a reference where we extensively studied the shear rate

dependence of the formation of inhomogeneous flow patterns in the super-cooled liquid state. We will present and discuss the results for this part of the work in section 5.1.4.

2.2.5 *Effect of micro-alloying on mechanical properties of metallic glasses*

Even though BMGs have many promising mechanical properties like high strength and corrosion resistance or extended elasticity [Ashby and Greer (2006)], still, a major drawback associated with these materials is their limited ductility and catastrophic failures in tension after reaching the elastic limit. Therefore, designing new methods to enhance the mechanical properties of the BMGs has been an active topic of research during the last decades. One of the methods in which one can adjust the mechanical properties of a BMG, at large deformation, is making a tiny change in the alloy composition of the material [Hofmann, Suh, et al. (2008)]. This is called *minor-* or *micro-alloying*. This is a method in which a small change has a huge impact on the mechanical and thermodynamical properties of the BMGs.

The motivation for this part of the project came from the work of our collaborators (check footnote 6 in section 5.3.3) who reported a significant change in the mechanical properties of their Pd based metallic glass-former, by adding 1% of Co to the samples. As a result of minor micro-alloying, the $(Pd_{40}Ni_{40}P_{20})_{99}Co_1$ showed much more ductility [Nollmann, Binkowski, et al. (2016)] under compression and bending. They were able to deform the material up to very large strains without breaking. Also, very interestingly, the Boson peak in the specific heat changed significantly [Hubek, Seleznev, et al. (2018)] in their experiments for both as-cast and cold rolled samples. The Boson peak appeared to increase slightly and saturate at a finite value at low temperatures. Therefore, to investigate the effect of micro-alloying on mechanical properties and the Boson peak of metallic glasses, we also tried to obtain a new ternary model based on the original binary Kob-Anderson mixture [Kob and Andersen (1994)]. The details of this model in computer simulation is discussed in section 4.3.4 and we will discuss the results in section 5.5.

3 Quantities of interest

"As she has the beauty of glass, she has its brittleness."
Pierre Corneille, Polyeucte Martyr - 1643

In this study, our primary focus is studying the effect of deformation and the residual stresses on mechanical properties of bulk metallic glasses. In this chapter, we define mechanical properties (including the elastic moduli) and also quantities such as the vibrational density of states and current correlation functions that are well suited to characterize the vibrational dynamics of amorphous solids. In particular, we used these quantities to compare undeformed glass states with deformed ones, i.e., glass states with residual stresses.

3.1 Elastic constant tensor

3.1.1 Lamé coefficients and the elastic moduli

The elastic constants of a solid are obtained from correlation functions, which are defined in terms of microscopic variables. Therefore, the elastic constants represent the macroscopic response of the material having the information about the microscopic state of the system. Understanding and linking these microscopic events to the macroscopic response of the system is one of the central issues in the studying of the mechanical response of solids.

The elastic constants of an isotropic solid can be expressed in terms of two independent constants, the so-called Lamé coefficients λ and μ [Chaikin, Lubensky, and Witten (1995)]. These constants can be calculated from the elastic constant tensor $C_{\alpha\beta\chi\kappa}$ in the framework of the stress fluctuation formalism as it was discussed earlier [Barrat, Roux, Hansen, and Klein (1988) and Wittmer, Xu, et al. (2013)]. The elastic constant tensor is defined as [Ray, Moody, and Rahman (1985)]:

$$C_{\alpha\beta\chi\kappa} = C^{B}_{\alpha\beta\chi\kappa} + C^{K}_{\alpha\beta\chi\kappa} - C^{F}_{\alpha\beta\chi\kappa} \, , \tag{3.1}$$

in which C^{B} is the Born term (corresponding to affine deformations [Born and Huang (1954) and Tsamados, Tanguy, Goldenberg, and Barrat (2009)]), C^{F} is the term related to mean-squared stress fluctuations (corresponding to non-affine displacement [Maloney and Lemaître (2004)]), and C^{K} is a constant tensor related to the temperature and number density of the system as:

$$C^{K}_{\alpha\beta\chi\kappa} = 2k_B T\rho \left(\delta_{\alpha\kappa}\delta_{\beta\chi} + \delta_{\alpha\chi}\delta_{\beta\kappa}\right) \, , \tag{3.2}$$

with $\alpha\beta\chi\kappa$ components of Cartesian coordinates in 3D, k_B the Boltzmann constant, T the temperature, ρ the number density of the system and $\delta_{\alpha\beta}$ the Kronecker delta defined as:

$$\delta_{\alpha\beta} = \begin{cases} 0 & \text{if } \alpha \neq \beta \\ 1 & \text{if } \alpha = \beta \end{cases} \tag{3.3}$$

The Born term is defined as:

$$C^{B}_{\alpha\beta\chi\kappa} = \frac{1}{V}\sum_{i<j}\left\langle \left(\frac{\partial^2 U}{\partial r_{ij}^2} - \frac{1}{r_{ij}}\frac{\partial U}{\partial r_{ij}}\right)\frac{r_{ij}^{\alpha} r_{ij}^{\beta} r_{ij}^{\chi} r_{ij}^{\kappa}}{r_{ij}^2}\right\rangle \, , \tag{3.4}$$

in which V corresponds to the volume of the system, $r_{ij} = |\vec{r}_i - \vec{r}_j|$ is the distance between particles i and j, and U is the pair potential. The $\langle\rangle$ bracket represents a canonical average. The Born term takes into account displacements on the microscopic level solely due to particle interactions. Therefore, the terms in the brackets correspond to forces acting between the particles and their relative

positions which, has been obtained via a Taylor expansion of the potential energy around the reference positions of the particles. The Born term expresses the *Hooke's Law* [Hooke (2016)], meaning, as the Hooke's law denotes a linear relation between the applied force and displacement caused by this force in a spring-mass system, the Born term also describes the affine displacements caused by an external force considering there is a linear relation between the applied force and the displacement.

[Hoover, Holt, and Squire (1969)] found a correction term to the Born expression of elastic constants at finite temperature [Born and Huang (1954)], showing that, rather than affine displacements (elastic/reversible deformations, cf. section 2.2.2), there are also non-affine displacements (irreversible/plastic deformations, cf. section 2.2.2) which effect the material's mechanical properties. Therefore, they introduced the *fluctuation formalism* as an extension to Born's theory. Initially, the correction term related the non-affine displacements to mean-square fluctuations of the strain (*strain-fluctuation formalism*) [Parrinello and Rahman (1982) and Ray and Rahman (1987)]. But, several disadvantages (e.g. slow converging elastic moduli, difficulties in performing constant-stress computer simulations, etc.) with the method [Gusev, Zehnder, and Suter (1996)] result in a different approach in which, the non-affine displacement were related to mean-squared fluctuation of stresses [Schnell, Meyer, et al. (2011), Voyiatzis (2013), and Yoshimoto, Jain, et al. (2004)], in the so-called *stress-fluctuation formalism* method. Implementing the latter method in computer simulations has been a valuable and reliable tool to study elastic moduli of different systems [Lutsko (1989)] such as hard-sphere system [Farago and Kantor (2000)], polymeric nanocomposites [Papakonstantopoulos, Yoshimoto, et al. (2005)] etc.

The stress fluctuation term C^F is defined as:

$$C^F_{\alpha\beta\chi\kappa} = \frac{V}{k_B T}\left[\langle\sigma_{\alpha\beta}\sigma_{\chi\kappa}\rangle - \langle\sigma_{\alpha\beta}\rangle\langle\sigma_{\chi\kappa}\rangle\right] , \tag{3.5}$$

$$\sigma_{\alpha\beta} = \frac{1}{V}\left[\sum_{i<j}\left(\frac{\partial U}{\partial r_{ij}}\right)\frac{r^\alpha_{ij}r^\beta_{ij}}{r_{ij}} - \sum_{i=1}^{N} m v^\alpha_i v^\beta_i\right] , \tag{3.6}$$

$\sigma_{\alpha\beta}$ are the components of virial stress tensor, in which m is the mass of particle i with a velocity v_i [Schnell, Meyer, et al. (2011)]. Eq. (3.5) measures the width of fluctuations in stress components of the virial stress tensor Eq. (3.6) [Tsai (1979)]. The first sum in the brackets in Eq. (3.6) measures the forces acting on particles across the plane of reference and the second sum corresponds to the momentum transfer by the particle motion towards the plane of reference (cf. Fig. 3.1). At zero temperature the second sum vanishes and the stress in the system only corresponds to particle interactions in the system in the absence of external force [Morante, Rossi, and Testa (2006)].

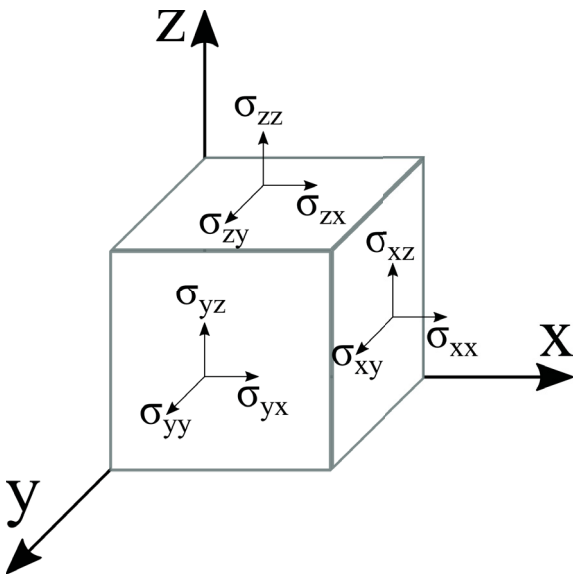

Figure 3.1: Schematic representation of different components of the stress tensor.

The elastic constant tensor is related to the Lamé coefficients λ and μ via [Chaikin, Lubensky, and Witten (1995)]:

$$C_{\alpha\beta\chi\kappa} = \lambda\delta_{\alpha\beta}\delta_{\chi\kappa} + \mu\left(\delta_{\alpha\chi}\delta_{\beta\kappa} + \delta_{\alpha\kappa}\delta_{\beta\chi}\right). \tag{3.7}$$

Once we have the information about the elastic constant tensor Eq. (3.1), we can obtain the two independent Lamé coefficients. Here for simplicity we present the tensor components in Voigt notation [Voigt (1928)]. The Voigt notation is an easy way to represent a symmetric tensor by reducing its order. For example, considering the stress tensor as follows:

$$\boldsymbol{\sigma} = \begin{bmatrix} \sigma_{xx}^{1} & \sigma_{xy}^{6} & \sigma_{xz}^{5} \\ \sigma_{yx} & \sigma_{yy}^{2} & \sigma_{yz}^{4} \\ \sigma_{zx} & \sigma_{zy} & \sigma_{zz}^{3} \end{bmatrix}, \tag{3.8}$$

using the upper-diagonal and diagonal terms with the red notation, one can rewrite the stress tensor using Voigt notation as a 6-dimensional vector $\tilde{\sigma} = (\sigma_1, \sigma_2, \sigma_3, \sigma_4, \sigma_5, \sigma_6)$. In the same manner the elastic constants tensor can be rewritten in Voigt notation such that:

$$\mathbf{C} = \begin{bmatrix} C_{11} & C_{12} & C_{13} & C_{14} & C_{15} & C_{16} \\ C_{21} & C_{22} & C_{23} & C_{24} & C_{25} & C_{26} \\ C_{31} & C_{32} & C_{33} & C_{34} & C_{35} & C_{36} \\ C_{41} & C_{42} & C_{43} & C_{44} & C_{45} & C_{46} \\ C_{51} & C_{52} & C_{53} & C_{54} & C_{55} & C_{56} \\ C_{61} & C_{62} & C_{63} & C_{64} & C_{65} & C_{66} \end{bmatrix}. \tag{3.9}$$

with $1, 2, 3$ corresponding to x, y, z Cartesian coordinates in 3D respectively, and

$$\begin{aligned} 11 &\to 1 \quad & 23 &\to 4 \\ 22 &\to 2 \quad & 13 &\to 5 \\ 33 &\to 3 \quad & 12 &\to 6 \end{aligned}$$

such that, e.g. $C_{11} \equiv C_{1111} \equiv C_{xxxx}$ or $C_{44} \equiv C_{2323} \equiv C_{yzyz}$. Therefore, using this notation, the Lamé coefficients can be obtained from:

$$C_{12} = \lambda \, (= C_{21} = C_{13} = C_{31} = C_{23} = C_{32}) \ , \tag{3.10}$$

$$C_{44} = \mu \, (= C_{55} = C_{66}) \ . \tag{3.11}$$

The elastic moduli of the system (i.e., shear modulus, bulk modulus, Young's modulus, and Poisson's ratio) can be defined in terms of the Lamé coefficients [Barrat, Roux, Hansen, and Klein (1988) and Barron and Klein (1965)]. For example, the shear modulus G is defined as,

$$G = \mu - p_{exc} \ , \tag{3.12}$$

where p_{exc} is the excess pressure. Care has to be taken here about the appearance of p_{exc} in the calculation of the elastic moduli. The excess pressure $p_{exc} \equiv p - p_{id}$, with p the total pressure of the system and $p_{id} = k_B T \rho$ the ideal gas pressure, appears in the systems with pair potentials interactions as [Wittmer, Xu, et al. (2013)]:

$$\sigma^{ex}_{\alpha\alpha} \stackrel{!}{=} -p_{exc} = \frac{1}{dV} \left\langle \sum_l r_l u'(r_l) \right\rangle \ , \tag{3.13}$$

with d the spatial dimension, V the volume of the system, r the distance between two particles and $u'(r_l)$ the first derivative of the pair potential. Here $\sigma^{ex}_{\alpha\alpha}$ is the Kirkwood expression for the excess stress tensor [Allen and Tildesley (2017)]:

$$\sigma^{ex}_{\alpha\alpha} = \langle \hat{\sigma}^{ex}_{\alpha\alpha} \rangle \equiv \frac{1}{V} \sum_l r_l u'(r_l) \, n_{\alpha,l} n_{\beta,l} \ , \tag{3.14}$$

with $n_{\alpha,l}$ and $n_{\beta,l}$ being the normalized distance vectors.

The shear modulus measures the material's resistance against shear deformation (being imposed to an external force, perpendicular to the normal of the plane to which the force has been applied, cf. Fig. 3.2). This means, the larger the value of G, the more force we need to apply to deform the system. Therefore, as a measure of material rigidity, it is also called modulus of rigidity.

[1] Wang (2012b)
[2] McSkimin and Andreatch Jr (1972)
[3] Ledbetter (1981)
[4] Archer, Crandall, et al. (2012)

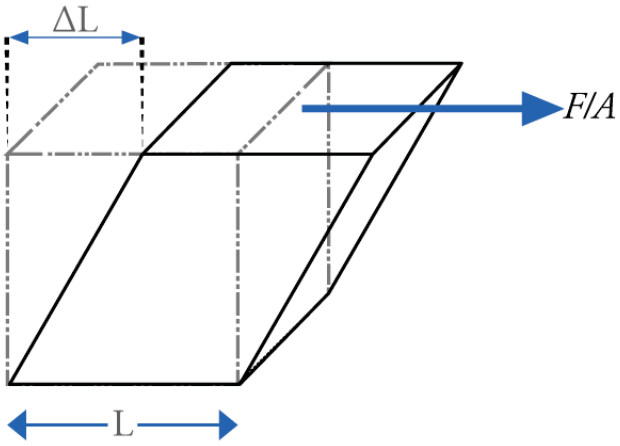

Figure 3.2: Schematic representation of a system being imposed to shear deformation. Shear modulus of the system is then defined as $G = \frac{F/A}{\Delta L/L} = \frac{\text{shear stress}}{\text{shear strain}}$.

Shear modulus (GPa)	
$Ni_{80}P_{20}$	36.7[1]
Diamond	478.0[2]
Stainless steel 316 (at 5°K)	81.0[3]
Polyethylene	0.117[4]

Table 3.1: Reported values of shear modulus in literature for some typical materials, compared to $Ni_{80}P_{20}$ being the subject of this study.

The bulk modulus K is defined as:

$$K = \lambda + \frac{(2\mu + p_{exc})}{3} . \tag{3.15}$$

The bulk modulus (check Fig. 3.3) measures a material's resistance against volumetric compression.

Bulk modulus (GPa)	
$Ni_{80}P_{20}$	161.0[5]
Diamond (at 4°K)	443.0[6]
Stainless steel 316 (at 5°K)	158.9[7]
Silicon rubber	$1.5 - 2$[8]

Table 3.2: Reported values of bulk modulus in literature for some typical materials, compared to $Ni_{80}P_{20}$ being the subject of this study.

[5] Wang (2012b)
[6] Kittel (1968)
[7] Ledbetter (1981)
[8] O'hara (1983)

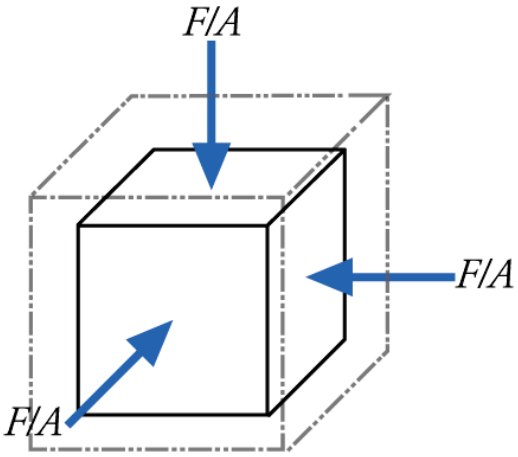

Figure 3.3: Schematic representation of a system being imposed to volumetric compression. Bulk modulus of the system is then defined as $K = -V\frac{d(F/A)}{dV}$. V being the volume of the system.

The Young's modulus E is defined as:

$$E = \frac{9KG}{3K + G} \,. \tag{3.16}$$

The Young's modulus (check Fig. 3.4) measures a material's resistance against uniaxial tensile or compressive stress. Young's modulus is a measure of stiffness of the system.

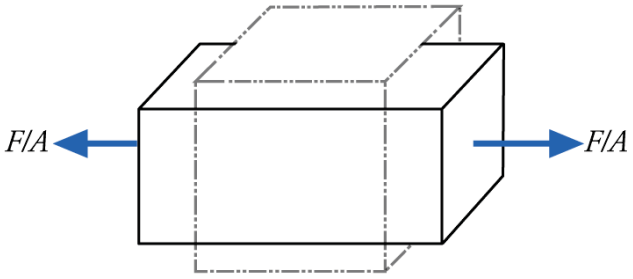

Figure 3.4: Schematic representation of a system being imposed to uniaxial tensile. Bulk modulus of the system is then defined as $E = \frac{\sigma}{\epsilon}$. Where, σ is the uniaxial stress and ϵ is the strain.

The Poisson's ratio ν is defined as:

$$\nu = \frac{3K - 2G}{2\,(3K + G)} \,. \tag{3.17}$$

The Poisson's ratio (check Fig. 3.5) is the ratio of transverse strain to axial strain (i.e., the rate of transverse compression/contraction to axial expansion).

[9] Wang (2012b)
[10] Spear and Dismukes (1994)
[11] Ledbetter (1981)
[12] O'hara (1983)

Young's modulus (GPa)	
$Ni_{80}P_{20}$	102.5[9]
Diamond	1220.0[10]
Stainless steel 316 (at 5°K)	207.7[11]
Silicon rubber	0.01–0.1[12]

Table 3.3: Reported values of bulk modulus in literature for some typical materials, compared to $Ni_{80}P_{20}$ being the subject of this study.

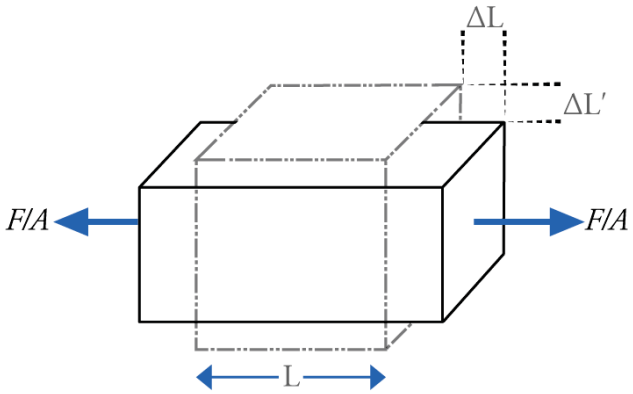

Figure 3.5: Schematic representation of a system being imposed to uniaxial tensile. The Poisson's ratio of the system, for small strains, can then be defined as $\nu = -\frac{\Delta L'}{\Delta L}$.

Poisson's ratio	
$Ni_{80}P_{20}$	0.394[13]
Diamond	0.2[14]
Stainless steel 316 (at 5°K)	0.282[15]
Silicon rubber	0.499[16]

Table 3.4: Reported values of Poisson's ratio in literature for some typical materials, compared to $Ni_{80}P_{20}$ being the subject of this study.

In this study, using molecular dynamics computer simulations, the stress-fluctuation formalism has been performed to calculate different elastic moduli of the bulk metallic glasses. The obtained values for the deformed glass states are then compared to those of the undeformed states (as reference). The simulation details will be presented in chapter 4, and we will discuss the results in chapter 5.

[13] Wang (2012b)
[14] Spear and Dismukes (1994)
[15] Ledbetter (1981)
[16] O'hara (1983)

3.2 Vibrational modes in solids

In solids, at low-temperatures (i.e. well below melting temperatures for crystalline solids and far from glass transition temperature for amorphous solids), atoms perform small amplitude oscillations around their equilibrium position (quasi-equilibrium position for amorphous solids). These oscillatory motions result in collective vibrational modes in the system. Understanding these vibrational modes is of great importance as these microscopic features (depending on the range of frequencies and wavenumbers) make a strong connection to mechanical and thermodynamical properties of the material (throughout this section our primary references were [Balucani and Zoppi (1995), Boon and Yip (1991), and Sólyom (2007)]).

3.2.1 Harmonic approximation

Both classical and quantum mechanical descriptions of atomic vibrations in harmonic solids are constructed under the basis of the so-called *harmonic approximation*. Considering the rest position of particle i as $\vec{R}_i^{(0)}$, from which it show's an oscillatory motion, we can write the quasi-equilibrium configuration of a N-particle system as:

$$\underline{\vec{R}}^{(0)} = (\vec{R}_1^{(0)}, \vec{R}_2^{(0)}, \cdots, \vec{R}_N^{(0)}) \, . \tag{3.18}$$

therefore the particle positions can be written as:

$$\vec{R}_i = \vec{R}_i^{(0)} + \vec{u}_i \, , \tag{3.19}$$

with $\vec{u}_i$ the displacement vector from the rest position[18]. The Hamiltonian of the system can be written as:

$$\mathcal{H} = \sum_{i=1}^{N} \frac{\vec{P}_i^2}{2M_i} + V(\vec{R}_1 \, , \vec{R}_2, \cdots, \vec{R}_N) \, , \tag{3.20}$$

with $\vec{P}_i$ and M_i the momentum and mass of particle i, respectively. But, this is a many-body problem that only can be solved analytically under certain assumptions. The first assumption was already mentioned above that; the atoms have vibrational motion around their rest position. Secondly, we assume that the interacting potential between particles has an absolute minimum for $\vec{R}_i^{(0)}$. Thirdly, we assume that the particle displacements are much smaller than interatomic

[18] It should be mentioned that the reason why within harmonic approximation particles are considered to be at their rest position is due to the fact that, the potential energy of the system has its minimum (quasi-local minimum). Therefore, the particles only show small amplitude oscillatory motion around this point. In amorphous solids, this quasi-rest position can be obtained at very low temperatures where there is no particle hopping from one cage to another. For example, one can quench the system to $T = 0$ and consider this stage as a rest position where the potential energy has its minima.

distances. Now we perform a Taylor expansion on the potential energy around $\vec{u} = 0$:

$$V(\underline{\vec{R}}) = V(\underline{\vec{R}}^{(0)}) + \sum_{i=1}^{N}\sum_{\alpha=1}^{3} \frac{\partial V}{\partial R_{i\alpha}}|_{\underline{\vec{R}}^{(0)}} u_{i\alpha} + \frac{1}{2}\sum_{i,j}\sum_{\alpha,\beta} \frac{\partial^2 V}{\partial R_{i\alpha}\partial R_{i\beta}}|_{\underline{\vec{R}}^{(0)}} u_{i\alpha}u_{j\beta} + O(u^3) \ . \tag{3.21}$$

Since we made the assumption that the potential has a minimum at $\vec{R}_i^{(0)}$, the terms linear in the displacement ($\propto u_{i\alpha}$) will vanish, and we can set the equilibrium energy to zero ($V(\underline{\vec{R}}^{(0)}) = 0$). Therefore, by making the substitution $\tilde{u}_{i\alpha} = \sqrt{M_i}u_{i\alpha}$ and $\tilde{P}_{i\alpha} = \frac{1}{\sqrt{M_i}}P_{i\alpha}$, we can rewrite the Hamiltonian as:

$$\mathcal{H} = \sum_{i=1}^{N} \frac{1}{2}\tilde{\vec{P}}_i^2 + \frac{1}{2}\sum_{i,j}\sum_{\alpha,\beta} \frac{1}{\sqrt{M_i M_j}} \frac{\partial^2 V}{\partial R_{i\alpha}\partial R_{i\beta}}|_{\underline{\vec{R}}^{(0)}} \tilde{u}_{i\alpha}\tilde{u}_{j\beta} \ . \tag{3.22}$$

This is the Hamiltonian of 3N coupled harmonic oscillators. As a result of this approximation, the potential only consists of the second-order terms, and thus, it is called the *harmonic approximation*. The Hamiltonian can be further simplified by defining the so-called *dynamical matrix* as follows:

$$(\underline{\underline{D}})_{i\alpha,j\beta} = \frac{1}{\sqrt{M_i M_j}} \frac{\partial^2 V}{\partial R_{i\alpha}\partial R_{i\beta}}|_{\underline{\vec{R}}^{(0)}} \ . \tag{3.23}$$

The dynamical matrix is a $3N \times 3N$ matrix, which is symmetrical and real. By diagonalization of the dynamical matrix numerically, we can decouple the harmonic oscillators and rewrite the Hamiltonian as:

$$\mathcal{H} = \frac{1}{2}\sum_{i=1}^{3N} \left(\hat{\vec{P}}_i^2 + \omega_i^2 \hat{\vec{u}}_i^2\right) \ . \tag{3.24}$$

This is the Hamiltonian of 3N independent harmonic oscillators. Therefore, we have simplified the many-body problem effectively to a one-particle problem by approximating the potential at its minimum with a harmonic potential.

3.2.2 Einstein model vs. Debye model

Having described the thermal motion of particles at a finite temperature about their rest position in the framework of the harmonic approximation, one can also make a connection between these thermal excitations and the thermal properties of the solid. Among these properties, the specific heat is of great interest, as it describes the energy fluctuations in the system. The specific heat at constant volume is defined as:

$$C_v = \left.\frac{\partial E}{\partial T}\right|_V \ . \tag{3.25}$$

In which, E is the total thermal energy of the system, which can be obtained from [Sólyom (2007)]:

$$E = \frac{\int d\Gamma \mathcal{H} e^{-\beta \mathcal{H}}}{\int d\Gamma e^{-\beta \mathcal{H}}} , \tag{3.26}$$

with $\beta = 1/k_B T$ and $d\Gamma = \prod_{\vec{q},j} d|Q_j(\vec{q})|\,d|P_j(\vec{q})|$ the volume element in the phase space in terms of normal coordinates $Q_j(\vec{q})$ and its conjugate momentum $P_j(\vec{q})$. Therefore, the total thermal energy can be written as:

$$E = \sum_{\vec{q},j} \frac{\int d\Gamma_j(\vec{q})\, \mathcal{H}_j(\vec{q})\, e^{-\beta \mathcal{H}_j(\vec{q})}}{\int d\Gamma_j(\vec{q})\, e^{-\beta \mathcal{H}_j(\vec{q})}} , \tag{3.27}$$

in which the Hamiltonian for each mode j has the form:

$$\mathcal{H}_j(\vec{q}) = \frac{1}{2}\left\{ \left|P_j(\vec{q})\right|^2 + \omega_j^2(q) \left|Q_j(\vec{q})\right|^2 \right\} . \tag{3.28}$$

The terms in the curly brackets in Eq. (3.28), correspond to the kinetic and potential energy of the vibrational modes, correspondingly. Based on the equipartition theorem, potential and kinetic energies of the system have $k_B T/2$ contribution in total energy. Therefore, for a system having $3N$ possible modes, each contributing $k_B T$, the total energy can be written as:

$$E = 3N k_B T . \tag{3.29}$$

Using Eq. (3.25) and plugging in Eq. (3.29), we obtain the *Dulong-Petit law* for the specific heat [Petit and Dulong (1819)]:

$$C_v = \frac{\partial E}{\partial T} = 3N k_B = 24.943\ \mathrm{J/molK} . \tag{3.30}$$

The classical expression for the specific heat given by Dulong-Petit is a constant. Although the theory is in good agreement with experimental results at high temperatures, it does not provide reliable results at low temperatures compared to experimental data. Here we should also remark that at high temperatures close to the melting temperature of a solid, the vibrations of the atoms increase such that higher-order corrections become important. Therefore, the harmonic approximation becomes less accurate, the phonons cannot be considered as well defined elementary excitation, and anharmonicities appear as deviations from the Dulong-Petit law. [Sólyom (2007) and Stern (1958)].

The most important result of the classical description of atomic vibration is that the motion of particles in the solid is described as harmonic oscillators for which the solutions are propagating plane waves. Based on this, Einstein applied the quantum mechanical description on atomic vibrations and assumed that a given harmonic oscillator with a vibrating frequency of ω has a quanta of energy

$\epsilon_n = \hbar\omega$ [Einstein (1907)]. Therefore, the mean thermal energy of a vibrational mode is given by [Sólyom (2007)]:

$$\langle\epsilon\rangle = \frac{\sum_{n=0}^{\infty} n\hbar\omega e^{-n\hbar\omega/k_B T}}{\sum_{n=0}^{\infty} e^{-n\hbar\omega/k_B T}} . \tag{3.31}$$

Einstein assumed that all the atoms in the solid are oscillating with the same frequency and in all directions (i.e., frequency is independent of the wave vector). This is called the *Einstein model for solids*, and the frequency with which the atoms are oscillating is called the *Einstein frequency* ω_E. Therefore, one can write the total internal energy of a system of N particles, all oscillating in the three spatial directions, as:

$$E = 3N\langle\epsilon\rangle = 3N\frac{\hbar\omega}{e^{\hbar\omega/k_B T} - 1} . \tag{3.32}$$

As a result, the specific heat based on Einstein description has the form of (cf. Fig. 3.6):

$$C_V = 3Nk_B \left(\frac{\hbar\omega_E}{k_B T}\right)^2 \frac{e^{\hbar\omega/k_B T}}{\left(e^{\hbar\omega/k_B T} - 1\right)^2} . \tag{3.33}$$

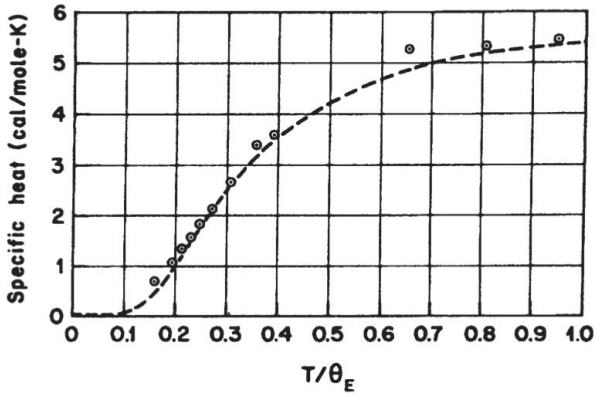

Figure 3.6: Temperature dependence of specific heat from Einstein model fitted to experimental data for diamond. *Image source:* [Einstein (1907)]

At high temperatures (i.e., $k_B T \gg \hbar\omega$), the Einstein model approaches $3Nk_B$, as predicted by the Dulong-Petit law. But, in the limit of low temperatures (i.e., $\hbar\omega \gg k_B T$), although the model agrees with experimental data to some extent at intermediate temperatures, the Einstein model of specific heat shows a rapid exponential decay toward zero. This is not in agreement with experimental data, in which the specific heat shows a slower decay compared to the Einstein model. The reason behind the fast decay of Einstein's model can be understood from the fact that in the long-wavelength limit (wavenumber $q \to 0$ and, frequency $\omega \to 0$) the atomic vibrations are acoustic sound waves which can be excited easily. But, as long as in the Einstein model, all the vibrations have the same

frequency, the long-wavelength limit (i.e., low-frequency, low-energy) collective modes are ignored.

In order to obtain a model for low temperatures, Debye proposed a model in which he assumed the vibrational modes are propagating in the system as acoustic waves and there is a linear dispersion relation between the frequencies and the wavenumber $\omega(\vec{q}) = c_s q$ (c_s being the average sound velocity for longitudinal and transverse sound waves). Therefore, the acoustic modes based on their polarization (i.e. longitudinal with frequency ω_L or transverse with frequency ω_T), carry quanta of energies $\hbar\omega_L$ or $\hbar\omega_T$ [Debye (1912)]. Based on this description, we can write the thermal energy associated with vibrations with polarization λ (longitudinal or transverse) and wave vector $\vec{q}$ as:

$$\langle \epsilon_\lambda(\vec{q}) \rangle = \frac{\hbar\omega_\lambda(\vec{q})}{e^{\hbar\omega_\lambda(\vec{q})/k_B T} - 1} , \tag{3.34}$$

and therefore, the total thermal energy would be:

$$E = \sum_{\vec{q},\lambda} \frac{\hbar\omega_\lambda(\vec{q})}{e^{\hbar\omega_\lambda(\vec{q})/k_B T} - 1} . \tag{3.35}$$

By this description, Debye proposed a reasonable prediction for the specific heat at low temperatures ($\hbar\omega(\vec{q}) \gg k_B T$) in good agreement with experimental results (cf. Fig. 3.7). It can be shown [Sólyom (2007)] that by Debye's description

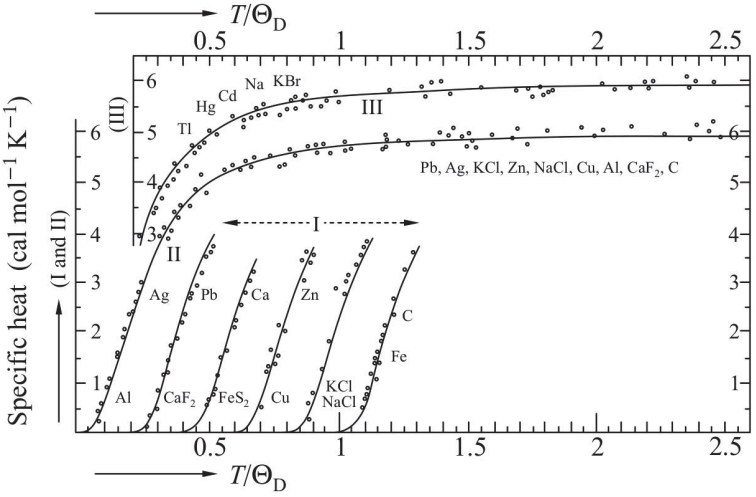

Figure 3.7: Experimental results for temperature dependence of the specific heat of different metals and crystals. The solid lines are from Debye interpolation formula. *Image source:* [Born and Huang (1954)]

at low temperatures ($\hbar\omega(\vec{q}) \gg k_B T$) the specific heat shows a cubic temperature dependence as:

$$C_V = \left.\frac{\partial E}{\partial T}\right|_V = \frac{12\pi^4}{5} N k_B \left(\frac{T}{\theta_D}\right)^3 . \tag{3.36}$$

The above expression can be obtained by plugging in Eq. (3.35) in Eq. (3.25), and defining the *Debye temperature* as $\theta_D = \hbar\omega_D/k_B$. Here, $\omega_D = c_s q_D$ is the *Debye frequency* and $q_D = \left(6\pi^2 N/V\right)^{1/3}$ the *Debye wave number*.

3.2.3 Density of phonons states

So far, we have discussed that the thermally excited vibrations (propagating as acoustic waves) can be considered as quasi-particles (fictitious particles carrying the quanta of energy) called *phonons* (the name phonon, has been chosen for quanta of acoustic vibrations in the same analogy that the quanta of the electromagnetic field are called a photon). Therefore, by having information about the phonons in the system, one obtains all the necessary data about the system energy/thermal state. But, all this is achieved once we have enough information about the contribution of all individual phonons in a specific state of the system. This is obtained by *density of state* $g(\omega)$. The density of states in d dimension is defined as:

$$g(\omega) = \sum_{\lambda} \int \frac{d\vec{q}}{(2\pi)^d} \delta\left(\omega - \omega_\lambda(\vec{q})\right) , \tag{3.37}$$

such that the quantity $g_\lambda(\omega)\, d\omega$ gives us the number of states with energies between $\hbar\omega$ and $\hbar(\omega + d\omega)$ and the role of the delta function in the above definition is to count the number of phonons within this energy interval. The above expression is obtained by replacing the sum over all possible wave vectors $\vec{q}$ (cf. Eq. (3.35)), by an integral over frequencies $\omega_\lambda(\vec{q})$ using $g(\omega)$ as a weight function. The total density in three dimensions, in the framework of Debye's model, can be written as:

$$g(\omega) = \frac{\omega^2}{2\pi^2}\left[\frac{1}{c_L^3} + \frac{2}{c_T^3}\right] . \tag{3.38}$$

Where, there are one longitudinal and two transverse propagating waves with the sound velocity c_L and c_T, respectively.

From Debye's density of states Eq. (3.38), assuming $\omega_\lambda(\vec{q}) = c_s|\vec{q}|$ and c_s being the mean sound velocity $3/c_s^3 = 1/c_L^3 + 2/c_T^3$, we can rewrite the total density of states based on Debye's description as:

$$g(\omega) = \begin{cases} \dfrac{9N}{V}\dfrac{\omega^2}{\omega_D^3} & \text{for } \omega \leqslant \omega_D , \\ 0 & \text{for } \omega > \omega_D . \end{cases} \tag{3.39}$$

The most important message from the above relation is the quadratic dependence of the density of states on frequency (in three dimensions). It has been shown that, in general for the limit of small frequencies where the dispersion relation of

the acoustic phonons is linear, the density of states (in d dimensions) shows the following proportionality to the frequency:

$$g(\omega) \propto \omega^{d-1} . \tag{3.40}$$

In computer simulations the density of states can be obtained by a Fourier transform of the velocity autocorrelation function, using the relation [Dove (1993)]:

$$g(\omega) = \frac{1}{Nk_B T} \sum_j \int_{-\infty}^{\infty} m_j dt e^{i\omega t} \langle \vec{v}_j(t) \vec{v}_j(0) \rangle . \tag{3.41}$$

As long as we are interested in studying the vibrational modes in the system, we are interested in the power spectrum of the time correlation functions, rather than their time dependence. The Fourier transform of the velocity autocorrelation function gives an equal weight contribution for each normal mode in the system. Therefore, the power spectrum of the mass-weighted velocity autocorrelation function is equal to the vibrational density of states.

Earlier in this section, it was mentioned that, by having information about the phonons (in terms of the density of states), we could obtain the thermal properties of the system. In Eq. (3.35), we obtained the relation for the total energy of the system. By applying the same treatment as for the density of states (replacing some overall possible wave vectors by an integral over frequencies), we can rewrite the total energy as:

$$E = V \int \frac{\hbar\omega}{e^{\hbar\omega/k_B T} - 1} g(\omega) \, d\omega . \tag{3.42}$$

Therefore, we can obtain a relation for the specific heat as:

$$\begin{aligned} C_V &= V \int \frac{\partial}{\partial T} \frac{\hbar\omega}{e^{\hbar\omega/k_B T} - 1} g(\omega) \, d\omega \\ &= V k_B \int \left(\frac{\hbar\omega}{2k_B T} \right)^2 \sinh^{-2} \left(\frac{\hbar\omega}{2k_B T} \right) g(\omega) \, d\omega . \end{aligned} \tag{3.43}$$

In this work, to study the effect of deformation and the residual stresses on the density of states and specific heat, using Eqs. (3.41) and (3.43), these quantities are calculated for both the undeformed (as the reference) and deformed states. A detailed comparison between these states will be presented in chapter 5.

3.2.4 The Boson peak

Two important messages from the last section were the frequency dependence of the density of states (in the long-wavelength limit, low frequencies) and temperature dependence of specific heat (at low temperatures). We have seen that, in the framework of Debye's model in three dimensions, $g(\omega) \propto \omega^2$ and $C_V \propto T^3$. Another characteristic behavior of the amorphous solids arises from deviations of

the density of states and specific heat from these proportionalities. This deviation appears as a peak in $g(\omega)/\omega^2$ and C_v/T^3, in the frequency/temperature spectra as the so-called *Boson peak*.

The boson peak, sometimes referred to in the literature as the *excess over Debye's squared-frequency law*, has been the subject of many studies on different glass-forming materials. For example, for silica glass, the Raman and neutron scattering experiments [Foret, Courtens, Vacher, and Suck (1996) and Winterling (1975)] showed a boson peak around frequencies $\omega \approx 1\text{THz}$, the simulation studies also reported occurrence of a boson peak around the same frequency range [Horbach, Kob, and Binder (2001)]. The boson peak was also observed in the specific heat around $T \approx 10\text{K}$, both in experiment [Buchenau, Prager, et al. (1986) and Zeller and Pohl (1971)] and simulation studies [Horbach, Kob, and Binder (1999) and Scheidler, Kob, et al. (2001)]. Also similar observations were made in experiments [Jiang, Peterlechner, et al. (2017), Li, Yu, and Bai (2008), and Mitrofanov, Peterlechner, Divinski, and Wilde (2014)] on metallic glasses. But the most important question here is,

"What is the nature of the Boson peak?"

The discussion on the origin of the boson peak has been very controversial, e.g., while [Benassi, Krisch, et al. (1996)] argued that the boson peak has its origin in the propagating acoustic waves which, even up to frequencies above the location of the boson peak, can be considered as plane waves, [Courtens, Foret, et al. (2003)] showed that around the frequencies in which the boson peak is observed ($\omega \approx 1\text{THz}$) the acoustic vibrational modes are strongly scattered by disorder, and this leads to the occurrence of the boson peak. [Buchenau, Galperin, et al. (1992)] used a soft potential model and related the coexistence of an-harmonic localized vibrations with the high-frequency acoustic modes within the frequency range around the occurrence of the boson peak. [Grigera, Martin-Mayor, Parisi, and Verrocchio (2003)] used the inherent structures (local minima of the potential energy) of a realistic glass model and claimed that the boson peak is a signature of a phase transition, from a minima-dominated phase (with phonons) at low energy, to a saddle-dominated phase (without phonons). [Taraskin and Elliott (2000)] used the criteria which correspond to a crossover between weakly and strongly scattered acoustic waves (the Ioffe-Regel crossover [Ioffe and Regel (1960)]) to investigate the propagation of the vibrational acoustic modes. By this analogy, the boson peak appears beyond the Ioffe-Regel limit, in which the longitudinal and transverse excitation become proportional to the lifetime of the modes, and they cannot be considered as plane waves anymore. In other words, around the frequency range in which the boson peak occurs, the phonons are not independent anymore. Therefore, we have the contribution of

phonon-phonon interaction as an excess over the Debye prediction. This corresponds to length-scales beyond the nearest neighbors of a single particle, where there are no more short-range orders, and the sound waves see the disorder in the system and become scattered. Despite all the descriptions mentioned above, still, the phenomena of the boson peak are under a lot of debates.

In this study, we tried to investigate the effects of deformation and the residual stresses on the boson peak and the acoustic sound modes. The boson peak (by means of the density of states and the specific heat) in the undeformed state (as the reference) has been compared to the corresponding deformed states. We will discuss this in detail in chapter 5.

3.3 Dynamic correlation functions

3.3.1 Microscopic dynamical variables

To begin this section, as we are interested in the time evolution of spatial correlations, we take into account the time dependence of particle coordinates $\vec{r}_i$. The time dependence of particle coordinates can be studied in terms of *microscopic dynamical variables*. A dynamical variable of a system of N particles is a function of some or all of the time-varying coordinates of the system. In general, a microscopic dynamical variable is defined as [Hansen and McDonald (2013)]:

$$A(\vec{r},t) = \sum_{i=1}^{N} a_i(t)\,\delta[\vec{r} - \vec{r}_i(t)] \ , \tag{3.44}$$

in which a_i is a physical quantity such as mass, velocity, energy, etc. of particle i. The spatial Fourier components of Eq. (3.44) can be written as:

$$A(\vec{q},t) = \int A(\vec{r},t)\, e^{-i\vec{q}.\vec{r}} d\vec{r} = \sum_{i=1}^{N} a_i(t)\, e^{-i\vec{q}.r_i(t)} \ . \tag{3.45}$$

When a microscopic dynamical variable satisfies the so-called *continuity equation*:

$$\frac{\partial A(\vec{r},t)}{\partial t} + \nabla \cdot \vec{J}^A(\vec{r},t) = 0 \ , \tag{3.46}$$

in which $\vec{J}^A$ is the current associated with the variable A, the microscopic dynamical variable is said to be conserved. The corresponding Fourier components of the continuity equation can be written as:

$$\frac{\partial A(\vec{q},t)}{\partial t} + i\vec{q} \cdot \vec{J}^A(\vec{q},t) = 0 \ . \tag{3.47}$$

In the limit $q \to 0$ and $\omega \to 0$ Eq. (3.47) shows the slow decay of the spontaneous fluctuations in a conserved variable. An example of a conserved local variable,

for the case of $a_i = 1$, is the time-dependent microscopic particle density:

$$\rho(\vec{r}, t) = \sum_{i=1}^{N} \delta[\vec{r} - \vec{r}_i(t)] \ . \tag{3.48}$$

The associated particle current then can be defined as:

$$\vec{J}(\vec{r}, t) = \sum_{i=1}^{N} \dot{\vec{r}}(t)\, \delta[\vec{r} - \vec{r}_i(t)] \ , \tag{3.49}$$

in which, $\dot{\vec{r}}(t)$ is the velocity of particle i. The Fourier components of the particle current can be written as:

$$\vec{J}_\alpha(\vec{q}, t) = \sum_{i=1}^{N} \dot{\vec{r}}(t)\, e^{-i\vec{q}\cdot r_i(t)} \ , \tag{3.50}$$

in which, α denotes whether the corresponding current is longitudinal (parallel to wavevector $\vec{q}$) or, transverse (perpendicular to wavevector $\vec{q}$). We will discuss these current correlations in more detail in the next section.

3.3.2 *Current correlations*

In this study, we tried to characterize the properties of the vibrational acoustic modes in terms of longitudinal and transverse current correlation functions ($\vec{J}_L(\vec{q}, t)$ and $\vec{J}_T(\vec{q}, t)$, respectively). By calculating these quantities, we were able to obtain the information about the longitudinal and transverse sound velocities from the corresponding dispersion branches of the dispersion relation. We were also able to investigate the properties of the corresponding longitudinal and transverse vibrations in the range of frequencies around the occurrence of the boson peak. This is associated with the time and length scales at which the vibrational modes can no longer be described as plane waves (although still, one can consider longitudinal and transverse projections), which will be discussed in detail in chapter 5. The longitudinal and transverse current correlation functions are defined as [Boon and Yip (1991)]:

$$J_\alpha(q, \omega) = \frac{1}{N} \int_{-\infty}^{\infty} dt e^{(i\omega t)} \langle \vec{J}_\alpha(\vec{q}, t) \cdot \vec{J}_\alpha(-\vec{q}, 0) \rangle \ , \tag{3.51}$$

in which $\alpha = L,\ T$ stands for the corresponding longitudinal and transverse currents. Since $\vec{J}_\alpha(\vec{q}, t)$ is a vector, the current correlation function is a second-rank tensor, but rotational invariance implies that for an isotropic fluid the longitudinal and transverse currents are un-correlated and independent (we discussed earlier the regime in which these modes become correlated) [Hansen and McDonald (2013)]. Therefore, the longitudinal and transverse current can be obtained from the total current:

$$\vec{J}(\vec{q}, t) = \sum_{k} \dot{\vec{r}}_k(t)\, e^{(i\vec{q}\cdot\vec{r}_k(t))} \ , \tag{3.52}$$

as:

$$J_L(q,\omega) = \frac{\vec{q}\left(\vec{q}\cdot\vec{J}(\vec{q},t)\right)}{q^2}, \tag{3.53}$$

$$J_T(q,\omega) = \vec{J}(\vec{q},t) - \frac{\vec{q}\left(\vec{q}\cdot\vec{J}(\vec{q},t)\right)}{q^2}. \tag{3.54}$$

In this work, we made a comparison between the properties of the longitudinal and transverse currents in the undeformed state (as a reference) and the corresponding currents of the deformed state. By doing so, we were able to investigate the effect of deformation and residual stresses on acoustic modes and the corresponding sound velocities.

3.3.3 *Dynamic structure factor*

The dynamic structure factor $S(q,\omega)$, defined as:

$$S(q,\omega) = \frac{1}{N}\int_{-\infty}^{\infty} dt \langle e^{(i\omega t)} \sum_{k,l=1}^{N} e^{(i\vec{q}\cdot(\vec{r}_k(t)-\vec{r}_l(0)))}\rangle, \tag{3.55}$$

is a quantity of great interest. Firstly, because it can be directly measured in scattering experiments [Scopigno, Suck, et al. (2006) and Suck, Rudin, Güntherodt, and Beck (1983)], and secondly, because of its direct relation to the longitudinal current correlation function as [Boon and Yip (1991)]:

$$S(q,\omega) = \frac{q^2}{\omega^2} J_L(q,\omega). \tag{3.56}$$

Although, the above relation shows that, the dynamic structure factor contains the same information as the longitudinal current correlation function, but, at low frequencies the dynamic structure factor is a more sensitive quantity. This is because of the $1/\omega^2$ term which, enhances the features at low frequency range (occurrence of the boson peak in dynamic structure factor at low frequencies).

For the case of dynamic structure factor, also we have made a comparison between the $S(q,\omega)$ of the undeformed states with those of the deformed ones, to investigate the effect of deformation and residual stresses on these dynamic quantities. We will discuss this in detail in chapter 5.

4 Atomistic computer simulation

"Our brain simulates reality. So, our everyday experiences are a form of dreaming, which is to say, they are mental models, simulations, not the things they appear to be."
Stephen LaBerge

In this study, we performed extensive molecular dynamics computer simulations to study a model of the glass-forming system $Ni_{80}P_{20}$ under shear. In this chapter, we will give a brief introduction to molecular dynamics simulations, and discuss the tools we have used and the details of our simulations.

4.1 Molecular Dynamics simulation

Solving Newton's equation of motion for a many-body system (e.g., system of N particles interacting via a pair potentials) has been a challenging problem in theoretical soft condensed matter physics. Numerical computation, as part of statistical mechanics, plays a crucial role in solving these ordinary differential equations. Many particle-based simulation techniques have been developed during the last decades [Binder and Ciccotti (1996), Car and Parrinello (1985), and Landau and Binder (2014)]. Molecular dynamics (MD) simulations, being a well known method for atomistic simulations, was developed in 1950's [Alder and Wainwright (1959) and Rahman (1964)]. The main goal in MD simulations is to calculate the structural and dynamical properties of a model system [Allen and Tildesley (2017) and Frenkel and Smit (2001)]. The basis of MD simulations is classical mechanics, and the idea is to numerically solve Newton's equations of motion for a many-body system (i.e., a large number of particles interacting with each other, e.g., via a pair potential) [Binder, Horbach, et al. (2004) and Rapaport (2004)]. Let's consider a system of N particles (atoms) with position vector $\vec{r}_i$, with $i = 1, \cdots, N$, in d-dimensions. Then, we can write Newton's equations of motion [Newton (1687)] for this system as:

$$m_i \ddot{\vec{r}}_i = -\frac{\partial U_{pot}}{\partial \vec{r}_i} = \vec{f}_i \, , \tag{4.1}$$

with m_i the mass of the i'th particle, U_{pot} the total potential energy and $\vec{f}_i$ the total force acting on particle i due to other particles in the system. The total potential energy (assuming a pairwise-additive potential which is only a function of distances between the particles) can be written as:

$$U_{pot} = \sum_{i=1}^{N-1} \sum_{j>i}^{N} u\left(\vec{r}_{ij}\right) \, , \tag{4.2}$$

where, $\vec{r}_{ij} = \vec{r}_i - \vec{r}_j$ is the distance vector between particle i and j. Therefore,

$$\vec{f}_i = -\sum_{j(\neq i)} \frac{\partial u\left(\vec{r}_{ij}\right)}{\partial \vec{r}_i} = \sum_{j(\neq i)} \vec{f}_{ij} \, , \tag{4.3}$$

with $\vec{f}_{ij}$ the force of particle j on particle i. As a result the total energy of the system can be written as:

$$E = E_{kin} + E_{pot} = \sum_{i=1}^{N} \frac{m_i \dot{\vec{r}}_i^2}{2} + U_{pot} \, , \tag{4.4}$$

which is constant in time,

$$\frac{dE}{dt} = \sum_{i=1}^{N} m_i \dot{\vec{r}}_i \ddot{\vec{r}}_i - \sum_{i=1}^{N} m_i \dot{\vec{r}}_i \cdot \vec{f}_i = 0 \, . \tag{4.5}$$

Thus, the role of MD simulations is to find the evolution of particle trajectories in time; i.e. position and velocities ($\vec{r}_i$ and $\dot{\vec{r}}_i \equiv \vec{v}_i$), for a many body systems. A numerical solution of Eq. (4.1) requires a discretization of these equations with respect to time. Numerical integration requires a discretization of time into equidistant time steps with steps of length δt. Among many different methods for performing numerical integration, the so-called *Velocity-Verlet algorithm* as a stable and accurate method, is mostly used in MD simulations.

4.1.1 *Velocity-Verlet algorithm*

Energy conservation, time reversibility and accuracy (at least up to $O(\delta t)^2$) are requirements for a good numerical integration algorithm. The velocity-Verlet algorithm which is originated from the *Verlet* algorithm [Verlet (1967)], satisfies these requirements. The idea in Verlet algorithm (like other numerical methods) is that, by knowing the previous and the current position of particles (also knowing the forces acting on them), we can obtain the position of the particles in the next step. And, with the updated positions then, we are able to get the updated velocities in the next step. The Verlet algorithm can be obtained by performing a second order Taylor expansion of particle positions, once forward and once backward in time, as follows:

$$\vec{r}_i(t+\delta t) = \vec{r}_i(t) + \delta t \vec{v}_i(t) + \frac{1}{2m_i}(\delta t)^2 \vec{f}_i(t) + \frac{1}{6}(\delta t)^3 \vec{b}_i(t) + O\left((\delta t)^4\right) , \quad (4.6)$$

$$\vec{r}_i(t-\delta t) = \vec{r}_i(t) - \delta t \vec{v}_i(t) + \frac{1}{2m_i}(\delta t)^2 \vec{f}_i(t) - \frac{1}{6}(\delta t)^3 \vec{b}_i(t) + O\left((\delta t)^4\right) . \quad (4.7)$$

With $\dot{\vec{r}}_i \equiv \vec{v}_i$, $\ddot{\vec{r}}_i \equiv \vec{f}_i/m_i$ (making use of Eq. (4.1), m_i the mass of particle i) and $\dddot{\vec{r}}_i \equiv \vec{b}_i$. Adding and subtracting Eq. (4.6) and (4.7) gives:

$$\vec{r}_i(t+\delta t) = 2\vec{r}_i(t) - \vec{r}_i(t-\delta t) + \frac{1}{m_i}(\delta t)^2 \vec{f}_i(t) + O\left((\delta t)^4\right) , \quad (4.8)$$

$$\vec{v}_i(t) = \frac{1}{2(\delta t)}\left[\vec{r}_i(t+\delta t) - \vec{r}_i(t-\delta t)\right] + O\left((\delta t)^3\right) . \quad (4.9)$$

The Verlet algorithm is time-reversible [Allen and Tildesley (2017), Frenkel and Smit (2001), and Verlet (1967)]. This means using $-\delta t$ and writing $\vec{r}_i(t+\delta t)$ as $\vec{r}_i(t-\delta t)$ the particles will follow their trajectories back in time. One of the drawbacks of the Verlet algorithm is that, the velocities are always updated one step behind (cf. Eq. (4.9)). This is also problematic in terms of computational costs, as one has to store too much data (meaning, previous and next positions, including all the information about the current status of the system). An alternative solution for this problem was introduced as the so-called *velocity-Verlet* algorithm [Andersen (1983) and Swope, Andersen, Berens, and Wilson (1982)]. In velocity-Verlet algorithm, the positions are updated via [Tuckerman (2010)]:

$$\vec{r}_i(t+\delta t) = \vec{r}_i(t) + \delta t \vec{v}_i(t) + \frac{1}{2m_i}(\delta t)^2 \vec{f}_i(t) . \quad (4.10)$$

One can also start from $\vec{r}_i(t+\delta t)$ and $\vec{v}_i(t+\delta t)$, compute $\vec{f}_i(t+\delta t)$ and by backward evolution in time obtain $\vec{r}_i(t)$ from:

$$\vec{r}_i(t) = \vec{r}_i(t+\delta t) - \delta t \vec{v}_i(t+\delta t) + \frac{1}{2m_i}(\delta t)^2 \vec{f}_i(t+\delta t) \ . \tag{4.11}$$

And therefore, by substituting Eq. (4.10) into Eq. (4.11), in the same analogy as in Verlet algorithm, one can obtain a relation for updating velocities as follows:

$$\vec{v}_i(t+\delta t) = \vec{v}_i(t) + \frac{\delta t}{2m_i}\left[\vec{f}_i(t) + \vec{f}_i(t+\delta t)\right] \ . \tag{4.12}$$

Velocity-Verlet is equivalent to Verlet algorithm[1]. The advantage of the velocity-Verlet algorithm, as a method which conserves the energy of the system, in comparison with the Verlet algorithm is that, in order to update the velocities we need only need the current and updated forces acting on particles, and the updated forces is accessible right after updating the positions of the particles.

4.1.2 *Dissipative particle dynamics thermostat*

Up to here, a simulation can be carried out in the micro-canonical ensemble (NVE) in which, the number of particles N, the volume of the system V and the total energy of the system E are kept constant. As the main focus of this work, we study the response of glass-forming systems when subjected to an external field. This means as a result of the external field, extra energy is pumped into the system which produces heat. Therefore, in order to be able to control this extra heat and perform non-equilibrium simulations under fixed temperature, one needs to couple the system to a thermostat [Golkia, Shrivastav, Chaudhuri, and Horbach (2020)]. In canonical ensemble (NVT), making use of the equipartition

[1] In order to show this alikeness, we can write [Frenkel and Smit (2001)]:

$$\vec{r}_i(t+2\delta t) = \vec{r}_i(t+\delta t) + \vec{v}_i(t+\delta t)\,\delta t + \frac{1}{2m_i}(\delta t)^2 \vec{f}_i(t+\delta t) \ . \tag{4.13}$$

By rewriting Eq. (4.10) in the following form:

$$\vec{r}_i(t) = \vec{r}_i(t+\delta t) - \vec{v}_i(t)\,\delta t - \frac{1}{2m_i}(\delta t)^2 \vec{f}_i(t) \ ,$$

and adding the latter two equations we get:

$$\vec{r}_i(t+2\delta t) + \vec{r}_i(t) = 2\vec{r}_i(t+\delta t) + [\vec{v}_i(t+\delta t) - \vec{v}_i(t)]\,\delta t + \frac{\left[\vec{f}_i(t+\delta t) - \vec{f}_i(t)\right]}{2m_i}(\delta t)^2 \ . \tag{4.14}$$

By substituting Eq. (4.12) in the above expression we obtain:

$$\vec{r}_i(t+2\delta t) + \vec{r}_i(t) = 2\vec{r}_i(t+\delta t) + \frac{\vec{f}_i(t+\delta t)}{m_i}(\delta t)^2 \ , \tag{4.15}$$

which is the coordinate version of the Verlet algorithm.

theorem [Boltzmann (1871)] one can obtain the temperature T of the system. For a system of N particles in equilibrium (i.e. the properties of the system no longer change with time and saturate at a finite value), the distributions of positions and velocities follow Maxwell–Boltzmann distribution. Therefore, the temperature can be inferred from the kinetic energy of the particles such that, for all degrees of freedom in the system one can obtain the *kinetic temperature* $\mathcal{T}$ (in three dimension) as:

$$\mathcal{T} = \frac{2E_{kin}}{3k_B N} = \frac{1}{3k_B N} \sum_{i=1}^{N} m_i \vec{v}_i^2 \, . \tag{4.16}$$

Then, the systems temperature is obtain from an average over these instantaneous temperatures via $T = \langle \mathcal{T} \rangle$. In which, the brackets $\langle\rangle$ represent a time average.

Here, we introduce the *Dissipative Particle Dynamics* (DPD) thermostat [Hoogerbrugge and Koelman (1992)]. DPD thermostat is Galilean invariant, gives the correct hydrodynamic behavior on the sufficiently large length and time scales, and conserves local momentum [Frenkel and Smit (2001)]. The latter is an essential advantage of the DPD thermostat in comparison to other thermostating methods and is a direct result of considering relative velocities between pairs of particles. These advantages make DPD thermostat a reliable method for performing non-equilibrium simulations [Soddemann, Dünweg, and Kremer (2003)].

In DPD thermostat, a pairwise random ($\vec{f}_R$) and dissipative ($\vec{f}_D$) force is added to the conservative force acting between particles ($\vec{f}_C$) such that, the total force acting on particle i has the form:

$$\vec{F}_i = \sum_{j \neq i} \left[\vec{f}_C \left(\vec{r}_{ij} \right) + \vec{f}_D \left(\vec{r}_{ij}, \vec{v}_{ij} \right) + \vec{f}_R \left(\vec{r}_{ij} \right) \right] \, , \tag{4.17}$$

in which, $\vec{r}_{ij} = \vec{r}_i - \vec{r}_j$ and $\vec{v}_{ij} = \vec{v}_i - \vec{v}_j$ are relative distance and velocities between particle i and j , respectively. The conservative force ($\vec{f}_C$) can be obtained via Eq. (4.3), as it was discussed earlier in this chapter, from the interaction potential. The dissipative force ($\vec{f}_D$) is a function of relative distance and relative velocities of the particles and is defined as:

$$\vec{f}_D \left(\vec{r}_{ij}, \vec{v}_{ij} \right) = -\gamma \omega^D \left(r_{ij} \right) \left(\vec{v}_{ij} . \hat{r}_{ij} \right) \hat{r}_{ij} \, , \tag{4.18}$$

in which, $\hat{r}_{ij}$ is the unit vector in the direction of $\vec{r}_{ij}$, γ is the coupling coefficient, controlling the strength of friction force and $\omega^D \left(r_{ij} \right)$ describes the variation of the friction coefficient (cut-off function of dissipative force) with distance. The random force ($\vec{f}_R$) is defined as:

$$\vec{f}_R \left(\vec{r}_{ij} \right) = \sigma \omega^R \left(r_{ij} \right) \xi_{ij} \hat{r}_{ij} \, , \tag{4.19}$$

in which, σ controls the magnitude of the random force and $\omega^R \left(r_{ij} \right)$ controls the variation of random force with distance (cut-off function of random force).

ξ_{ij} are random variables from a Gaussian distribution with a zero mean and a unit variance, which are independent for different pairs of particles and different times. The condition $\xi_{ij} = \xi_{ji}$ is employed to ensure momentum conservation. The cut-off functions of the dissipative and random force cannot be chosen independently and they are related to each other via:

$$\omega^D\left(r_{ij}\right) = \left[\omega^R\left(r_{ij}\right)\right]^2 , \tag{4.20}$$

in order to satisfy the fluctuation-dissipation theorem and give the correct distribution of particle positions and velocities [Español and Warren (1995)]. Therefore, σ and γ are also related to temperature via:

$$\sigma^2 = 2k_B T\gamma . \tag{4.21}$$

The additional force terms in DPD thermostat has the functional form such that the method conserves local momentum. This is also essential for recovering correct hydrodynamics while performing simulations on sufficiently large length and time scales, specially under specific situations e.g. being imposed to an external force.

4.1.3 Lees-Edwards boundary conditions

In computer simulations, in order to mimic an infinite bulk surrounding the model system, boundary conditions play a very important role. The importance of the boundary conditions is due to the fact that, although the modern technological resources make it possible to simulate very large systems, containing millions of particles but nevertheless, still we are far from thermodynamic limit ($N \to \infty$ and $V \to \infty$). Also, in computer simulations, in order to prevent particles from spreading away, they are bound within a fictitious box (the so-called *simulation box*). But, this consideration also has consequences, as the particle-wall interactions (surface effects) might change the force acting on particles. In order to overcome these problems one often uses *periodic boundary conditions* (pbc) [Allen and Tildesley (2017), Born and Huang (1954), and Frenkel and Smit (2001)] (cf. Fig. 4.1).

Fig. 4.1 shows a schematic representation of pbc in computer simulations in which the central box containing N atoms is considered as the primitive cell of particles, surrounded by infinite identical replicas. With this representation, not only the particles within the simulation box will interact with each other, but also, they interact with all their image particles in their neighboring cells (although the range of the interactions depends on the interaction potential). Let's consider particle i shown in Fig. 4.1 in red. What pbc implies is that, when particle i leaves the primitive simulation box, its image comes back into the simulation box from

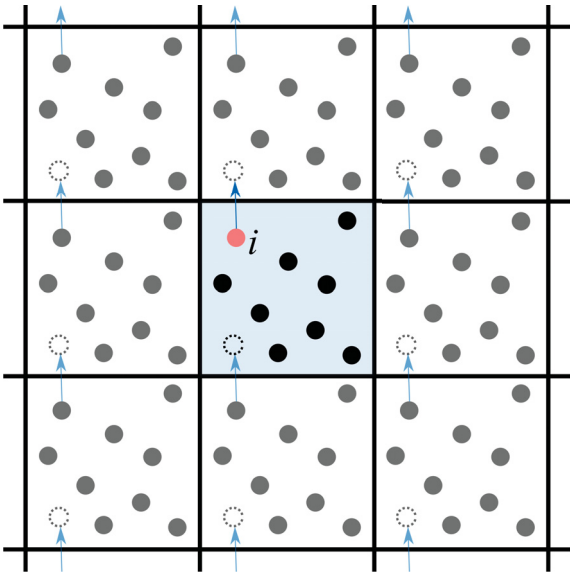

Figure 4.1: Schematic representation of periodic boundary conditions.

exactly the opposite side. With this approach, we can simulate the bulk of the material without particles being affected at the surface.

As it was mentioned earlier, one important role of pbc comes into play when the system is subjected to a deformation in non-equilibrium situations. [Lees and Edwards (1972)] introduced a technique (named after them as *Lees-Edwards bondary conditions* LEbc) with which one can perform purely boundary driven shear deformation in MD simulation without modifying the equations of motion. The technique is based on the original pbc (discussed earlier) with some modification (cf. Fig. 4.2). Considering a shear deformation in x-direction with a flow gradient in z-direction, meaning that the xz plane is being deformed (shown schematically in Fig. 4.2), the LEbc implies:

- The upper and lower periodic replicas (C and B in Fig. 4.2, respectively) of the principal simulation box (the blue box (A) in Fig. 4.2), drift in opposite directions with a constant velocity v_d.
- $v_d = \dot{\gamma} L_{box}$, L_{box} being the length of the simulation box (here considered to be a cubic box, otherwise the corresponding length in the gradient direction).
- As a result of this drift velocity, when particle i leaves the simulation box (A) at point P_1, instead of returning into the simulation box at point P_2 (as expected from pbc), it will enter the simulation box at point P_3.
- The pbc is applied in the conventional way in the other directions.

As a result of this drift, a linear velocity profile in z-direction is obtained [Lees and Edwards (1972)]:

$$\vec{v}_x(z) = \dot{\gamma} z \hat{e}_x \,, \tag{4.22}$$

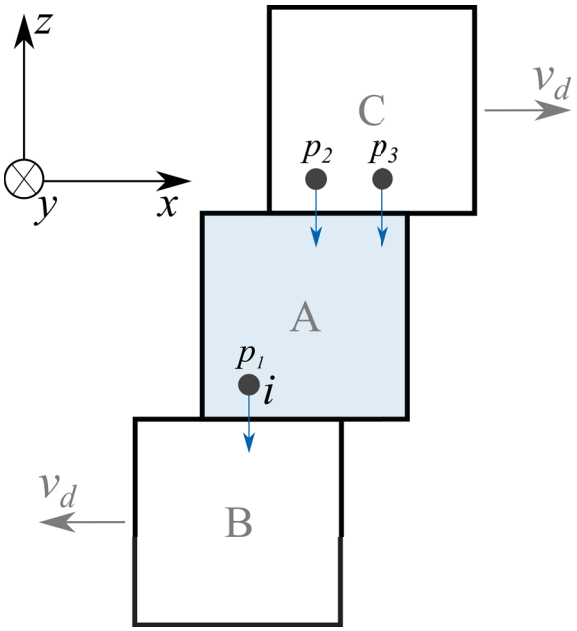

Figure 4.2: Schematic representation of Lees-Edwards periodic boundary conditions.

with $\dot{\gamma}$ the shear rate, z the z-component of the particle position and $\hat{e}_x$ the unit vector in x-direction. This linear velocity profile is a consequence of an extra term Δv being added to particles velocity in the direction of the shear load, defined as:

$$\Delta v = v_d \left(\frac{z}{L_{box}} - \frac{1}{2} \right) . \tag{4.23}$$

Therefore, the corresponding component of particle velocity in the direction of the shear will be effected after applying LEbc while, the other components will be intact. This means in the example above:

$$\begin{aligned} v'_x &= v_x + \Delta v \\ v'_y &= v_y \\ v'_z &= v_z , \end{aligned} \tag{4.24}$$

with prime indices indicating the new velocity components after applying LEbc. Another consequence of LEbc is that, as the simulation box are slipping on each other and particles are feeling the shear deformation as an additional term in their velocities, their positions also gets drifted in the direction of shear (cf. Fig. 4.3). As it was discussed earlier, within the framework of pbc, particle i (at position x_i) not only will interact with particle j (at position x_j) in the simulation box, but also, will interact with its image at position $x_{j'}$. But, as a result of LEbc, particle's j image, is at position $x_{j''}$. This means, particle i will interact with particle j at position x_j and its image at $x_{j''}$, while, there is a $x_{j''} - x_{j'}$ displacement in x-direction. Therefore, this drift in particle's position is a very important point to be considered while updating the forces at each MD time-step.

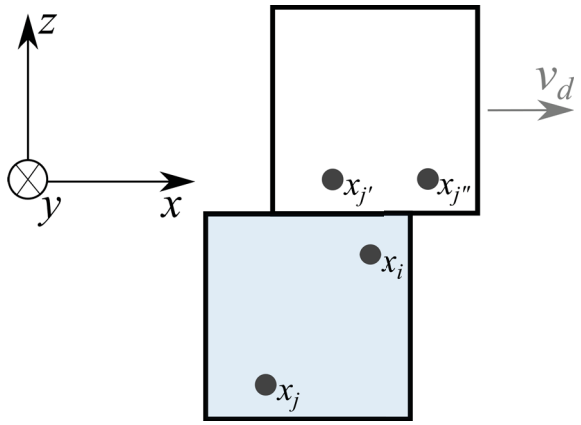

Figure 4.3: Particles position drift in the direction of the shear deformation.

4.2 Potential model for the glass forming system $Ni_{80}P_{20}$

In order to study the effect of deformation on mechanical properties of the glass-forming system $Ni_{80}P_{20}$, as the main focus of this study, we performed extensive MD simulations. Up to now, we briefly discussed how to perform MD simulations and implement the shear deformation technique in these simulations. But so far, a big building block of our simulations, which is, the model which we are using to study $Ni_{80}P_{20}$ in computer simulations, is missing. In this study, we considered a Kob-Andersen binary Lennard-Jones (KABLJ) model glass former. The model has it's origin in the earlier studies of [Weber and Stillinger (1985)] on $Ni_{80}P_{20}$ in computer simulations and introduced by [Kob and Andersen (1994)]. Since that time, the model has been developed [Kob and Andersen (1995a) and Kob and Andersen (1995b)] and extensively used in many computer simulations [Golkia, Shrivastav, Chaudhuri, and Horbach (2020) and Shrivastav, Chaudhuri, and Horbach (2016)].

The KABLJ model consists of a binary mixture of particles (of two species A and B), with 80 : 20 ratio of A and B types, interacting via Lennard-Jones (LJ) [Hansen and McDonald (2013) and Lennard-Jones (1924)] potential which is defined as:

$$\phi_{\alpha\beta} = 4\epsilon_{\alpha\beta}\left[\left(\frac{\sigma_{\alpha\beta}}{r}\right)^{12} - \left(\frac{\sigma_{\alpha\beta}}{r}\right)^{6}\right], \tag{4.25}$$

with α and β corresponding to the particle types of A and B and $r = |\vec{r}_i - \vec{r}_j|$ the relative distance between pairs of particles. In order to save computing time while using periodic boundary conditions, a cut-off radius r_c is considered for the range of particle interactions and therefore the potential is modified such

that:

$$\phi_{\alpha\beta} = \begin{cases} 4\epsilon_{\alpha\beta}\left[\left(\frac{\sigma_{\alpha\beta}}{r}\right)^{12} - \left(\frac{\sigma_{\alpha\beta}}{r}\right)^{6}\right] & \text{for } r \leqslant r_c\ , \\ 0 & \text{for } r > r_c\ . \end{cases} \tag{4.26}$$

The LJ potential is smoothly truncated and shifted to zero at the cut-off [Frenkel and Smit (2001) and Smit (1992)] such that:

$$U_{LJ} = \phi_{\alpha\beta}(r) - \phi_{\alpha\beta}(r_c) - (r - r_c)\frac{d\phi_{\alpha\beta}}{dr}(r_c)\ . \tag{4.27}$$

Both particle types have the same mass, i.e. $m_A = m_B = 1.0$ and other interaction parameters between different species are listed in table (4.1) [Kob and Andersen (1994)]. σ_{AA} and ϵ_{AA} set the length scale and energy of the system, respectively.

interactions	AA	AB	BB
$\epsilon_{\alpha\beta}$	1.0	1.5	0.5
$\sigma_{\alpha\beta}$	1.0	0.8	0.88

Table 4.1: Interaction parameters between different particle types for KABLJ system. α and β denote A and B type particles respectively.

In this work we use reduced LJ units [Rapaport (2004)]. In table (4.2) we have listed the conversion parameters with which on can convert the reduced LJ units to the corresponding real units.

quantities	LJ unites	real units
mass	m^*	$m^* \cdot m$
length	L	$L \cdot \sigma$
energy	E	$E \cdot \epsilon$
time	τ	$\tau \cdot \sqrt{\frac{m\sigma^2}{\epsilon}}$
force	F	$F \cdot \frac{\epsilon}{\sigma}$
temperature	T	$T \cdot \frac{\epsilon}{k_B}$
number density	ρ	$\rho \cdot \sigma^{-3}$
shear rate	$\dot{\gamma}$	$\dot{\gamma} \cdot \sqrt{\frac{\epsilon}{m\sigma^2}}$

Table 4.2: Conversion parameters between LJ reduced units and real units. k_B the Boltzmann factor is set to $:= 1.0$.

In this thesis, we used LAMMPS [Plimpton (1995)], which is an open-source MD simulation package. The LAMMPS package allows running large-scale

atomic/molecular parallel simulations. In the following, we will discuss the details of our simulations (i.e., sample preparation, deformation), and then, the results will be discussed in chapter 5.

4.3 Details of simulations

In this section, for convenience purposes, we will present the simulation details of each part of the project, independently. Therefore, this section is divided into the following subsections:

- Effect of deformation on elastic constants of BMGs
- Effect of deformation on vibrational modes in BMGs
- Shear-bands in glasses, and in-homogeneous flow patterns in super-cooled liquids
- Effect of micro-alloying on mechanical properties of BMGs

4.3.1 Effect of deformation on elastic constants of BMGs

- ***Glass preparation***

The number density is fixed at $\rho = 1.2m_A/\sigma_{AA}^3$, and cubic box geometry of linear size $30\sigma_{AA}$ is considered. Therefore, the number of particles is fixed at $N = N_A + N_B = 32400$, consisting of $N_A = 25920$ and $N_B = 6480$ particles of A and B type, respectively. The equations of motion are integrated via the velocity-Verlet algorithm using an integration time step $\Delta t = 0.005$. The initial sample was generated at $T = 5$ in the liquid state, and equilibrated at this temperature for $t = 10^4\tau_{LJ}$. Using the equilibrated liquid configuration, we stored configurations in time intervals of 500 time steps in a production run. We used these configurations as independent samples for the rest of the simulations (in total, 250 samples were generated). The samples were then equilibrated at $T = 0.44$ in the super-cooled liquid state above glass transition temperature for $t = 2 \times 10^5\tau_{LJ}$. The glass state was obtained by quenching the super-cooled samples to a temperature $T = 0.2$, well below the mode coupling glass transition temperature $T_c = 0.435$, known for the model glass former [Kob and Andersen (1994)]. The glass samples were then relaxed for a waiting time of $t_w = 10^4\tau_{LJ}$ in canonical ensemble and in addition a production run of $t_w = 10^4\tau_{LJ}$ in micro-canonical ensemble (NVE). Samples at this stage are considered as "*undeformed*" glass samples. To obtain instantaneous values of the elastic constants in the undeformed state, short production runs in micro-canonical (NVE) ensemble was performed and data (stresses, configuration, etc.) for each sample (in a short time

window of the order of $t = 500\tau_{LJ}$) was stored. Elastic constants tensor (Eq. 3.1) was then calculated for the undeformed samples, as a reference, during this short time window and then averaged over all samples.

As was discussed earlier in this chapter, we used the DPD thermostat in our simulations. The thermostat has been used for fixing the temperature during canonical runs (NVT), quenching, and also during the shear deformation. DPD thermostat is implemented in LAMMPS package [Plimpton (1995)] and can be used via the following input scripts. *pair_style* calls DPD thermostat to start the simulations with *Tstart* as the starting temperature and fixing the temperature at *Tstop*. *cutoff* is the pairwise interaction cut-off radius, and the argument *seed* is used as an input in the random number generator. The *pair_coeff* command is used to define different pairwise interaction parameters between particle types i and j, and the *args* gets the friction coefficient, cut-off radius, etc. as input. The canonical run is achieved, therefore, by fixing the temperature with thermostat while performing a micro-canonical run using the *fix nve* command applied on the specified particle IDs by *group-ID*.

```
pair_style[1]  dpd/tstat Tstart Tstop cutoff seed
pair_coeff[2]  i j dpd/tstat args
fix[3]         ID group-ID nve
```

- ***Shear deformation***

Shear deformation was applied in x-direction (gradient direction in z-direction, such that, the corresponding component of the stress tensor would be σ_{xz}), with a variety of shear rates $\dot{\gamma} = \left[10^2,\ 3\times10^3,\ 10^3,\ 3\times10^4,\ 10^4,\ 3\times10^5,\ 10^5\right]\ \tau_{LJ}^{-1}$. The samples were deformed up to strain $\gamma = 3$ (except for the shear rate $\dot{\gamma} = 10^5\tau_{LJ}^{-1}$ for which samples were deformed up to $\gamma = 2$) in order to make sure that we reach a homogeneous flow [Barrat and Lemaître (2011) and Rodney, Tanguy, and Vandembroucq (2011)]. At this point shear was switched off and we allowed the samples to relax for $t = 4\times10^4\tau_{LJ}$, until the stresses reach a finite value [Ballauff, Brader, et al. (2013)]. The glass samples at this stage with residual stresses are considered as "*deformed*" glass samples.

The shear deformation in LAMMPS can be performed after preparing the simulation box for deformation via *change_box* command, by using a *fix deform* command. Then, to trace the formation of stresses in the system and obtain the stress-strain curve of the system, one can access different components of the stress tensor with a *compute stress/atom* command. This command contains the

[1] **https://lammps.sandia.gov/doc/pair_dpd.html**.
[2] **https://lammps.sandia.gov/doc/pair_coeff.html**.
[3] **https://lammps.sandia.gov/doc/fix_nve.html**.

whole stress tensor information per-atom, which can then be averaged over a specific group of atoms or the whole system with a *compute reduce ave* command. Different components of the stress tensor can be stored as an output via a *fix print* command. Here is a list of commands used in our simulations:

change_box[4]	group–ID parameter args
fix[5]	ID group–ID deform N parameter args
compute[6]	ID group–ID stress/atom temp–ID keyword
compute[7]	ID group–ID style arg mode input
fix[8]	ID group–ID print N string keyword value

In order to obtain the elastic constants for deformed glasses, as the stresses are relaxing, at the long tail of the stress-relaxation curve, we took six different time origins. At each of these time origins, we again performed short production runs in micro-canonical (NVE) ensemble and stored data. By doing so, we were able to calculate the instantaneous elastic constants of the samples while the stresses are relaxing and with different amounts of residual stresses in the system (details will be discussed in chapter 5). These values were then compared to those of the undeformed ones (as reference) to study the effect of deformation and the residual stresses on elastic constants.

4.3.2 *Effect of deformation on vibrational modes in BMGs*

- ***Glass preparation***

In order to study the vibrational modes at low temperatures, the number density is fixed at $\rho = 1.3m_A/\sigma_{AA}^3$ to avoid negative pressure after quenching to low temperatures. At very low temperatures, for lower densities, the system enters a mechanically unstable state. This unstable two-phase region becomes stable by formation of cavities in the system [Chaudhuri and Horbach (2016)]. A cubic box geometry of linear size of $L \approx 31.336\sigma_{AA}$ (in order to study finite size effects other system sizes with the same number density were also considered which, will be discussed in chapter 5) is considered. Therefore, the number of particles is fixed at $N = N_A + N_B = 40000$, consisting $N_A = 32000$ and $N_B = 8000$ of A and B type particles, respectively (in order to study the finite size effects in our calculations we also considered the following system sizes with $N = [1300, 3000, 200000, 1500000]$ particles). The equations of motion are integrated via the velocity-Verlet algorithm using an integration time step

[4] **https://lammps.sandia.gov/doc/change_box.html**.
[5] **https://lammps.sandia.gov/doc/fix_deform.html**.
[6] **https://lammps.sandia.gov/doc/compute_stress_atom.html**.
[7] **https://lammps.sandia.gov/doc/compute_reduce.html**.
[8] **https://lammps.sandia.gov/doc/fix_print.html**.

$\Delta t = 0.002$. The initial sample was generated at $T = 5$ in the liquid state, which was then equilibrated at this temperature for $t = 10^4\tau_{LJ}$.

Using the equilibrated liquid configuration, we stored configurations in time intervals of 500 time steps and used these configurations as independent samples for the rest of simulation (in total 20 samples were generated). The samples were then equilibrated at $T = 0.75$ in the super-cooled liquid state above the glass transition for $t = 2 \times 10^4\tau_{LJ}$. The glass state is obtained by quenching the super-cooled binary mixture to a temperature $T = 10^{-4}$ which is well below the glass transition temperature $T_g \approx 0.65$ (in LJ units) known for the same model glass former following the same quench protocol [Chaudhuri and Horbach (2016)]. We prepare the glass samples aged up to waiting time $t_w = 2 \times 10^3\tau_{LJ}$ in canonical NVT ensemble followed by a production run of $t_w = 10^4\tau_{LJ}$ in the micro-canonical NVE ensemble. Samples at this stage were then, considered as "*undeformed*".

- ***Shear deformation***

Shear deformation was then applied to the system in the same manner as it was discussed in the previous section with only a single shear rate of $\dot{\gamma} = 10^4\tau_{LJ}^{-1}$ up to strain $\gamma = 1$ from which, we switched off the shear load. We allowed the glass samples to relax for a waiting time of $t = 4 \times 10^4\tau_{LJ}$ until we obtained glass samples with residual stresses. At this point, in the same manner, as for the undeformed samples, the thermostat was switched off, followed by a production run of $t_w = 10^4\tau_{LJ}$ in the micro-canonical NVE ensemble. The glass samples at this stage, with residual stresses, were considered as "*deformed*".

In order to calculate the density of states for both undeformed and deformed samples, we performed production runs of length 131076 time-steps (26.215ps in real time), and stored configurations every 32 time-steps. By doing so, we had a resolution of $\Delta\omega \approx 0.023$THz in frequency domain and reached a maximum frequency of $\omega_{max} = 47.1$THz. Density of states was then calculated by applying a Fast Fourier Transform (FFT) [Press, Teukolsky, Vetterling, and Flannery (2007)] on velocities [Dove (1993)].

4.3.3 *Shear-bands in glasses vs. in-homogeneous flow patterns in super-cooled liquids*

For this part of the work the glass samples were prepared as it was discussed earlier in the previous sections (4.3.1,4.3.2). For the super-cooled liquids following the previous protocol, the number density is fixed at $\rho = 1.2m_A/\sigma_{AA}^3$. Three simulation box sizes of $30\sigma_{AA}$, $40\sigma_{AA}$, $50\sigma_{AA}$ is considered. Therefore, the number of particles is fixed at $N = N_A + N_B = [32400, 76800, 150000]$, consisting

of $N_A = [25920, 61440, 120000]$ and $N_B = [6480, 15360, 30000]$ particles of A and B type, respectively. The equations of motion are integrated via the velocity-Verlet algorithm using an integration time step $\Delta t = 0.005$. The initial samples were generated at $T = 5$ in the liquid state, and equilibrated at this temperature for $t = 10^4\tau_{LJ}$. Using the equilibrated liquid configuration, we stored configurations in time intervals of 500 time-steps in a production run, and used these configurations as independent samples for the rest of the simulations. The 30^3 samples were equilibrated at $T = 0.44$ (also equilibrated at $T = 0.45$ and $T = 0.5$) in the super-cooled liquid state above glass transition temperature for $t = 2 \times 10^5\tau_{LJ}$ and 40^3, 50^3 samples were each equilibrated for $t = 5 \times 10^4\tau_{LJ}$ at $T = 0.44$. Then, in order to study the flow patterns in the super-cooled liquids while being imposed to shear deformation (in the same manner as it was discussed earlier in this section) shear deformation was imposed to systems with a variety of shear rates $\dot{\gamma} = \left[10^2,\ 3 \times 10^3,\ 10^3,\ 3 \times 10^4,\ 10^4,\ 3 \times 10^5,\ 10^5,\ 3 \times 10^6,\ 10^6,\ 10^7\right] \tau_{LJ}^{-1}$. Results of these simulations will be discussed in chapter 5.

4.3.4 *Effect of micro-alloying on mechanical properties of BMGs*

In order to study the effect of micro-alloying on mechanical properties of BMGs, we made a minor modification on the KABLJ [Kob and Andersen (1994)] by adding 1% of a third species (type C) in the system. Therefore, a ternary mixture of 79% particles of type A, 20% of type B and 1% of type C has been obtained. All particles have the same mass ($m_A = m_B = m_C = 1.0$) and the interaction parameters are as follows:

interactions	AA/CC	AB/BC	BB	AC
$\epsilon_{\alpha\beta}$	1.0	1.5	0.5	0.1
$\sigma_{\alpha\beta}$	1.0	0.8	0.88	1.0

Table 4.3: Interaction parameters for the ternary system.

α and β correspond to different particle types. We made the minimum change in the original model by changing only one parameter ϵ_{AC}. Therefore, for $\epsilon_{AC} = 1.0$, we reproduce the original results.

- ***Glass preparation***

Following the same protocol as in (4.3.2), the number density is fixed at $\rho = 1.3m_A/\sigma_{AA}^3$. A cubic box geometry of linear size of $L \approx 31.336\sigma_{AA}$ is considered. Therefore, the number of particles is fixed at $N = N_A + N_B + N_C = 40000$, consisting $N_A = 31600$, $N_B = 8000$ and $N_C = 400$ of A, B and C type particles

respectively. The equations of motion are integrated via the velocity-Verlet algorithm using an integration time step $\Delta t = 0.002$. The initial sample was generated at $T = 5$ in the liquid state, which was then equilibrated at this temperature for $t = 2 \times 10^3 \tau_{LJ}$. Using the equilibrated liquid configuration we stored configurations in time intervals of 500 time-steps and used these configurations as independent samples for the rest of simulation (in total 20 samples were generated). The samples were then equilibrated at $T = 0.75$ in the super-cooled liquid state for $t = 2 \times 10^4 \tau_{LJ}$. The glass state is obtained by quenching the super-cooled binary mixture to a temperature $T = 10^{-4}$. We prepare the glass samples aged up to waiting time $t_w = 2 \times 10^3 \tau_{LJ}$ in canonical NVT run followed by a production run of $t_w = 10^4 \tau_{LJ}$ in micro-canonical ensemble NVE. The micro-alloyed samples at this stage are then considered as "*undeformed*" samples.

- ***Shear deformation***

Shear deformation was applied to the system in the same manner as it was discussed in the previous section, with only a single shear rate of $\dot{\gamma} = 10^4 \tau_{LJ}^{-1}$ up to strain $\gamma = 1$ from which, we switched off the shear load. We allowed the glass samples to relax for a waiting time of $t = 4 \times 10^4 \tau_{LJ}$ until we obtained glass samples with residual stresses. At this point, in the same manner, as for the undeformed samples, the thermostat was switched off, a production run of $t_w = 10^4 \tau_{LJ}$ was performed in micro-canonical ensemble NVE. The glass samples at this stage, with residual stresses, were considered as "*deformed*".

The mechanical properties and the vibrational modes of the new ternary system were then compared to those of the binary mixtures, and also between the undeformed and deformed states. Details of these results will be discussed in chapter 5.

5 Results

"People love chopping wood. In this activity one immediately sees results."
Albert Einstein

As the main focus of this work, we studied the effect of deformation on mechanical properties of a $Ni_{80}P_{20}$ model glass-forming system. In order to get a more comprehensive picture, we tried to investigate these effects from different angles. This consists of the changes in elastic constants and vibrational modes of the material, formation of shear bands, and micro-alloying. All the obtained results from the deformed samples are compared to those of the undeformed states (as a reference).

In this chapter, we will discuss the results obtained from extensive MD simulations. The chapter is divided into five sections:

- Glasses and super-cooled liquids under shear deformation
- Stress relaxation and residual stresses
- Effect of deformation on elastic constants
- Effect of deformation on time-dependent vibrational properties
- Micro-alloying

5.1 Glasses and super-cooled liquids under shear deformation

We open the result section by discussing the response of the SCLs being subjected to a shear deformation with a constant shear rate $\dot{\gamma}$, in terms of the stress-strain curves. The results for SCLs will be then used later, as a reference, to compare to the obtained results for glasses. When a highly viscous liquid is subjected to shear deformation with a constant shear rate $\dot{\gamma}$, a new time scale is introduced by $1/\dot{\gamma}$. If the latter time scale becomes smaller than the time scale for structural relaxation in the system, the response of the system exhibits a crossover from a Newtonian to non-Newtonian liquid with the steady-state shear stress σ_{ss}, being no longer proportional to the shear rate $\dot{\gamma}$. Here, we investigate this crossover response in the SCLs, which is reflected in the transient regime of stress-strain curve.

5.1.1 Transient response of SCLs to shear deformation

The macroscopic response of the samples in the super-cooled liquid state (at $T = 0.44$ and $\rho = 1.2$) being imposed to shear deformation with a wide range of shear rates $\dot{\gamma} = [10^3, 3\times10^4, 10^4, 3\times10^5, 10^5, 3\times10^6, 10^6, 10^7]\,\tau_{LJ}^{-1}$ is shown in Fig. 5.1. The shear rate dependence of the stress-strain curves is clearly visible from the figure such that, for high shear rates (e.g. $\dot{\gamma} = 10^{-3}$ presented with green lines) the stress-strain curves exhibit three distinguishable regimes, namely an early elastic regime, a transient regime and the steady-state regime. For low shear rates (e.g. $\dot{\gamma} = 10^{-5}$ presented with dark-gray lines) there is a shoulder type increase and the system reaches the steady-state in a rather small strain window. This shoulder type increase disappears in the limit of low shear rates, such that, for example for $\dot{\gamma} = 10^{-7}$ (light-gray curve) the increase in the stresses are so small that the stress-strain curve almost fluctuates around its equilibrium stress values (dashed black line). The overshoot peak maximum increases by increasing shear rate (direction of the black arrow) towards larger strains. The occurrence of the overshoot in the transient regime, marks the onset of plastic flow and the non-Newtonian response of the SCLs to shear deformation, we will come back to this point later in this section.

In panel (a) and (b) of Fig. 5.2, we investigate the behavior of the overshoot peak position[1] γ_p and height σ_p, as a function of shear rate at different temperatures in the SCL state. The symbols corresponding to different temperatures are shown in Fig. 5.2(b) and in panel (a) the corresponding shear rates are marked

[1] In order to obtain γ_p and σ_p, the corresponding stress-strain curves data are fitted with a Gaussian function of the form $A exp(B(x-C)^2)$ around the overshoot, in which, $A \equiv \sigma_p$ and $C \equiv \gamma_p$.

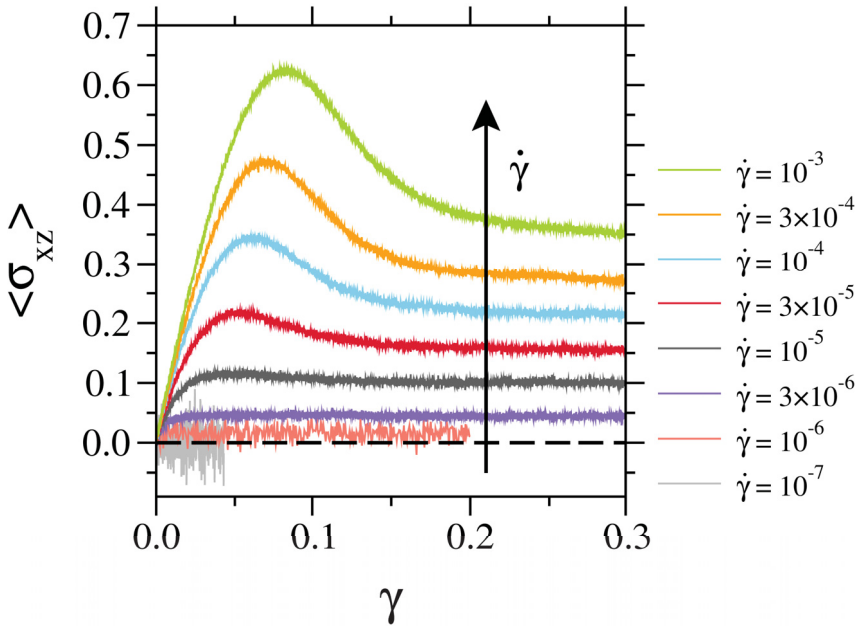

Figure 5.1: Stress-strain curves for super-cooled liquids (T = 0.44, N = 32400, ρ = 1.2) being imposed to shear deformation with different shear rates. The dashed black line is drawn at $\sigma_{xz} = 0.0$.

with vertical solid lines. In panel (a) of Fig. 5.2 we see that, irrespective of temperature, in the SCL state the values for γ_p of different shear rates sit very closely on top of each other. In order to investigate the functional behavior of the result, the data is fitted with a function of the form $A_0 + A_1 x^{A_2}$ (dashed gray line). The values obtained for the fit parameters are shown in table (5.1). The obtained

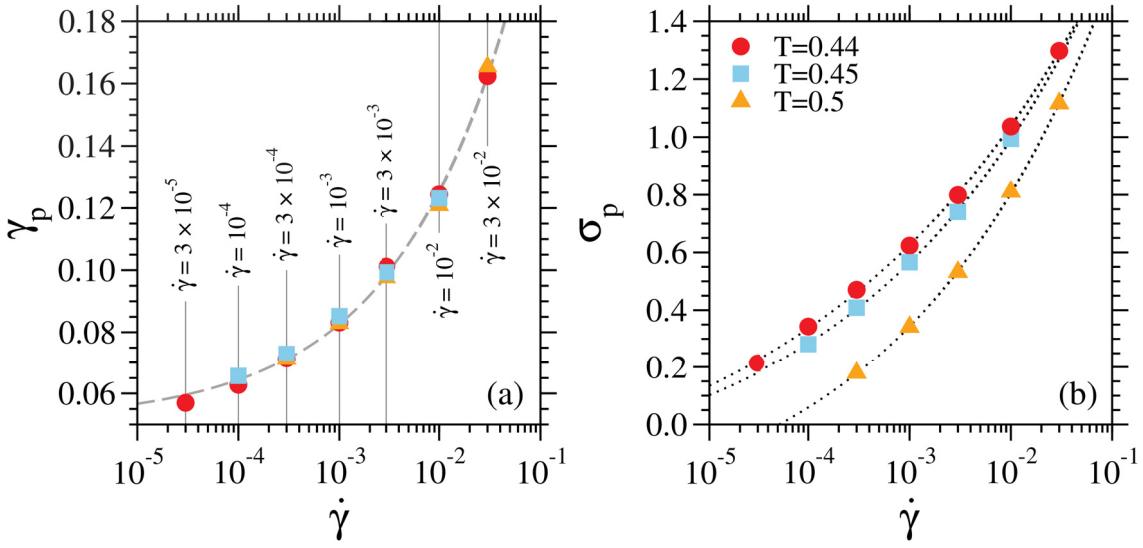

Figure 5.2: *panel (a)*: the overshoot peak position γ_p as a function of shear rate $\dot{\gamma}$ (the corresponding shear rates are marked with solid vertical lines) in the SCL state. *panel (b)*: the stress maximum at the overshoot σ_p as a function of shear rate $\dot{\gamma}$, in the SCL states. The corresponding colors for each temperatures are shown in this panel.

data for σ_p in panel (b) of Fig. 5.2 is also fitted with the same function (dotted black lines). The obtained values are presented in table (5.2). By comparing the

Fit parameters for γ_p in the SCL state

	A_0	A_1	A_2
SCL	0.051	0.407	0.369

Table 5.1: Values are obtained by fitting the results with a function of the form $A_0 + A_1 x^{A_2}$

results in panel (a) and (b) of Fig. 5.2 we can see that, σ_p shows a slightly stronger temperature dependence compared to γ_p. In highly viscous SCLs, the elastic response to the applied shear load becomes more pronounced with decreasing temperature, denoting an increase in the elastic modulus of the system. Therefore, the temperature dependence of σ_p and γ_p can be well understood by the change in the elastic modulus of the system. Comparing the values shown in tables (5.1) and (5.2) we can see that, γ_p, having a power-law exponent of ≈ 0.4, shows a stronger power-law behavior, with respect to the applied shear rates, compared σ_p with a power-law exponent of ≈ 0.2.

Fit parameters for σ_p in the SCL state

	A_0	A_1	A_2
$SCL\|_{T=0.44}$	-0.336	2.810	0.155
$SCL\|_{T=0.45}$	-0.243	2.891	0.185
$SCL\|_{T=0.5}$	-0.393	3.174	0.212

Table 5.2: Values are obtained by fitting the results with a function of the form $A_0 + A_1 x^{A_2}$

In order to further investigate the temperature dependence of the transient regime in the SCLs, in Fig. 5.3 we present the stress-strain curves for SCLs at $\rho = 1.2$ and for $T = 0.44,\ 0.45,\ 0.5$ in red, blue and orange, respectively. Here, we compare the response of the super-cooled liquids being imposed to two constant shear rates $\dot{\gamma} = 10^{-3},\ 10^{-5}$, the upper and lower curves, respectively. In Fig. 5.3 we can see that, for temperatures $T = 0.44,\ 0.45$ and shear rate $\dot{\gamma} = 10^{-3}$ (upper curves) the stress-strain curves show a pronounced overshoot. But, the non-Newtonian response to the applied shear deformation becomes less pronounced for SCLs at $T = 0.5$ at the same shear rate. This difference becomes less pronounced at lower shear rates, $\dot{\gamma} = 10^{-5}$ in this case. For the latter shear rate in Fig. 5.3 we can see that, although the increase in the stresses are more pronounced for SCLs at $T = 0.44$, but the differences between the curves are not as large as the responses to $\dot{\gamma} = 10^{-3}$. This is due to the fact that, for shear rate

$\dot{\gamma} = 10^{-5}$ the samples are already in the Newtonian regime, therefore, irrespective of temperature, the samples exhibit a similar response to the applied shear load.

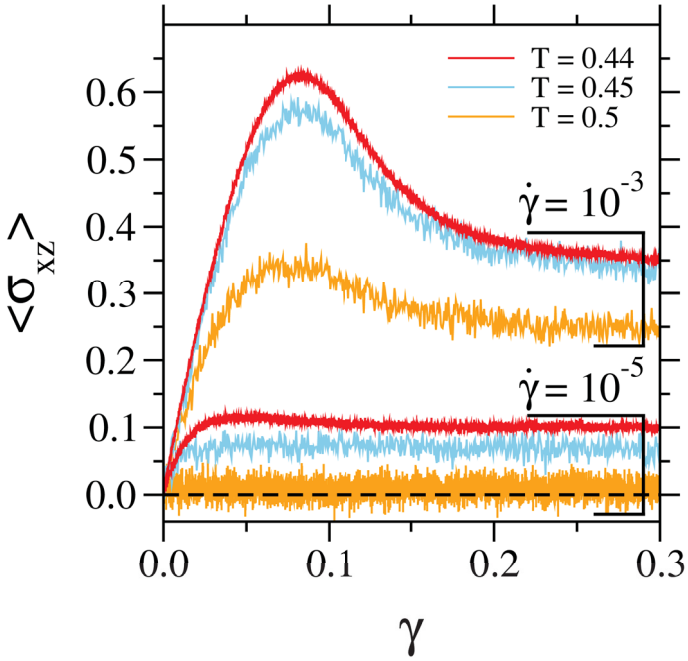

Figure 5.3: Comparison between the stress-strain curves of SCLs at $\rho = 1.2$ and for $T = 0.44,\ 0.45,\ 0.5$ in red, blue and orange, respectively. The samples at each temperature are subjected to shear deformations with constant shear rates $\dot{\gamma} = 10^{-3},\ 10^{-5}$, the upper and lower curves, respectively.

As it was mentioned before, the occurrence of the overshoot in the transient regime, marks the non-Newtonian response of the SCLs to a shear deformation. The crossover response of SCLs from a Newtonian to a non-Newtonian liquid can be characterized by $\Delta_\sigma = \sigma_p - \sigma_{ss}$, the difference between the σ_p and the steady-state stress σ_{ss}, which decreases with decreasing shear rate and vanishes in the Newtonian regime. This is shown in Fig. 5.4 where we see that, for the SCLs at $\rho = 1.2$ and $T = 0.44,\ 0.45,\ 0.5$, Δ_σ disappears at a critical shear rate $\dot{\gamma}_c$ for which the value of $\Delta_\sigma = 0$. In Fig. 5.4 one can extrapolate a critical shear rate $\dot{\gamma}_c$ which marks the crossover response from a Newtonian to a non-Newtonian liquid at $\Delta_\sigma = 0$. Therefore, in Fig. 5.4 we fit the results for Δ_σ, for different temperatures, with a function of the form $f(\dot{\gamma}) = a + b\,(\ln(\dot{\gamma}))$ (dashed black lines). The obtained values are shown in table (5.3). Now, we scale the results shown in Fig. 5.4 with the obtained values for the $\dot{\gamma}_c$. This is shown in Fig. 5.5. From the figure we see that, irrespective of temperature, all the data collapse on top of each other which can be well fitted with a function of the form $B_c \ln(\dot{\gamma}/\dot{\gamma}_c)$ (B_c is the fit parameter). By fitting the data for SCLs at $\rho = 1.2$ and $T = 0.44,\ 0.45,\ 0.5$ in red, blue and orange, respectively, in Fig. 5.5 we obtained a fit parameter $B_c = 0.0699007$ (dashed black line).

The crossover response of the SCLs is also reflected in the flow curve (σ_{ss} as a function of shear rate $\dot{\gamma}$) shown in Fig. 5.6 where we see that, the flow

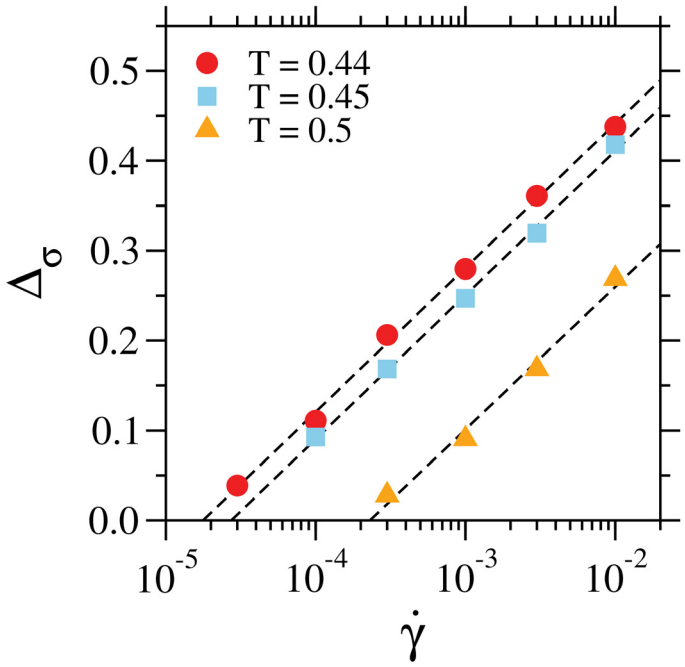

Figure 5.4: Comparison between Δ_σ in SCLs. The dashed black lines are fits (check the text) to data with the given values in table (5.3).

Comparison between the $\dot{\gamma}_c$ in SCL state

	a	b	$\dot{\gamma}_c = exp(-(\frac{a}{b}))$
$SCL\|_{T=0.44}$	0.762	0.070	1.8×10^{-5}
$SCL\|_{T=0.45}$	0.732	0.070	2.7×10^{-5}
$SCL\|_{T=0.5}$	0.577	0.069	2.3×10^{-4}

Table 5.3: Critical shear rate $\dot{\gamma}_c$, obtained for SCLs from fits to the shown data in Fig. 5.4 with function of the form $f(\dot{\gamma}) = a + b\,(\ln(\dot{\gamma}))$.

curve of the SCLs shows a crossover from a linear response (fitted with a linear function shown with dashed gray line) for $\dot{\gamma} < \dot{\gamma}_c$ to a non-linear response for $\dot{\gamma} > \dot{\gamma}_c$. In Fig. 5.6 the data has been scaled with the corresponding values of $\dot{\gamma}_c$ for each temperature, presented in table (5.3), and the vertical black dotted line at $\dot{\gamma}/\dot{\gamma}_c = 1.0$ marks the crossover point. In the non-Newtonian regime for $\dot{\gamma} > \dot{\gamma}_c$ the data for the SCL at $T = 0.44$ is fitted with a Herschel–Bulkley function of the form $\sigma_{ss} = \sigma_{yield} + A\,(\dot{\gamma}/\dot{\gamma}_c)^\alpha$ with the "yield stress" $\sigma_{yield} = 0.127334$, the amplitude $A = 0.0502496$ and the exponent $\alpha = 0.357024$ (dashed green line). The latter behavior in the flow curve is directly reflected in the evolution of the viscosity of SCLs as a function of shear rate. This is shown Fig. 5.7. The viscosity η of the samples in the super-cooled liquid state at $\rho = 1.2$ and $T = 0.44, 0.45, 0.5$ in red, blue and orange, respectively, is scaled with the viscosity in the Newtonian regime at low shear rates η_N in Fig. 5.7, and the x-axis is scaled

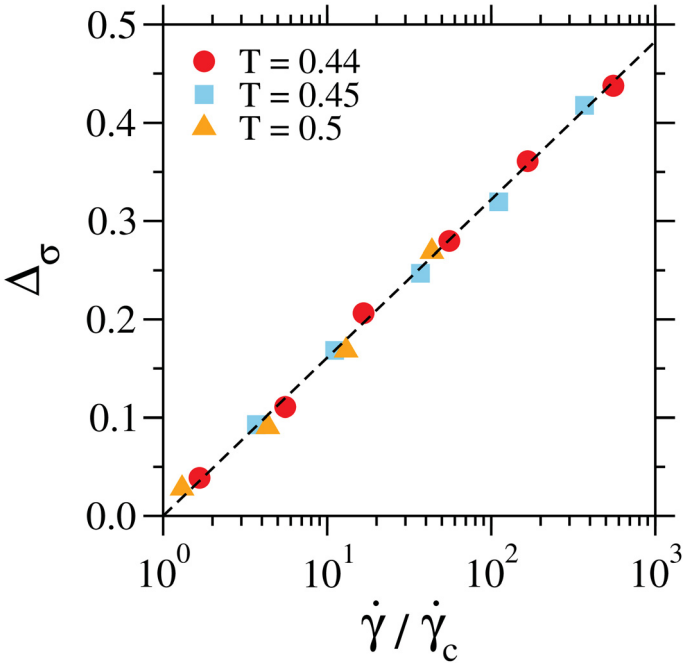

Figure 5.5: Scaled Δ_σ for super-cooled liquids at $\rho = 1.2$ and $T = 0.44$, 0.45, 0.5 in red, blue and orange, respectively. The dashed black line is a function of the form $\ln(\dot{\gamma}/\dot{\gamma}_c)$ (see text).

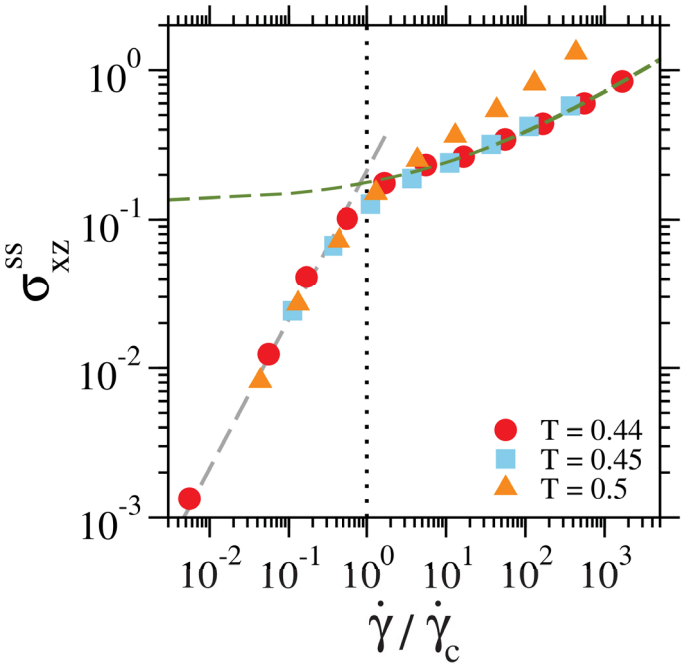

Figure 5.6: Flow curves for super-cooled liquids at $\rho = 1.2$ and $T = 0.44$, 0.45, 0.5 in red, blue and orange, respectively. The x-axis is scaled with the corresponding critical shear rate $\dot{\gamma}_c$ for each temperature. The gray dashed line is a linear function and dotted vertical line marks the crossover point. The green dashed line is a Herschel–Bulkley type fit function applied to the data for $T = 0.44$ in the non-Newtonian regime (see text).

with the corresponding $\dot{\gamma}_c$ for each temperature. Here we can see that, while in the Newtonian regime, in the limit of very small shear rates, the viscosity of the samples is (on average) constant, the response of the system shows a crossover (marked by the vertical black dotted line) to a non-Newtonian liquid with a power-law decrease of viscosity (shear thinning) which can be fitted with the scaled Herschel–Bulkley function from Fig. 5.6 (the dashed green line).

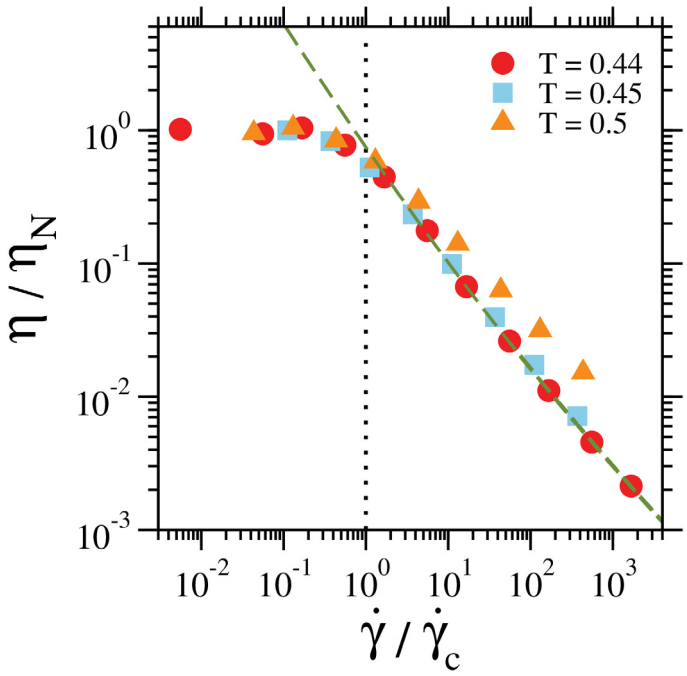

Figure 5.7: Scaled viscosity with respect to the viscosity in the Newtonian regime for supercooled liquids at $\rho = 1.2$ and $T = 0.44$, 0.45, 0.5 in red, blue and orange, respectively. The x-axis is scaled with the corresponding critical shear rate $\dot{\gamma}_c$ for each temperature. The black dotted vertical line marks the crossover point. The dashed green line is a Herschel–Bulkley type fit function from Fig. 5.6 (see text).

The change in response of SCLs from a Newtonian to the non-Newtonian liquid, can also be studied in terms of one-particle dynamics by means of the mean-squared displacement. This is shown in Fig. 5.8. The z-component of the MSD (Eq. 2.3) for both particle types A and B, with solid and dashed lines, respectively, is shown in Fig. 5.8 for SCLs at $T = 0.44$ and $\rho = 1.2$, as a function of time. The samples are subjected to shear deformation with constant shear rates $\dot{\gamma}$ shown in Fig. 5.8. Also, the MSD of undeformed samples is shown in the plot with gray squares for A type particles, and black squares for B type particles. From the figure we can see that, while, at high shear rates ($\dot{\gamma} = 10^{-3}$ and $\dot{\gamma} = 10^{-4}$ in green and light blue, respectively) the MSD shows a super-diffusive behavior before reaching the diffusion regime (for both particle types), at low shear rates ($\dot{\gamma} = 10^{-6}$ and $\dot{\gamma} = 10^{-7}$ in light orange and red, respectively) the MSD sits on top of their respective quiescent undeformed state and shows a Newtonian response. The dashed black line is a linear function of time with slope 1.0. In order to have

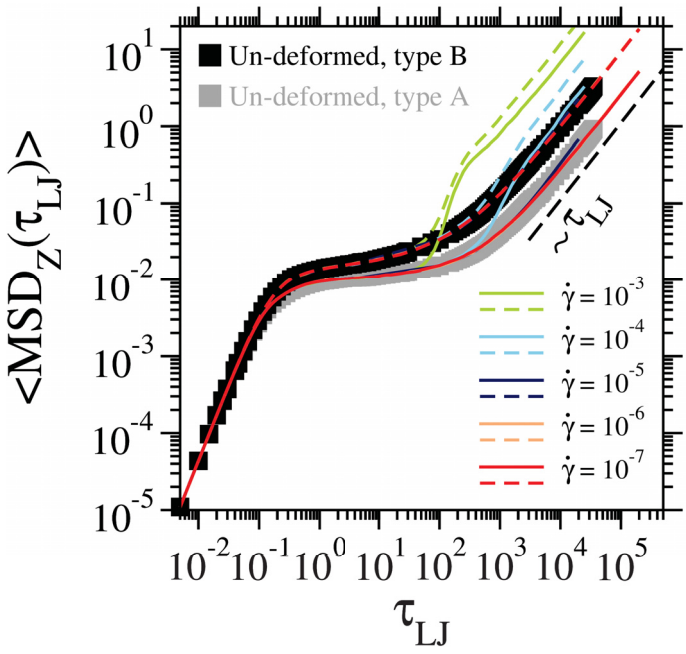

Figure 5.8: Mean-squared displacement (for particle types A and B, solid and dashed lines, respectively) as a function of time for SCLs at T = 0.44 under shear load and in the undeformed state (gray squares for A type particles and black squares for A type particles). The dashed black line denotes a linear function with slope = 1.

a more clear picture, in Fig. 5.9 we show only the MSD of A type particles for SCLs at T = 0.44 and for more shear rates.

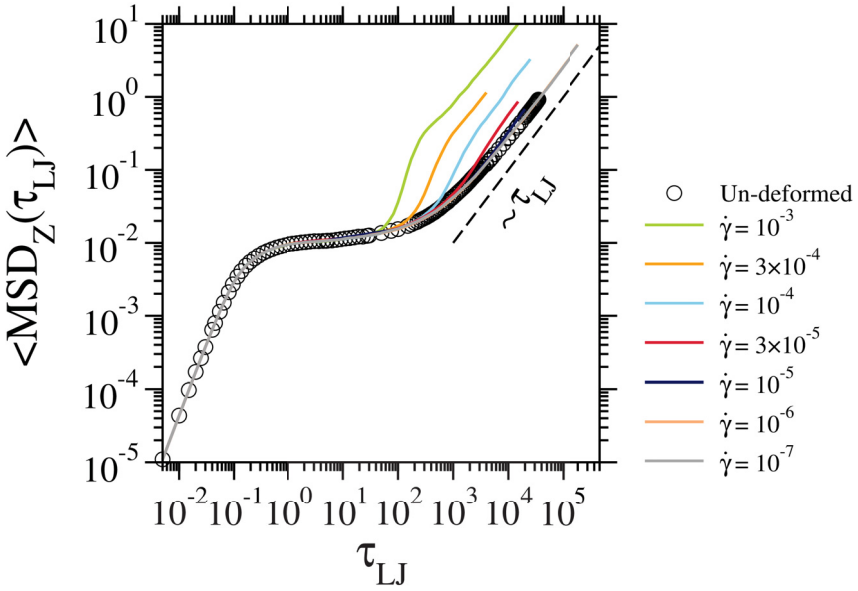

Figure 5.9: Mean-squared displacement of A type particle as a function of time for SCLs at T = 0.44 under shear load and in the undeformed state (black circles). The dashed black line denotes a linear function with slope = 1.

We also investigate the change in potential energy ($< U >$, the brackets denote average over many samples) of SCLs as a function of strain, while the samples are subjected to a shear load. This is shown in Fig. 5.10 for SCL at T = 0.44 and a variety of different shear rates. In Fig. 5.10 we can see that, the potential

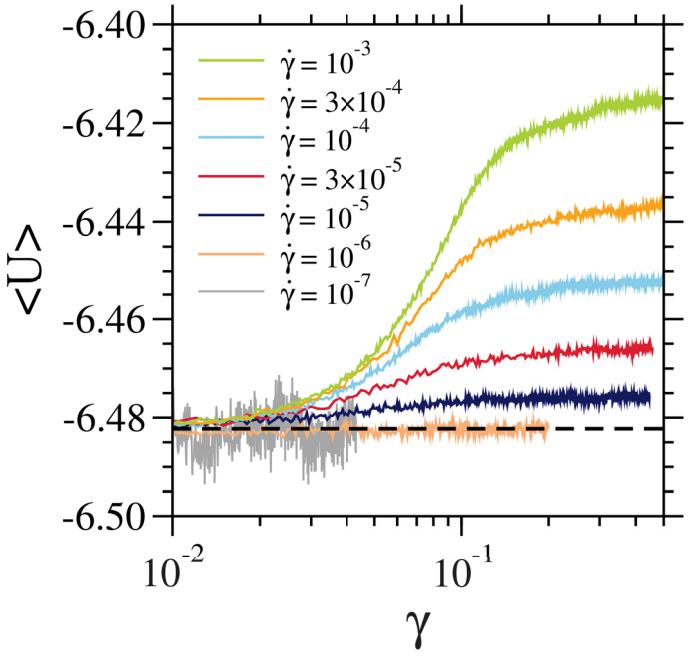

Figure 5.10: Evolution of potential energy as a function of strain, for SCLs at $T = 0.44$ under shear load. The dashed black line is the averaged potential energy obtained from undeformed samples.

energy for shear rates well above the $\dot{\gamma}_c$ (e.g. $\dot{\gamma} = 10^{-3}$, 3×10^{-4}), shows a step like increase around strain ~ 0.1, before reaching the steady state regime. This step like increase disappears for shear rates below $\dot{\gamma}_c$ in the Newtonian regime (e.g. $\dot{\gamma} = 10^{-6}$, 10^{-7}) where, the potential energy just fluctuates around the values of its initial undeformed state $U_0 = -6.48224$ (dashed black line). We also characterize the increase in potential energy of the samples subjected to shear load, by looking at $\Delta U = \langle U_{ss} \rangle - \langle U_0 \rangle$, which is the difference between the averaged potential energies of the samples under shear load in the steady state, $\langle U_{ss} \rangle$, and their quiescent undeformed state, $\langle U_0 \rangle$. This is shown in Fig. 5.11.

In Fig. 5.11 we compare ΔU between SCLs samples at $T = 0.44$, 0.5 (red and orange symbols, respectively) as a function of shear rate $\dot{\gamma}$. The fit to the data shows a power law increase with increasing shear rate. The power law exponents are shown in the figure for different temperature. Figure 5.11 represents the ΔU for a range of shear rates above the $\dot{\gamma}_c$ in the non-Newtonian regime. In Fig. 5.12 we present the $\Delta U / |\langle U_0 \rangle|$ as a function of scaled shear rates $\dot{\gamma}/\dot{\gamma}_c$, for super-cooled liquids at $T = 0.44$, 0.45, 0.5. With this representation, we can see a clear crossover from the Newtonian regime towards the non-Newtonian regime around $\dot{\gamma}/\dot{\gamma}_c = 1.0$. In the Newtonian regime we see a clear linear response for all the super-cooled liquids. For $\dot{\gamma}/\dot{\gamma}_c > 1.0$ the data for super-cooled liquids at $T = 0.44$, 0.45 can be well fitted with a power law function ($(\dot{\gamma}/\dot{\gamma}_c)^{\beta}$) with a component $\beta \sim 0.38$.

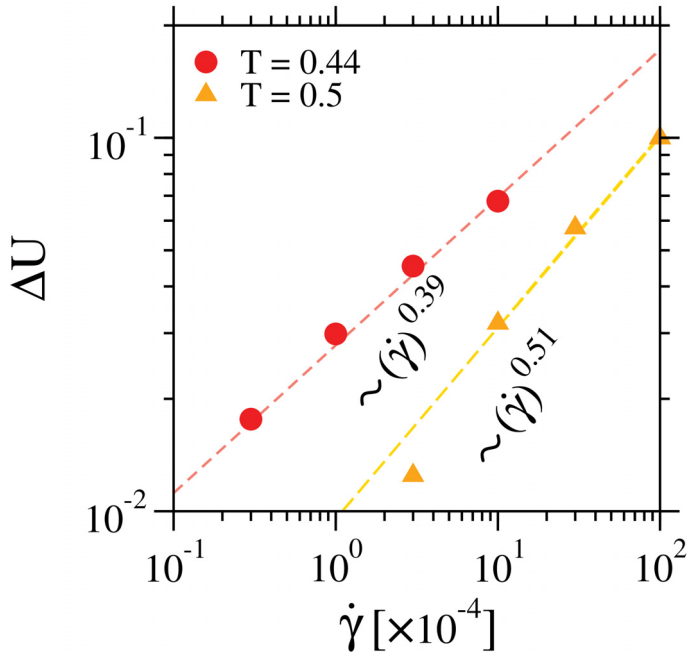

Figure 5.11: ΔU as a function of shear rate for SCLs at $T = 0.44, 0.5$ (red and orange closed symbols, respectively) and $\rho = 1.2$. The dashed lines are power law fits to data with exponents shown in the plot.

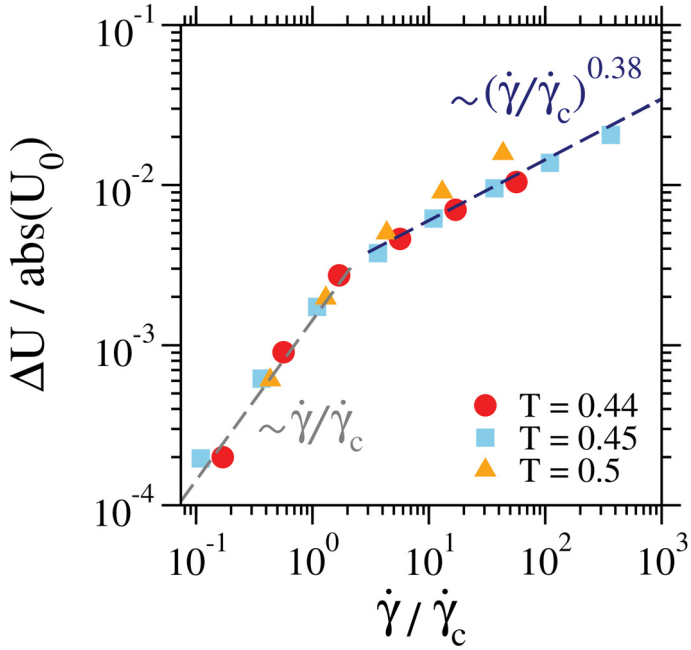

Figure 5.12: $\Delta U/|\langle U_0\rangle|$ as a function of scaled shear rates $\dot\gamma/\dot\gamma_c$ for super-cooled liquids at $\rho = 1.2$ and $T = 0.44,\ 0.45,\ 0.5$ in red, blue and orange, respectively.

5.1.2 *In-homogeneous flow patterns in super-cooled liquids*

Up to now, we characterized the macroscopic response of SCLs when subjected to a shear deformation with a constant shear rate. We showed that the macroscopic response in the SCLs shows a crossover from a Newtonian to a non-Newtonian behavior. In the non-Newtonian regime, local events such as local mobilities result in the formation of inhomogeneities in the system. In this section, we study these in-homogeneous flow patterns in super-cooled liquids.

In SCLs the decay of the stress from the overshoot maximum towards the steady-state regime, occurs in a strain window of the order of $\Delta\gamma = 0.1$. This stress decay appears to occur in a much smaller strain window for glasses with horizontal shear bands (we will come back to this point when we discuss about Fig. 5.27). In Fig. 5.13 we present the stress decay σ_r for SCLs at $T = 0.44$ obtained from the stress-strain curve shown in Fig. 5.1.

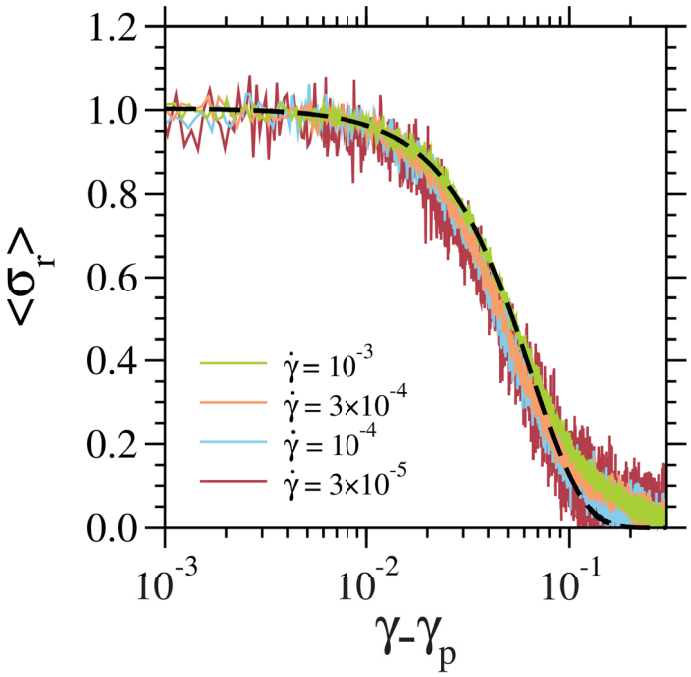

Figure 5.13: Stress decay from the overshoot maximum towards the steady-state (check 5.2) for SCLs at $T = 0.44$ under shear load.

In Fig. 5.13 we can see that, as it was mentioned before, the stress decay occurs in a strain window of $\Delta\gamma = 0.1$ and can be well fitted with a compressed exponential function (dashed black line[2]) $\exp(x^{\alpha})$ with $\alpha > 1$. Note that the fit with the compressed exponential does not provide a perfect description of the data over the whole strain window, but it just gives a rough idea about the functional form of the decay of σ from σ_p to σ_{ss}. The plastic events in this strain window, which result in a stress release towards the steady-state

[2]In order to fit the data we used a Kohlrausch-Williams-Watts (KWW) function [Zausch and Horbach (2009)], $f(x) = A\exp\left(-Bx^{C}\right)$. The fitting values are as follows, $A = 1.004$, $B = 103.823$ and $C = 1.699$.

regime, occur in a much smaller time window than the structural relaxation times in an undeformed SCL. Therefore, for a given $\dot{\gamma} > \dot{\gamma}_c$ in-homogeneous flow patterns may occur in SCL by the formation of vertical bands at strains right after the overshoot on the stress-strain curve. Although these inhomogeneities are short-lived and span the whole system in a rather short strain window in SCLs, later we will show that in glasses, these inhomogeneities are more stable and localized, and often result in the formation of shear bands. In order to investigate the formation of these inhomogeneities, we have calculated per-particle MSD and assigned these values as a mobility factor to each particle. We have traced the inhomogeneities via these *mobility maps*[3] a long the stress-strain curve in SCL state for two shear rates, one well above $\dot{\gamma}_c$ ($\dot{\gamma} = 10^{-3}$) and also below $\dot{\gamma}_c$ ($\dot{\gamma} = 10^{-6}$). These results are shown in Fig. 5.14. The mobility maps of the non-Newtonian regime, for shear rate $\dot{\gamma} = 10^{-3}$, are shown in panel A of Fig. 5.14, and the mobility maps for the Newtonian regime, for the shear rate $\dot{\gamma} = 10^{-6}$, are shown in panel B. The corresponding strain points at which the mobility maps are calculated are indicated on the stress-strain curve. From Fig. 5.14 following the stress-strain curve for the shear rate $\dot{\gamma} = 10^{-3}$, we can see that at the overshoot maximum ($\gamma = 0.08$) some small hot spots (locally mobile regions shown in red) are appearing in the system. Right after the overshoot ($\gamma = 0.15$), these hot spots evolve towards some vertical band-like regions. But, as it was discussed before, these vertical bands are short-lived and, in a short strain window, span the whole system such that, at $\gamma = 0.3$, they have already spanned the whole system before reaching the steady-state. The behavior of the sample is different for the shear rate of $\dot{\gamma} = 10^{-6}$. From panel B of Fig. 5.14 we can see that, while at very early times (strain point $\gamma = 0.01$) the hot spots start to appear in the system, these hot spots are not localized, and they span the whole system in a tiny strain window such that, at $\gamma = 0.03$ in Fig. 5.14 we can see that, the hot spots have covered the whole system. Therefore, the SCL subjected to shear deformation with the constant shear rate $\dot{\gamma} = 10^{-5}$ reaches the steady-state regime much earlier compared to the other sample subjected to a constant shear rate $\dot{\gamma} = 10^{-3}$ such that already at $\gamma = 0.06$ the whole system is flowing almost homogeneously.

In order to further investigate the inhomogeneities, we characterize the non-Gaussian behavior of the stress fluctuations by calculating the so-called *Kurtosis* [Pearson (1905)] as:

$$\kappa = \frac{\left\langle (\Delta\sigma_{xz})^4 \right\rangle}{\left\langle (\Delta\sigma_{xz})^2 \right\rangle^2}, \tag{5.1}$$

where $\Delta\sigma_{xz} = \sigma_{xz} - \langle\sigma_{xz}\rangle$ denotes the fluctuation in the xz-component of the stress tensor σ_{xz} Eq. (3.6) and $\langle\sigma_{xz}\rangle$ defines the mean stress averaged over independent

[3]Because of large sample to sample fluctuations; these features can only be seen in single samples, therefore, here we present non-averaged results for single samples.

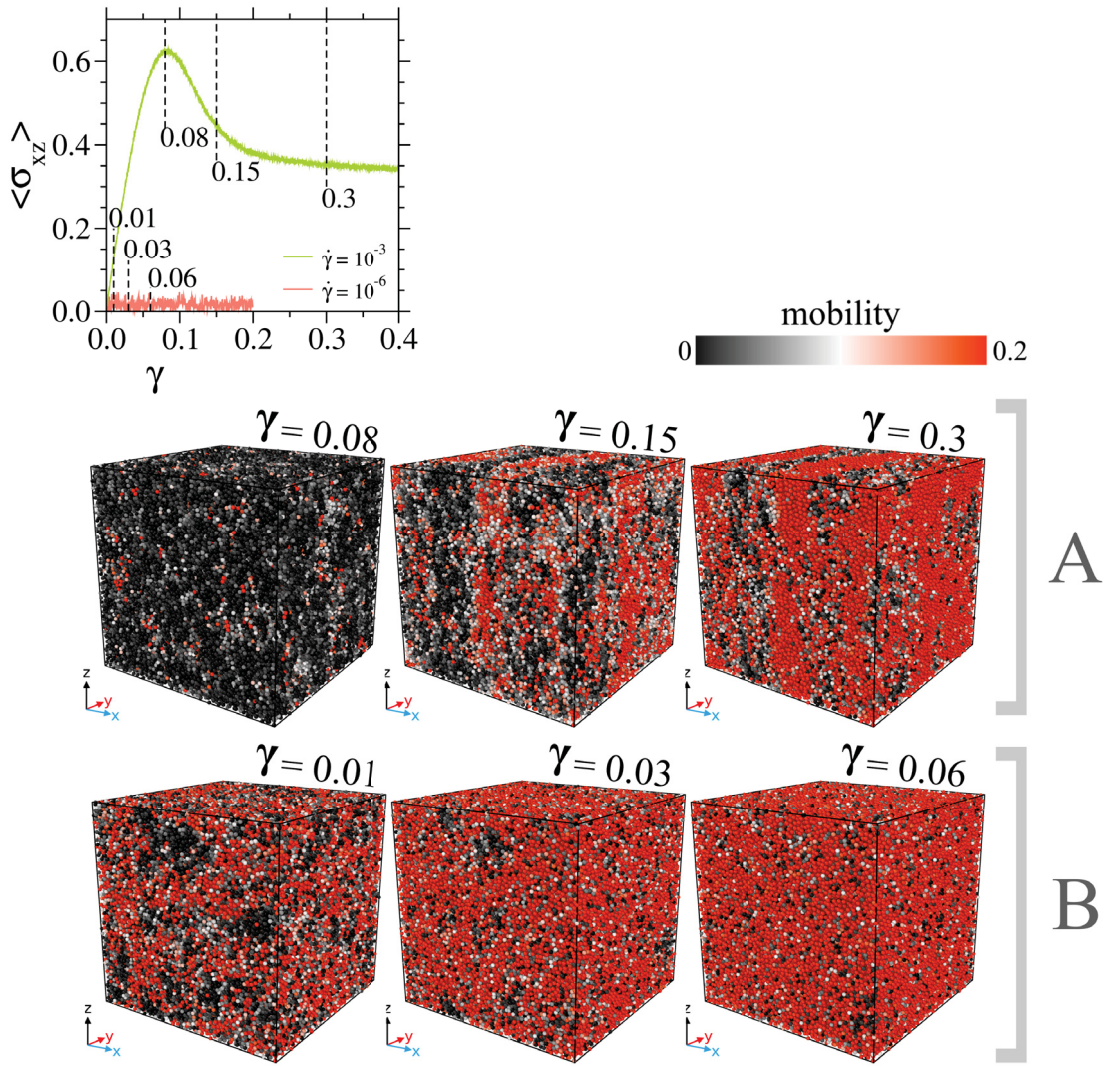

Figure 5.14: *panel A*: Mobility maps for a SCL sample at T = 0.44 being imposed to constant shear rate $\dot{\gamma} = 10^{-3}$ in the non-Newtonian regime, at different strain points indicated on the corresponding stress-strain curve. *panel B*: Mobility maps for a SCL sample at T = 0.44 being imposed to constant shear rate $\dot{\gamma} = 10^{-6}$ in the Newtonian regime, at different strain points indicated on the corresponding stress-strain curve.

samples. $(\Delta\sigma_{xz})^4$ and $(\Delta\sigma_{xz})^2$ in Eq. (5.1), denote the fourth and second moments of the stress probability distribution, respectively. In Fig. 5.15 we present the non-Gaussian behavior of the stresses for SCLs at T = 0.44, and for three different shear rates $\dot{\gamma} = 10^{-3}$, 10^{-4}, 10^{-6}. From Fig. 5.15 we can see that, irrespective of the shear rate, κ fluctuates around $\kappa_0 = 3.055$ (dashed black line) obtained from the samples in the quiescence undeformed state (for a Gaussian distribution $\kappa = 3$). Therefore, the inhomogeneities are so short-lived and small that they do not change the Gaussian behavior of the stress distribution in the system with respect to the quiescence undeformed states.

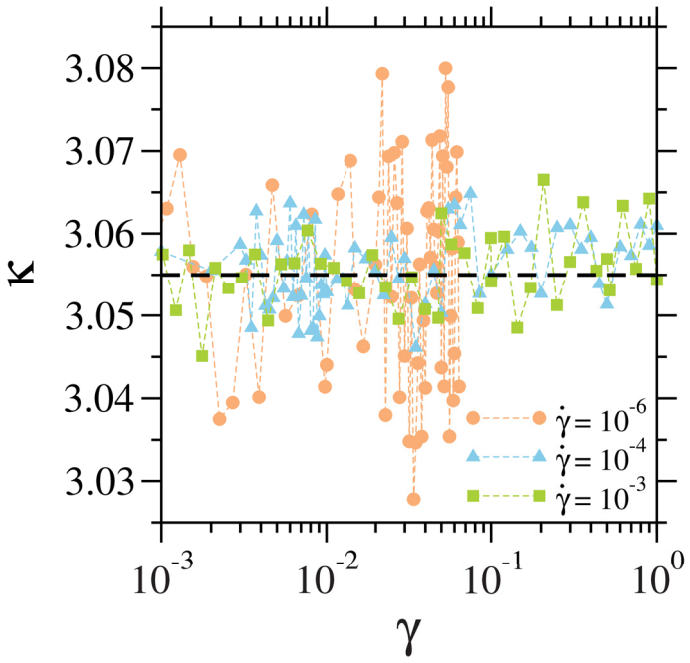

Figure 5.15: κ as a function of strain, for SCL samples at $T = 0.44$, being imposed to a shear deformation with shear rates $\dot{\gamma} = 10^{-3}$, 10^{-4}, 10^{-6} in pale orange, blue and green, respectively. The dashed black line is the averaged κ obtained from the undeformed samples.

5.1.3 Glasses under shear

Up to now, we discussed the response of SCLs being subjected to shear deformation. We showed that the SCL's response shows a crossover from a Newtonian to non-Newtonian liquid, wherein the non-Newtonian regime short-lived inhomogeneous flow patterns might appear in the system. Here, we discuss the response of glasses when subjected to a shear deformation with a constant shear rate and make a comparison to the results which we showed for SCLs.

In Fig. 5.16 we present the stress-strain curves obtained from the glass samples at $T = 0.2$ and $\rho = 1.2$, subjected to shear deformation with a variety of shear rates $\dot{\gamma} = [10^2, 3 \times 10^3, 10^3, 3 \times 10^4, 10^4, 3 \times 10^5, 10^5]\, \tau_{LJ}^{-1}$. The stress-strain curves shown in Fig. 5.16, for all shear rates, shows three clear distinguishable regimes, same as SCLs in non-Newtonian regime. In Fig. 5.16, we can clearly see the shear rates dependence of the stress-strain curves. By increasing shear rate (direction of the black arrow in the plot), the peak maximum of the stress-strain overshoot also increases. This is similar to the results which we discussed earlier for SCLs with the exception that, even for small shear rates ($\dot{\gamma} = 10^{-5}$, gray lines), the stress-strain curve shows a non-Newtonian response marked by a pronounced overshoot. The response of the samples in the elastic regime (cf. 2.2.2), shows no shear rate dependence. This is expected as the linear response of the stress-strain curve, in the limit of small strains, gives the shear modulus of the samples. Therefore, no matter what shear rate is imposed to the system, the shear modulus should not change. Here, in order to study the transient response of glasses to

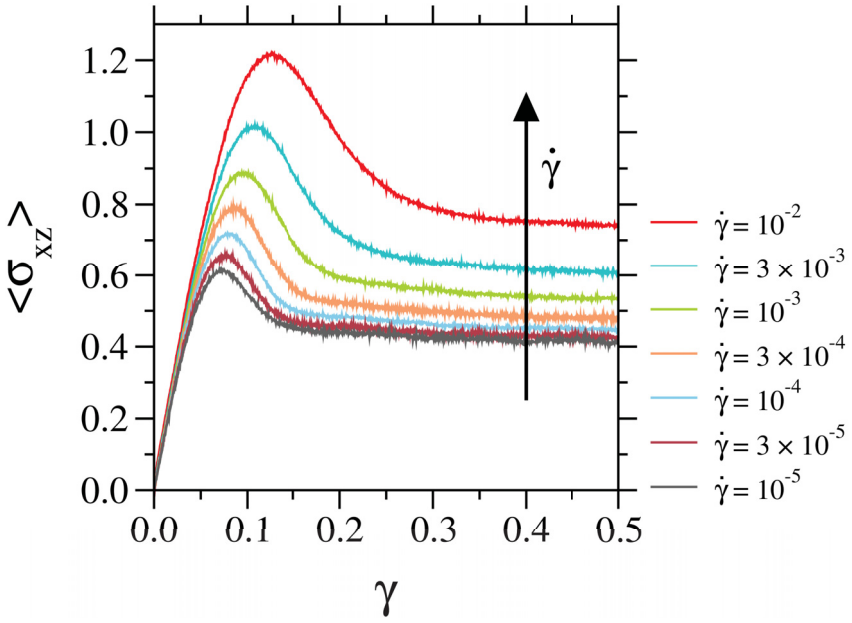

Figure 5.16: Stress-strain curves for glasses (T = 0.2, N = 32400, ρ = 1.2) being imposed to shear deformation with different shear rates.

shear deformation in more details, and make a comparison to the results which we discussed earlier for SCLs, we look at the same quantities as presented in section (5.1.1).

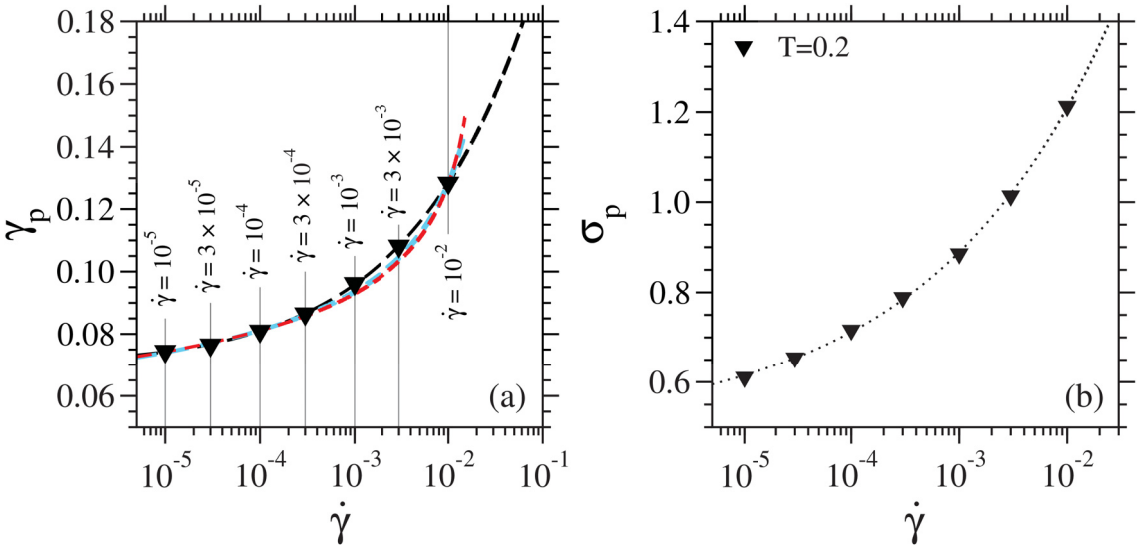

Figure 5.17: *panel (a)*: the overshoot peak position γ_p as a function of shear rate $\dot{\gamma}$ (the corresponding shear rates are marked with solid vertical lines) in the glass state at $\rho = 1.2$ and $T = 0.2$. The dashed lines are fit functions (see the text). *panel (b)*: the stress maximum at the overshoot σ_p as a function of shear rate $\dot{\gamma}$.

In panel (a) of Fig. 5.17 we present γ_p as a function of shear rate (shear rates are marked with vertical solid lines) for glass samples at $\rho = 1.2$ and $T = 0.2$. Here we can see that, similar to the results we showed for SCLs, γ_p increases with increasing shear rate. Similarly, here we also fit the data with a function of the form $A_0 + A_1 x^{A_2}$ and obtained the values shown in table (5.4). The fit

parameters show a small difference between the power law behavior of γ_p for glasses and SCLs where, the power-law behavior of glasses appears to be slightly weaker. Further, following the results reported recently by [Reddy, Nath, et al. (2020)] on the shear rate dependence of γ_p in crystals, we fitted the data from the glass samples shown in panel (a) of Fig. 5.17, with a function of the form:

$$\gamma_p = \left(\frac{W[2(d-1)\alpha(\dot{\gamma}\tau_0)^{-2(d-1)}]}{2(d-1)\alpha} \right)^{-1/[2(d-1)]}, \tag{5.2}$$

with d the dimensionality of the system, τ_0 a kinetic time scale and α describing the interfacial free energy cost and W a Lambert W function [Hayes (2005)]. The Lambert W function is used to solve equations in which the unknown appears both outside and inside an exponential function or a logarithm, e.g. if $xe^x = f(x) = y$, then $x = f^{-1}(x) = W(y)$. Using the asymptotic behavior [de Bruijn (1981)] of $W(y) = \ln(y) - \ln(\ln(y)) + \cdots$ for small shear rates, we have fitted the data once only with the first leading order term (red dashed line, with fit values $\alpha = 0.000237694$ and $\tau_0 = 7.26094$) and also by considering the second leading order term (blue dashed line, with fit values $\alpha = 0.000217689$ and $\tau_0 = 5.20679$). In Fig. 5.17 we can see that, although the function has been tested for shear rate dependence of γ_p in crystals, it also shows good agreement with the results for the glass samples. We should also mention that, keeping the second leading order term, the fit function (dashed blue line) seems to agree better with the data.

Fit parameters for γ_p in the glass state

	A_0	A_1	A_2
Glass	0.068	0.287	0.340

Table 5.4: Values are obtained by fitting the results with a function of the form $A_0 + A_1 x^{A_2}$

In panel (b) of Fig. 5.17 we show the shear rate dependence of σ_p as a function of shear rate. Similar to the analysis before, here also the data has been fitted with a function of the form $A_0 + A_1 x^{A_2}$ (dotted black line) and the obtained values are shown in table (5.5). Making a comparison between tables fit parameters in tables (5.2) and (5.5) we can see that, σ_p shows a stronger power-law behavior in glasses compared to the SCLs.

Here, in order to compare the transient response between SCLs and glasses, we compare the temperature dependence of σ_p between, glasses at temperatures $T = 10^{-4}$, 0.2 and SCLs at temperatures $T = 0.44$, 0.5, being imposed to a single constant shear rate $\dot{\gamma} = 10^{-4}$. This is shown in Fig. 5.18. At low temperatures (light-blue curve) in the glass state, we have a well pronounced overshoot. But, the

Fit parameters for σ_p in the glass state

	A_0	A_1	A_2
Glass	0.494	2.350	0.258

Table 5.5: Values are obtained by fitting the results with a function of the form $A_0 + A_1 x^{A_2}$

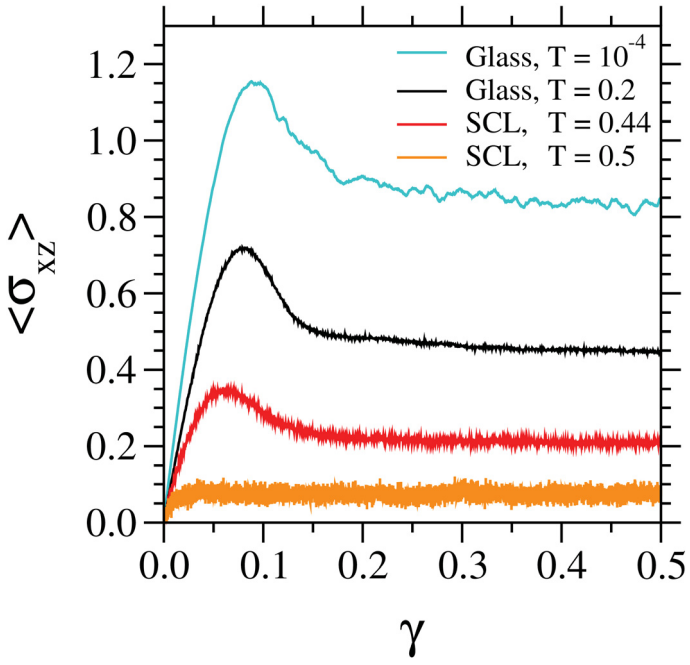

Figure 5.18: Temperature dependence of the overshoot for glasses at $T = 10^{-4}$, 0.2, $N = 40000$, 32400, $\rho = 1.3$, 1.2, respectively, and super-cooled liquids at $T = 0.44$, 0.5, $N = 32400$, $\rho = 1.2$, being imposed to a single constant shear rate $\dot{\gamma} = 10^{-4}$.

overshoot maximum decreases by increasing temperature such that, it vanishes for super-cooled liquid at $T = 0.5$ (orange curve). The peak maximum position also shifts towards larger strain points with decreasing temperatures, indicating a larger strain window in the glass state in which, the response of the system is elastic. Therefore, the glass samples are reaching the steady-state regime at larger strains compared to SCLs. Here, we should mention that, although the results shown in Fig. 5.18 for SCLs and glasses are obtained from samples which are prepared with the same cooling rate, the transient response of the samples in the glass state strongly depends on the annealing time and the history of preparation.

The temperature dependence, and the effect of annealing on the transient response of a glass forming system, being subjected to a shear deformation with constant shear rates, has been extensively studied by [Shrivastav, Chaudhuri, and Horbach (2016)]. In this work, using a Kob-Andersen binary Lennard-Jones mixture [Kob and Andersen (1994)], the authors showed that at a given temperature in the glass state, σ_p increases with increasing annealing time (waiting time t_w) for the samples which are imposed to a single constant shear

rate $\dot{\gamma}$. They showed that, the latter increase (for a wide range of shear rates $\dot{\gamma}$) can be well fitted with a logarithmic function of the form $\sigma_p = C(\dot{\gamma}, T) + A(T)\ln(\dot{\gamma} t_w)$, with $A(T)$ a temperature-dependent amplitude that is independent of $\dot{\gamma}$ and t_w, and $C(\dot{\gamma}, T)$ a function that solely depends on $\dot{\gamma}$ and T. They also showed that, σ_p decreases by increasing temperature, which is consistent with our findings.

The transient response of glasses under shear load can be further investigated by looking at the shear rate dependence of Δ_σ. Similar to the results shown for SCLs (cf. Fig. 5.4), here, in Fig. 5.19 we show Δ_σ for glasses at $\rho = 1.2$ and $T = 0.2$, as a function of shear rate. In comparison to the results for SCLs, here we can see that, in case of glasses the non-Newtonian response holds up to much smaller shear rates. Following the same analysis for SCLs, here we also fit the

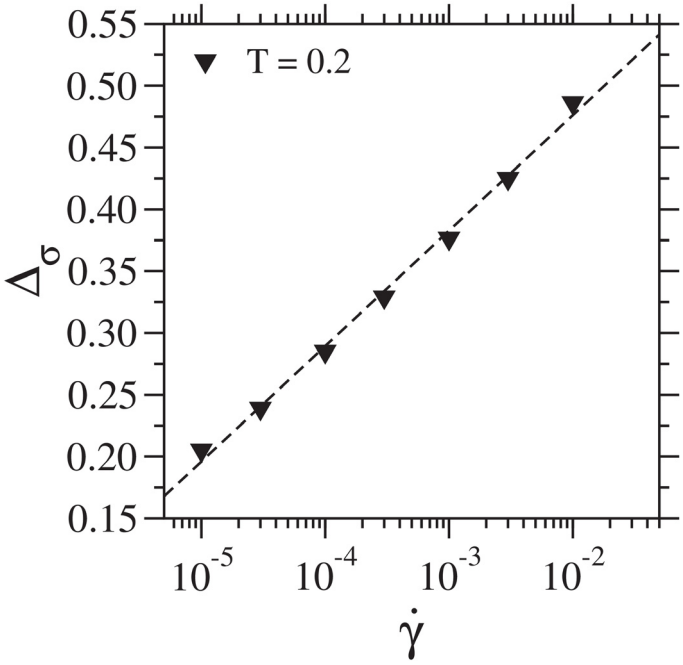

Figure 5.19: Δ_σ as a function o shear rate in glass state at $\rho = 1.2$ and $T = 0.2$. The dashed black line is a fit (check the text).

data with a function of the form $f(\dot{\gamma}) = a + b(\ln(\dot{\gamma}))$ (dashed black line) with the fit parameters, $a = 0.663$ and $b = 0.041$. Here we should note that, as we discussed earlier, the transient responses in the glass state highly depend on the history with which the samples are prepared, therefore, a change in annealing of the samples may affect these results.

As it was discussed before (cf. section (2.2.2)), the flow curve of glasses under shear load shows a Herschel–Bulkley behavior. This is shown in Fig. 5.20, where, steady state stress σ_{ss} is plotted as a function shear rate $\dot{\gamma}$ for glasses at $\rho = 1.2$ and $T = 0.2$. In Fig. 5.20 the data is fitted with a Herschel–Bulkley function of the form $\sigma_{ss} = \sigma_{yield} + A(\dot{\gamma})^\alpha$ with the "yield stress" $\sigma_{yield} = 0.389395$, the amplitude $A = 2.63875$ and the exponent $\alpha = 0.446392$ (dashed gray line).

We also characterize the response of glass samples at $\rho = 1.2$ and $T = 0.2$ being

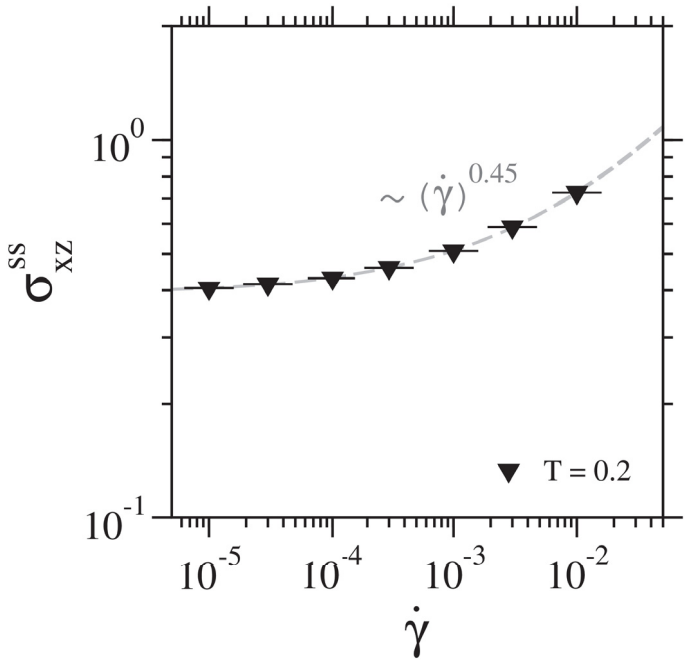

Figure 5.20: Flow curve for glasses at $\rho = 1.2$ and $T = 0.2$. The dashed gray line is a Herschel–Bulkley type fit function (see the text).

subjected to shear deformation (with constant shear rates shown in Fig. 5.21) in terms of single particle dynamics by looking at $MSD_z(\tau_{LJ})$ and $MSD_y(\tau_{LJ})$ of the A type particles in panel (a) and (b) of Fig. 5.21, respectively. In panel

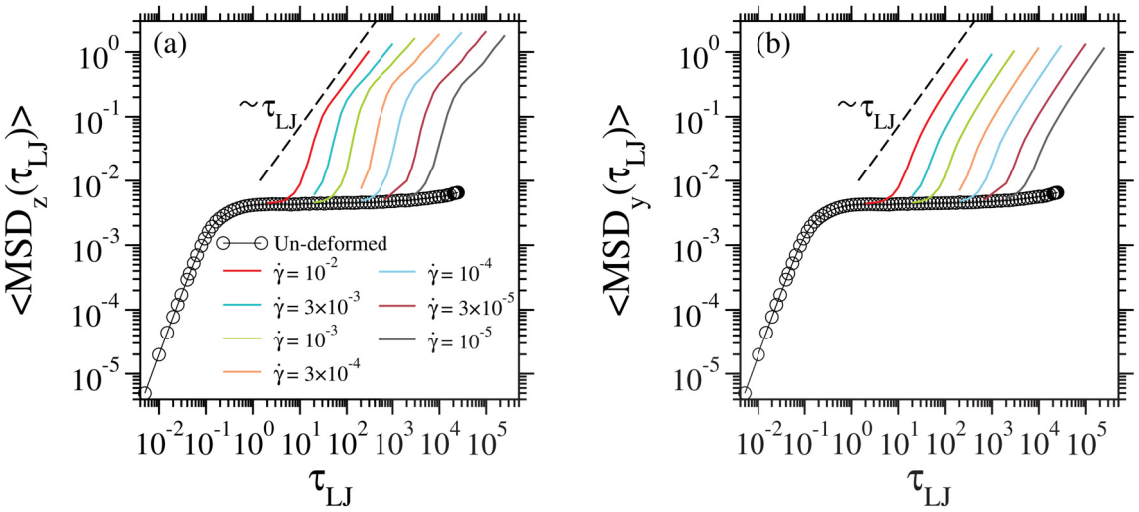

Figure 5.21: *panel (a)*: $MSD_z(\tau_{LJ})$ as a function of time for glass samples imposed to shear deformation with shear rate shown in the plot. The curve with black open circles shows the $MSD_z(\tau_{LJ})$ of an undeformed glass sample over time. *panel (b)*: same as in panel (a) for $MSD_y(\tau_{LJ})$.

(a) and (b) of Fig. 5.21 $MSD_z(\tau_{LJ})$ and $MSD_y(\tau_{LJ})$ of samples subjected to shear deformation are compared to the corresponding MSD of the undeformed states (curves with black open circles). The data for the deformed samples, are shown only for the time scales at which the particles are leaving the plateau region and cage breaking happens. By comparing the two panels in Fig. 5.21 we can see

that, the $MSD_z(\tau_{LJ})$[4] shows a jump-like increase after the cage breaking happens, before reaching the diffusion regime. This response is not that pronounced for $MSD_y(\tau_{LJ})$. Another difference between the two panels of Fig. 5.21 is that, for high shear rates (10^{-2}, red curve) $MSD_z(\tau_{LJ})$ appears to reach diffusion regime after showing a super-diffusive increase, but, for lower shear rates the samples appear to need more time to reach the diffusion regime, and show a sub-diffusive behavior over a large strain window. This is not the case for $MSD_y(\tau_{LJ})$. In panel (b) of Fig. 5.21 the MSDs appear to reach diffusion regime after showing a super-diffusive increase in a very small strain window. Later in section (5.1.4) we will show that, the super-diffusive increase of $MSD_z(\tau_{LJ})$ is the fingerprint of in-homogeneous flow patterns which result in formation vertical shear bands in the glass samples. Before closing this section we make another important comparison between $MSD_z(\tau_{LJ})$ for SCLs at $\rho = 1.2$ at $T = 0.44$ and glass samples at $T = 0.2$ and same number density. This is shown in Fig. 5.22.

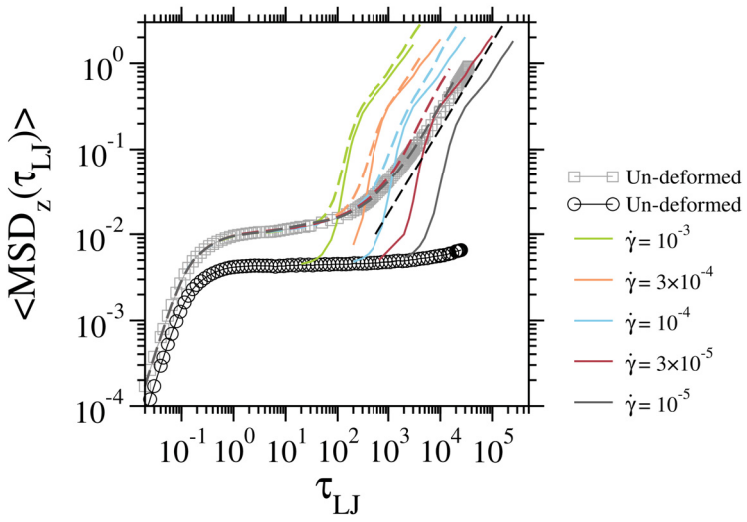

Figure 5.22: $MSD_z(\tau_{LJ})$ as a function of time for SCLs and glass at $\rho = 1.2$, $T = 0.44$ and $T = 0.2$, respectively. Samples are imposed to shear deformation with shear rate shown in the plot. The curve with black open circles and gray open squares, shows the $MSD_z(\tau_{LJ})$ of an undeformed glass and SCLs samples over time, respectively.

The $MSD_z(\tau_{LJ})$ of undeformed samples is shown in Fig. 5.22 with open black circles and open gray square for glasses and SCLs, respectively. Both SCL and glass samples are subjected to constant shear rates, which are shown in the figure with a different color. From Fig. 5.22 we can see that, at high shear rates (10^{-3}, green solid and dashed lines for glass and SCL samples, respectively) in the non-Newtonian regime, the curves sit very close to each other showing a super-diffusive increase followed by a diffusion regime. At lower shear rates, where there is a crossover from non-Newtonian to a Newtonian in the response SCLs the curves start to show deviations from each other. While, in the SCL state

[4]Here we should remind the reader that, the shear deformation has been applied in x-direction, therefore, z-direction corresponds to the gradient direction.

for shear rate, $\dot{\gamma} = 10^{-5}$ (gray dashed line) $MSD_z(\tau_{LJ})$ sits on top of the curve for undeformed states, in the glass state, at the same shear rate, the glass samples (solid gray line) still show a super-diffusive increase after leaving the plateau. This means, as we discussed before, the non-Newtonian response in glasses holds even at very low shear rates.

Here, we also characterize the macroscopic response of glass samples subjected to shear deformation, in terms of the changes occurring in the potential energy $< U >$. This is shown in Fig. 5.23 where, we show the evolution of averaged (over many samples) potential energy $< U >$ as a function of strain γ for glass samples at $\rho = 1.2$ and $T = 0.2$ subjected to shear defamation with a wide range of constant shear rates shown in the figure in different colors. In Fig. 5.23 we

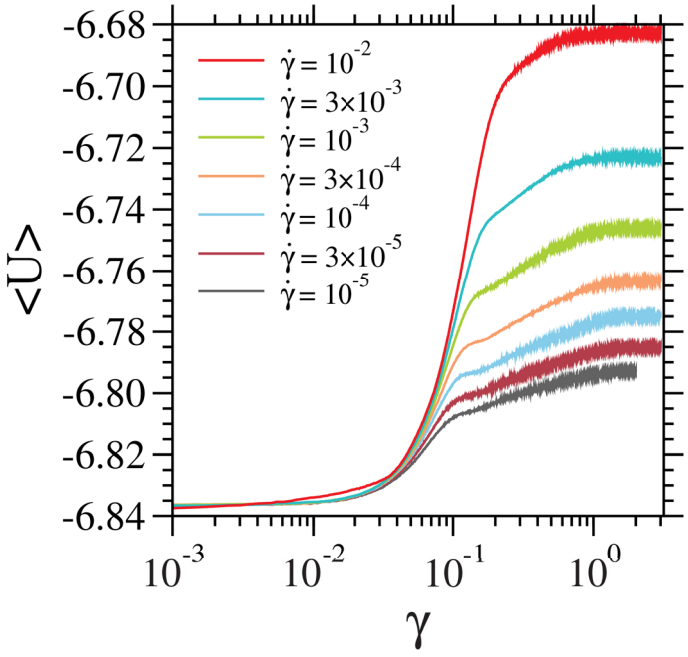

Figure 5.23: Evolution of potential energy as a function of strain, for glasses at $T = 0.2$ and $\rho = 1.2$ under shear load.

can see that, $< U >$ shows a step-like increase which has a higher amplitude for larger shear rates and stays at a finite value in the steady-state regime. An interesting observation from Fig. 5.23 is the occurrence of a shallow overshoot around $\gamma = 0.1$, for shear rates $\dot{\gamma} = 10^{-3},\ 3 \times 10^{-4},\ 10^{-4}$. Later in section (5.1.4) we will come back to this point. Similar to the analysis for SCLs (shown in Fig. 5.11), here we also look at ΔU for the glass samples. This is shown in Fig. 5.24 where we present ΔU, the difference between the steady state value of potential energy $< U_{ss} >$ and the initial undeformed values $< U_0 >$, as a function of shear rate $\dot{\gamma}$. In Fig. 5.24 we can see that, ΔU increases by increasing shear rate and shows a power law behavior shown in the figure with dashed gray line. In contrast to SCLs ΔU does not disappear at small shear rates and shows a non-Newtonian response even for very small shear rates. But, the data shows a

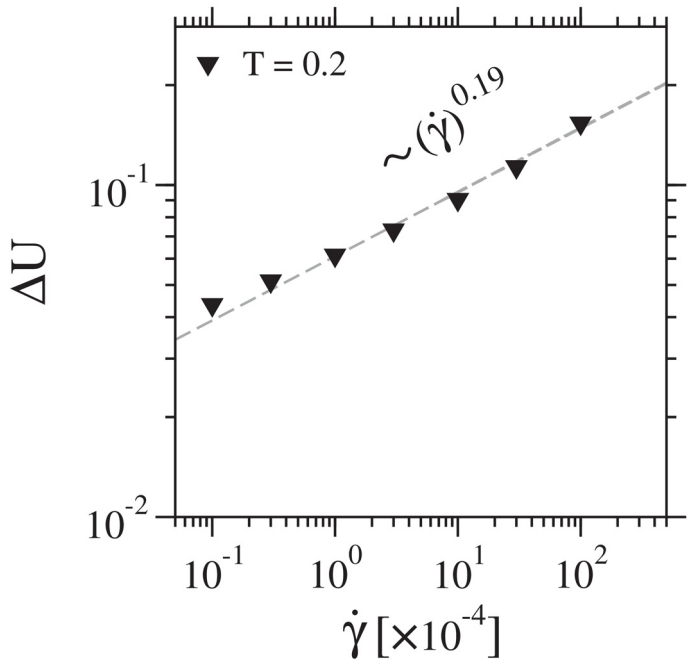

Figure 5.24: ΔU as a function of shear rate for glass samples at $T = 0.2$ and $\rho = 1.2$. The dashed line is power law fit to data with exponent shown in the plot.

weaker power law behavior compared to the results for SCLs (cf. Fig. 5.11).

5.1.4 *Shear bands in glasses*

Up to now, we discussed the macroscopic response of SCLs and glasses when subjected to shear deformation. We also showed that at a microscopic level, in the non-Newtonian regime of the SCLs, in-homogeneous flow patterns appear by the formation of short-lived vertical bands. In this section, we try to characterize the formation and evolution of long-lived in-homogeneous flow patterns in glasses, which can result in the formation of shear bands. The results discussed in this section are for two glass samples at $\rho = 1.3$ and $T = 10^{-4}$, with a cubic simulation box of length $L = 104.886\sigma_A$ containing $N = 1.5M$ particles (cf. 4.3.2), being imposed to shear deformation with a constant shear rate $\dot{\gamma} = 10^{-4}$.

5.1.5 *Horizontal bands vs. vertical bands*

The shear bands appear to start to form right after the overshoot of the stress-strain curve in glasses. The hot spots of locally mobile regions begin to create larger clusters of mobile particles and eventually evolve towards the formation of shear bands [Shrivastav, Chaudhuri, and Horbach (2016)]. These local mobile regions are long-lived in contrast to what we showed for SCLs. In a computer simulation, the local mobile regions tend to create vertical or horizontal shear bands [Golkia, Shrivastav, Chaudhuri, and Horbach (2020)]. The mechanisms which result in the formation of a vertical or a horizontal shear band are still

under debate. From now on, we will present the results which we have obtained for a sample with a horizontal shear band (will be referred to as SWHB) and a sample with a vertical band (will be referred to as SWVB).

As it was shown and discussed before, we use per-particle mean-squared displacement to characterize the mobile regions in the system. In Fig. 5.25 we present the mobility maps of a SWHB and a SWVB (being imposed to shear deformation with a constant shear rate $\dot{\gamma} = 10^{-4}$) at different strain points, which are shown on the corresponding stress-strain curve of these two samples. By

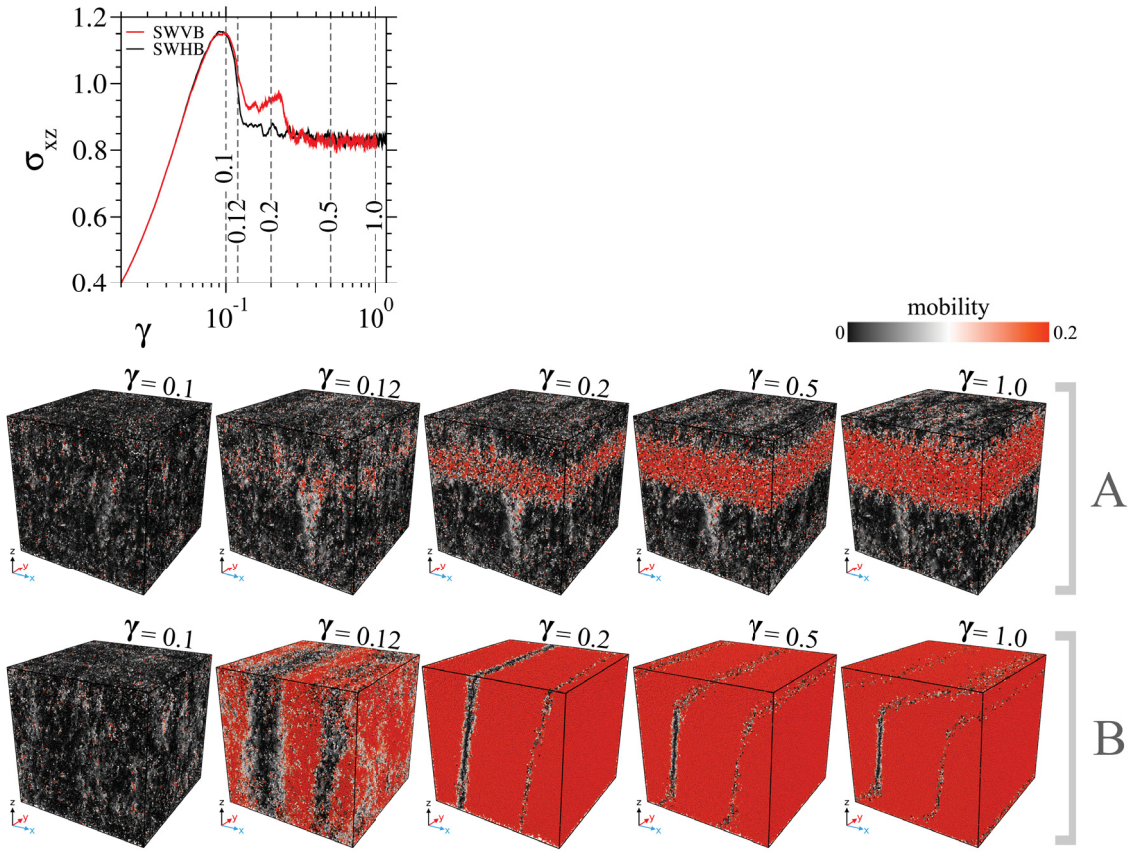

Figure 5.25: *panel A*: Mobility maps for a SWHB, being imposed to constant shear rate $\dot{\gamma} = 10^{-4}$, at different strain points indicated on the corresponding stress-strain curve (black curve). *panel B*: Mobility maps for a SWVB, being imposed to constant shear rate $\dot{\gamma} = 10^{-4}$, at different strain points indicated on the corresponding stress-strain curve (red curve).

comparing the mobility maps in panel A and B of Fig. 5.25, we can see that around the overshoot maximum ($\gamma = 0.1$) the mobile zones are almost homogeneously distributed in both samples. The stress-strain curve of the SWHB shows a sharp stress decay after the overshoot (check discussion for Fig. 5.27), and a secondary overshoot is visible in the stress-strain curve of the SWVB. The sharp release of the stresses in the SWHB results in the formation of the shear bands at later strain points such that, while around strain, $\gamma = 0.12$ pronounced shear bands are forming in the SWVB, in the SWHB only some local mobile zones are visible. The shear band in the SWHB is well pronounced at a strain of $\gamma = 0.2$. On the

other hand, in the SWVB around this range of strains, the vertical bands already spanned the whole system and left two small planes of immobile particles. The width of the shear band in the SWHB increases by increasing strain such that, at a strain of $\gamma = 1.0$, the width of the shear band is almost double the size of the shear band at strain $\gamma = 0.2$. The vertical bands in the SWVB also span more regions in the system making the immobile regions narrower and narrower such that, eventually at a strain of $\gamma = 1.0$, the dark immobile planes in the middle of the system tilt a little in the direction of the applied shear and the regions close to the boundaries of the simulation box start to flow in opposite directions in the system, resulting an 'S' shaped dark region between the bands.

In a set of plots in Fig. 5.26(a-d), we compare different quantities (stress-strain curve, the evolution of the potential energy, kurtosis, and mean-squared displacement) between the SWHB and the SWVB. In Fig. 5.26(a) we compare the stress-strain curves of the SWHB (black curve) and the SWVB (red curve). The stress-strain curve peak maximum position $\gamma_p = 0.0932$ is marked with vertical dashed blue line in panel (a-d) of Fig. 5.26. As it was discussed before, the stress-strain curve of the SWHB shows a sharp stress decay after the overshoot, which is a characteristic behavior for samples with horizontal bands in comparison to those with vertical bands. Another characteristic behavior of SWHB is the occurrence of an overshoot in the potential energy in the range of strains where the stress decay towards the steady-state occurs in the stress-strain curve ($\gamma \approx 0.11 - 0.12$ in this case). This is in the range of strains after stress-strain overshoot maximum, marked with the vertical dashed blue line. As it is shown in Fig. 5.26(b), while the potential energy of the SWHB shows an overshoot (black curve), the potential energy of the SWVB has a small plateau shape which follows by a sudden step-like (exactly in the same strain window where the secondary overshoot occurs in the stress-strain curve) increase towards the steady-state. In Fig. 5.26(c) we compare the kurtosis κ for the SWHB and SWVB (in black and red, respectively), as a function of strain. From the figure, we can see that κ (for both samples) is constant in the early elastic regime and shows a decrease before reaching γ_p (dashed blue vertical line). The slight decrease in κ follows with a slight increase, as the samples leave the transient regime and, eventually, start to fluctuate around a finite value in the steady-state regime. In Fig. 5.26(d) we present the mean-squared displacement in y and z-direction for both particle types A and B, for the SWHB and the SWVB (the corresponding color coding for different components are shown in the plot). Different regimes, with different power-law behaviors, are visible in the plot. Both MSD_y and MSD_z for both samples and both particle types show a ballistic regime at short times (marked with a solid blue line), which is followed by a plateau regime. The plateau regime, as it was shown before and expected, shows a slight off-set between the B and A-type particles (B type particles showing slightly higher mobilities). The mean-squared displacements

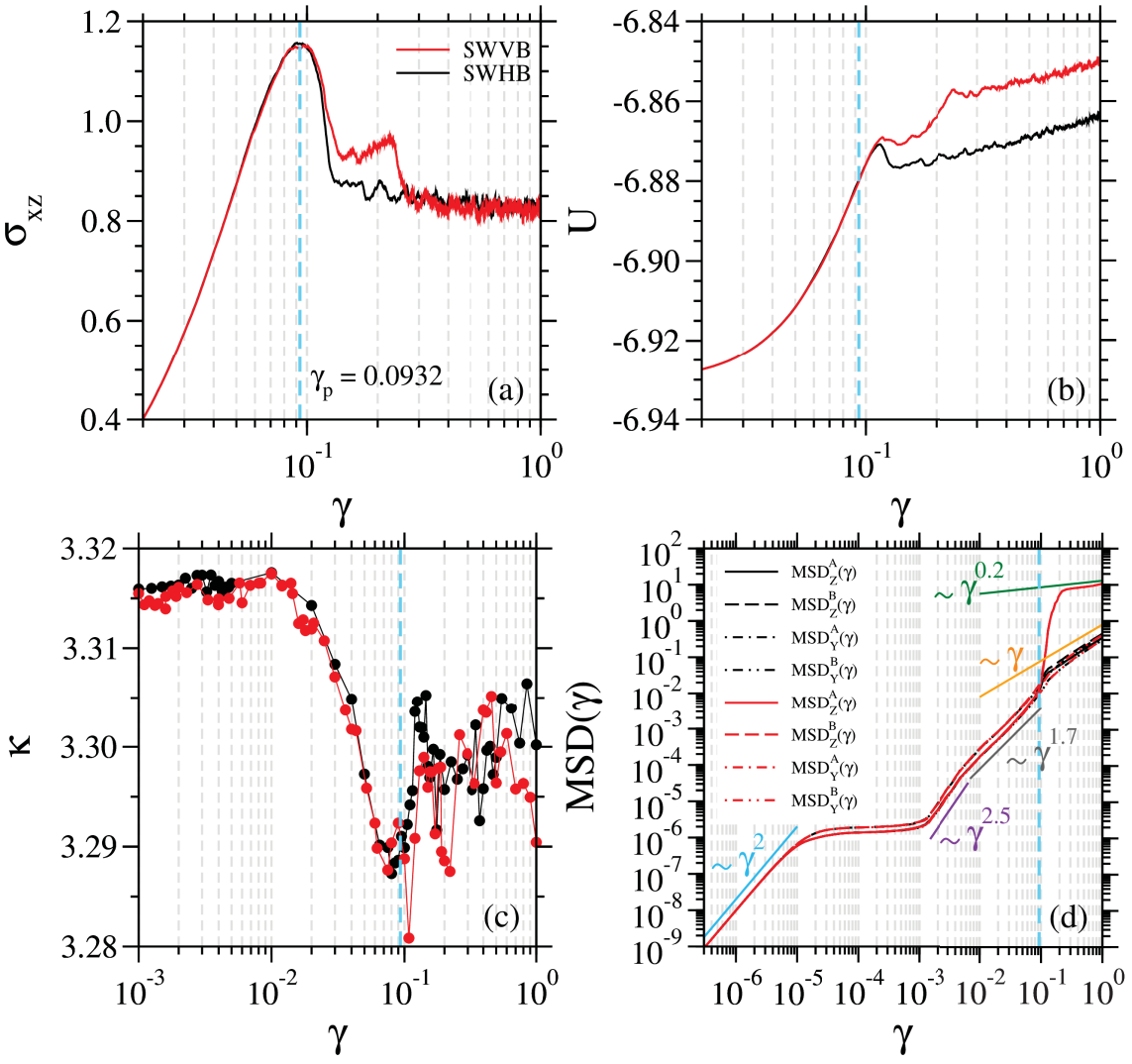

Figure 5.26: *panel (a)*: Stress-strain curves for SWHB and SWVB (black and red curve, respectively), being imposed to a constant shear rate $\dot{\gamma} = 10^{-4}$. *panel (b)*: Evolution of potential energy of the SWHB and the SWVB (black and red curve, respectively), as a function of strain. *panel (c)*: $\kappa_{\sigma_{xz}}$ (close black circles and red close circles for SWHB and SWVB, respectively) and κ_p (black open squares and red open squares for SWHB and SWVB, respectively) for the SWHB and the SWVB as a function of strain.

show a super-diffusive regime (marked with a solid purple line) after leaving the caging regime, for both y and z-components of the SWHB and SWVB and both particle types, with an exponent of ≈ 2.5. This power-law behavior shows a slight decrease to ≈ 1.7 (solid gray line), in a very small strain window. Around γ_p (marked with the vertical dashed blue line), the MSD_z for the SWVB (for both A and B type particles) shows a sudden jump. This sharp increase is due to the formation of vertical bands around this strain window, as it was shown in panel B of Fig. 5.25. Eventually in the steady-state regime, the MSD_y for both samples (and for both A and B type particles) reaches the diffusion regime. The MSD_z of the SWHB also, shows a similar behavior and reach a diffusive regime (marked with linear orange solid line). In contrast, the MSD_z of the SWVB (for both A and B type particles) shows a sub-diffusive behavior with a power-law exponent

of ≈ 0.2 (marked with a solid green line).

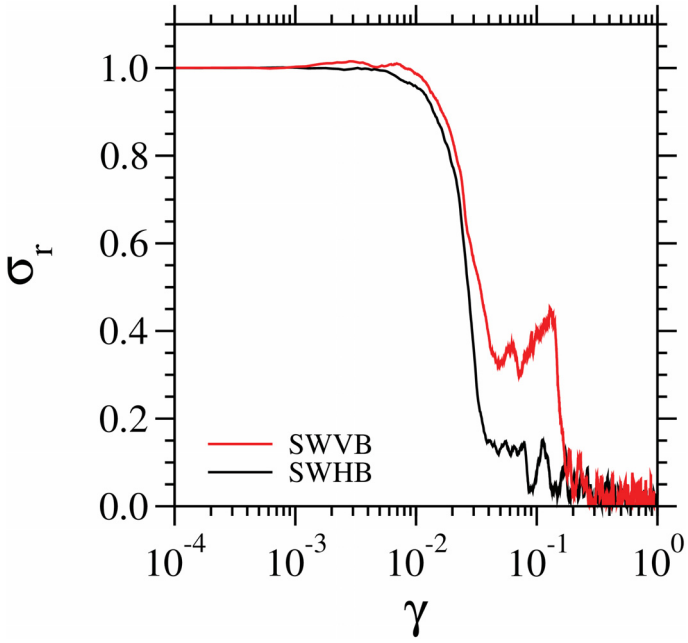

Figure 5.27: σ_r for the SWHB and the SWVB (in back and red, respectively) as a function of strain.

As we discussed earlier in this section, the stress-strain curve of the SWHB shows a sharp stress decay from the overshoot maximum. In Fig. 5.27 we compare σ_r for the SWHB with that for the SWVB. In Fig. 5.27, we see that, the SWHB (black curve) shows a much faster stress decay from the overshoot maximum towards the steady-state in a strain window of $\Delta\gamma < 0.1$. On the other hand, the SWVB shows an initial stress drop which follows by a secondary increase and eventually in a strain window of $\Delta\gamma > 0.1$ the stresses reach the stead-state value.

Further, in Fig. 5.28 we slice the SWHB into 5 layers and look at the averaged stress and potential energy in each layer as a function of strain. In Fig. 5.28(a), we show the layer-wise stress-strain curve, and, as it is clear from the plot, no difference is visible between the stress-strain curve of different layers, and they all sit on top of each other. On the other hand in Fig. 5.28(b) we can see that, the layers out and far from the shear band (L1 and L2, blue and green curves, respectively) show an overshoot followed by a steady-state regime, but, the layer exactly in the middle of the shear band (L4, red curve) shows an increase to the steady-state without overshoot and the potential energy is higher than the layers out of the shear bands. Layers L3 and L5 (orange and black curve, respectively), below and above layer L4 (which partially cover the shear band), also show an overshoot, but they tend to reach the steady-state potential of L4.

Before closing this section, in Fig. 5.29 we present a final plot for evolution of the averaged potential energy $< U >$ as a function of strain γ for 250 glass samples at $T = 0.2$ and $\rho = 1.2$, being subjected to shear deformation with shear rates $\dot{\gamma} = 10^{-2}$, 10^{-3}, 10^{-4}, 10^{-5} (with black, gray, pale red and pale blue,

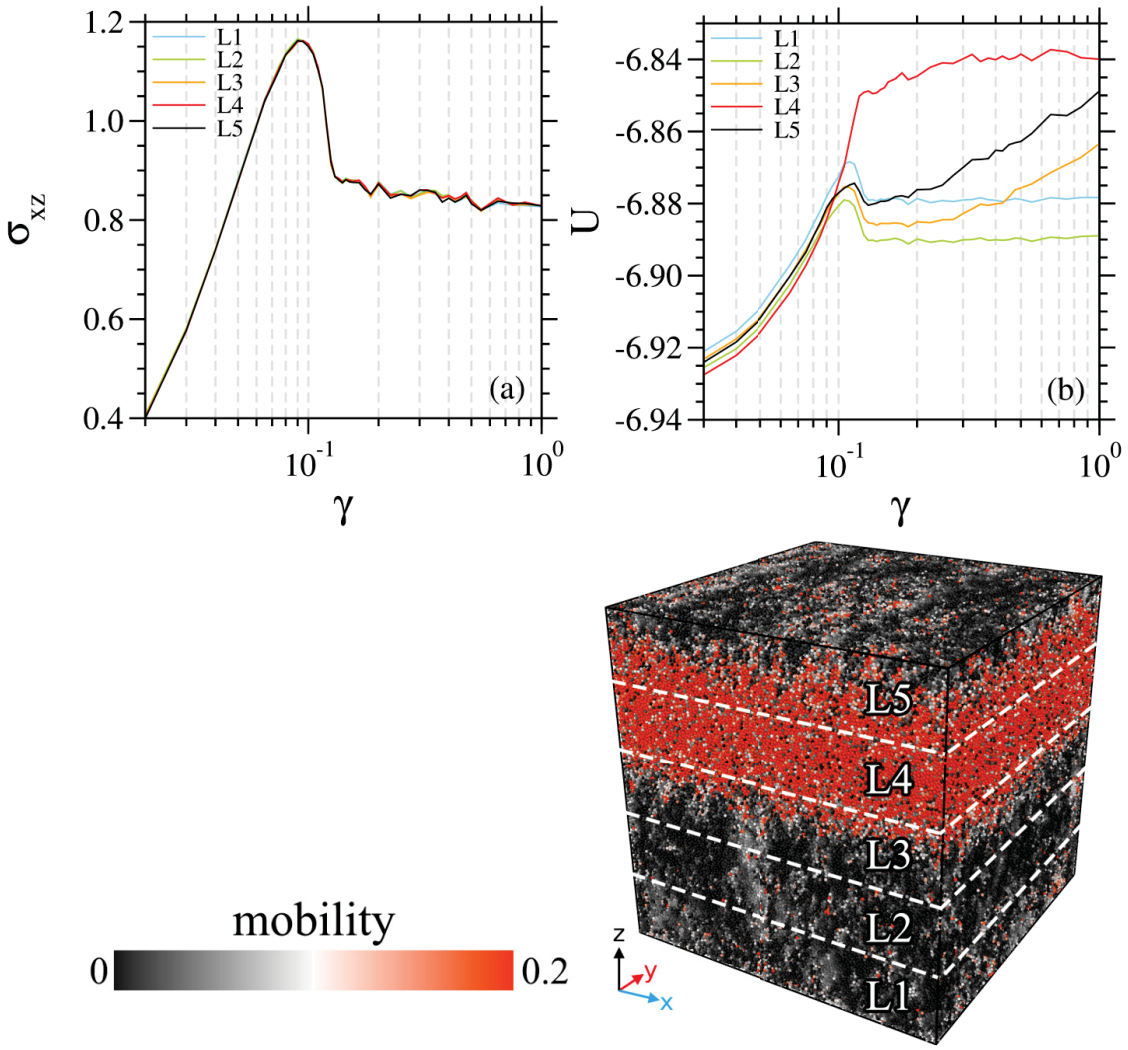

Figure 5.28: *panel (a)*: Layer wise stress-strain curve for the SWHB. *panel (b)*: Layer wise evolution of potential energy as a function of strain. Different layers are shown schematically in the figure.

respectively). For better visibility the data for shear rates $\dot{\gamma} = 10^{-3}$, 10^{-4}, 10^{-5} are shifted down by subtracting a factor 0.03, respectively. The steady-state value $< U_{ss} >$ is shown in the figure with a dashed turquoise line, and the values are written in the figure for each shear rate. While, for shear rate $\dot{\gamma} = 10^{-2}$ we observe a step-like increase in potential energy around strain $\gamma \approx 0.1$ (the white line represents the averaged result over all samples), as it was discussed before in Fig. 5.23, for the other lower shear rates, one can divide the curves into three different regimes of samples with vertical bands ("V bands" in the figure), horizontal bands ("H bands" in the figure) and a regime of mixed vertical and horizontal bands ("M bands" in the figure). These different regimes are highlighted for shear rate $\dot{\gamma} = 10^{-3}$ such that the upper curve (which shows a step-like increase) corresponds to samples with vertical shear bands and the lower curve (which shows a small overshoot) corresponds to samples with horizontal bands. In between, we have the samples with a mixture of vertical and horizontal

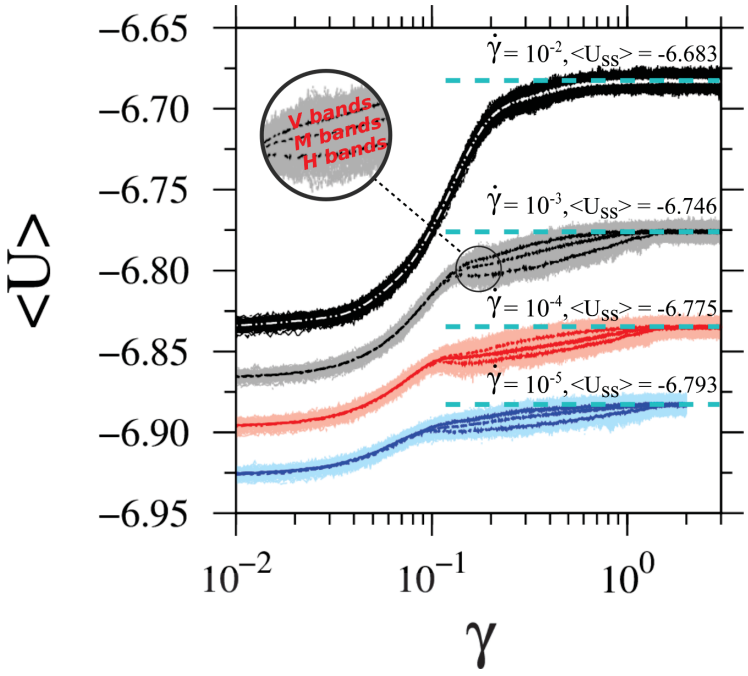

Figure 5.29: Averaged potential energy $< U >$ as a function of strain γ for 250 glass samples at $T = 0.2$ and $\rho = 1.2$, subjected to shear deformation with the mentioned shear rates in the figure. The data for shear rates $\dot{\gamma} = 10^{-3}, 10^{-4}, 10^{-5}$ are shifted down by subtracting a factor 0.03, respectively. The values of the steady state values are shown in mentioned in the figure and shown for each shear rates with dashed turquoise line.

bands. For shear rates $\dot{\gamma} = 10^{-3}, 10^{-4}, 10^{-5}$ the curves for these three regimes (shown in black, red, and blue) are obtained by averaging over all the samples with the corresponding band. The number of samples with a specific kind of shear band for different shear rates are shown in the table (5.6).

Variation of different kinds of shear bands in glass state at $T = 0.2$ and $\rho = 1.2$

	H band	V band	M band
$\dot{\gamma} = 10^{-3}$	25	88	137
$\dot{\gamma} = 10^{-4}$	39	95	116
$\dot{\gamma} = 10^{-5}$	17	50	183

Table 5.6: Number of samples with horizontal, vertical and mixed shear bands out of 250 glass samples, being subjected to shear deformation with the mentioned shear rates in the table.

From table (5.6), we can see that the maximum number of horizontal and vertical bands are observed for the shear rate of $\dot{\gamma} = 10^{-4}$. This can be due to the fact that the latter shear rate introduces a new time scale $1/\dot{\gamma}$ in the system which is in the time range of some aging processes in the system and also, it

is in the range of structural relaxation times of the initial super-cooled liquid state from which the glass samples are obtained. As a result, we observe more distinguishable shear bands (less mixed states) for this shear rate.

5.1.6 Remarks

The response of the SCLs to an external shear load shows a crossover from a Newtonian to non-Newtonian liquid around a critical shear rate of $\dot{\gamma}_c$. This crossover response can be marked via Δ_σ, which decreases with decreasing shear rate in the non-Newtonian regime and vanishes in the Newtonian regime. The stress-strain curve overshoot maximum σ_p shows a dependence on shear rate $\dot{\gamma}$ and temperature T, such that it increases by increasing shear rate and decreases by increasing temperature. The stress-strain curve overshoot maximum position γ_p also shows a shear rate dependence such that, by increasing shear rate, it moves towards larger strains but has a much weaker temperature dependence compared to σ_p. Short-lived inhomogeneous flow patterns are observed in SCLs when subjected to a shear load with a shear rate of $\dot{\gamma} > \dot{\gamma}_c$ by the formation of vertical band-like regions which span the whole system in a small strain window before reaching the steady-state. The stress decay from the overshoot maximum towards the steady-state occurs in a strain window of the order of $\Delta\gamma = 0.1$. The potential energy also shows a step-like increase towards the steady-state values in a strain window of the order of $\Delta\gamma = 0.1$. In the case of glasses, the inhomogeneous flow pasterns are more persistent, and rather than only vertical bands, we also observed long-living horizontal bands (even mixed states with vertical and horizontal bands). The sharp decay of the stresses from the overshoot maximum towards the steady-state value (occurring in a strain window in the order of $\Delta\gamma < 0.1$), followed by an overshoot in the potential energy of the system marks the occurrence of a horizontal band in the system while, in case of the vertical bands, the stress decay is slower and there is no overshoot in the potential energy.

5.2 Stress relaxation and residual stresses

Up to here, we showed that the stresses start to form in the samples, in the SCL and glass state, when the samples are subjected to a shear deformation with a constant shear rate. Now, we would like to characterize the evolution of the stresses when the shear load is switched off. As it was discussed in section 2.2.2, stresses remain at a finite value in metallic glasses when the external load is switched off as residual stresses and do not decay to zero. Therefore, understanding the effect of the residual stresses on mechanical properties is of great importance.

After the samples reached the steady state regime (check Fig. 5.16) at strain $\gamma = 3$ ($\gamma = 2$ for shear rate 10^{-5}), the shear load was switched off and we let the samples relax. This is shown in Fig. 5.30. The figure represents the stress

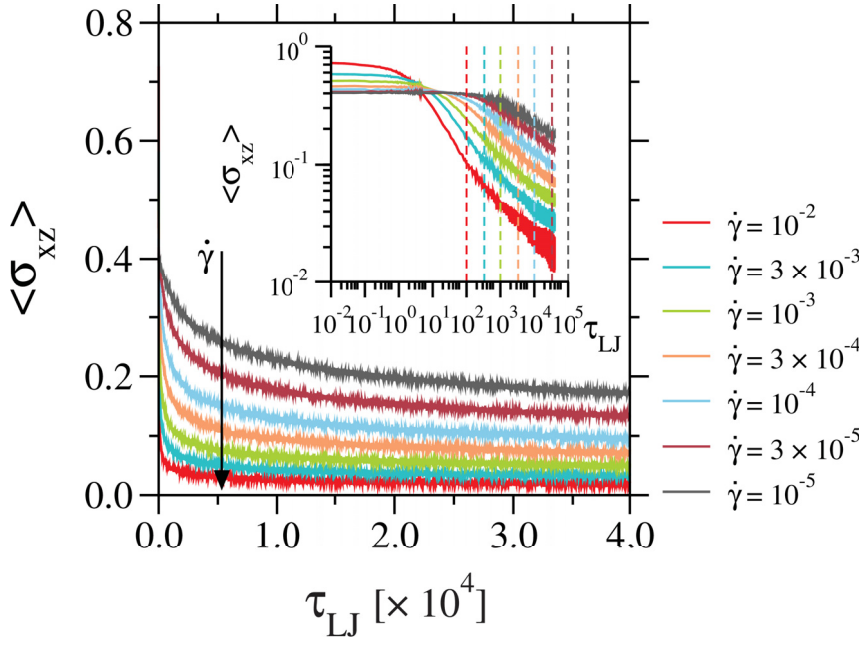

Figure 5.30: Stress relaxation as a function of time, after switching off the shear load from the steady state in Fig. 5.16. The dashed lines indicate the $\tau_{LJ} = 1/\dot{\gamma}$ with the corresponding color for each shear rate.

relaxation for different shear rates as a function of time (double logarithmic scale in the inset). From the plot we can clearly see a significant difference in the stress relaxation for different shear rates. While for high shear rates (10^{-2}, red curve) the stresses drop quite fast, for lower shear rates (10^{-5}, dark-gray curve) the relaxation processes are much slower. This is due to the fact that, as we discussed earlier in section (2.2.2), after switching off the imposed shear load (with the rate $\dot{\gamma}$) in glasses, initially one observes typical stress relaxation times of the order of $1/\dot{\gamma}$, from which, the stress relaxation behavior changes (see in the inset of Fig. 5.30 for shear rate $\dot{\gamma} = 10^{-2}$, the red curve. $1/\dot{\gamma}$ is marked with dashed red line). But, what is similar between all the curves is that, the stresses saturate at a finite value for all the shear rates, which then results in obtaining deformed glass samples with different amount of residual stresses. In Fig. 5.31 we show that, if we take a first derivative of the stress relaxation data (shown in Fig. 5.30), all the curves (irrespective of shear rate), saturate at a finite value (dashed pale orange line) at the long tail of the relaxation curves.

The stress relaxation behavior also depends on the stage at which the shear load is switched off. In Fig. 5.32(b), the shear load is switched off at three different stages while the system is being deformed (marked by vertical dashed lines in panel (a)). In panel (b) of Fig. 5.32, we see the stress relaxations (scaled to one) from these switch off points (marked with vertical dashed lines). From the plot,

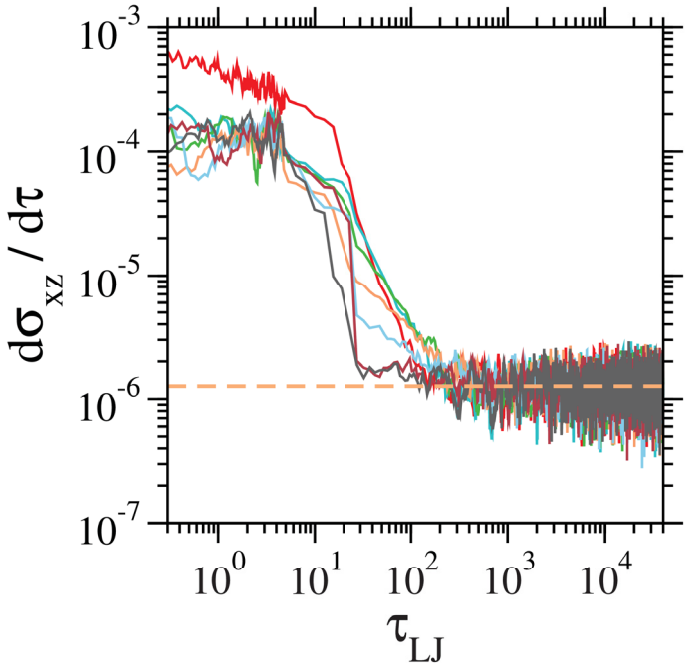

Figure 5.31: First derivative of the stresses as a function of time, after switching off the shear load.

we can see that; the stress relaxations are much faster when the shear load is switched off at the long tail of the steady-state regime (red curve) at strain $\gamma = 4$, compared to the initial times (blue curve) before the overshoot. This is due to the fact that, for the small strains before the overshoot, the system shows slow dynamics similar to the initial undeformed glass state, but, at large strains, the whole system fluidizes and therefore, the dynamics (relaxation processes) are much faster than the initial times.

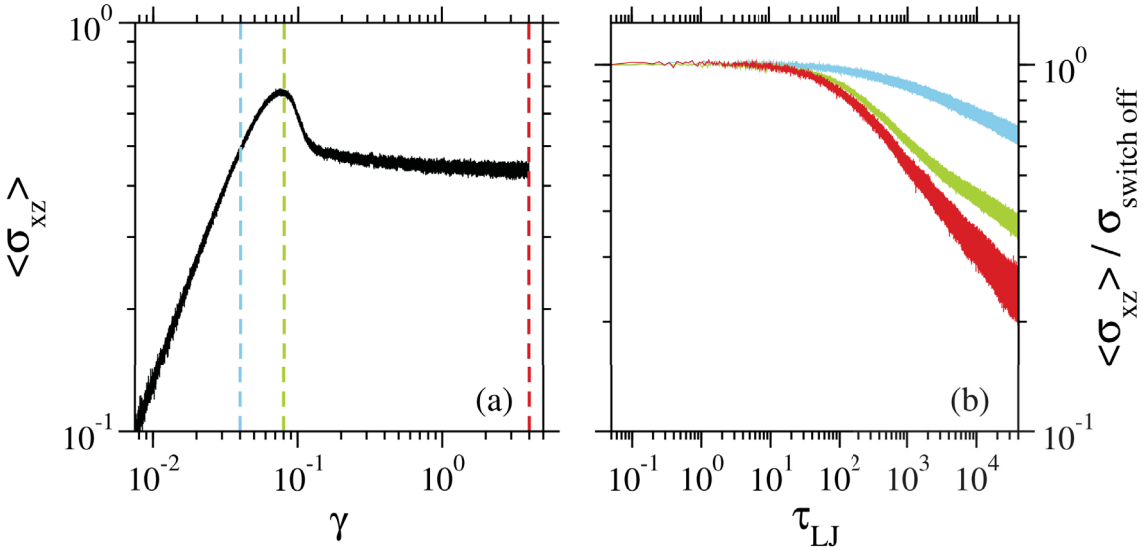

Figure 5.32: *left panel:* stress-strain curve for a glass system at T = 0.2, N = 38400, ρ = 1.2 being imposed to a constant shear rate $\dot{\gamma} = 10^{-4}$. The vertical dashed line represents the strain points at which the shear load was switched off, and the system was allowed to relax. *right panel:* stress relaxation as a function of time, after switching off the shear load from the marked point in the left panel, scaled to one.

Furthermore, we also investigate the temperature dependence of stress relaxation in glasses and SCL. This is shown in Fig. 5.33. In this figure, we compare the stress relaxation after switching off the shear load in the steady state regime. Here, the glasses are at $T = 10^{-4}$ and $T = 0.2$ and the super-cooled is liquid at $T = 0.44$. All the systems have been imposed to a constant shear rate $\dot{\gamma} = 10^{-4}$. From Fig. 5.33, we can clearly see that, stress relaxations are much faster in super-cooled liquids (red curve) and there are no residual stresses (stresses drop to zero after switching off the shear load). But, deep in the glass state at very low temperatures, the stress relaxations are very slow and they saturate at a finite/constant value of residual stress (blue curve). We will discuss this in more details in the next subsection.

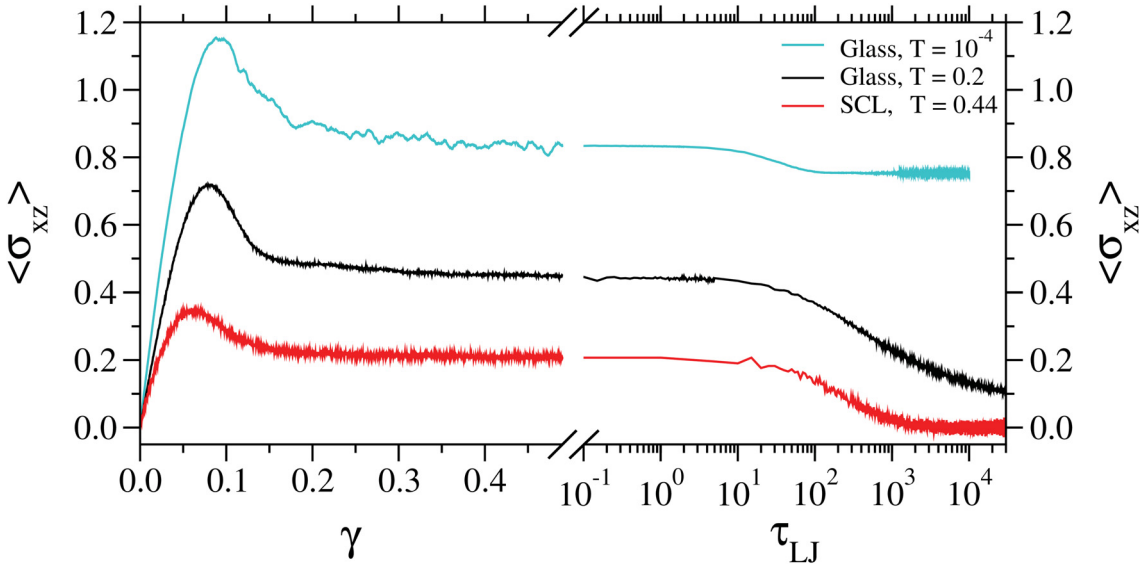

Figure 5.33: *left panel:* stress-strain curve for glass systems at $T = 10^{-4}$, 0.2, and a super-cooled liquid at $T = 0.44$, being imposed to a constant shear rate $\dot{\gamma} = 10^{-4}$. The shear load was switched off at the long tail of the steady state regime. *right panel:* stress relaxation as a function of time, after switching off the shear load.

Before closing this section, we make a final comparison between the stress decay from the overshoot towards the stead state $\langle \sigma_r \rangle = \langle \sigma_p - \langle \sigma_{ss} \rangle \rangle$, in the glass (at $T = 0.2$) for different shear rates, with the stress relaxation after switching off the shear load in the long tail of the stress-strain curve. These results are shown in Fig. 5.34. In order to obtain this figure, the corresponding γ_p for each shear rate (shown in Fig. 5.16) is subtracted from the stress-strain curves. Therefore, the stress-strain curve maximum at the overshoot is shifted to zero. Then, the corresponding steady-state stress σ_{ss} is subtracted from the data, and finally, we normalized the results to one. The stress relaxation from the overshoot maximum are shown with gray curves in Fig. 5.34. The stress relaxation curves after switching off the shear load in the steady-state regime (shown in Fig. 5.30) are first scaled with their corresponding shear rates. Then, the data is shifted to zero by subtracting corresponding residual stresses, and finally, the results

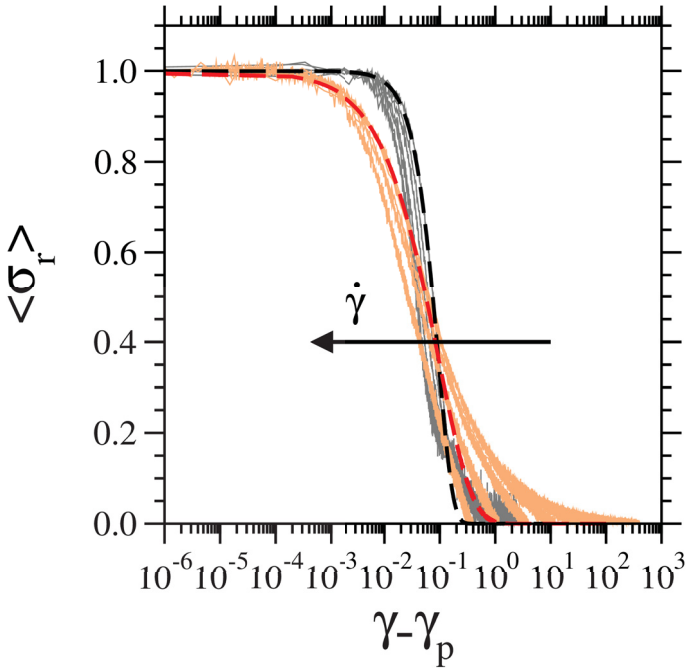

Figure 5.34: Stress relaxation from the overshoot maximum to the steady-state (gray curves), compared to the stress relaxation after switching off the shear load in the long tail of the stress-strain curve. The dashed lines are exponential fits to the data.

are normalized to one. The stress relaxation after switching off the shear load, is shown with pale orange curves in Fig. 5.34. The arrow shows the direction of decreasing shear rate for both sets of curves. By fitting these curves with an exponential function, we can see the difference between the behavior of stress decay in these two states. While, the stress decay from the overshoot maximum fits a compressed exponential function $exp\left(x^{1.7}\right)$, the dashed black line, the stress relaxation after switching off the shear load has a stretched exponential form $exp\left(x^{0.65}\right)$, red dashed line. The sharp compressed exponential decay of the stresses from the overshoot maximum is a result of the imposed external field which, forces the cages to break and results in a fast stress release from the maximum. But, the stretched exponential response of the stress relaxation after switching off the shear load is only due to structural relaxations in the absence of the external field. As we discussed before, it follows an initial stress relaxation in a time window of the order of $1/\dot{\gamma}$ from which, the relaxation processes become slower.

5.2.1 *Residual stresses in glasses at* $T = 10^{-4}$ *vs.* $T = 0.2$

Earlier in this section we made a comparison between the stress relaxation in SCL and glasses at different temperature in Fig. 5.33. We showed that at low temperatures one obtains deformed glass samples with higher residual stresses. Here, we make a comparison between stress relaxations in samples at $T = 10^{-4}$ and $T = 0.2$ an with $\rho = 1.3$ and $\rho = 1.2$, respectively, subjected to constant

shear rates $\dot{\gamma} = 10^{-3},\ 10^{-4}$. This is shown in Fig. 5.35. The glass samples at

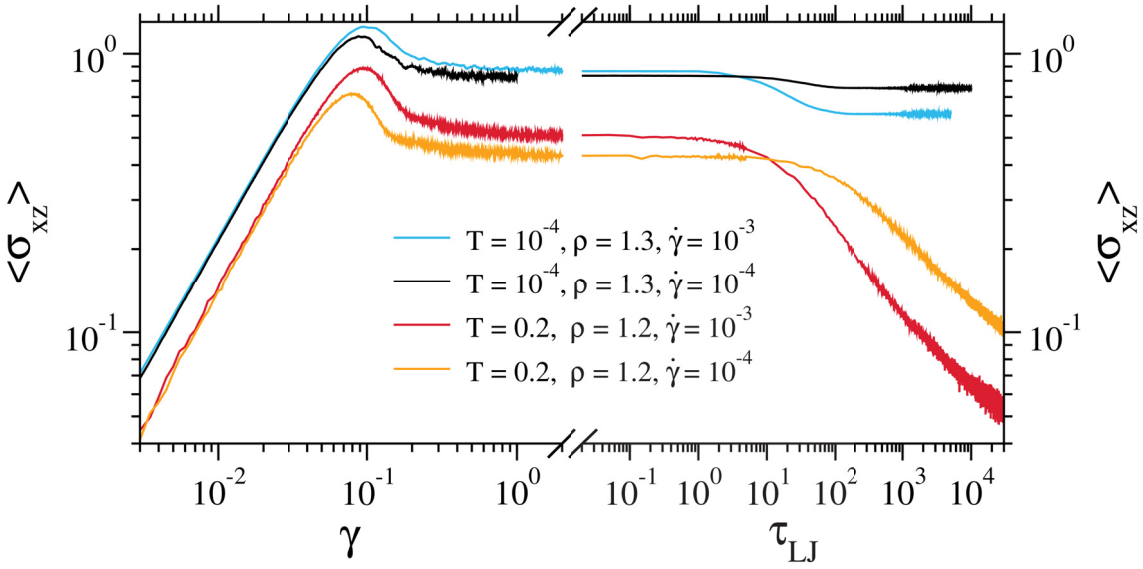

Figure 5.35: *left panel:* stress-strain curve for glass samples at $T = 10^{-4}$, 0.2 and $\rho = 1.3,\ 1.2$, respectively, being imposed to constant shear rates $\dot{\gamma} = 10^{-3},\ 10^{-4}$. *right panel:* stress relaxation as a function of time, after switching off the shear load.

$\rho = 1.3$ are subjected to constant shear rates $\dot{\gamma} = 10^{-3},\ 10^{-4}$ (blue and black lines, respectively) and the shear load was switched off at the strains $\gamma = 5,\ 1$, respectively. The glass samples at $\rho = 1.2$ are also deformed with same shear rates (red and orange lines, respectively) up to strain $\gamma = 3$, where, the shear load is switched off. Form Fig. 5.35 we can see that, at both temperatures the stresses decay to lower values after shear switch off for higher shear rates ($\dot{\gamma} = 10^{-3}$). As we discussed earlier, when a glass sample is subjected to shear deformation with a constant shear rate $\dot{\gamma}$, a new time scale is introduced in the system by $1/\dot{\gamma}$, therefore, the higher the shear rate the faster the stress decays. What is important here is that, at low temperatures ($T = 10^{-4}$) where the thermal noises are negligible, the stress decay is much smaller than the stress decay at higher temperature ($T = 0.2$). At the latter temperature in Fig. 5.35, the glass samples show an initial $1/\dot{\gamma}$ stress decay but this follows with further decay due to thermal noises, and in the time window shown in the figure, still the stresses are decaying. On the other hand, the samples at $T = 10^{-4}$ show an initial decay in a small time window after shear switch off after which, the stresses saturate at a finite value of residual stresses and remain at this finite value for a very long time.

But, the finite amount of residual stresses in samples at $T = 10^{-4}$ sometimes shows secondary stress decay processes. This is shown in Fig. 5.36. The initial undeformed glass sample is subjected to a shear deformation with a constant shear rate of $\dot{\gamma} = 10^{-4}$. At the strain $\gamma = 1$, the shear load is switched off, and stresses start to decay in the system[5]. This corresponds to the black curve in

[5]These features vary from sample to sample, therefore, here we show only results for single samples.

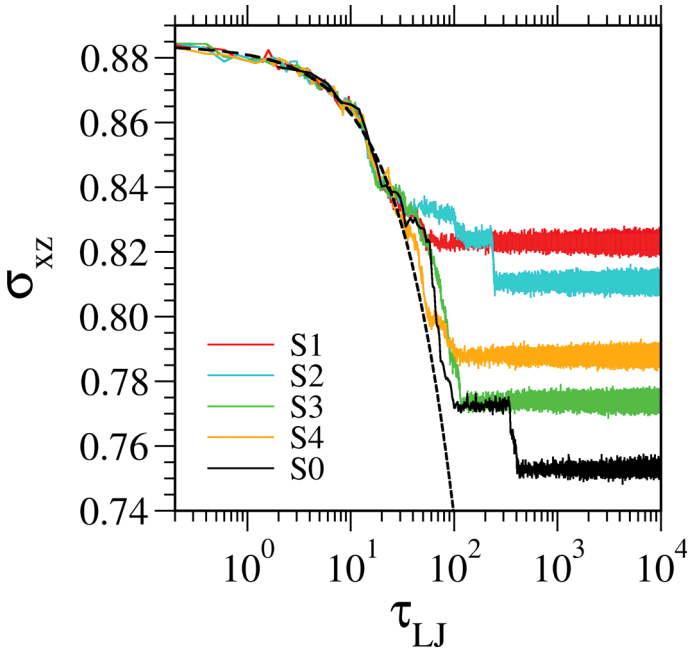

Figure 5.36: Stress decay after shear switch-off for samples at $T = 10^{-4}$ and $\rho = 1.3$. The dashed line is a stretched exponential fit to the data (see the text).

Fig. 5.36 considered as *S0*. After detecting this secondary relaxation processes, we used the same deformed sample at strain $\gamma = 1$ and performed four additional production runs, all with the same starting deformed configuration, and only with different seeding numbers for the thermostat random number generator. These samples are considered in Fig. 5.36 as *S1* to *S4*. From the figure, we can see that, only by changing the seed numbers, the stress relaxation changes stochastically and significantly. This is consistent with the results which we showed in [Golkia, Shrivastav, Chaudhuri, and Horbach (2020)] where, following the same protocol, using a similar starting configuration and changing the seed numbers for glass samples under shear load, we obtained samples with different shear bands.

By performing the latter production runs, we obtained four deformed samples with different amounts of residual stresses, and only one sample (*S2*, shown with blue line) showed secondary relaxation processes. To further investigate these relaxation processes, we calculated the total MSD for samples *S1* to *S4*, to study the changes in the dynamics of different samples after shear switch-off. This is shown in Fig. 5.37. The total MSD is shown in Fig. 5.37 for samples *S1* to *S4* in red, blue, green and orange, respectively, as a function of time τ_{LJ}. The MSD of all samples shows an initial ballistic regime at early times, marked with a dashed black line. In a time window between $\tau_{LJ} \approx 0.05$ and $\tau_{LJ} \approx 20$, before reaching the caging regime, still, the MSDs for different samples sit on top of each other showing similar dynamics. This time window corresponds to the initial stretched exponential decay of the stresses marked with black dashed line in Fig. 5.36 where, the data is fitted with a function of the form $f(x) = Aexp(-Bx^C)$ with fit

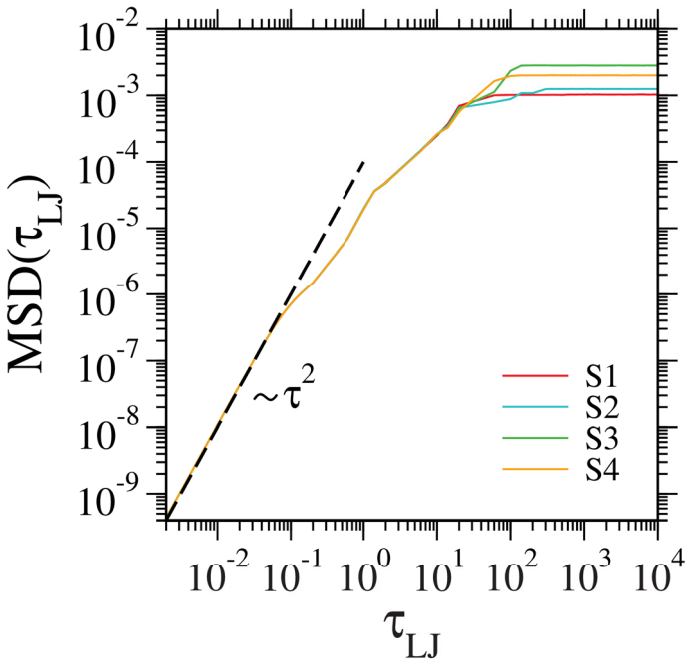

Figure 5.37: MSD of samples at $T = 10^{-4}$ and $\rho = 1.3$ after the shear load is switched off. The dashed black line marks the ballistic regime.

parameters $A = 0.883816$, $B = -0.00322023$ and $C = 0.873818$. In a rather small time window, the curves start to separate and saturate at different values in the plateau regime. Here, the lower the residual stress (*S3* in Fig. 5.36) means more structural rearrangements after the shear switch off and therefore, the higher the MSD stands in Fig. 5.37. Interestingly, the MSD of *S2* follows the curve for *S1* up to $\tau_{LJ} \approx 20$. At this point, the stresses in *S2* stay at a finite value for a very small time window but, the stresses in *S1* saturate at a slightly lower value. This results in the first separation of the MSD curves between these to samples. Around $\tau_{LJ} \approx 100$, the stresses in *S2* show a small decay and, again, saturate at a finite value for another small time window, very close to stress values for *S1*. This narrow time window is where the MSDs of the latter samples meet again. The more pronounced step-like decay of stresses in sample *S2* around $\tau_{LJ} \approx 220$, separates both the stress curves in Fig. 5.36 and the MSDs in Fig. 5.37 of samples.

To further investigate the secondary stress relaxations in sample *S2*, in Fig. 5.38, we look at mobility maps and the layer-wise MSD of the sample after the shear switch-off, as a function of time. The sample is sliced into ten layers of the width $L \approx 3\sigma_{AA}$ in the x-direction, and the corresponding MSD of each layer is shown in the upper panel of Fig. 5.38, as a function of time. Further, the total per-particle MSD is assigned to each particle as a mobility parameter. Therefore, in the lower panel of Fig. 5.38, we show mobility maps of the system at the time origins marked with vertical gray dashed lines on the MSD curves. From the figure, we can see that the MSD curves for all the layers show an early ballistic regime marked with a black dashed line in the figure. At these early times, the

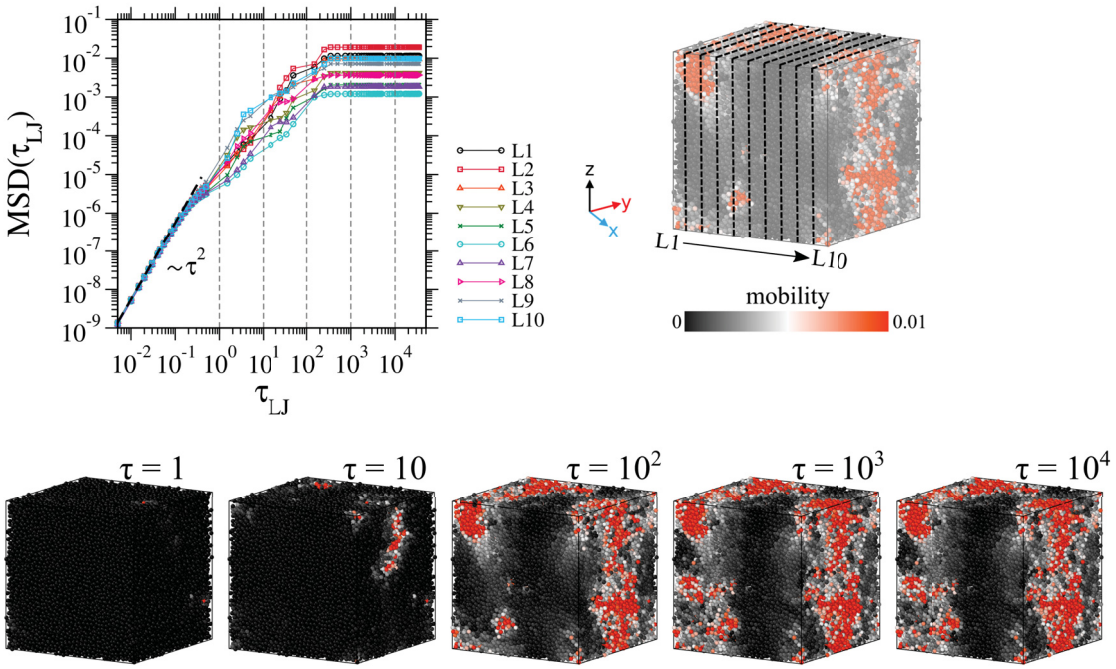

Figure 5.38: *upper panel*: layer-wise total MSD for the layers shown schematically on the snapshot, as a function of time. *lower panel*: mobility maps of the sample at the time origins marked with vertical gray dashed lines on the MSD curves.

mobilities are so small that even the snapshot corresponding to $\tau_{LJ} \approx 1$ shows no activity in the system. Around a time window between $\tau_{LJ} \approx 10$ and $\tau_{LJ} \approx 100$, some activities appear in the system, resulting in the formation of some red spots in the snapshots. This time window corresponds to the regime where the MSD curves for different layers start to divide and saturate at different values. By comparing the mobility maps with MSD curves, we can see that the local mobilities are concentrated in the first three layers (L1, L2 and L3) and the last two layers (L9 and L10). This resulted in two slaps with higher local mobilites, which does not change in the plateau regime for $\tau_{LJ} > 1000$, as the particles become frozen in the cages of neighboring particles.

5.2.2 *Remarks*

After switching off the external load, the stresses relax to zero in SCLs. But in glasses, they remain in the system at a finite value, as residual stresses. In contrast to the stress decay from the overshoot maximum towards the steady-state, which shows a compressed exponential behavior, after the shear switch-off, the stress decay shows an initial stretched exponential decay before saturating at a finite value. After canceling the external load, one obtains a new glass state with residual stresses. The amount of residual stresses depends on the stage at which the external load is canceled and also temperature. At low temperatures where the thermal noises are negligible, one obtains deformed glass samples

with a higher amount of residual stresses. The stress relaxation in some of the glass samples at $T = 10^{-4}$ and $\rho = 1.3$ shows a secondary, step-like release of stresses. The latter secondary relaxation processes correspond to local particle rearrangements in some regions of the system.

5.3 Effect of deformation on elastic constants

As it was discussed earlier in this thesis, the main focus of this work was studying the effect of the residual stresses (discussed in the previous section) and deformation on the mechanical properties of metallic glasses. In this section, we present the results which we have obtained by calculating the elastic moduli in the undeformed and deformed states.

5.3.1 Evolution of elastic constants during stress relaxation

The elastic moduli, namely the shear modulus (G) Eq. (3.12), bulk modulus (K) Eq. (3.15), Young's modulus (E) Eq. (3.16) and Poisson's ratio (ν) Eq. (3.17), of the system are obtained by calculating the Lamé coefficients as defined by Eq. (3.7), from the elastic constants tensor, Eq. (3.1). The calculation is initially done for the quiescent undeformed states (check table (5.7)). These values are then used as a reference with which the results from the deformed states are compared to.

Elastic constants values for the undeformed states

$\bar{C}^a$	$\bar{\lambda}^b$	$\bar{\mu}^c$	E	G	K	ν
80.360	54.514	12.875	33.185	11.744	63.475	0.413

Table 5.7: The values obtained for the elastic moduli of the undeformed samples by calculation of the elastic constant tensor, Eq. (3.1). The elastic moduli are calculated using Eq. (3.12-3.17)

[a] $\bar{C} = (C_{11} + C_{22} + C_{33})/3$
[b] $\bar{\lambda} = (C_{12} + C_{13} + C_{23})/3$
[c] $\bar{\mu} = (C_{44} + C_{55} + C_{66})/3$

As it was discussed earlier, the deformed states are obtained after switching off the shear load in the steady-state regime (shown in Fig. 5.39). To investigate the effect of the residual stresses more systematically, while the stresses are relaxing in the system, we took six-time origins on the long tail of the stress relaxation curve (vertical gray dashed lines in Fig. 5.39). The elastic moduli of the system are calculated at each of these time origins with different amount of residual stresses, and for all the shear rates. By doing so, we can probe the effect of the residual stresses on the elastic moduli from points with high residual stresses (single dotted dashed lines in Fig. 5.39) to the points at the long tail of the stress

relaxation, with low residual stresses (double dotted dashed lines in Fig. 5.39). Another question that we addressed here is about anisotropies in the system with residual stresses. To this end, we have calculated the elastic moduli of the system, for each Cartesian coordinate independently. This means for example for shear modulus G, different components G_{xz}, G_{xy}, G_{yz} are calculated (the symmetries in elastic constant tensor imply that, $G_{xz} = G_{zx}$, $G_{xy} = G_{yx}$, $G_{yz} = G_{zy}$). For an isotropic system, these values should be (on average) the same in all directions. Therefore, we can identify anisotropies by checking these symmetries.

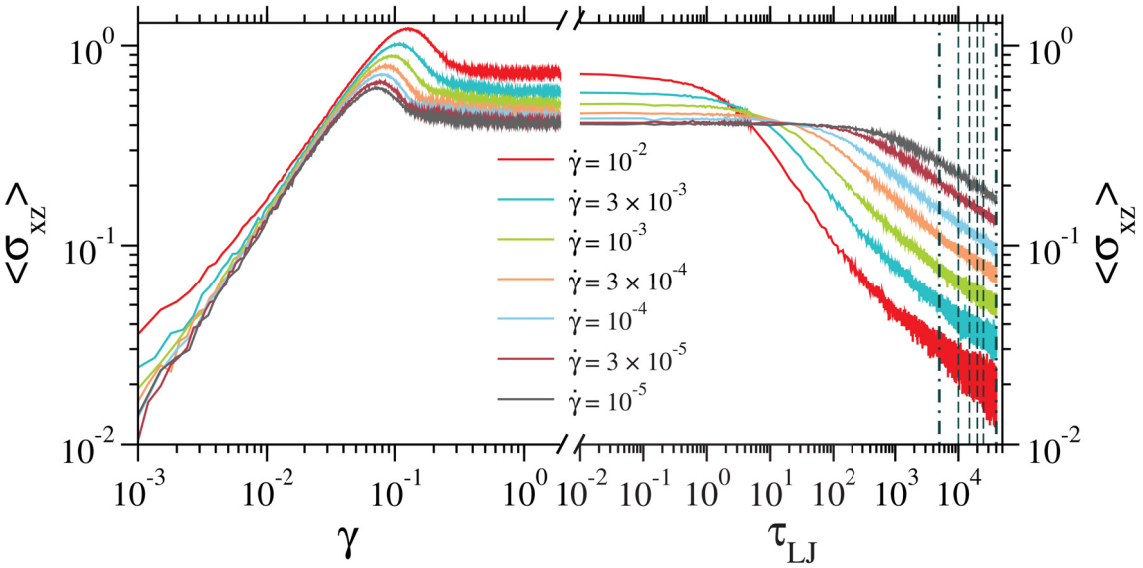

Figure 5.39: Stress-strain curves in the left panel, obtained for different shear rates and the corresponding stress relaxation curves after switching off the shear load from the steady-state regime, in the right panel. The vertical dashed gray lines mark the time origins at which the elastic moduli have been calculated for the deformed samples. The first time origin at high residual stresses is marked with single dotted dashed gray line and the time origin at low residual stresses is marked with a double dotted dashed gray line.

The first set of results are shown in Fig. 5.40(a-c) for the Young's modulus. In Fig. 5.40(a-c) we can see the evolution of different components of the Young's modulus as a function of scaled time (in order to have a more clear picture the obtained values for each time origin are scaled with the corresponding shear rate) for all the six time origins (shown in Fig. 5.39) and for all the shear rates (with the same colors as shown in Fig. 5.39). Therefore, it should be clear that the six data points of the same color represent the obtained values of the moduli, from the six time origins (left to right), and the horizontal dashed blue line represents the values of the undeformed state.

The overall behavior of the Young's modulus is shown in Fig. 5.40(a-c) for all three components. For all the components, with longer relaxation times the values of the moduli, irrespective of the shear rate, evolve towards their initial undeformed values. But, the values saturate at a lower value before reaching the initial undeformed value (this will be shown more clearly in Fig.5.47), showing minor softening in the system. Another interesting observation from the plot

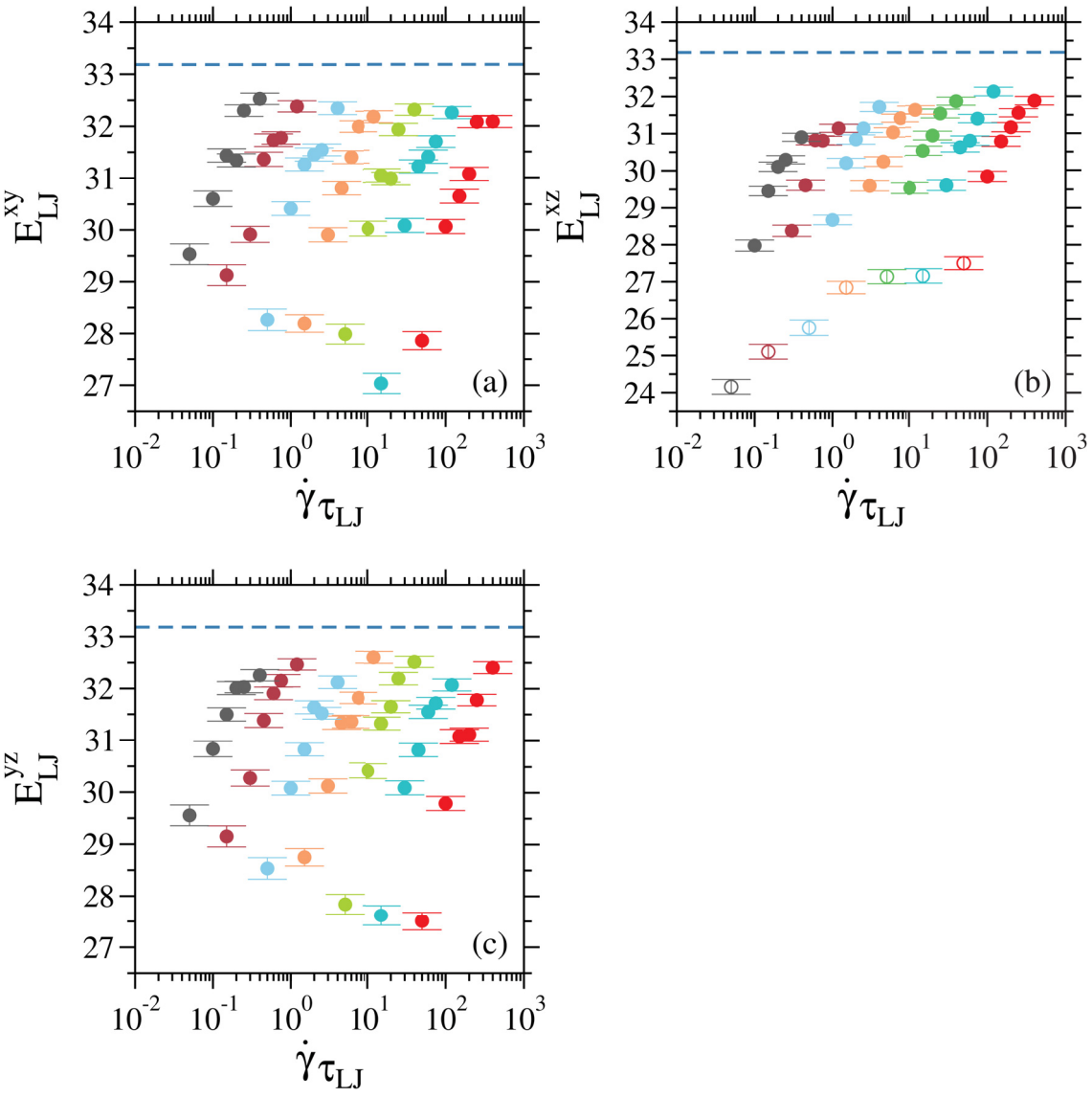

Figure 5.40: Evolution of different components (E_{xy}, E_{xz}, E_{yz}, in a,b and c respectively) of the Young's modulus as a function of scaled time with the corresponding shear rate. The dashed blue horizontal line represents the values obtained for the undeformed state.

is the variation of different components. By comparing Fig. 5.40(a and c) with Fig. 5.40(b), we can clearly see that, the component which is directly related to the direction of the applied shear deformation (E_{xz} component) has been effected more, and shows a larger variation. While, the other two perpendicular components (E_{xy} and E_{yz}) show less variation, they also have a very similar behavior. This indicates small anisotropies in the system which will be discussed in more details later in this section. The same behavior is observed for the shear modulus and Poisson's ratio, shown in Fig. 5.41(a and c) and 5.42(a and c). From these figures we also see the same behavior. The moduli tend to evolve towards their initial undeformed values (horizontal dashed blue line), and while the term corresponding to the direction of the shear shows the most changes and

variation, the other two perpendicular components have a similar behavior with less variations. Both moduli (shear modulus and Poisson's ratio), in the same manner as for the Young's modulus, saturate at a finite value before reaching the initial undeformed values, showing slight softening in the system.

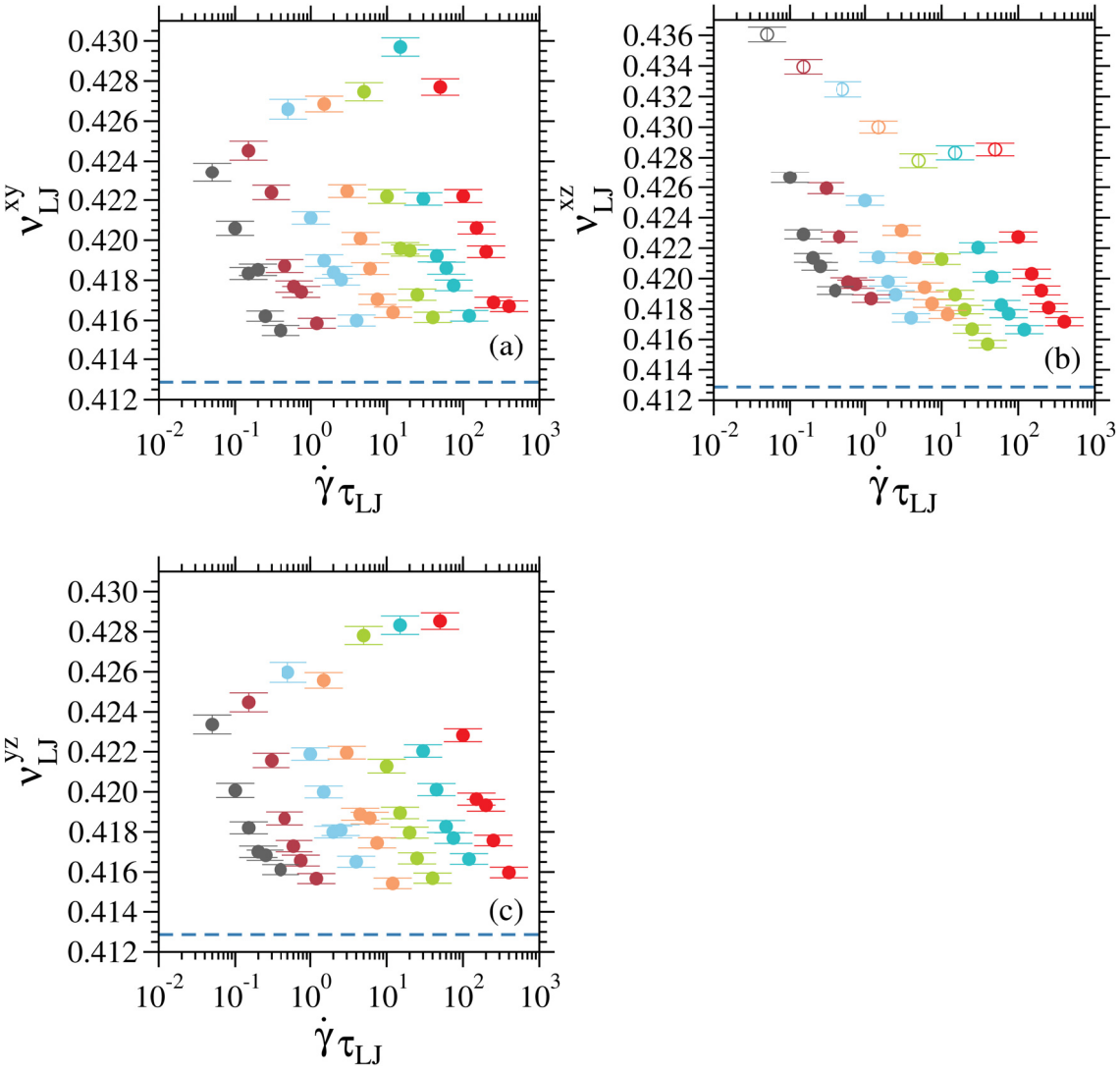

Figure 5.41: Evolution of different components (ν_{xy}, ν_{xz}, ν_{yz}, in a,b and c respectively) of the Poisson's ratio as a function of scaled time with the corresponding shear rate. The dashed blue horizontal line represents the values obtained for the undeformed state.

One important point to be mentioned here is the behavior of the data points corresponding to the xz-components of the moduli at the first time origin. These data points are shown with open symbols in panel (b) of Fig. (5.40-5.43), and the time origin to which we are referring to, is shown in Fig. 5.39 with single dotted vertical dashed line. The samples have the highest amount of residual stresses at this time origin, compared to the other time origins. From these data points, we can see that the higher the residual stresses, the larger the change in the moduli. For all the moduli, the first open dark-gray circle corresponding to

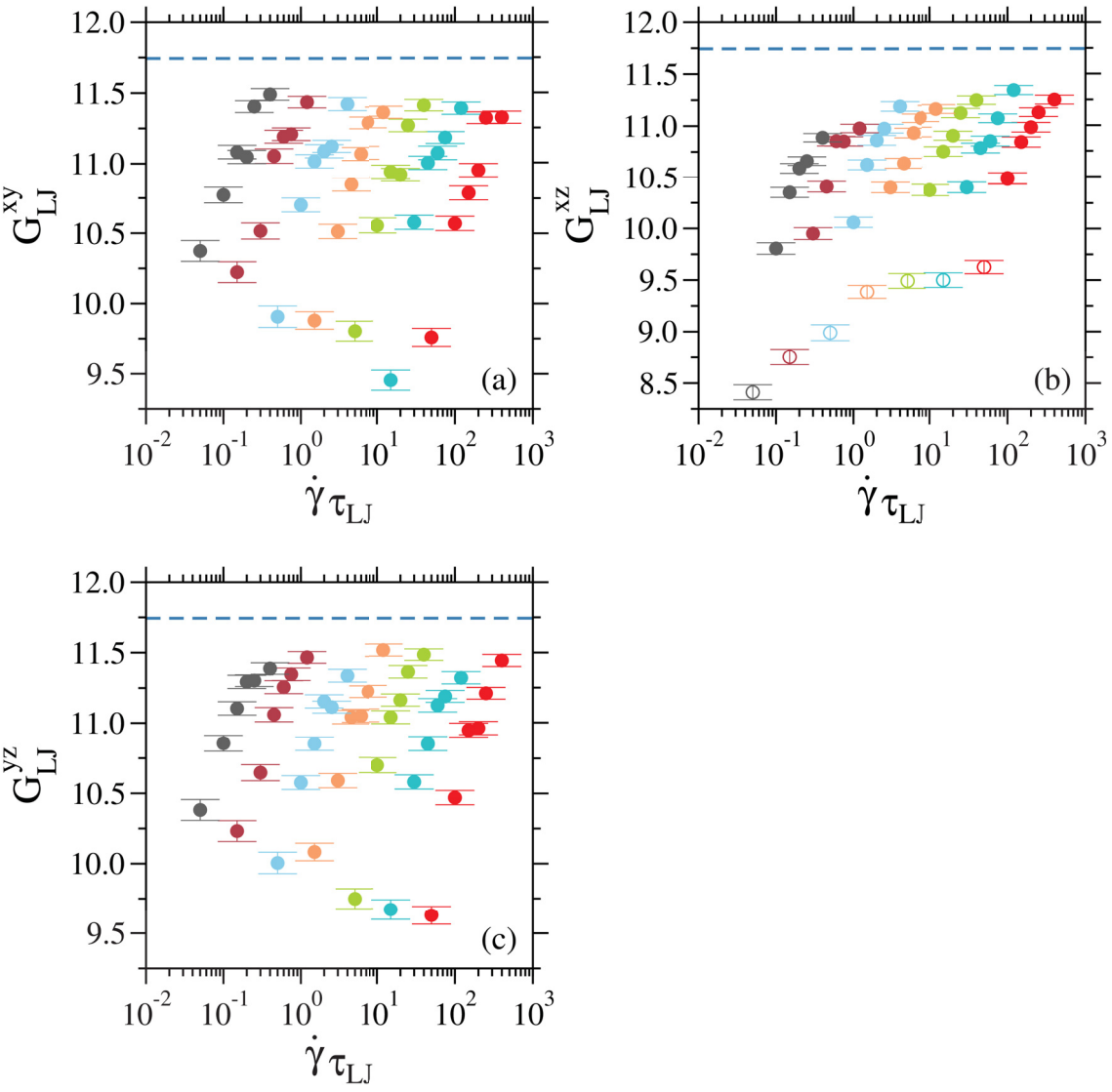

Figure 5.42: Evolution of different components (G_{xy}, G_{xz}, G_{yz}, in a,b and c respectively) of the shear modulus as a function of scaled time with the corresponding shear rate. The dashed blue horizontal line represents the values obtained for the undeformed state.

the first time origin of the shear rate 10^{-5} with the highest residual stress (check Fig. 5.39), shows the largest deviation from the undeformed values, while, the first open red circle corresponding to the first time origin of the shear rate 10^{-2} with the lowest residual stress (check Fig. 5.39), shows smaller changes. One important point here is that the corresponding stress tensor component related to the applied shear deformation is σ_{xz}. Therefore, after switching off the shear load, the residual stresses are stored in the σ_{xz} component of the stress tensor. As a result of these residual stresses, the non-affine component of the elastic constant tensor (C^{F}_{xz}) Eq. (3.5), shows larger deviations from its initial undeformed values (we will come back to this point shortly when we discuss the results shown in Fig. 5.45). Here, the question is, can we conclude that the elastic constants of the system are mostly affected by the plastic deformations as a result of non-affine

displacements? We will come back to this shortly.

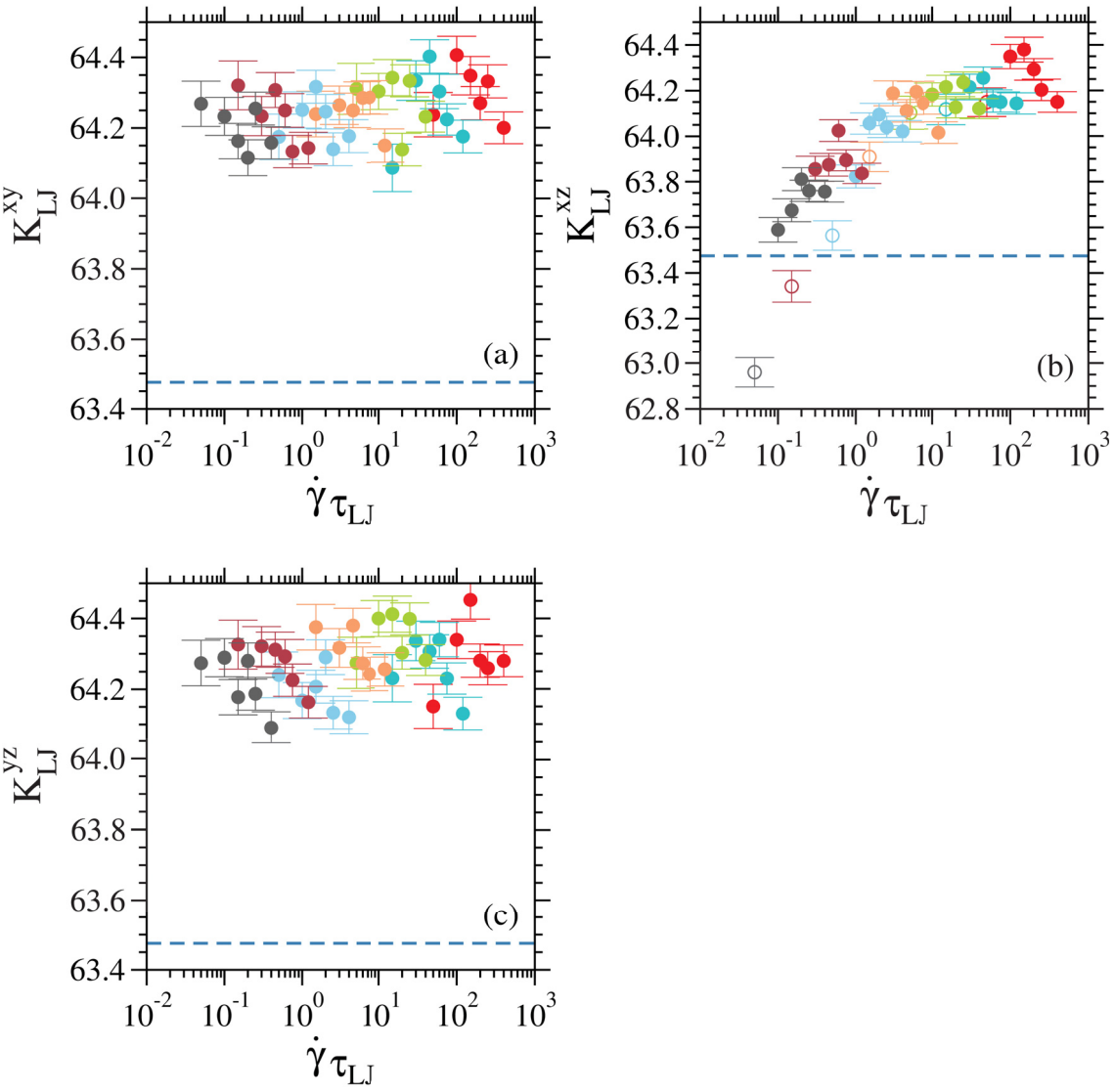

Figure 5.43: Evolution of different components (K_{xy}, K_{xz}, K_{yz}, in a,b and c respectively) of the bulk modulus as a function of scaled time with the corresponding shear rate. The dashed blue horizontal line represents the values obtained for the undeformed state.

The last set of plots (Fig. 5.43(a and c)) represent the obtained results for the bulk modulus. The first evident difference by looking at these plots comes from the fact that the bulk modulus seems to increase and stay at a finite value. While we observed a gradual evolution towards the initial undeformed values for the other moduli, in the case of bulk modulus, the values show an increase and stay at a finite value above the initial undeformed results. Even for the xz component, the behavior is similar. Initially, K_{xz} (Fig. 5.43(c)), for low shear rates and high residual stresses at first time origin, shows deviations below the undeformed value, and with decreasing stress (longer stress relaxation time), starts to increase and saturates at a finite value. The other difference compared to other moduli rises from the fact that, despite the minor deviation described for the K_{xz} at early

times, all the moduli seem to have similar behavior by an increase and saturating at the same value (on average). Here, we try to investigate what causes the increase in bulk modulus and why should the behavior of the bulk modulus be different from other moduli. Therefore, we need to recall the definition of different moduli shown in Fig. 3.2-3.5. From these schematic figures, we can see that what is different for bulk modulus compared to the other moduli is that the bulk modulus (by definition) is the resistance of the material against volumetric compression. This means that the bulk modulus is sensitive to all Cartesian directions. While all the other moduli are only sensitive to one axial direction. Therefore, the bulk modulus should indeed behave differently compared to the other moduli. Also, we need to recall the mathematical definition of the bulk modulus Eq. (3.15). The excess pressure p_{exc} in Eq. (3.15) is a constant and has a small contribution in the changes. Therefore, the main contribution to the changes occurring in the bulk modulus should be related to the other terms, λ and μ. Here, we investigate the changes occurring in the Lamé coefficients after deformation and while the stresses are decaying in the system.

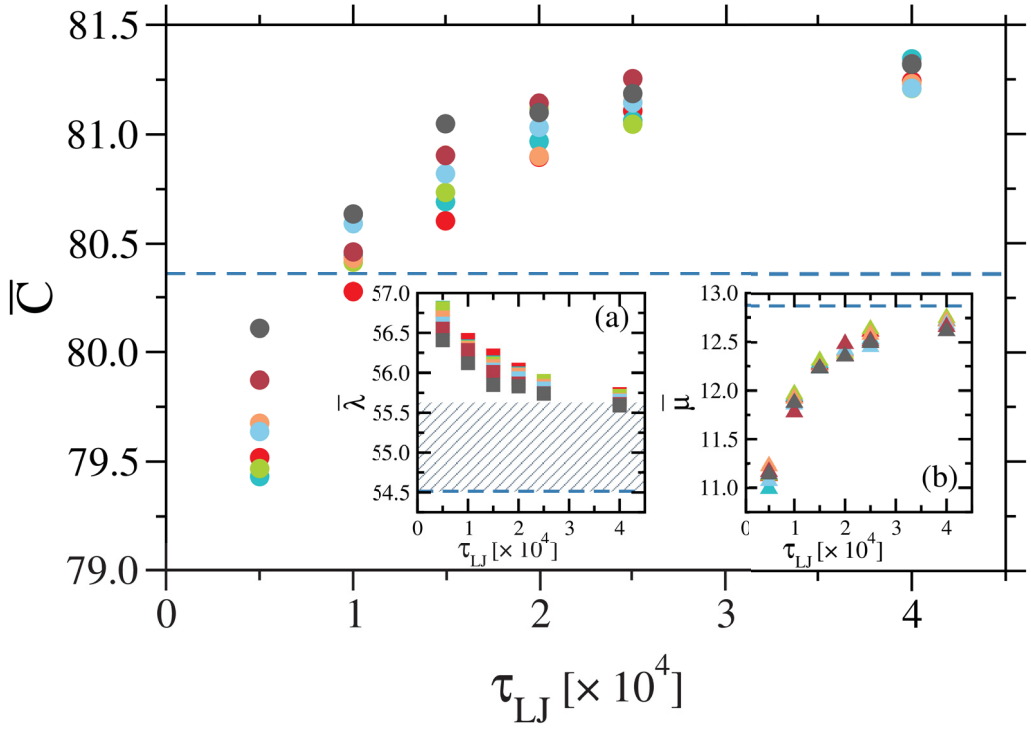

Figure 5.44: Evolution of $\bar{C}$ as a function of relaxation time for all the time origins shown in Fig. 5.39, and for all the shear rates in the *main panel* and $\bar{\lambda}$ and $\bar{\mu}$ in the *inset a* and *b* respectively. The horizontal dashed blue lines represent the initial undeformed values.

The main panel of Fig. 5.44 shows the evolution of $\bar{C} = (C_{11} + C_{22} + C_{33})/3$ (check section 3.1.1) as a function of relaxation time, for all the time origins shown in Fig. 5.39, and for all the shear rates. The horizontal dashed blue line represents the initial undeformed value. It is clear from the plot that, $\bar{C}$ shows an initial decrease from its undeformed value for the first time origin

with the highest residual stresses and then increases as the stresses further relax, and eventually saturates at a finite value above its undeformed value. This is quite a similar behavior which we also observed for the bulk modulus, and as long as by definition $\bar{C} = \bar{\lambda} + 2\bar{\mu}$ (in which, $\bar{\lambda} = (C_{12} + C_{13} + C_{23})/3$ and $\bar{\mu} = (C_{44} + C_{55} + C_{66})/3$), which is very similar to the definition of bulk modulus Eq. (3.15), it makes sense to look at the evolution of λ and μ to see what is causing the offset increase in $\bar{C}$. The evolution of λ and μ as a function of relaxation time, is represented in the insets (a,b) of Fig. 5.44 respectively, for all the six time origins shown in Fig. 5.39 and for all the shear rates. The horizontal dashed blue lines represent the initial undeformed values. From the insets we can see that, $\bar{\mu}$ (inset (b)) evolves towards its initial undeformed values and saturates at a finite value very close to that. But, $\bar{\lambda}$ (inset (a)) saturates at a finite value above its initial undeformed value. Therefore, from this result it is evident that the offset in the final value of $\bar{C}$ is caused by $\bar{\lambda}$. As it was discussed in chapter 3, the elastic constant tensor Eq. 3.1 consist of three different components. Therefore, in order to understand the offset in $\bar{C}$ caused by $\bar{\lambda}$, we need to check the evolution of each of these components. Meaning, $\bar{\lambda}_B$ and $\bar{\mu}_B$ corresponding to the Born term Eq. 3.4, and $\bar{\lambda}_F$ and $\bar{\mu}_F$ corresponding to the stress fluctuation component Eq. 3.5. This is shown in Fig. 5.45(a-c).

Fig. 5.45(a-c) shows the evolution of $\bar{\lambda}_B = \left(C^B_{12} + C^B_{13} + C^B_{23}\right)/3$, $\bar{\mu}_B = (C^B_{44} + C^B_{55} + C^B_{66})/3$, $\bar{\lambda}_F = \left(C^F_{12} + C^F_{13} + C^F_{23}\right)/3$ and $\bar{\mu}_F = \left(C^F_{44} + C^F_{55} + C^F_{66}\right)/3$ as a function of relaxation time, for all the time origins shown in Fig. 5.39 and for all the shear rates. By comparing Fig. 5.45(a,b) with Fig. 5.45(c) we can clearly see that the contribution of the non-affine components of the elastic constant tensor is much more pronounced than the affine (Born) term. Although, all the components show an evolution towards their initial undeformed values (the horizontal dashed blue line) and saturate at a finite value before reaching these values, the offset contribution of the non-affine terms, is larger than the affine terms. Therefore we can conclude that the main contributions in the changes occurring in the elastic constant tensor (caused by the residual stresses), comes from the non-affine deformations (with respect to the initial undeformed states) in the system. This is expected, because the shear load is switched off in the steady state regime where, the system has under gone plastic deformation and the plastic deformations are associated to non-affine displacements.

One last cross-check on the bulk modulus was done by performing simulations under constant pressure (NPT). To do so, we took the relaxed undeformed samples from the canonical simulations (NVT) and calculated the average pressure of the samples. The samples were then coupled to a barostat, and the pressure was fixed at the obtained mean pressures. Then, the samples were relaxed at fixed pressure by performing a production run of the order of $10^4\tau_{LJ}$ in the NPT ensemble. Shear deformation was then applied to the relaxed samples

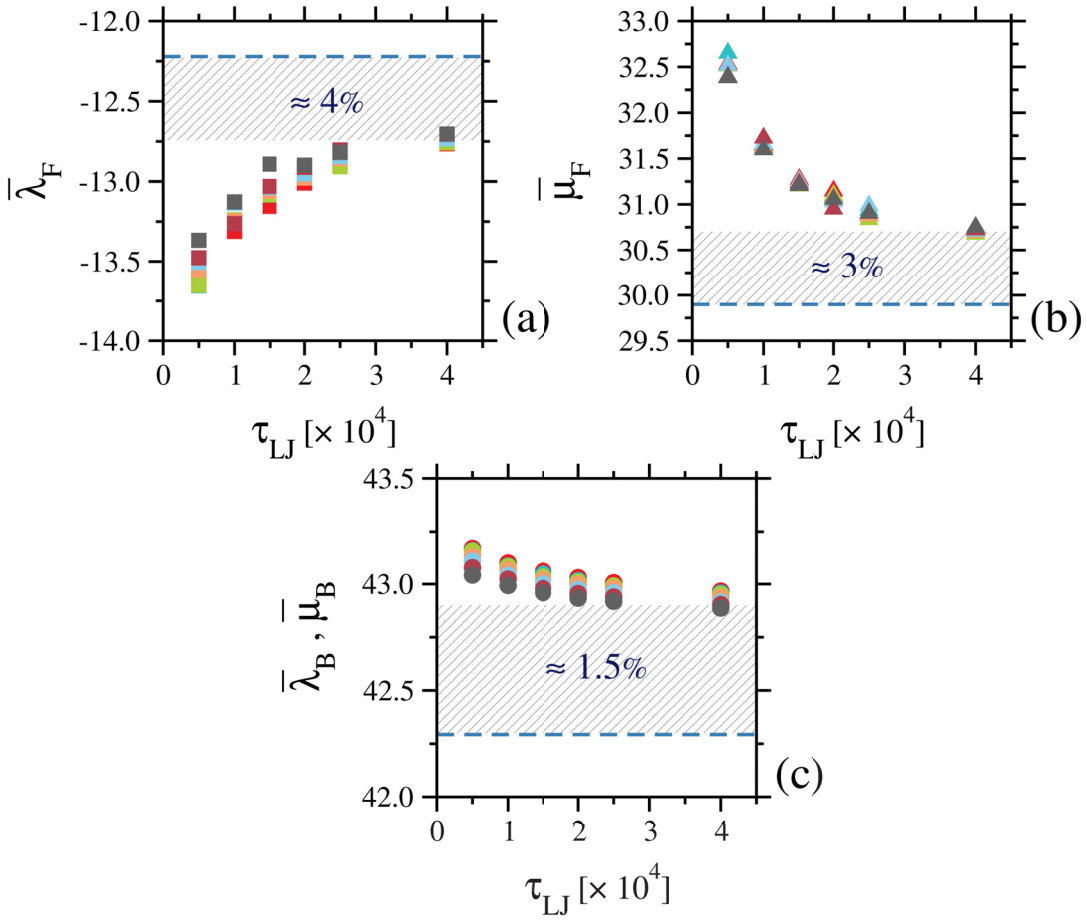

Figure 5.45: Evolution of $\bar{\lambda}_F$, $\bar{\mu}_F$, $\bar{\lambda}_B$ and $\bar{\mu}_B$ as a function of relaxation time for all the time origins shown in Fig. 5.39, and for all the shear rates. The horizontal dashed blue lines represents the initial undeformed values. The shaded are shows the percentage of deviation from the undeformed value.

with a constant shear rate of $\dot{\gamma} = 10^{-4}$. Then shear load was switched off in the steady-state regime, and we followed the same protocol, as it was discussed earlier in this section, to calculate the elastic constant tensor from the six-time origins (cf. Fig. 5.39). These results are shown in Fig. 5.46.

Fig. 5.46 shows the obtained values for different components of the bulk modulus (the open circles represent the xy components, open squares the yz component and the open triangles the xz components. The closed triangles show the averaged values overall components.) for NVT runs in sharp and light blue and NPT runs in gray and black. The horizontal dashed line (in light blue) and dotted line (in black) are the obtained values for the undeformed states of the NVT and NPT runs, respectively. From Fig. 5.46 we can see that we observe qualitatively the same behavior for the NPT runs. The bulk modulus also increases and stays at a finite value. While the undeformed values agree for both cases, the final values after deformation seem to be slightly different which can be caused by minor increases in the volume of the system at constant pressure (by coupling the system to a barostat to fix the pressure, we allow the

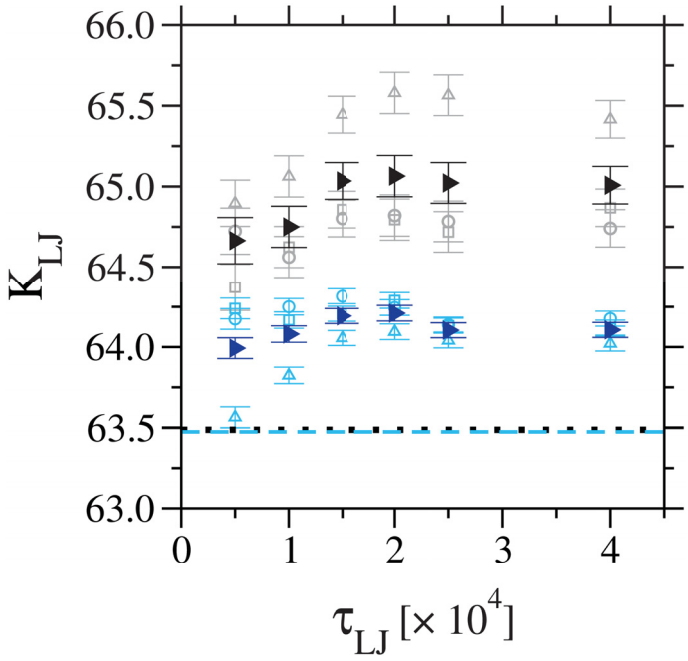

Figure 5.46: Comparison between the obtained results for the evolution of different components of the bulk modulus as a function of relaxation time, for NVT runs (in sharp and light blue), and NPT runs (in gray and black).

simulation box to fluctuate).

As it was discussed earlier in this section, by calculating all different components of the elastic moduli, we tried to investigate anisotropies in the system while the stresses are relaxing. The signs of these anisotropies were already visible in the results which we have shown so far. In order to give a more clear picture on these anisotropies, we present in a set of plots (Fig. 5.47(a-d)), the obtained values for all the components of the elastic moduli for a single shear rate ($\dot{\gamma} = 10^{-4}$), and for all three different components in a single plot.

From Fig. 5.47(a-d), we can see that, while the xy and yz components of the moduli stay close to each other even at early times, the xz component shows minor deviations. Especially at the early times for the first time origins shown in Fig. 5.39. But, these minor anisotropies seem to vanish the more the stresses are relaxing in the system, and the system becomes isotropic. Therefore we can see that the residual stresses are inducing anisotropies in the system, and the higher the residual stresses, the more pronounced the anisotropies. In the next section, we will try to investigate these anisotropies in the macroscopic response of the system.

5.3.2 *Macroscopic response of deformed glasses with residual stresses*

In the previous section, we observed minor anisotropies in the elastic moduli of the system. To cross-check these results and see whether we can observe the same anisotropies in the macroscopic response of the system, we performed a

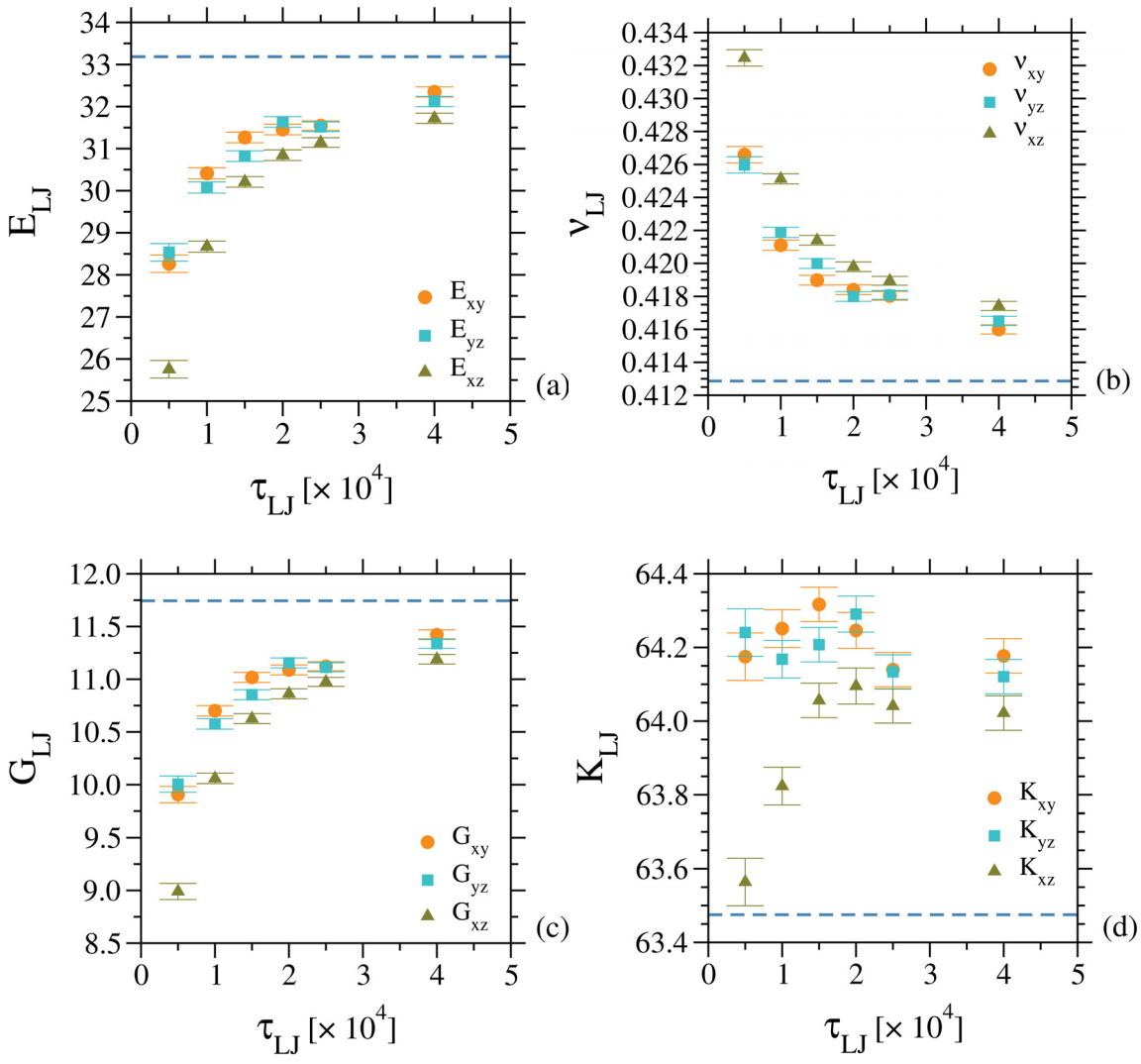

Figure 5.47: Evolution of different components of the Young's modulus (a), the Poisson's ratio (b), the shear modulus (c) and the bulk modulus (d) as a function of relaxation time for a single shear rate $\dot{\gamma} = 10^{-4}$, and for all the time origins shown in Fig. 5.39.

simulation in which we took the deformed samples from the first and last time origins shown in Fig. 5.39. The first time origin is at early times after switching off the shear load where the samples have high residual stresses (single dotted dashed line in Fig. 5.39) and the last time origin at the late relaxation times where the samples have less residual stresses (double dotted dashed line in Fig. 5.39). From these points, we started to deform the samples again by applying a shear deformation, in the same direction as it was initially imposed to the samples (x-direction) and also in the two other perpendicular directions (y and z-direction). By doing so, we were able to obtain the stress-strain curves shown in Fig. 5.48 and 5.49.

Fig. 5.48 represents the stress-strain curve obtained for the samples which are deformed from the initial undeformed state (in black) by performing a shear deformation in x-direction with a constant shear rate $\dot{\gamma} = 10^{-4}$. The deformed

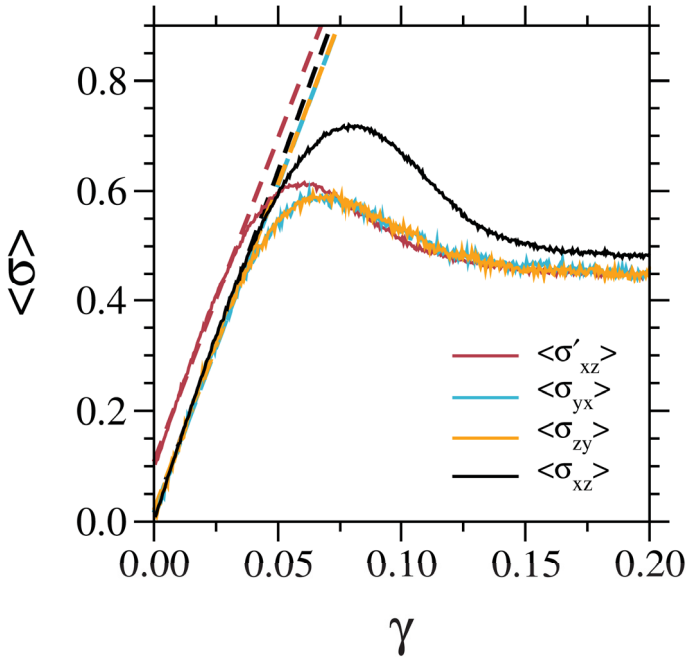

Figure 5.48: Stress-strain curves for the samples being deformed from the initial undeformed state (in black) in x-direction, and from the last time origin on the stress relaxation curve (double dotted dashed line in Fig. 5.39) in x, y and z directions in red, blue and orange respectively. All the samples are deformed with a single constant shear rate $\dot{\gamma} = 10^{-4}$.

samples, after switching off the shear load from the steady states, were then taken from the last time origin on the stress relaxation curve (double dotted dashed line in Fig. 5.39). The red curve represents the stress-strain curve obtained by performing the shear deformation on these deformed samples in x-direction. The blue and the orange curves represent the stress-strain curves obtained by performing the shear deformation on deformed samples in y and z-directions, respectively. The dashed lines in the elastic regime are linear fits to the data. By fitting the data in the elastic regime with a linear function of the form $\sigma(\gamma) = G\gamma$, we are able to read off the slope of these linear functions G (which corresponds to the shear modulus of the samples) and cross check these values with the values we have obtained from calculation of the elastic constants tensor. These values are shown in table (5.8). By looking at the linear fits in the elastic regime of the stress-strain curves in Fig. 5.48 we can see that, the dashed lines have similar slopes (on average) and therefore the values of the shear modulus should not vary a lot. By comparing the obtained values from the linear fits in the elastic regime and the obtained values from the calculation of the elastic constant tensor (shown in table (5.8)) we can clearly see that, both calculations agree nicely with each other within an error of about 5%. Minor softenings are visible by the small decrease and shift of the stress overshoots to lower strains of the stress-strain curves. These softenings are also observed in the obtained values of the shear modulus from the calculation of the elastic constant tensor and the linear fits in the elastic regime of the stress-strain curves, compared to the undeformed states.

Comparison[a] between the shear modulus obtained from ECT[b] and fits on SSC[c]		
	G_{ECT}	G_{SSC}
G_{xz}	11.744	12.406
G_{xz}	11.190	11.771
G_{yx}	11.422	11.906
G_{zy}	11.338	11.860

Table 5.8: Comparison between the values of different component os the shear modulus, obtained from the calculation of the elastic constant tensor and linear fits in the elastic regime of the stress-strain curves shown in Fig. 5.48. The colors are chosen in accordance to

[a] For the deformed samples taken from the last time origin on the stress relaxation curve (double dotted dashed line in Fig. 5.39).
[b] Elastic constant tensor
[c] Fits in the linear regime of stress-strain curve

Also, another remark which should be made here is that from both calculations (elastic constant tensor and linear fits in the elastic regime of the stress-strain curve) we can see that, as it was also discussed earlier, the system seems to recover its isotropies, and different component of the shear modulus have similar values on average.

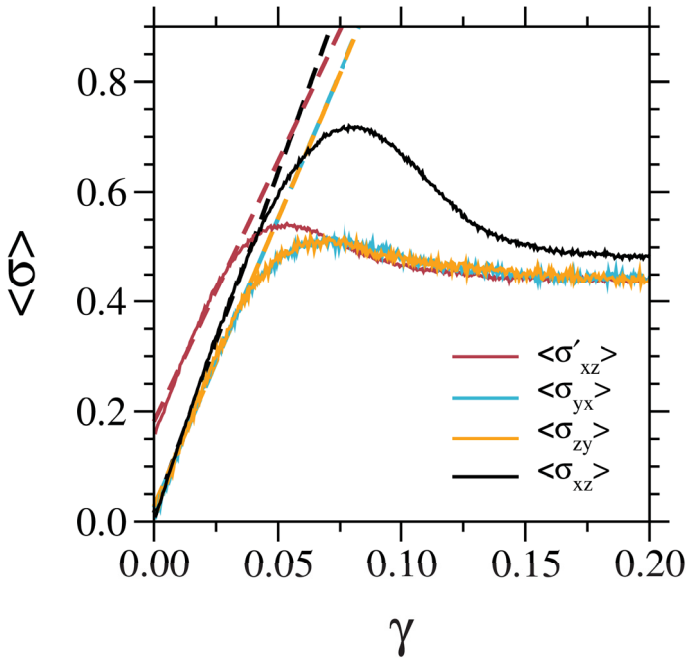

Figure 5.49: Stress-strain curves for the samples being deformed from the initial undeformed state (in black) in x-direction, and from the first time origin on the stress relaxation curve (single dotted dashed line in Fig. 5.39) in x, y and z directions in red, blue and orange respectively. All the samples are deformed with a single constant shear rate $\dot{\gamma} = 10^{-4}$.

Comparison[a] between the shear modulus obtained from ECT and fits on SSC

	G_{ECT}	G_{SSC}
G_{xz}	11.744	12.406
G_{xz}	8.990	9.499
G_{yx}	9.906	10.543
G_{zy}	10.005	10.490

Table 5.9: Comparison between the values of different component os the shear modulus, obtained from the calculation of the elastic constant tensor and linear fits in the elastic regime of the stress-strain curves shown in Fig. 5.49.

[a] For the deformed samples taken from the first time origin on the stress relaxation curve (single dotted dashed line in Fig. 5.39).

The linear fits in the elastic regime of the stress-strain curves in Fig. 5.49, show much more variation compared to the previous plot and they have rather different slopes. Also, the softenings in the system are much pronounced here, as the overshoot in the stress-strain curves shows even a larger decrease and the samples seem to be more ductile. By looking at the obtained values in table (5.9) we can see that, the shear modulus shows a large decrease compared to the values of the initial undeformed state, and also, from both calculations (elastic constant tensor and linear fits in the linear regime of the stress-strain curve) we are able to observe anisotropies in the system. While, the values for yx and zy components are very close to each other, the xz component has a lower value and shows a large deviation from the initial undeformed values. This means, the system seem to be more ductile in x-direction compared to the other two perpendicular directions.

Before closing this section, we present one last result, which is obtained by applying shear deformation on deformed samples with residual stresses. In Fig. 5.50 we compare between the stress-strain curve obtained by performing shear deformation with a constant shear rate $\dot{\gamma} = 10^{-4}$ on samples from the initial undeformed states (black curve) and the deformed samples are taken from the first and last time origin, shown in Fig. 5.39, with the highest ($abs(< \sigma_{-xz} >)_S$) and lowest ($abs(< \sigma_{-xz} >)_L$) residual stresses (in orange and green, respectively) subjected to shear deformation with a constant shear rate $\dot{\gamma} = -10^{-4}$, in the opposite direction with respect to the initial deformation. From the figure, we can see that the deformed samples show an initial release of stresses followed by an elastic response after the release of the stresses. In both cases (samples with high and low residual stresses), samples appear to be more ductile. The softenings are reflected in the stress-strain curve overshoot where, for the samples with lowest

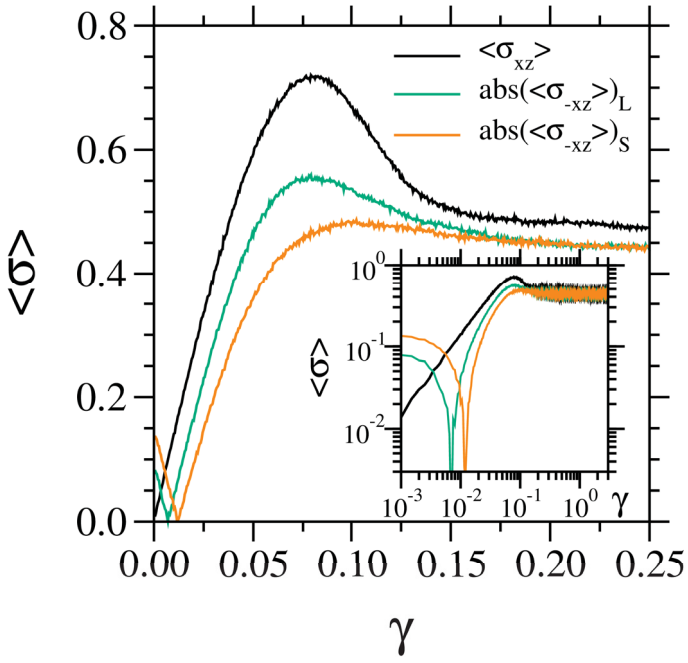

Figure 5.50: *main panel*: Stress-strain curve obtained by performing shear deformation with a constant shear rate $\dot{\gamma} = 10^{-4}$ on samples from the initial undeformed states (black curve) and the deformed samples are taken from the first and last time origin, shown in Fig. 5.39, with the highest and lowest residual stresses (in orange and green, respectively) subjected to shear deformation with a constant shear rate $\dot{\gamma} = -10^{-4}$, in the opposite direction with respect to the initial deformation. *inset*: represents the same data in double-logarithmic scales.

residual stresses, we observe a large decrease in the overshoot maximum. In the case of samples with high residual stresses, the stress-strain curve does not show any overshoot and shows a shoulder type increase. The shear modulus (reflected in the linear response of the samples in the elastic regime) seems to show minor changes with respect to the initial undeformed samples, which is in good agreement with the results which we have shown before. The inset in Fig. 5.50 corresponds to the full stress-strain curve for all cases in double-logarithmic scales. As expected (the steady-state response should be the same for samples at a fixed temperature and a constant shear rate), in the steady-state regime, all the curves sit on top of each other.

5.3.3 *Simulation results vs. experimental results*

This part of our work (effect of deformation on elastic constants of BMGs) was in collaboration with our experimental collaborators at the University of Münster[6]. They studied the effects on elastic constants of a $Pd_{40}Ni_{40}P_{20}$ metallic glass-former by deforming the samples via cold rolling. In their studies, they also measured the elastic constants of the system both for the undeformed and the deformed samples. In table (5.10) we present a comparison between the experimental

[6]Group of Prof. Dr. Gerhard Wilde, Institut für Materialphysik, Westfälische Wilhelms-Universität Münster, Germany

and simulation results. From table (5.10) we can see that, both simulations and

Comparison between elastic moduli, obtained from simulation[a] and experiment

	Un-deformed glass		Deformed glass	
	Simulation	Experiment	Simulation	Experiment
E	97.06 ± 2.5 (GPa)	101 ± 2 (GPa)	93.78 ± 2.8 (GPa)	100 ± 2 (GPa)
K	185.65 ± 1.1 (GPa)	175 ± 76 (GPa)	187.5 ± 1.1 (GPa)	172 ± 75 (GPa)
G	34.35 ± 0.9 (GPa)	36.1 ± 0.7 (GPa)	33.10 ± 1.1 (GPa)	35.5 ± 0.7 (GPa)
ν	0.413 ± 0.002	0.404 ± 0.003	0.417 ± 0.002	0.403 ± 0.003

Table 5.10: A comparison between the obtained values of elastic moduli, from simulation and experiment, for both undeformed and deformed samples of a $Ni_{80}P_{20}$ (in simulation) and $Pd_{40}Ni_{40}P_{20}$ (in experiment) glass former.

[a] The simulation results are converted from reduced units (table (4.2)) to real units, with a single factor (2.925×10^9), by considering Nickel's atomic information. In order to do so, we have used the Van der Waals Radii of Nickel $\sigma_{Ni} = 1.9$Å, atomic mass $m_{Ni} = 9.75 \times 10^{-26}$kg, melting temperature $T_m^{Ni} = 1453$°K [Batsanov (2001), Hu, Zhou, and Robertson (2009), and Ruben (1985)] and the Boltzmann's constant $k_B = 1.38 \times 10^{-23} m^2 kg/s^2 K$ [Pitre, Plimmer, Sparasci, and Himbert (2019)].

experimental results show softenings in the system after deformation (here it should be mentioned that, the reported simulation values for the deformed cases are obtained by calculating the elastic constants for the deformed samples at the longest relaxation time origin shown in Fig. 5.39 (double dotted dashed line). The shear modulus and the Young's modulus show a decrease, both in simulation and experiment. But, the bulk modulus appears to decrease in experiment after deformation, which is not completely reliable because of the large statistical errors in the measurements.

But, as a general conclusion, the appearance of these softenings both in simulation and experiment were impressive results that needed to be investigated in more detail. Therefore, we tried to study the effect of deformation on elastic properties of the system using the vibrational modes and see whether we can observe the same softenings or not?! These results will be presented in the next section.

5.3.4 Remarks

The elastic constants (shear modulus, Young's modulus, and Poisson's ratio) of the deformed samples with residual stresses, evolve towards their initial undeformed values as the stresses relax in the system. But, the bulk modulus

increases and stays at a finite value. This increase, compared to the quiescence values, is caused by non-affine displacements in the system and is reflected in the non-affine component of the elastic constant tensor. Residual stresses induce minor anisotropies in the elastic constants of the system while the stresses are relaxing in the system. The macroscopic response of the deformed samples with residual stresses also reflects the same minor anisotropies when subjected to secondary shear deformation. The deformed samples show softenings after deformation compared to their quiescence states. Therefore, here we can conclude that, rather than last minor changes in the mechanical responses of the system, the elastic constants appear not to be very sensitive to deformation.

5.4 Effect of deformation on time-dependent vibrational properties

As the main focus of this work, in order to investigate the effect of deformation and the residual stresses on the mechanical properties of BMGs, we also studied the time-dependent vibrational properties of BMGs in terms of current correlation functions and dynamic structure factor. We also looked at the density of vibrational states and the Boson peak. The elastic properties of a physical system are related to the low-frequency regime of the density of states where the collective modes appear as acoustic sound waves. Therefore, one can obtain the sound velocities in the system and also the specific heat. For all the mentioned quantities, the calculation has been done both for the undeformed (as a reference) and the deformed states.

5.4.1 Density of states and the Boson peak

The density of vibrational states was obtained using Eq. (3.41), by performing a FFT (as it was discussed in section 4.3.2) on the velocities of the prepared samples in the undeformed state and transforming the time domain to the frequency domain (check Fig. 5.51). Fig. 5.51 shows the total density of states (in black) and the partial density of states for A and B-type particles (in blue and red, respectively), for the initial undeformed states. From the figure we can see that, while $g_A(\omega)$ (corresponding to A-type particles) has quite a symmetric distribution, $g_B(\omega)$ (corresponding to B-type particles) is skewed to the lower frequencies. This corresponds to a frequency window of $\approx 5-20[\tau_{LJ}^{-1}]$ (which is far from the frequency range of our interest. Our main focus is on the low-frequency limit ($\omega \rightarrow 0$) of the density of states where the collective modes appear as acoustic waves.). This means that the phonons, corresponding to B-type particles, are slightly easier to excite with lower energies, and the main

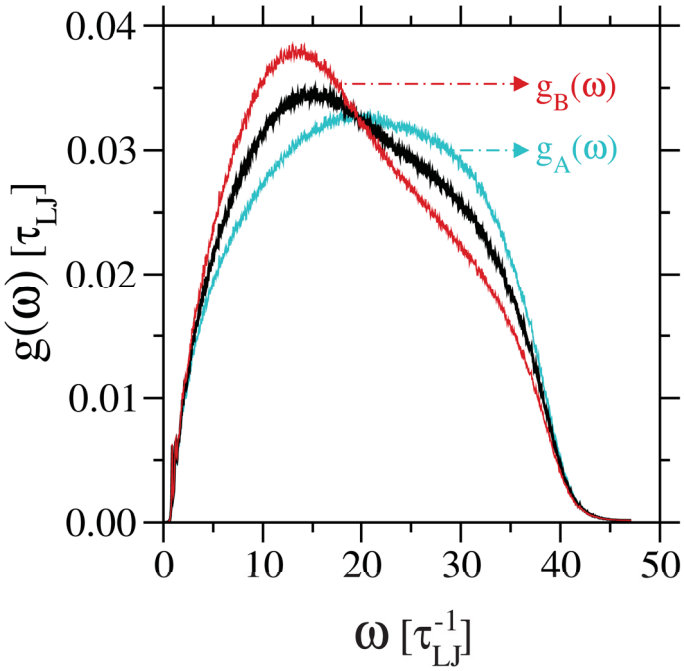

Figure 5.51: Total density of states (in black) and the density of states corresponding to A and B-type particles (in blue and red respectively).

energy carriers in the system are the phonons corresponding to A-type particles. This can also be understood since, the B-type particles are slightly smaller in size (effective radius, check table (4.1)), and they have faster dynamics compared to A-type particles (check Fig. 2.5).

To study the finite-size effects in our calculations, we performed extensive MD simulations and calculated the density of states for different system sizes (see section 4.3.2). In Fig. 5.52 we show a comparison between the total density of states of a small system (with $N = 1300$ particles in a cubic simulation box size of $L \approx 10\sigma_{AA}$, in green) and a large system (with $N = 40000$ particles in a cubic simulation box size of $L \approx 31.34\sigma_{AA}$, in black), for the initial undeformed states[7]. In the main panel of Fig. 5.52 we can see that the total density of states corresponding to two system sizes seems to be consistent with each other and sit on top of each other. But, the finite-size effects emerge in the inset where we have plotted the same data in double logarithmic scales. In the inset of Fig. 5.52 one can see that, while at higher frequencies the curves sit on top of each other, at lower frequencies we are detecting some modes in the large system (by the appearance of the spikes) which are not visible in the small system for this frequency range. The Boson peak was obtained, for both system sizes, by $g(\omega)/\omega^2$ for the initial undeformed states (check Fig. 5.53).

In the main panel of Fig. 5.53, we show $g(\omega)/\omega^2$ which, shows a peak around

[7]Hereafter, all the results we are presenting are for the large system with $N = 40000$ particles. Whenever we make a comparison between different system sizes, we will mention the corresponding system sizes.

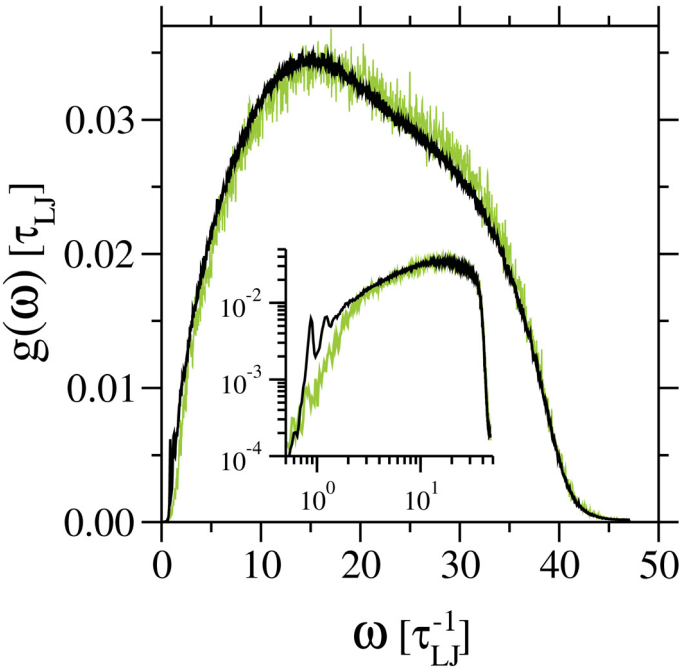

Figure 5.52: *main panel:* Total density of states for a system of 40000 particles (in black) compared to the total density of states of a system 1300 particles (in blue). *inset:* The same data is presented in logarithmic representation.

$\approx$ 1THz for the large system (the total $g(\omega)/\omega^2$ in black and the corresponding Boson peak associated to the A and B type particles in blue and red, respectively) and the small system (in green). What is important here, as we discussed earlier in this section, is the appearance of the finite size effects in our calculations by the emergence of two sharp spikes in the low frequency limit of the Boson peak for the large system (in black). While, in the small system (the green curve) we do not detect them. Later when we make a comparison between the Boson peak of the undeformed and deformed states we present a more comprehensive picture of these finite size effects. What is shown in the inset of Fig. 5.53 is basically the same data from the main panel by performing a running average of length 20[8]. By performing a small averaging on the data we get a typical Boson peak shown in many literature but, we loose a lot of valuable information. An important question to ask here is that: *what is the origin of these spikes in the low frequency limit*? We will answer this question in section 5.4.3.

Shear load was then applied on the undeformed samples (as it was discussed in 4.3.2) with a single shear rate $\dot{\gamma} = 10^{-4}$. Therefore, we obtained the stress-strain curve shown in the main panel of Fig. 5.54. The samples were deformed up to strain $\gamma = 1$. At this point the shear load was switched off, and we allow the samples to relax. Therefore, we obtained deformed samples with a finite amount

[8]In a running average (RA) of length m over N data points $D(n)$ with $n = 1, \cdots, N$, the data points are averaged in windows of length m around a central value y such that, $RAD(n) = \frac{1}{m}\sum_{j=-k}^{k} y_{n+j}$ with $k = \frac{m-1}{2}$.

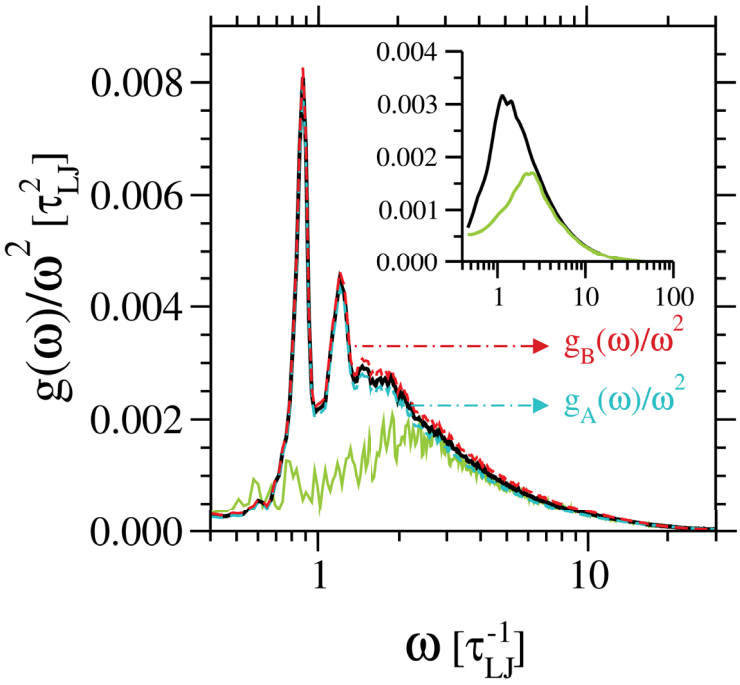

Figure 5.53: *main panel:* The Bososn peak obtained by $g(\omega)/\omega^2$ for the large system (in black) and the small system (in blue). *inset:* Represents the same data by performing a running average of length 20.

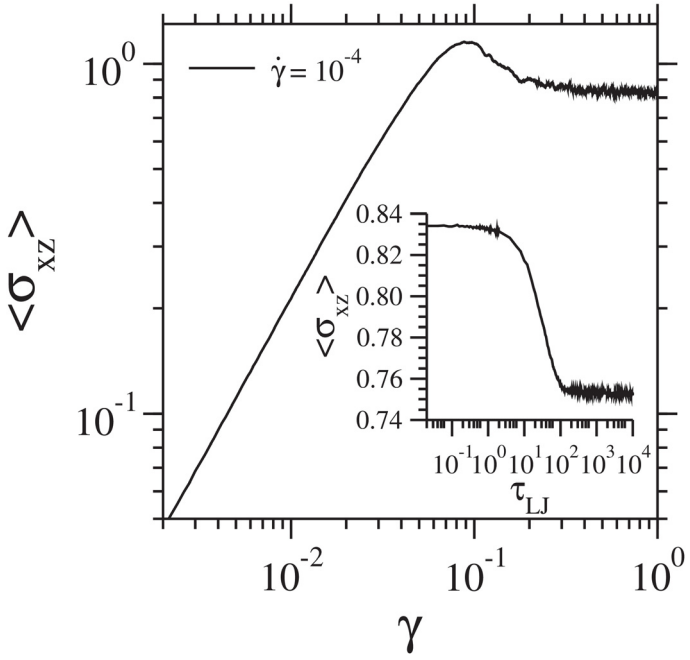

Figure 5.54: *main panel:* Stress-strain curve obtained by performing a shear deformation on the prepared samples (check 4.3.2) with a constant shear rate $\dot{\gamma} = 10^{-4}$. *inset:* Stress relaxation after switching off the shear load at strain $\gamma = 1$ as a function of time.

of residual stresses, as it is shown in the inset of Fig. 5.54. The density of states was then calculated for the deformed samples and the result was compared to the initial undeformed samples as a reference. This is shown in Fig. 5.55. In the

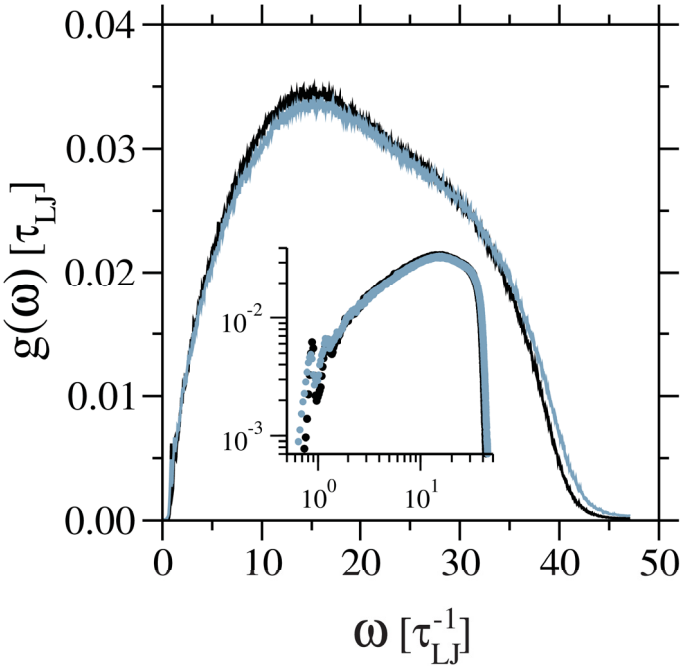

Figure 5.55: *main panel:* Comparison between the density of states of the undeformed samples (in black) with those of the deformed samples (in gray). *inset:* represents the same data in double logarithmic scales.

main panel of Fig. 5.55 the density of states of the undeformed samples (in black) is compared with those of the deformed samples (in gray). A slight decrease is noticeable in the maximum peak. Small changes are also happening in the density of states of the deformed samples both at high and low frequencies, where, at low frequencies these changes indicate small softenings in the system. In the inset of Fig. 5.55 we see the same data in double logarithmic scale, and we can see the minor effects after deformation in the low frequencies, where, the detected modes are showing slight decrease in their peaks.

These effects are much more pronounced when we obtain the Boson peak by dividing the density of states for the deformed samples by omega squared. This is shown in Fig. 5.56. In the main panel of Fig. 5.56, we see a comparison between the Bososn peak of the undeformed samples (in black) and the deformed samples with residual stresses (in gray). From the figure, we can see that the deformation has effected the low-frequency limit of the Bososn peak in the samples with residual stresses. The Boson peak has slightly shifted towards the lower frequencies, and spikes in the low-frequency limit show a small broadening with a decrease in the peak. These effects show the emergence of softenings in the system which is consistent with the results obtained from calculations of elastic constants, discussed in the previous section (in section 5.4.3 we will discuss the

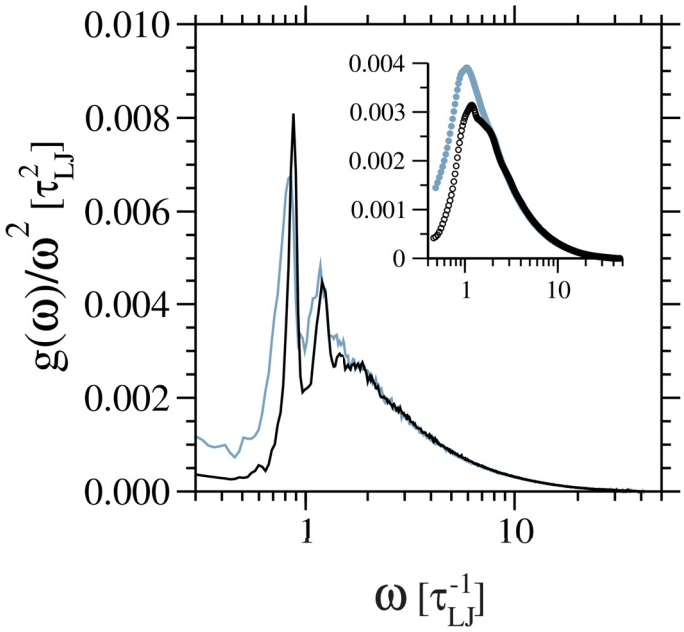

Figure 5.56: *main panel:* Comparison between the Boson peak of the undeformed samples (in black) with those of the deformed samples (in gray). *inset:* represents the same data by performing a running average of length 20.

effects on the low-frequency regime of the Bososn peak in more details when we present the results obtained from the time-correlation functions). The inset in Fig. 5.56 shows the same data by performing a running average of length 20 on the data. From the inset, we can also see that the Boson peak has shifted towards lower frequency by showing a minor increase in the peak.

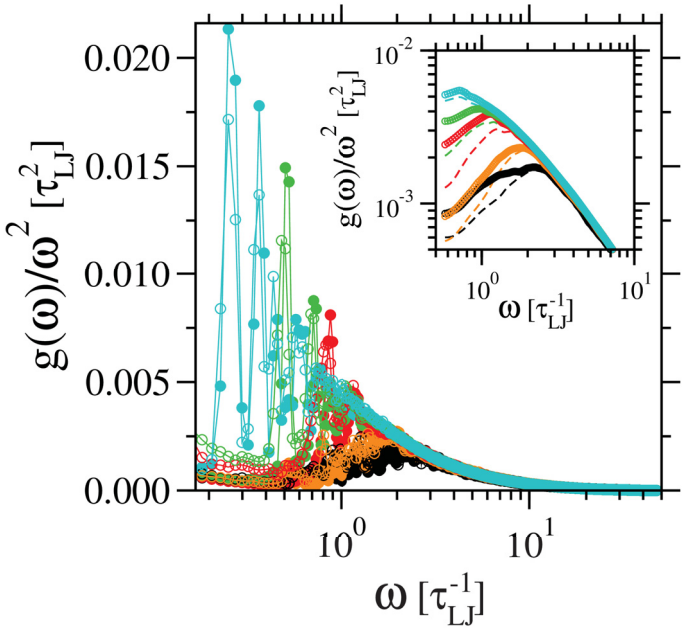

Figure 5.57: *main panel:* The Boson peak obtained for different system sizes (as it was discussed in 4.3.2) for undeformed states (the filled symbols). The black, orange, red, green and blue curves correspond to systems with N = [1300, 3000, 40000, 200000, 1500000] particles respectively. The open symbols represent the results for deformed states. *inset:* Represents the same data by performing a running average of length of 20.

As it was mentioned earlier in this section, to study the finite-size effects in our calculations, we have performed extensive MD simulations and calculated the density of states and the Boson peak for different system sizes (as it was discussed in 4.3.2). Fig. 5.57 shows a comparison between the Boson peak of different system sizes in the undeformed and deformed state. From the main panel, we can see that by increasing system size, we can detect more modes in the system (we will talk about this in more detail in section 5.4.3). The curves with closed symbols correspond to undeformed states, and the corresponding open symbols (with the same color, respectively) represent the result for deformed states. The inset shows the same data by performing a running average of length 20 on the data (dashed lines represent the undeformed states and the open symbols the deformed states). In large system sizes, as a result of the shift of the modes towards lower frequencies after deformation, the Boson peak shows a more pronounced change by an increase of the peak amplitude and shift towards lower frequencies. But, these effects are less pronounced for the small system sizes (black and orange curves) where only a small increase in the peak amplitude in the limit of low frequencies occurs. Another conclusion that can be made from the plot is that is simulations, the Boson peak in the low frequency of the density of state is mainly due to finite size effects and strong softenings. The fact that in experiments, much smoother Boson peak can be detected, might be due to better annealing of the samples.

5.4.2 Heat capacity

As it was discussed earlier in section 3.2.4, by Debye's description, the specific heat C_V is proportional to T^3 in the limit of low temperatures. In glasses, the specific heat deviates from the Debye's description by showing a Boson peak around $T \approx 10^{\circ}K$. To study the effect of deformation and the residual stresses on the specific heat and the Boson peak of the system, using Eq. (3.43), we have calculated the specific heat from the obtained density of states. The calculation was initially performed on the undeformed samples. Here also, to study the finite size effects, we have calculated the specific heat for all the system sizes shown in Fig. 5.57. These results are shown in Fig. 5.58.

The obtained specific heat C_V are shown in the inset of Fig. 5.58 for different system sizes. From the figure, we can see that irrespective of the system size, all the curves sit on top of each other, and as expected (check 3.2.2), they saturate at a finite value at high temperatures. In the main panel, we see the obtained Boson peak by C_V/T^3, for different system sizes. The first interesting observation is that the spikes appearing in the low-frequency limit of the Boson peak do not appear in the low-temperature limit of the Boson peak in specific heat. But, the Boson peak appears to be shifted towards lower temperatures in the larger

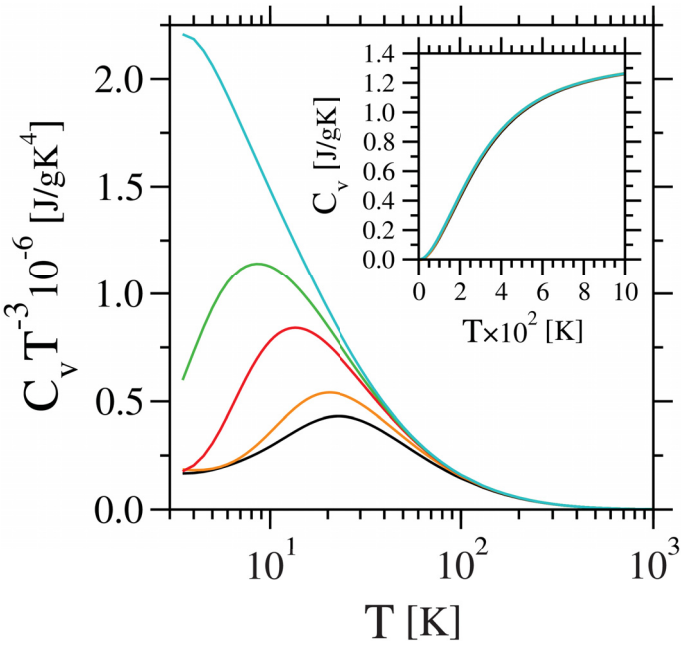

Figure 5.58: *main panel:* The Boson peak obtained by C_V/T^3 for different system sizes (for corresponding system sizes check caption in Fig. 5.57). *inset:* Specific heat obtained for different system sizes (system sizes are shown in Fig. 5.59).

systems, followed by an increase in the peak. This is an effect of the acoustic modes in the low-frequency range of the Boson peak. The same calculation was done to obtain the specific heat and the corresponding Boson peak appearing in the low-temperature limit of the specific heat of the deformed states. The latter results were then compared to those of the undeformed states as a reference. These results are shown in Fig. 5.59.

In Fig. 5.59 we can see that similar to the results presented for the Boson peak in the density of states (Fig. 5.57), the Boson peak in the specific heat also shows a slight increase after deformation (the open symbols in Fig. 5.59) compared to the initial undeformed states (the closed symbols in Fig. 5.59) with a shift towards the lower temperatures. This is consistent with the reported experimental and simulation results by [Bünz, Brink, et al. (2014)] for a $Zr_{50}Cu_{40}Al_{10}$ metallic glass-former. In the latter work, the authors showed that after deformation, the Boson peak amplitude shows a small increase for the deformed samples compared to the Boson peak of the undeformed samples. In the latter work, the authors also studied the effect of annealing on the Boson peak. We also studied these effects and found consistent results. In Fig. 5.60(a) we compare the Boson peak in the density of states of samples prepared via a fast quench (black open circles) and longer annealed samples with quench rates 2×10^{-3} and 2×10^{-4} (in orange and blue open squares, correspondingly). Panel (b) of Fig. 5.60 presents the Boson peak in the specific heat for the samples with the same temperature history. From Fig. 5.60(a), we can see that, for longer annealed samples, the amplitude of the spikes in the low-frequency range of the Boson peak increase and show a slight

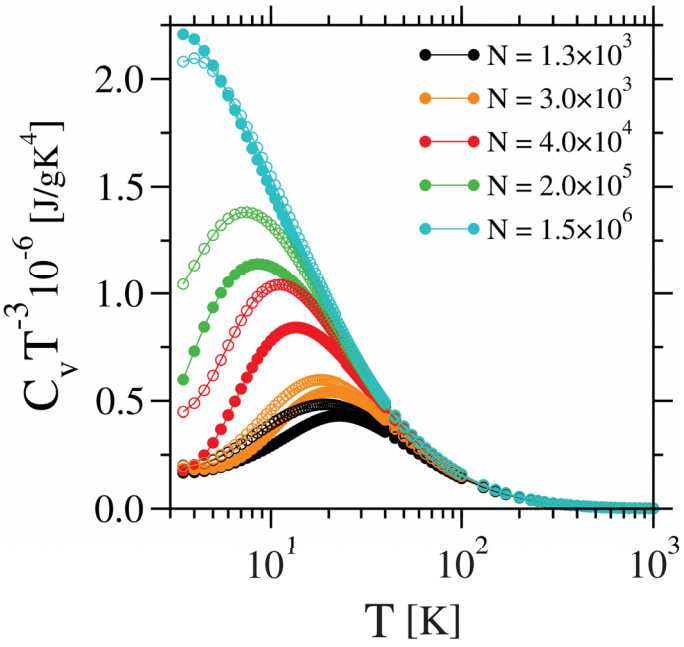

Figure 5.59: Comparison between the Boson peak, obtained by C_V/T^3, of the undeformed (close circles) and deformed (open circles) samples, for different system sizes. The number of particles N, is shown in the figure for different system sizes.

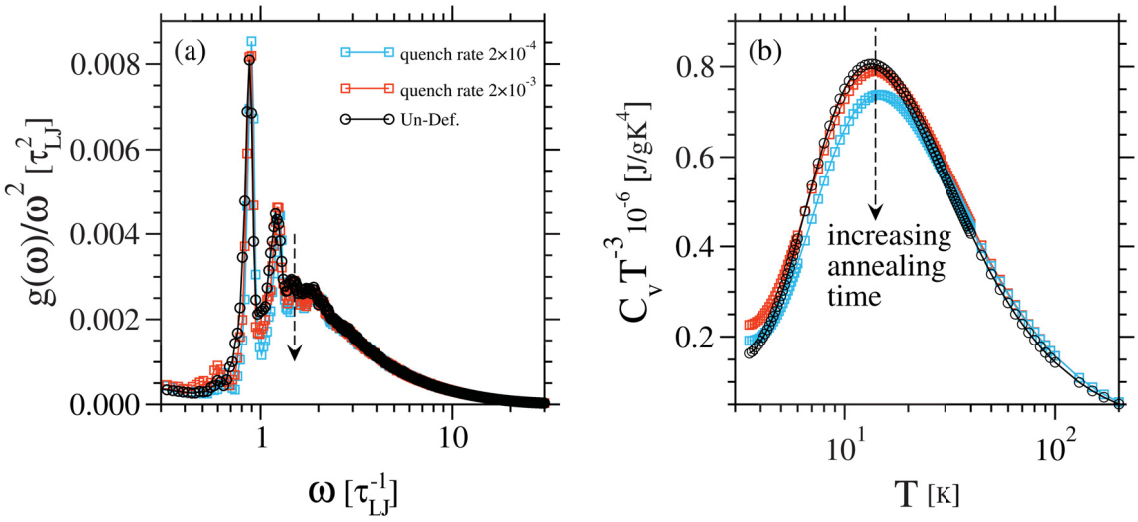

Figure 5.60: *panel (a)*: presents the Boson peak in the density of states obtained by $g(\omega)/\omega^2$, for glass samples obtained via a fast quench (black open circles) and longer annealed samples (in orange and blue open squares, correspondingly). *panel (a)*: presents the Boson peak in the specific heat, obtained by C_V/T^3, for the glass samples with the same temperature history. The arrows in both panels show the direction for longer annealing time.

shift towards larger frequencies. This is also reflected in the Boson peak in the specific heat in panel (b) of Fig. 5.60 where, for longer annealed samples, a small decrease is visible in the amplitude of the peaks.

5.4.3 *Correlation functions*

In this work, we also investigate the effect of deformation and the residual stresses on the vibrational modes in BMGs via studying the time-correlation functions (discussed in section 3.3). Similar to the results we have shown so far, these quantities are calculated initially for the undeformed states (as a reference) with which then, the corresponding deformed states are compared to.

Using Eq. (3.52), the total current correlation function is calculated for the undeformed samples (shown in Fig. 5.61). In the main panel of Fig. 5.61, we

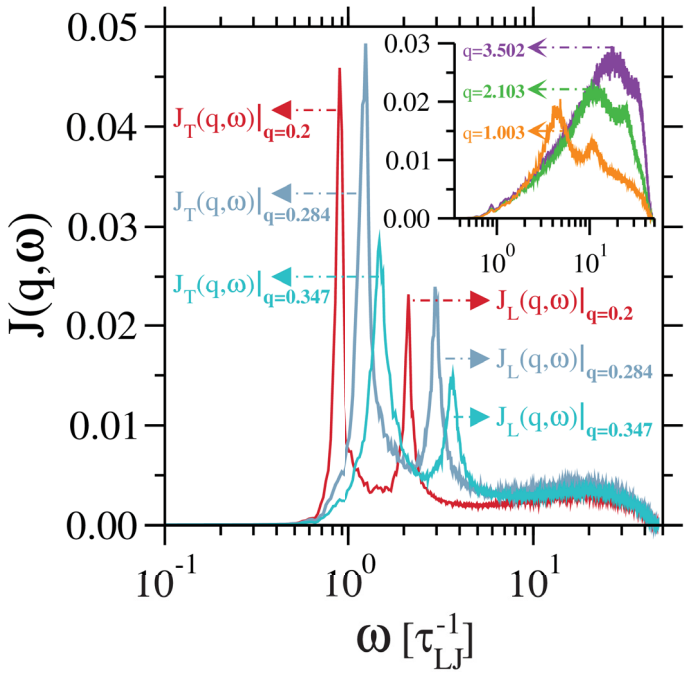

Figure 5.61: *main panel:* The total current correlation function for the three lowest wave numbers of the system. The corresponding transverse and longitudinal current correlations are shown, respectively. *inset:* The total current correlation function for three large wavenumbers of the system.

see the total current correlation function for the three lowest wave numbers $q = 0.2, 0.284, 0.347[\sigma_A^{-1}]$ of the system (large system). The total current correlation function shows two well distinguishable peaks for lowest q values of the system, corresponding to the transverse (J_T) and longitudinal (J_L) current correlation functions, respectively. In the hydrodynamic limit ($q \to 0$ and $\omega \to 0$), these correlation functions give information about the acoustic modes in the system. In Fig. 5.61, we see the transverse and longitudinal acoustic sound modes in the main panel. By increasing q, these modes become less pronounced and start to overlap. This is shown in the inset of Fig. 5.61 for three large wave

numbers $q = 1.003, 2.103, 3.502[\sigma_A^{-1}]$ of the system. By increasing q, we are probing the small length scales in which the acoustic modes are scattered by disorder in the system. Therefore, for example in the inset of Fig. 5.61 we can see for $q = 3.502[\sigma_A^{-1}]$ (purple curve), we cannot distinguish between these modes anymore, and they start to sit on top of each other on a single peak at higher frequencies. This corresponds to time and length scales beyond the Ioffe-Regel crossover at which the Boson peak has already occurred, and where the mean free path between plane waves becomes proportional to their wavelength (cf. 3.2.4). Here we should also mention that the higher amplitude and larger contribution of the transverse modes at low q, compared to those of longitudinal modes, is since the transverse modes have two degrees of freedom compared to those of the longitudinal modes.

Going back to results which we discussed on the Boson peak earlier in section 5.4.1, we have seen the occurrence of some sharp spike-like peaks in the low-frequency limit of the Boson peak in Fig. 5.54. So far, we have mentioned that these peaks are caused by vibrational modes in the system appearing in the low-frequency limit of the Boson peak. Here, we show that these peaks correspond to transverse acoustic modes in the system (shown in Fig. 5.62). In Fig. 5.62 we plot

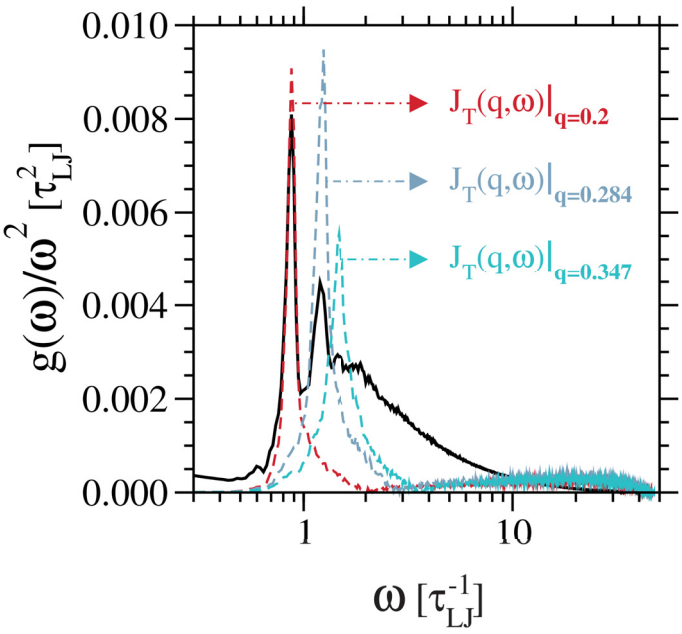

Figure 5.62: Transverse current correlation function for the three lowest wave numbers of the system plotted on top of the Boson peak (in the initial undeformed state). Note that the $J_T(q,\omega)$ curves are divided by a factor 5.

the transverse current correlation function (for the three lowest wave numbers of the system) on top of the Boson peak in the undeformed state. From the figure, we can see that the peaks sit exactly on top of spikes in the Boson peak. The low-frequency regime of the Boson peak corresponds to the range of frequencies where elastic scattering occurs, and one can observe collective acoustic modes.

But, the higher frequency regime of the Bososn peak corresponds to a higher q values where the modes are damped, and the scattering is not elastic anymore. Therefore, the Boson peak decays to zero. One more important thing to be mentioned here is that, earlier we showed the finite-size effects in our calculations (check Fig. 5.54 and Fig. 5.57). Here, we can see that the transverse acoustic modes appearing in the low-frequency regime of the Boson peak corresponds to the lowest wave numbers of the system. Therefore, they correspond to large wavelengths ($\lambda = 2\pi/q$). This means the system needs to be large enough such that the acoustic modes fit into the simulation box, and we can detect them.

Using the obtained longitudinal and transverse modes we are able to get some dispersion-like curves by reading off [9] the corresponding frequency at which the peaks occur (we call it $\omega_{max}(q)$) for each wave number, from the longitudinal and transverse current correlation functions, respectively. Also, the *full width at half maximum* (FWHM, we call it $\Gamma(q)$) of the corresponding longitudinal and transverse modes, will give us a length scale up to which the elasticity theory holds. These results are shown in Fig. 5.63 and Fig. 5.64.

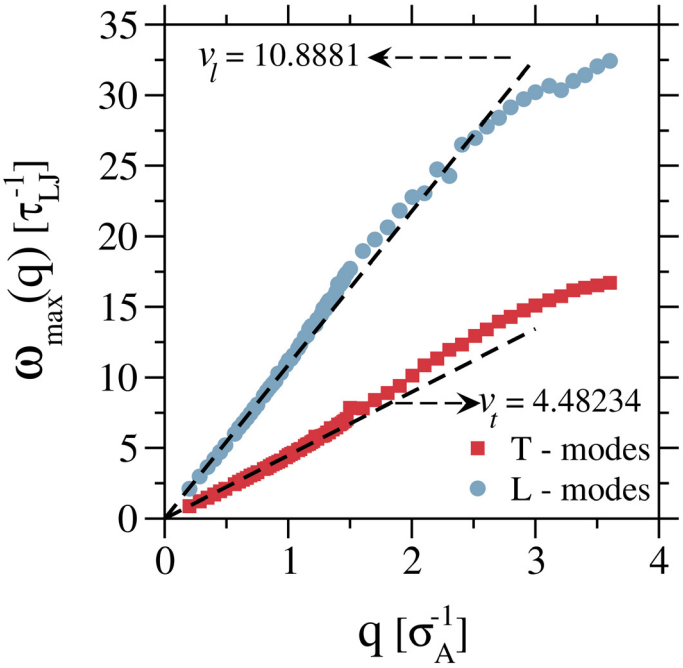

Figure 5.63: $\omega_{max}(q)$ as a function of q (in the initial undeformed state) for both longitudinal acoustic modes (L-modes, close gray circles) and transverse acoustic modes (T-modes, close red squares). The dashed lines are linear fits. The slopes at low frequency/low q limit, corresponds to transverse and longitudinal sound velocities (v_t and v_l respectively, in reduced units).

[9] In order to obtain $\omega_{max}(q)$ and $\Gamma(q)$, the corresponding longitudinal and transverse current correlation functions are fitted via a Lorentzian function as follow:

$$f(x) = \frac{A}{\pi}\left[\frac{F}{(x-M)^2+F^2}\right], \tag{5.3}$$

in which, A is the amplitude, F reads the FWHM and M reads the pick maximum position.

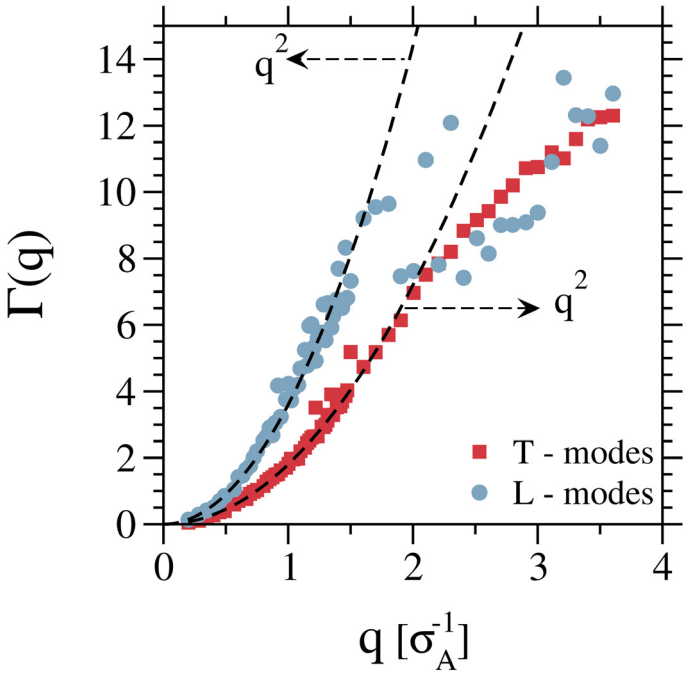

Figure 5.64: $\Gamma(q)$ of the transverse and longitudinal current correlation functions as a function of q (in the initial undeformed state) for both longitudinal acoustic modes (L-modes, close gray circles) and transverse acoustic modes (T-modes, close red squares). The dashed lines are quadratic fits at low frequency/low q limit.

In Fig. 5.63 we see the dispersion relations for the corresponding longitudinal (close gray circles) and transverse (close red squares) branches. As it was discussed earlier, in the hydrodynamic limit the dispersion relation, for each acoustic branch, shows a linear behavior. The dashed lines in Fig. 5.63 correspond to linear fits in the limit of low ω and q. The slope of these linear fits, on each acoustic branch, corresponds to the longitudinal and transverse sound velocities, respectively. These values are shown in the plot. In order to crosscheck our results, we also calculate the elastic constant tensor for these samples. Therefore, we obtained the corresponding longitudinal and transverse sound velocities via $v_l = \sqrt{\bar{C}_{ud}/\rho}$ and $v_t = \sqrt{\bar{C}_{ld}/\rho}$, in which, ρ is the number density, $\bar{C}_{ud}$ corresponds to *upper diagonal* elements of the elastic constant tensor ($\bar{C}_{ud} = (C_{11} + C_{22} + C_{33})/3$) and $\bar{C}_{ld}$ corresponds to *lower diagonal* elements of the elastic constant tensor ($\bar{C}_{ld} = (C_{44} + C_{55} + C_{66})/3$). These values are shown in table (5.11). In table (5.11) we see a good agreement between the obtained values for the sound velocities from the calculation of the elastic constant tensor and the linear fits in the low ω and low q regime of the dispersion relations shown in Fig. 5.63, with the experimental values reported in the literature. Later, we will compare the obtained values for the deformed states with the values in table (5.11) as reference. In Fig. 5.64 we see that, $\Gamma(q)$ for both longitudinal and transverse modes shows a quadratic q dependence in the limit of small wave numbers. This is shown by the quadratic fits on the data (dashed lines) in Fig. 5.64. The linear fits in Fig. 5.63 and the quadratic fits in Fig. 5.64, mark

Comparison between sound velocities obtained from simulation[a] and experiment

ECT[b]			Exp.[c]		
v_l(km/s)	v_t(km/s)	v_l/v_t	v_l(km/s)	v_t(km/s)	v_l/v_t
4.824	2.139	**2.256**	5.060	2.130	**2.38**

Table 5.11: A comparison between the sound velocities obtained from the calculation of elastic constant tensor and the reported values for $Ni_{80}P_{20}$ BMG in literature.

[a] For unit conversion we used the Nickel's atomic information (check table (5.10)).
[b] Elastic constant tensor.
[c] Experimental values reported for $Ni_{80}P_{20}$ BMG [Wang (2012b)].

(roughly) the time and length scales in which the system behaves as an isotropic elastic medium. The latter time scale and the frequency range is also indicated by $\Gamma(q)$ in Fig. 5.64. Comparing the corresponding $\Gamma(q)$ (which gives an inverse time scale) of the longitudinal and transverse modes in Fig. 5.64 with the dispersion-like curves in Fig. 5.63, we can give a rough estimate that, up to $\omega \approx 5-6[\tau_{LJ}^{-1}]$, the system response as an isotropic elastic medium.

Using Eq. (3.55), the dynamic structure factor was calculated for the undeformed samples (as it was discussed in 3.3.3). This is shown in Fig. 5.65. In the

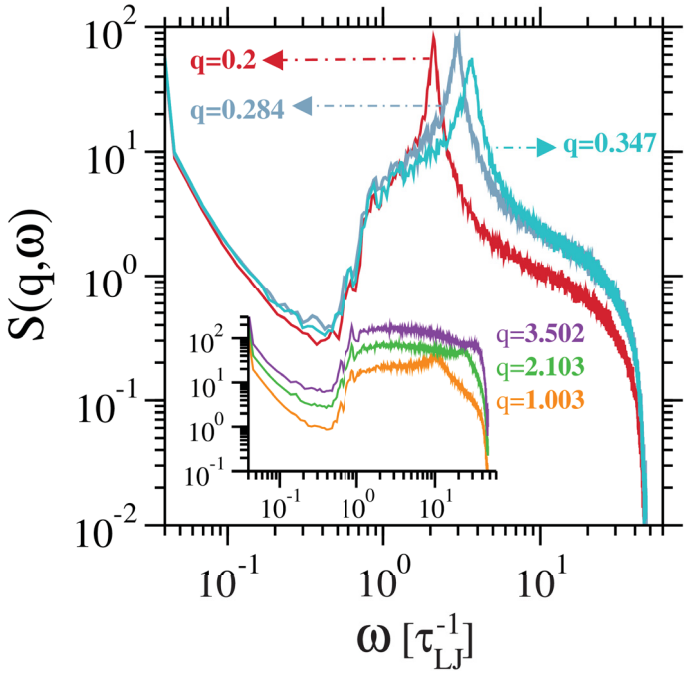

Figure 5.65: *main panel:* The dynamic structure factor for the three lowest wave numbers of the system. *inset:* The dynamic structure factor for three large wavenumbers of the system.

main panel of Fig. 5.62, we see the dynamic structure factor for the three lowest

wave numbers q = 0.2, 0.284, 0.347$[\sigma_A^{-1}]$, and in the inset we see the dynamic structure factor for the three large wave numbers q = 1.003, 2.103, 3.502$[\sigma_A^{-1}]$. As the relation between the dynamic structure factor and the longitudinal current correlation function was shown in Eq. (3.56), we see a similar behavior in the evolution of the dynamic structure factor in Fig. 5.65 compared to those of discussed in Fig. 5.61. Similar to the longitudinal current correlation functions, for small q values, the dynamic structure factor shows a sharp peak at low frequencies. The peak starts to move to higher frequencies by increasing q and eventually leaving a flat background behind and disappearing at high frequencies. This corresponds to the range of frequencies and wavenumbers for which the lifetime of the sound modes becomes so small that the acoustic waves cannot live long. Therefore, it is often mentioned in the literature that q is not a good wave number anymore to describe the propagation of the overdamped waves. Here we should mention that, rather than the acoustic modes, there are also optical modes in the system which are out of the scope of this thesis.

In order to investigate the effect of deformation and the residual stresses on the vibrational modes the same calculation was performed for the deformed samples, and the result was compared to the initial undeformed states. The first set of plots presented here, show a comparison between the longitudinal (ch. Fig. 5.66) and transverse (ch. Fig. 5.67) current correlations functions in the undeformed and deformed states. In Fig. 5.66 we compare the longitudinal

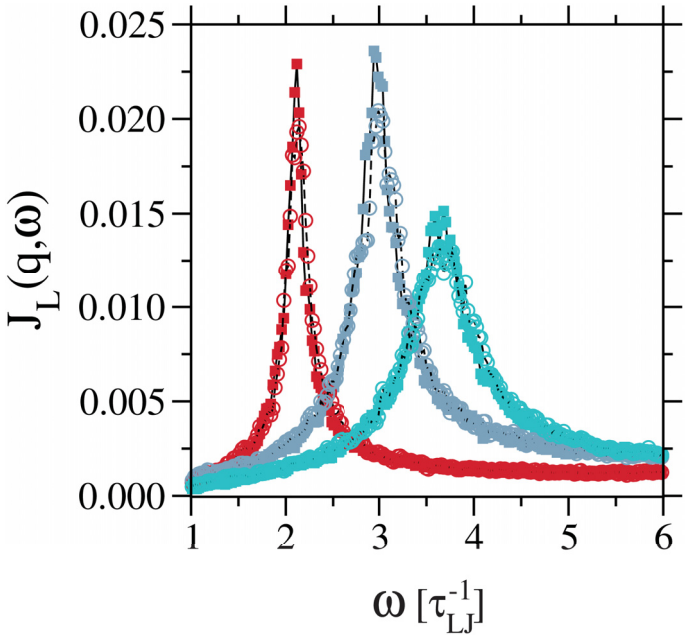

Figure 5.66: Comparison between the longitudinal current correlation functions in the undeformed states (close squares) and the deformed states (open circles), for the three lowest wave numbers q = 0.2, 0.284, 0.347$[\sigma_A^{-1}]$ (in red, gray and blue) of the system (in the same color respectively).

current correlation functions for the three lowest wave numbers of the system in

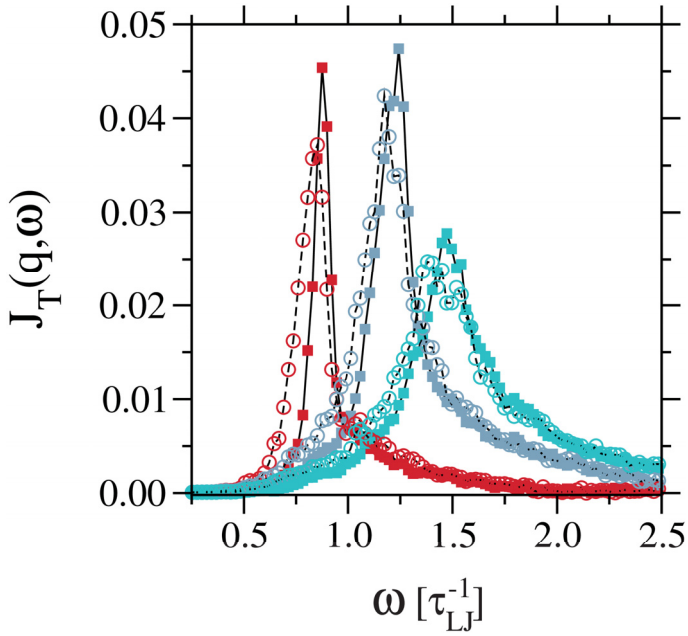

Figure 5.67: Comparison between the transverse current correlation functions in the undeformed states (close squares) and the deformed states (open circles), for the three lowest wave numbers $q = 0.2,\ 0.284,\ 0.347[\sigma_A^{-1}]$ (in red, gray and blue) of the system (in the same color respectively).

undeformed (closed symbols with lines) with the corresponding deformed values (open symbols with dashed lines) in the same color, respectively. From the figure we can see that, in the deformed state the peaks show a slight decrease and a very small shift towards the higher frequencies. In contrast, there is difference in the behavior of the transverse current correlation functions shown in Fig. 5.67. In Fig. 5.67 we compare the transverse current correlation functions for the three lowest wave numbers of the system in the undeformed states (closed symbols with lines) with the corresponding deformed values (open symbols with dashed lines) in the same color, respectively. Here, the peaks also show a decrease but they shift towards the lower frequencies followed by a slight broadening of the peaks. This is a fingerprint of appearance of softenings in the system after deformation. This is in good agreement with the results which we discussed earlier in Fig. 5.57 where we also see that after deformation the Boson peak shifts slightly to the lower frequencies by showing softenings in the system. Here, we can also perform the same calculation and obtain the dispersion relation and $\Gamma(q)$ in the same way that we did for the undeformed states. This is shown in Fig. 5.68 and Fig. 5.69.

In Fig. 5.68 and Fig. 5.69 the open symbols correspond to the deformed states and we can clearly see that, it is very difficult to observe the minor changes appearing in the deformed states at low wave numbers. While the effect of deformation appears to be more pronounced only at higher wave numbers, at low q regime still the dispersion relations show the linear response, for both

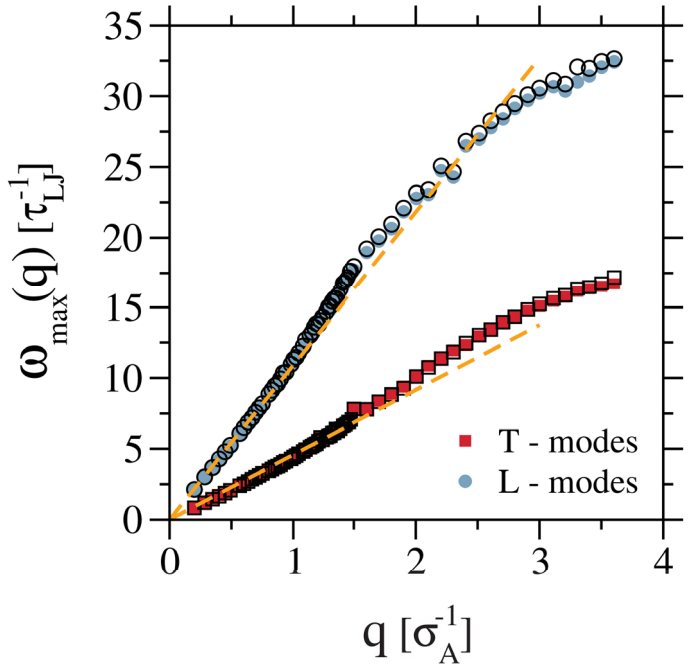

Figure 5.68: Comparison between the longitudinal branch (close gray circles) and the transverse branch (close red square) of the dispersion relation in the undeformed state with corresponding deformed states (same open black symbols respectively).

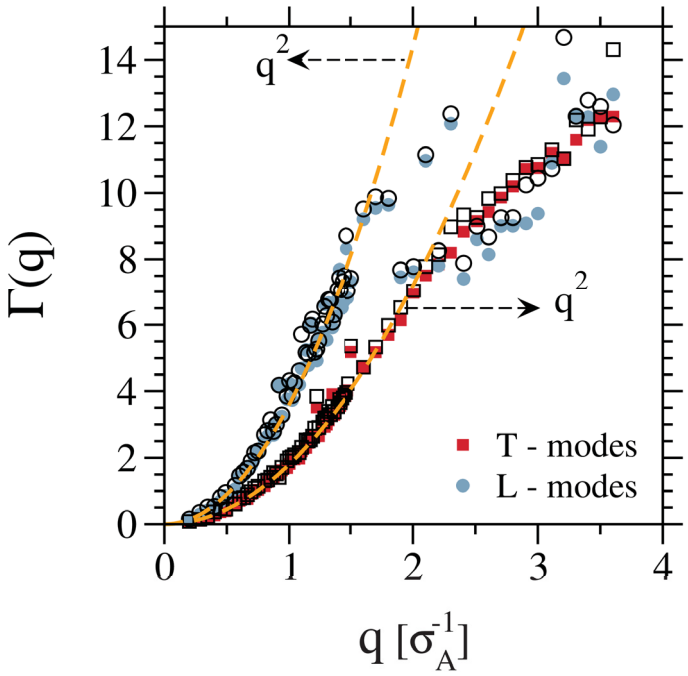

Figure 5.69: Comparison between the $\Gamma(q)$ for the longitudinal modes (close gray circles) and the transverse modes (close red square) in the undeformed state with corresponding deformed states (same open black symbols respectively).

longitudinal and transverse branches, and $\Gamma(q)$ shows a quadratic behavior. In order to investigate these minor changes in more details, we also looked at the corresponding longitudinal and transverse sound velocities for the deformed states and then compared these results with those of the initial undeformed states which we presented earlier. These results are shown in table (5.12). In table (5.12)

Comparison between sound velocities of undeformed and deformed states

Un-deformed			
ECT		**FDR**	
v_l	v_t	v_l	v_t
10.634	4.714	10.963	4.407
Deformed			
ECT		**FDR**	
v_l	v_t	v_l	v_t
10.74	4.543	11.119	4.364

Table 5.12: Comparison between the values of the longitudinal and transverse sound velocities, obtained from calculation of the elastic constant tensor and linear fits in the hydrodynamic regime of the dispersion relations, of the undeformed and deformed states.

we can see a nice agreement with the obtained values for the deformed states from the calculation of the elastic constant tensor and the fits on the dispersion relation. As we have discussed earlier, while the transverse sound velocities show a minor decrease after deformation (from both methods of calculation), the longitudinal sound velocities show a slight increase (from both methods of calculation). The reason behind this increase can be the fact that, by applying the shear deformation the particles are slightly compressed in the direction of shear. Therefore, the longitudinal sound velocities increase slightly, and as a result in perpendicular directions the transverse sound velocities show minor decreases with respect to their initial undeformed values.

Further, we make a comparison between the dynamic structure factor of the undeformed and deformed states. This is shown in Fig. 5.70. In Fig. 5.70(a), we make a comparison between the dynamic structure factor for the three lowest wave numbers of the system in the undeformed states (closed symbols) and the deformed states (open symbols) with the same color, respectively. In panel (b), the same comparison has been made for three large wavenumbers of the system (again, the closed symbols correspond to undeformed states, and the open symbols correspond to deformed states). What we observe from both panels is that the effect of deformation is only visible at low-frequency limits where the

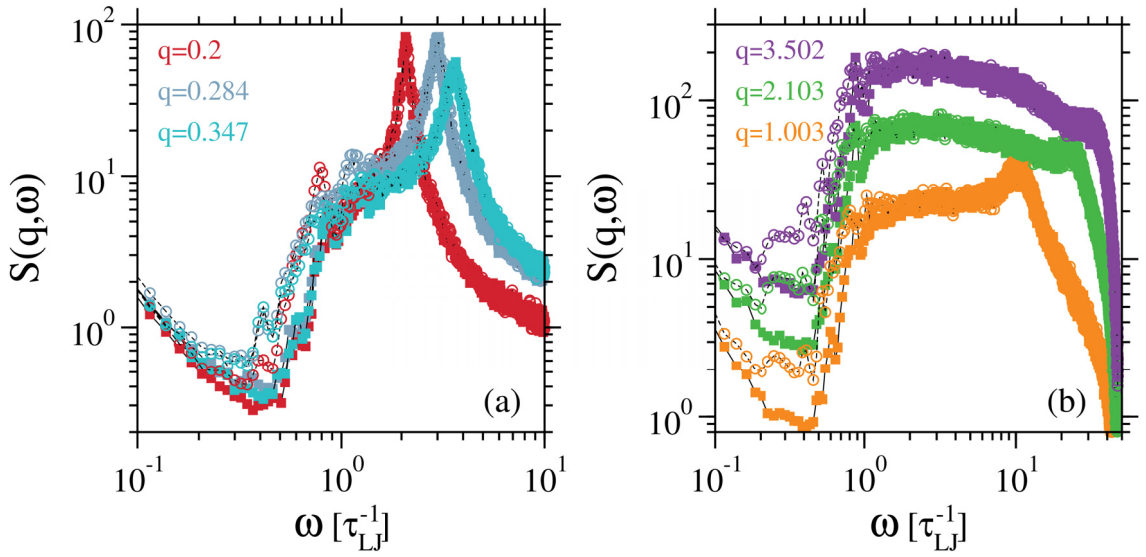

Figure 5.70: Comparison between the dynamic structure factor of the undeformed states (closed symbols) and the deformed symbols (open symbols), for the three lowest wave numbers of the system in (a) and three large wavenumbers in (b). The corresponding undeformed and deformed states are presented with the same color for each q value.

minimum valley of the deformed samples shows a slight increase which, might be due to some relaxation processes in the system after deformation. Rather than these minor effects, the large frequency limit of the dynamic structure factor shows similar behavior for both undeformed and deformed states. As it was discussed earlier, the peak shifts towards higher frequencies by increasing wave number and leaves a flat background behind. The peak disappears finally for large wavenumbers ($q = 3.502$ in panel (b) of Fig. 5.70) at high frequencies.

5.4.4 *Remarks*

Finite-size effects appear in the limit of $\omega \to 0$ of the DOS. These finite size effects are more pronounced in the low-frequency regime of the Boson peak where the transverse acoustic modes are detected for smallest wave numbers. Deformation results in a slight shift of the Boson peak towards lower frequencies. This shift is also visible in the Boson peak from the specific heat. In the limit of $q \to 0$, the total current correlation function has two distinct acoustic modes, which start to overlap by reaching the Ioffe-Regel limit. This is in the range of frequencies and wavenumbers where the lifetime of the waves becomes proportional to their width, and the modes become scattered (in-elastically) by the disorder in the system. The dynamic structure factor shows a sharp peak for small wavenumbers, which moves towards the more significant frequencies by increasing wave numbers and disappears at large wavenumbers, leaving a flat background behind. The transverse acoustic modes slightly shift towards lower frequencies after deformation, therefore, showing a slight decrease in the transverse sound velocities. On the other hand, the longitudinal acoustic modes show a very small

shift towards higher frequencies, and therefore, a minor increase in longitudinal sound velocities are observed. We cross-checked the latter results by calculating the elastic constant tensor and found similar results.

5.5 Micro-alloying in $Ni_{80}P_{20}$ metallic glass former

In this section, we will present the results[10] which we obtained for the micro-alloyed samples, by introducing a third species in the Kob-Andersen binary mixture (as it was discussed in section 2.2.5 and 4.3.4) and therefore, obtaining a ternary mixture. The first set of results, which we present are a comparison between the new ternary system and the original binary mixture.

As we discussed in section 2.2.5, we made the minimum change in the original model and therefore, we should be able to reproduce the original results from the binary mixture by switching back the value of the interaction parameter ϵ_{AC} between the A and C type particles. Therefore, hereafter it should be clear that, by assigning $\epsilon_{AC} = 1.0$ we obtain the results for the binary mixture, and by assigning $\epsilon_{AC} = 0.1$ we obtain the results for the ternary mixture. In Fig. 5.71 we compare the mean-squared displacement of the binary (open triangle-up) and the ternary mixture (closed circles), and for different particle types in the super-cooled liquid state at $T = 0.44$.

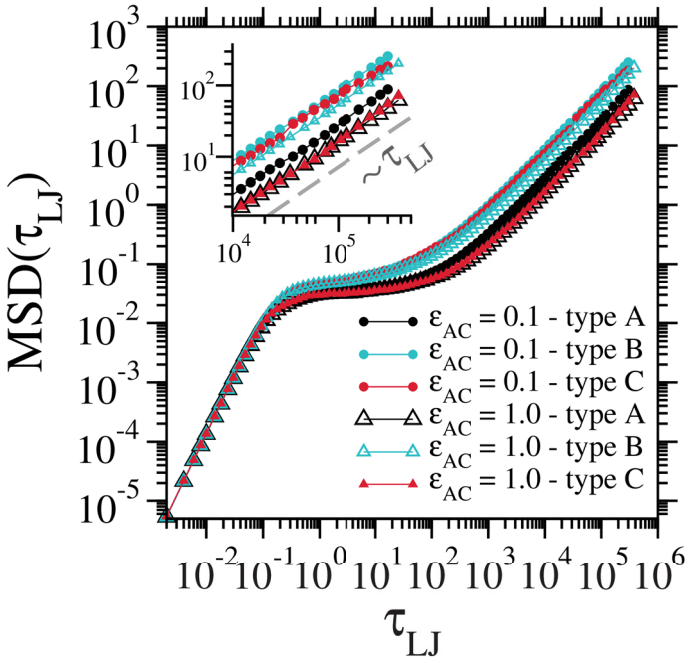

Figure 5.71: *main panel:* Comparison between the mean-squared displacement of different particle types in binary (triangle ups) and ternary (closed circles) system, in the super-cooled liquid state at $T = 0.44$ as a function of time. *inset:* The long tail of the MSDs in the diffusion regime. The gray-dashed line is a linear function for comparison.

[10]The results shown in (Fig. 5.71-5.74), are part of a project done by *Konstantin Lamp* who collaborated with us during his master studies in the group of Prof. Dr. Jürgen Horbach.

In the main panel of Fig. 5.71, we can see that, compared to the original model, the dynamics of the system in the new ternary model has slightly changed. The A type particles (closed black circles) and the B type particles (closed blue circles) in the new ternary system show slightly higher mobilities compared to the binary mixture. Another interesting result from the plot is that the C type particles seem to follow the B type particles in the new ternary system. From the plot, we can see that, by switching back the interaction parameter between the A and C type particles, as expected, the MSD of the A and C type particles (open black triangle-up and closed red triangle-up respectively) sit on top of each other. This is more visible in the inset of Fig. 5.71 where we show the MSD in the diffusion regime. The dashed gray line in the inset is just a linear function with a slope one. The slight increase in system mobilities is also visible in the inset of Fig. 5.71 for different particle types. The change in system dynamics is also visible if we compare the diffusion coefficients of the two systems. This is shown in Fig. 5.72.

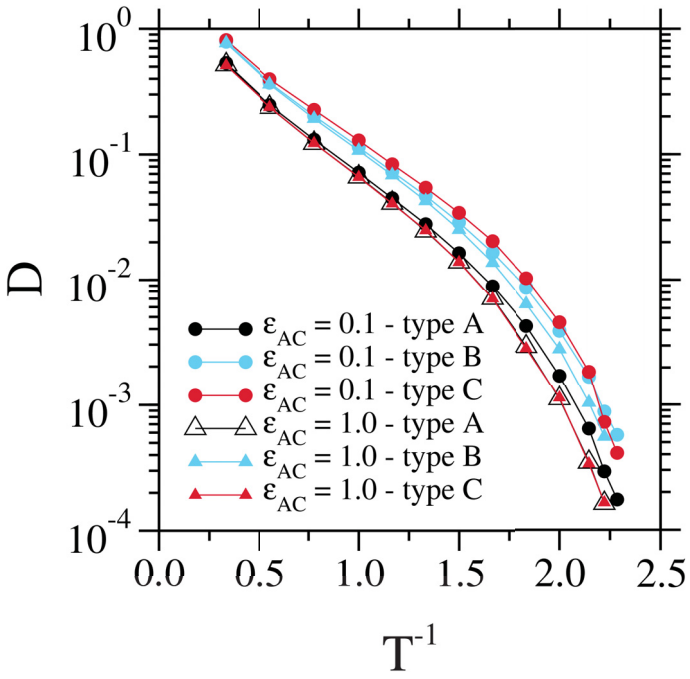

Figure 5.72: Comparison between the diffusion coefficient of different particle types in binary (triangle ups) and ternary (closed circles) system, as a function of inverse temperature.

In Fig. 5.72, we present the diffusion coefficient for different particle types in the binary and ternary system, as a function of inverse temperature. From the figure we can see that, similar to the previous results, the dynamics of the system has slightly changed in the new ternary system for all particle types (closed circles) compared to the original model, especially at lower temperatures. Also similar to the results of the MSD, the C type particles (closed red circles) seem to follow the B type particles (closed blue circles) in the new ternary system, and by switching back the interaction parameter to $\epsilon_{AC} = 1.0$ the diffusion coefficient of

the A and C type particles (open black triangle-up and closed red triangle-up, respectively) sit on top of each other, and we obtain a binary mixture.

In the next set of plots, we compare the correlations between different particle types in terms of radial distribution function and partial static structure factor, Fig. 5.73 and Fig. 5.74, respectively. The radial distribution function was already discussed in section 2.1.1 and partial static structure factor we discuss briefly here.

Considering a many component system consisting of n different species, the total number of particles N in the system is given by $N = \sum_{\alpha=1}^{n} N_\alpha$, where N_α denotes the number of particles of type α. Therefore, the local number density of the system in the reciprocal space, for a particle of type α is given by [Hansen and McDonald (2013)]:

$$\rho_\alpha(\vec{q}) = \sum_{k=1}^{N_\alpha} exp(i\vec{q}.\vec{r}_k) \ , \ \alpha = \{A, B, C\} \ , \tag{5.4}$$

where $\vec{q}$ is the wave vector and $\vec{r}_k$ is the position of kth particle of type α. Therefore, the partial static structure factor can be written as

$$S_{\alpha\beta}(q) = \frac{1}{N} \left\langle \rho_\alpha(\vec{q}) \, \rho_\beta(-\vec{q}) \right\rangle \ , \ \alpha, \beta = \{A, B, C\} \ . \tag{5.5}$$

The partial static structure factor only depends on the magnitude of the wave vector $\vec{q}$. The $S_{\alpha\beta}(q)$ functions are symmetric ($S_{\alpha\beta}(q) = S_{\beta\alpha}(q)$) and therefore there are $n(n+1)/2$ independent partial static structure factors. In the limit of $q \to \infty$ the partial structure factor saturates at the mean particle concentration $x_\alpha = N_\alpha/N$ for $\alpha = \beta$ and for $\alpha \neq \beta$ reaches zero.

In Fig. 5.73(a-f) we compare the radial distribution function for different particle types between the binary and ternary system. In Fig. 5.73(a and b) we can see that, $g_{AA}(r)$ and $g_{BB}(r)$ are not effected by introducing the new species in the system, and therefore, the AA and BB correlations sit on top of each other for both binary and ternary systems (open blue and closed black circles, respectively). This is also true for AB correlations in Fig. 5.73(d) where, the results for binary and ternary system sit very close to each other. This is in good agreement with the correlations in static structure factor shown in Fig. 5.73(a-b) and (d). Where we can see that, the preferred length scales for the AA, BB and AB correlations are not effected by micro-alloying, and we found very similar results both for the binary and ternary systems. In the main panel of Fig. 5.73(c), we look at the correlations between the C type particles in ternary system. From the figure we can see that $g_{CC}(r)$ shows a sharp peak followed by a sharp decay. Interestingly, the function does not show many oscillations while decaying compared to the other correlation functions. This is even more visible if we look at the long tail of $g_{CC}(r)$ in the inset of Fig. 5.73(c). The fast decay of $g_{CC}(r)$ is due to

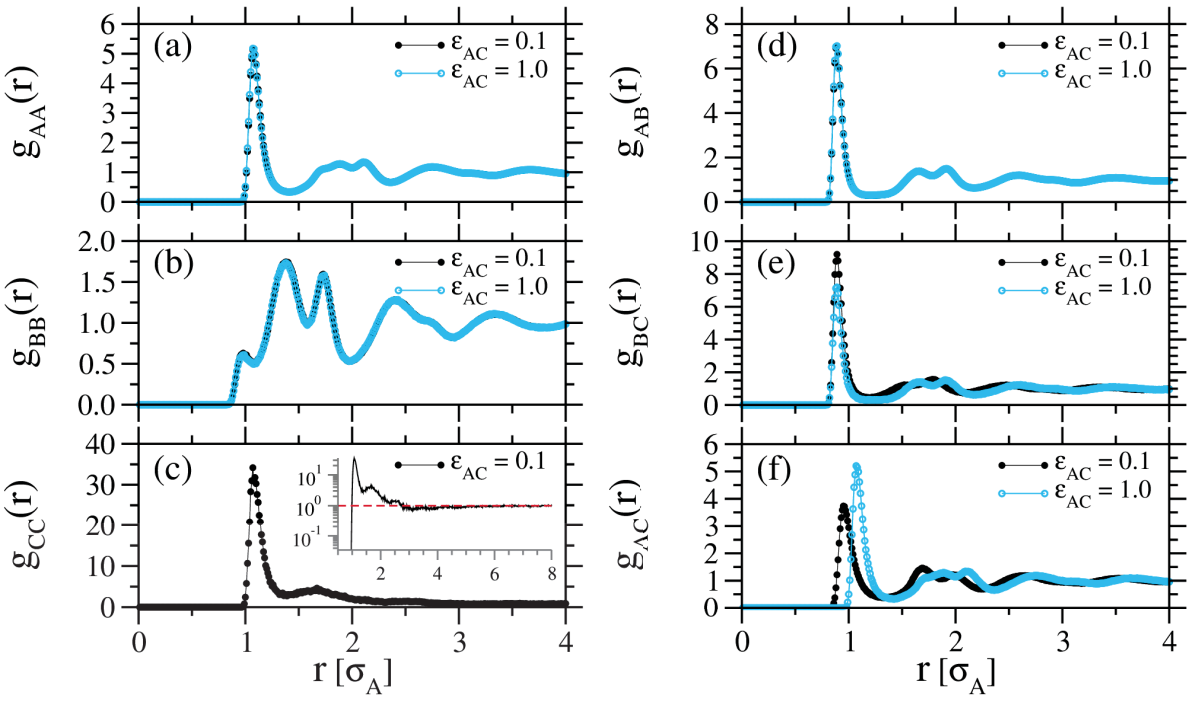

Figure 5.73: Comparison between the radial distribution function of the binary (open blue circles) and ternary (closed black circles) system in the glass state at T = 0.2. The correlations between different pairs of particles types, are shown in panels (a) to (f).

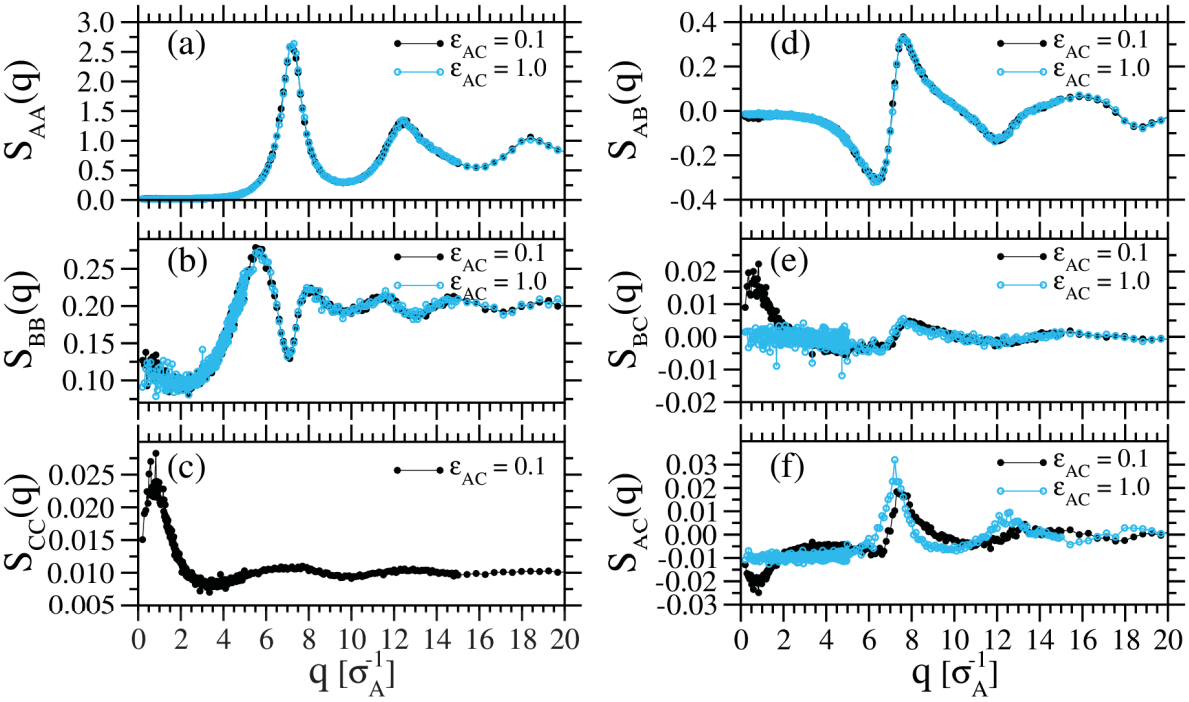

Figure 5.74: Comparison between the static structure factor of the binary (open blue circles) and ternary (closed black circles) system in the glass state at T = 0.2. The correlations between different pairs of particles types, are shown in panels (a) to (f).

the low concentration of C type particles which is also visible in Fig. 5.74(c) where, we show $S_{CC}(q)$. In Fig. 5.74(c) one can see the preferred length scales ($2\pi/q$) at 1st maximum in $S_{CC}(q)$, which are occupied by the C type particles. The distribution of different particle types is illustrated in a snapshot of the simulation box in Fig. 5.75. From Fig. 5.75 we can clearly see that there is no

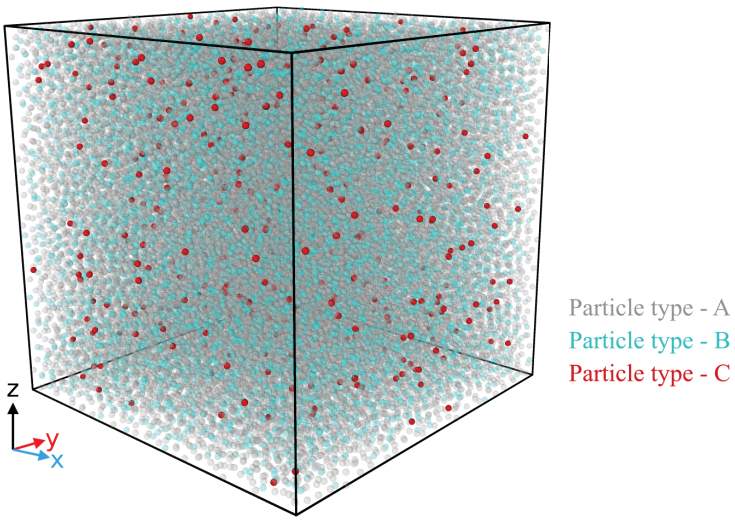

Figure 5.75: A snap shot of different particle types distribution in the simulation box for the ternary system. Different particle types are shown in different color.

clustering between the C type particles and they are homogeneously distributed in the system. The rather far distances between C type particles, corresponds to their preferred length scales around $q = 0.760953$, shown in Fig. 5.74(c). These results are nicely in agreement with Fig. 5.73(e) and Fig. 5.74(e) where, we present $g_{BC}(r)$ and$S_{BC}(q)$, respectively. As it was discussed earlier in this section, the C type particles tend to follow the B type particles. Therefore, in Fig. 5.73(e), we can see that the first peak (corresponding to the nearest neighbors) in $g_{BC}(r)$ shows a slight increase in the ternary system compared to binary mixture. These results are also reflected in the $S_{BC}(q)$ in Fig. 5.74(e) where, we can clearly see the preferred length scales around $q = 0.760953$ for BC interactions. At large q values the results for both systems sit on top of each. At low q values, $S_{BC}(q)$ of the binary mixture does not have any information because of the fact that basically, we are looking at the correlations between a very small fraction of A type particles and B type particles. Finally in Fig. 5.73(f) and Fig. 5.74(f) we show the $g_{AC}(r)$ and $S_{AC}(q)$, respectively. As a result of weaker interactions between A and C type particles in the ternary system, in Fig. 5.73(f), the first peak in $g_{AC}(r)$ has slightly shifted towards lower r values. This means that the particles can slightly get closer to each other. This is consistent with the results shown in Fig. 5.74(f) for $S_{AC}(q)$ where the main peak has slightly shifted towards larger q values. Another interesting result which is visible in Fig. 5.74(f) is the occurrence of anti-correlations (negative peak), exactly at the length scales shown

in Fig. 5.74(c and e) for CC and BC correlations.

In order to further investigate the structural correlations between the new ternary and binary mixture, following the calculations which have been done in reference [Pfleiderer, Horbach, and Binder (2006)] for amorphous aluminum silicates, we calculated the concentration-concentration structure factor from the partial structure factors of different particle types and for both systems. These results are shown in Fig. 5.76(a-c). The concentration-concentration structure factors

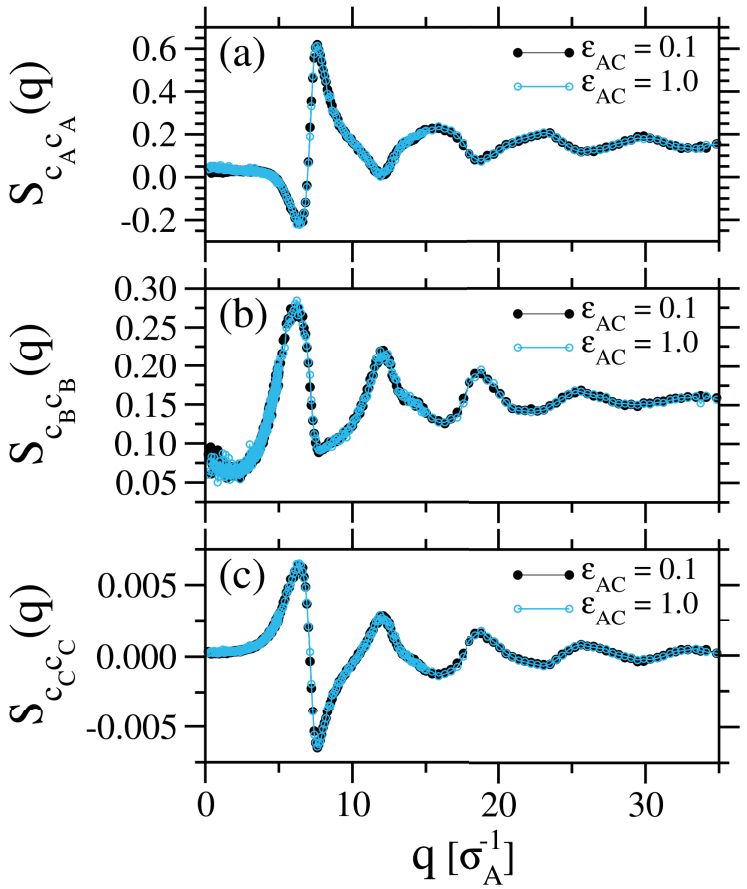

Figure 5.76: Comparison between concentration-concentration partial structure factor for particle types A, B and C in panel a, b an c respectively, for both binary (open blue circles) and ternary system (closed black circles).

are linear combinations of partial static structure factors defined as [Pfleiderer, Horbach, and Binder (2006)]:

$$S_{c_A c_A}(q) = (x_B + x_C)^2 S_{AA}(q) - 2x_A (x_B + x_C)[S_{AB}(q) + S_{AC}(q)] + x_A^2 [S_{BB}(q) + 2S_{BC}(q) + S_{CC}(q)] , \quad (5.6)$$

$$S_{c_B c_B}(q) = (x_A + x_C)^2 S_{BB}(q) - 2x_B (x_A + x_C)[S_{AB}(q) + S_{BC}(q)] + x_B^2 [S_{AA}(q) + 2S_{AC}(q) + S_{CC}(q)] , \quad (5.7)$$

$$S_{c_C c_C}(q) = (x_A + x_B)^2 S_{CC}(q) - 2x_C (x_A + x_B)[S_{AC}(q) + S_{BC}(q)] + x_C^2 [S_{AA}(q) + 2S_{AB}(q) + S_{BB}(q)] , \quad (5.8)$$

with c_α a concentration fluctuation for particle type α, which is given by:

$$c_\alpha(\vec{q}) = \rho_\alpha(\vec{q}) - x_\alpha \sum_{\beta=1}^{n} \rho_\beta(\vec{q}) \ , \ \alpha = \{A,\ B,\ C\} \ . \tag{5.9}$$

And therefore, the partial structure factors can be expressed in terms of these concentration fluctuation as:

$$S_{c_\alpha c_\beta}(q) = \frac{1}{N} \left\langle c_\alpha(\vec{q})\, c_\beta(-\vec{q}) \right\rangle \ , \ \alpha, \beta = \{A,\ B,\ C\} \ . \tag{5.10}$$

In Fig. 5.76(a-c) we present the results for concentration-concentration partial structure factor of the binary (open blue circles) and ternary system (closed black circles). The first visible result from these figures is that, by introducing the new species in the ternary system the overall behavior of concentration-concentration structure factors have not changed and both systems show similar results. In good agreement with our previous results, the concentration of C type particles ($S_{c_C c_C}(q)$ shown in Fig. 5.76(c)) shows a peak in the range of length scales ($q \approx 6.09629$) where, the concentration of B type particles also show a maximum peak. This means, there is a big concentration of C type particles around B type particles. In contrast, the C type particle tend to segregate from the A type particles. This is clearly visible by making a comparison between the anti-correlations shown in Fig. 5.76(a) for $S_{c_A c_A}(q)$ and in Fig. 5.76(c) for $S_{c_C c_C}(q)$. While around length scales $q \approx 7.67264$ there is large concentration of A type particles, the concentration of C type particles shows a negative peak (anti-correlation) within this length scales. In the limit of small q, all the concentration-concentration partial structure factors saturate finite value which indicates the microscopic concentration fluctuations.

In order to investigate the effect of micro-alloying on the vibrational modes of the system we also compared the density of the vibrational modes and the Boson peak between the binary and ternary mixture. These results are shown in Fig. 5.77(a-b).

In panel (a) of Fig. 5.77, partial $g(\omega)$ is compared between the binary and ternary system for different particle types. From the figure we can see that the density of states for A (black curve for ternary and gray curve for the binary system) and B (orange curve for ternary and green curve for the binary system) type particles stay very close to each other between the binary and ternary system. The $g(\omega)$ for C type particles (red curve) shows a higher peak and skewed to lower frequency. This is in good agreement with the results, which we presented earlier in this section, where we showed that the new C type particles show faster dynamics compared to other particle types. Therefore, as we can see here, they are thermally easier to excite. This is also in good agreement with the results which we present in panel (b) of Fig. 5.77 where we compare the

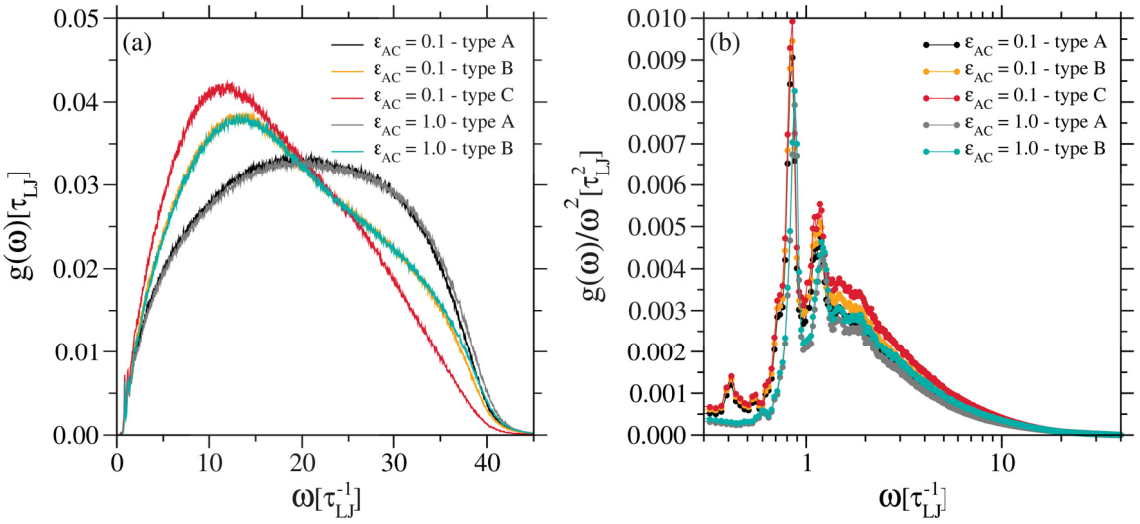

Figure 5.77: *panel (a):* comparison between the partial density of states of different particle types of the binary and ternary system. *panel (b):* comparison between the Boson peak for different species of the binary and ternary mixture.

$g(\omega)/\omega^2$ between different particle species in the binary and ternary system. As we can see in the figure, the main effect of micro-alloying on the Bososn peak is a slight shift towards lower frequencies followed by a slight increase in the peak, for all different particle types in the new ternary system, compared to the binary mixture. This was expected, as we showed earlier in this section that, as a result of micro-alloying, the dynamics of the system slightly become faster. Therefore, as a result of these minor changes, the system shows a slight softening in the Boson peak regime. These small softenings are slightly more pronounced for particle types with higher mobilities and therefore, following the results shown in Fig. 5.71, the Boson peak height has its maximum for C type particles followed by B and A particles (the red, orange, and black curves respectively). To test these softenings in the system, we imposed external load to the new ternary system by applying shear deformation, with a constant shear rate of $\dot{\gamma} = 10^{-4}$. We compared the obtained stress-strain curve with the original binary mixture. These results are shown in Fig. 5.78. In the main panel of Fig. 5.78, we can see that the overshoot maximum in the stress-strain curve of the new ternary system (red curve) shows a slight decrease. Also, in the elastic regime, if we compare the linear fits to the data (dashed lines in the inset), we can see that the slope of the linear fit function has slightly decreased for the ternary system compared to the binary mixture, meaning, the new ternary system has a lower shear modulus slightly compared to the original binary system. We can conclude here that microalloying induced some softenings in the new ternary system. These softenings are also visible if we compare the specific heat between the binary and ternary systems. This is shown in Fig. 5.79. In Fig. 5.79 the specific heat, for both undeformed and deformed states, are compared between the binary and ternary system (black curve with closed black circles for an undeformed

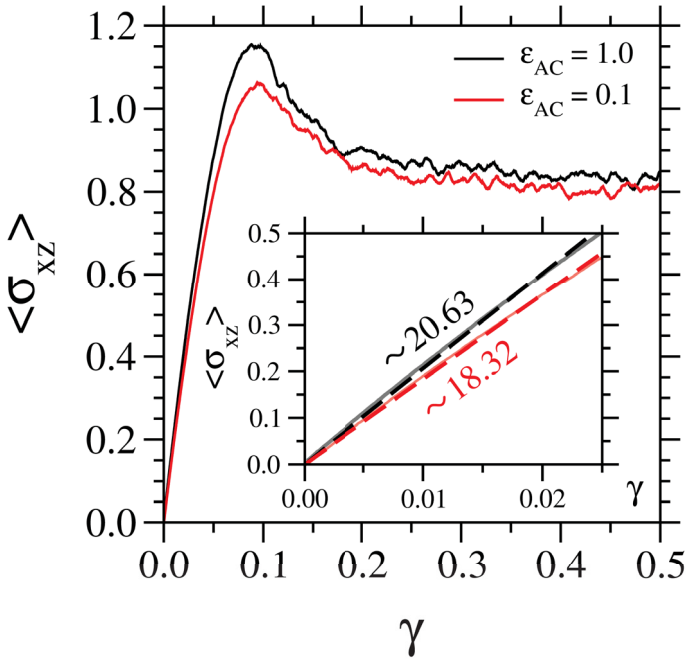

Figure 5.78: *main panel:* The stress-strain curve for the binary (in black) and the ternary (in red) system, being imposed to a constant shear rate $\dot{\gamma} = 10^{-4}$. inset: Linear fit in the early elastic regime of the stress-strain curve for both the binary and ternary system with black and red dashed lines, respectively.

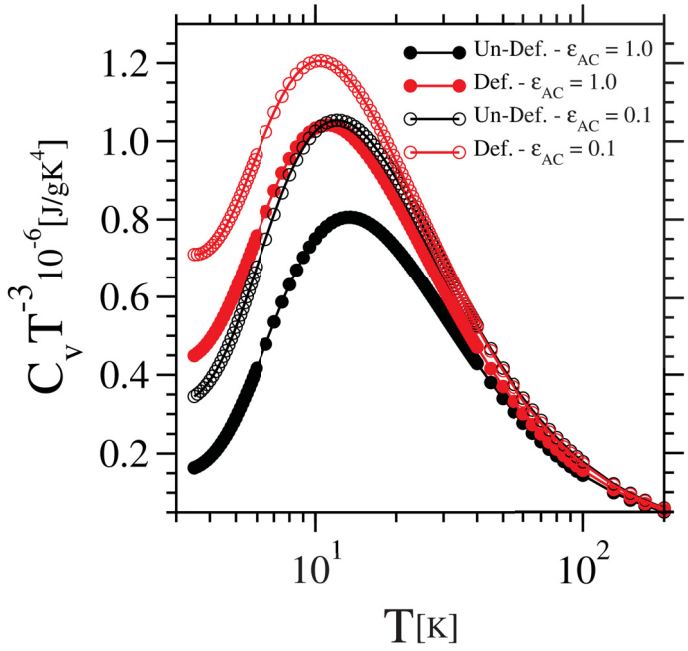

Figure 5.79: Comparison between the Boson peak in the specific heat for both undeformed (black curves) and deformed (red curves) states of the binary (curves with closed symbols) and ternary mixture (curves with open symbols).

binary system, black curve with open black circles for an undeformed ternary system, red curve with closed red circles for deformed binary system and red curve with open red circles for a deformed ternary system). Minor softenings are visible already in the undeformed state where the Boson peak amplitude for the ternary system shows a small increase and shifts slightly towards lower temperatures. After deformation, the same behavior, as we discussed earlier in the previous sections, is visible for the deformed states with an increase in Boson peak and shift towards lower temperatures compared to the undeformed state. What is interesting here is the behavior of the Boson peak of the ternary system in the deformed state in the limit of $T \to 0$. The curve appears to be saturating at a finite value. This behavior can be compared to the experimental observations reported in [Hubek, Seleznev, et al. (2018)], where they also reported that for a deformed micro-alloyed Pd base metallic glass the Boson peak appears to be saturating at a finite value in the limit of low temperatures.

5.5.1 Remarks

A new ternary model is developed by introducing a third species (type C) in the original Kob-Andersen binary mixture [Kob and Andersen (1994)]. The first evident result of the minor micro-alloying is the change in the dynamics of the system such that, in the new ternary model, the MSD of the A and B type particles shows slightly higher mobilities. This is also reflected in the low-frequency range of the Boson peak, where the peaks show a minor increase and shift towards the lower frequencies. These effects are more pronounced in the specific heat where the Boson peak shows a pronounced increase and shift towards lower temperatures. These changes are an indication of softenings in the system as a result of micro-alloying. These softenings are also visible in the stress-strain curve of the new ternary system compared to the original binary mixture (being subjected to a shear deformation with a constant shear rate $\dot{\gamma}$), showing a slight decrease in the overshoot maximum.

6 Conclusions & Outlook

As it was discussed earlier in this work, BMGs have many promising mechanical properties like high strength and corrosion resistance. But, the main drawback of their mechanical properties is their limited ductility. Therefore, studying the poorly understood plasticity, including the underlying features of yielding transition in BMGs, is a hot topic of research communities and also is of great technological interest. In this regard, SCLs play a key role in understanding elastic to plastic flow in metallic glasses. The response of highly viscous SCLs, subjected to a shear deformation with a constant shear rate, shows a crossover from a Newtonian to a non-Newtonian behavior. Therefore the SCLs, as a visco-elastic medium at equilibrium, on the one hand, have the features of well studied Newtonian liquids in literature, and on the other hand, show consistent non-Newtonian responses similar to those of glasses.

In this work, using MD simulations, we modeled a $Ni_{80}P_{20}$ glass-forming system. We showed that the response of samples to shear deformation with a constant shear rate ($\dot{\gamma}$) in the SCL state, becomes non-Newtonian when $\dot{\gamma} > \dot{\gamma}_c$, with $\dot{\gamma}_c$ being a critical shear rate. In the latter non-Newtonian regime, the steady-state shear stress σ_{ss} is no longer proportional to the shear rate $\dot{\gamma}$, and the flow curve of SCLs can be fitted with a Herschel–Bulkley type of function, similar to the response of glasses but, with weaker power-law behavior. However, one cannot extrapolate a yield stress from the latter power-law behavior for SCLs, as in the case of glasses. The onset of plastic flow is marked by the occurrence of an overshoot in the stress-strain curve. The stress-strain curve in the non-Newtonian regime shows three distinguishable regimes: namely an elastic, a transient, and a steady-state regime. A feature of yielding transition is the occurrence of in-homogeneous flow patterns in the transient regime.

In SCLs, short-lived in-homogeneous flow patterns appear in the system, perpendicular to the direction of flow, when $\dot{\gamma} > \dot{\gamma}_c$. In glasses, these homogeneities

are long-lived and form different types of shear bands: namely, horizontal, parallel to the direction of flow, vertical, perpendicular to the direction of flow, and mixed bands. The type of the shear band is not predetermined by the structure of the initial undeformed sample and appears to be a stochastic process. However, the formation of a horizontal shear band is marked by the occurrence of an overshoot in the potential energy of the system, which is not the case for samples with vertical shear bands. We showed that in both SCLs and glasses, the deformed samples eventually transform into a homogeneously flowing state that can be characterized as an anisotropic non-equilibrium fluid. For the sheared glass, the pathways with which the stationary fluid state is reached can completely differ from sample to sample. While in the case of samples with horizontal shear bands, one observes a kind of nucleation of the flowing fluid phase, which grows slowly towards the homogeneously flowing stationary state, in case of samples with vertical shear bands the steady-state is reached much earlier.

A characteristic feature of metallic glasses are the residual stresses. When the external load is canceled, the stresses do not fully relax to zero in the glass samples and remain at a finite value. Therefore, after deformation, one obtains deformed glass samples, which are in a new glass state with residual stress, unlike the initial undeformed state where the stress is zero on average. A crucial issue here is that, how do the residual stresses change the plasticity of the material after deformation.

Hence, as one of the main focuses of this study, we characterized the effects of the residual stresses on elastic-to-plastic responses of the glass samples. Keeping the quiescent undeformed states as a reference, we made a comparison between the results from the deformed and undeformed states. In the elastic regime, the elastic moduli of the deformed glass samples show small changes with respect to their initial undeformed values. They tend to evolve towards their initial undeformed values as the residual stresses decay in the system. Although the residual stresses induce small anisotropies in the elastic moduli of the deformed samples, these effects also appear to fade away with further stress relaxations. Therefore, the elastic responses of the system show very small sensitivity to deformation, and the residual stresses have minor effects on the elastic moduli. However, beyond the elastic limit, the yield point identified with the maximum in the stress-strain overshoot shows a pronounced decrease, which indicates small softenings in the deformed samples.

The latter small softenings are also reflected in the low-frequency spectrum of the density of states for the deformed samples, where the Boson peak shows a small shift towards lower frequencies. The same behavior was shown for the Boson peak of the deformed samples in the specific heat. In the latter case, the Boson peak shows a small increase and shift towards lower temperatures, in comparison to its quiescent state. We also showed that these small softenings

appear as a slight shift of transverse current correlation functions towards lower frequencies; therefore, a small decrease in the transverse sound velocity.

The ductility of metallic glasses can be adjusted by introducing micro-alloying. Experimental and theoretical works [Dasgupta, Mishra, Procaccia, and Samwer (2013), Hubek, Seleznev, et al. (2018), Peng and Zhang (2011), and Qiao, Yao, Pelletier, and Keer (2016)] showed that adding a small amount ($\approx 1\%$) of a new species in the alloying composition of the material can change the ductility of the material significantly.

Thus, in this work, we proposed a model for micro-alloying in the $Ni_{80}P_{20}$ metallic glass former and showed that by adding 1% of a new species in the Kob-Andersen binary mixture, therefore, turning the model into a ternary mixture, the material appears to be more ductile. We showed that the latter softenings are a direct result of dynamical enhancements, which are appearing in the new ternary system, as the particles tend to have higher mobilities. The latter softenings show a small decrease in the yield point of the stress-strain curve, marked by the maximum of the stress-strain overshoot. However, the transient responses of metallic glasses under mechanical load are highly dependent on the degree of annealing, and the history with which the samples are prepared. The better-annealed samples show a higher overshoot maximum, followed by a sharper stress decay from the maximum towards the steady-state.

Outlook. Following our previous discussion and the results shown in this work (cf. (5.4.2)) and also recent work by [Bünz, Brink, et al. (2014)], the degree of annealing has significant effects on plasticity of metallic glasses. Although in recent works by [Ozawa, Berthier, et al. (2018) and Ozawa, Berthier, Biroli, and Tarjus (2019)], using swap Monte Carlo algorithm [Grigera and Parisi (2001)], they were able to achieve large degrees of annealing at low temperatures; still, new algorithms need to be developed (especially for the binary Lennard-Jones mixture) such that, at a reasonable computation cost, one can study mechanical properties of well-annealed samples.

The new micro-alloyed model proposed in this work seems to have a lot of potential for further investigation. Similar to the results reported by [Nollmann, Binkowski, et al. (2016)], we also showed that micro-alloying results in a decrease of the overshoot maximum in the transient regime such that the material yields at lower stress. Also, we observed that the Boson peak curve in the specific heat (after deformation) seems to saturate at a finite value in the limit of low temperatures. This is a similar observation reported by [Hubek, Seleznev, et al. (2018)] where, adding 1% of Co in a $Pd_{40}Ni_{40}P_{20}$ metallic glass former, they showed that the Boson peak appears to saturate at a finite value at low temperatures. But, the effect of different alloying compositions on the mechanical properties of the system is a challenging problem. Developing new micro-alloyed models in computer simulations, with different alloying compositions, can make predictions which might give a more effortless directional guideline in experiments.

Bibliography

Aklonis, J. J., & Kovacs, A. J. (1979). A new look at the glass transition. In *Contemporary topics in polymer science* (pp. 267–295). Springer. (Cit. on p. 12).

Alder, B. J., & Wainwright, T. E. (1959). Studies in molecular dynamics. I. General method. *The Journal of Chemical Physics*, *31*(2), 459–466. (Cit. on pp. 4, 50).

Allen, M. P., & Tildesley, D. J. (2017). *Computer simulation of liquids*. Oxford University Press. (Cit. on pp. 2, 33, 50, 51, 54).

Andersen, H. C. (1983). Rattle: A "velocity" version of the shake algorithm for molecular dynamics calculations. *Journal of Computational Physics*, *52*(1), 24–34. (Cit. on p. 51).

Anderson, P. W. (1995). Through the glass lightly. *Science*, *267*(5204), 1618–1618. (Cit. on p. 2).

Angell, C. A., Poole, P. H., & Shao, J. (1994). Glass-forming liquids, anomalous liquids, and polyamorphism in liquids and biopolymers. *Il Nuovo Cimento D*, *16*(8), 993–1025. (Cit. on p. 10).

Angell, C. A. (1988). Perspective on the glass transition. *Journal of Physics and Chemistry of Solids*, *49*(8), 863–871. (Cit. on p. 11).

Archer, R. R., Crandall, S. H., Dahl, N. C., Lardner, T. J., & Sivakumar, M. S. (2012). *An introduction to mechanics of solids*. Tata McGraw-Hill Education. (Cit. on p. 33).

Ashby, M. F., & Greer, A. L. (2006). Metallic glasses as structural materials. *Scripta Materialia*, *54*(3), 321–326. (Cit. on pp. 3, 28).

Ballauff, M., Brader, J. M., Egelhaaf, S. U., Fuchs, M., Horbach, J., Koumakis, N., Krüger, M., Laurati, M., Mutch, K. J., Petekidis, G. et al. (2013). Residual stresses in glasses. *Physical Review Letters*, *110*(21), 215701. (Cit. on pp. 5, 25, 60).

Balucani, U., & Zoppi, M. (1995). *Dynamics of the liquid state*. Clarendon Press. (Cit. on p. 37).

Barrat, J. L., Roux, J. N., Hansen, J. P., & Klein, M. L. (1988). Elastic response of a simple amorphous binary alloy near the glass transition. *EPL (Europhysics Letters)*, *7*(8), 707–712. (Cit. on pp. 30, 33).

Barrat, J. L., & Lemaître, A. (2011). Heterogeneities in amorphous systems under shear. In L. Berthier, G. Biroli, J. P. Bouchaud, L. Cipelletti, & W. van Saarloos (Eds.), *Dynamical heterogeneities in glasses, colloids, and granular media* (Vol. 150, pp. 264–296). Oxford University Press. (Cit. on p. 60).

Barron, T., & Klein, M. L. (1965). Second-order elastic constants of a solid under stress. *Proceedings of the Physical Society*, *85*(3), 523. (Cit. on p. 33).

Batchelor, C. K., & Batchelor, G. K. (2000). *An introduction to fluid dynamics*. Cambridge University Press. (Cit. on p. 19).

Batsanov, S. S. (2001). Van der Waals radii of elements. *Inorganic Materials*, *37*(9), 871–885. (Cit. on p. 118).

Benassi, P., Krisch, M., Masciovecchio, C., Mazzacurati, V., Monaco, G., Ruocco, G., Sette, F., & Verbeni, R. (1996). Evidence of high frequency propagating modes in vitreous silica. *Physical Review Letters*, *77*(18), 3835–3838. (Cit. on p. 44).

Bengtzelius, U., Götze, W., & Sjölander, A. (1984). Dynamics of supercooled liquids and the glass transition. *Journal of Physics C: Solid State Physics*, *17*(33), 5915–5934. (Cit. on pp. 2, 15).

Binder, K., & Ciccotti, G. (1996). *Monte carlo and molecular dynamics of condensed matter systems: Euroconference on computer simulation in condensed matter physics and chemistry, Como, 3-28 july 1995*. Società Italiana di Fisica. (Cit. on p. 50).

Binder, K. (1987). Theory of first-order phase transitions. *Reports on Progress in Physics*, *50*(7), 783–859. (Cit. on p. 8).

Binder, K., Horbach, J., Kob, W., Paul, W., & Varnik, F. (2004). Molecular dynamics simulations. *Journal of Physics: Condensed Matter*, *16*(5), S429–S453. (Cit. on p. 50).

Binder, K., & Kob, W. (2011). *Glassy materials and disordered solids: An introduction to their statistical mechanics* (2nd ed.). World Scientific. (Cit. on pp. 1, 10, 11, 14, 15, 17–19).

Binkowski, I., Shrivastav, G. P., Horbach, J., Divinski, S. V., & Wilde, G. (2016). Shear band relaxation in a deformed bulk metallic glass. *Acta Materialia*, *109*, 330–340. (Cit. on pp. 23, 27).

Boltzmann, L. (1871). *Einige allgemeine Sätze über Wärmegleichgewicht*. k.k. Hof- und Staatsdruckerei. (Cit. on p. 53).

Boon, J. P., & Yip, S. (1991). *Molecular Hydrodynamics*. Dover Publications. (Cit. on pp. 4, 37, 46, 47).

Born, M., & Huang, K. (1954). *Dynamical theory of crystal lattices*. Clarendon Press. (Cit. on pp. 30, 31, 41, 54).

Buchenau, U., Galperin, Y. M., Gurevich, V., Parshin, D., Ramos, M., & Schober, H. (1992). Interaction of soft modes and sound waves in glasses. *Physical Review B*, *46*(5), 2798–2808. (Cit. on p. 44).

Buchenau, U., Prager, M., Nücker, N., Dianoux, A. J., Ahmad, N., & Phillips, W. A. (1986). Low-frequency modes in vitreous silica. *Physical Review B*, *34*(8), 5665–5673. (Cit. on p. 44).

Bünz, J., Brink, T., Tsuchiya, K., Meng, F., Wilde, G., & Albe, K. (2014). Low temperature heat capacity of a severely deformed metallic glass. *Physical Review Letters*, *112*(13), 135501. (Cit. on pp. 126, 152).

Car, R., & Parrinello, M. (1985). Unified approach for molecular dynamics and density-functional theory. *Physical Review Letters*, *55*(22), 2471–2474. (Cit. on p. 50).

Chaikin, P. M., Lubensky, T. C., & Witten, T. A. (1995). *Principles of condensed matter physics*. Cambridge University Press. (Cit. on pp. 30, 32).

Chaudhuri, P., & Horbach, J. (2016). Structural inhomogeneities in glasses via cavitation. *Physical Review B*, *94*(9), 094203. (Cit. on pp. 61, 62).

Courtens, E., Foret, M., Hehlen, B., Rufflé, B., & Vacher, R. (2003). The crossover from propagating to strongly scattered acoustic modes of glasses observed in densified silica. *Journal of Physics: Condensed Matter*, *15*(11), S1279–S1290. (Cit. on p. 44).

Dasgupta, R., Mishra, P., Procaccia, I., & Samwer, K. (2013). Micro-alloying and the toughness of glasses: Modeling with pinned particles. *Applied Physics Letters*, *102*(19), 191904. (Cit. on p. 151).

de Bruijn, N. G. (1981). *Asymptotic methods in analysis*. Dover Publications. (Cit. on p. 81).

Debenedetti, P. G., & Stillinger, F. H. (2001). Supercooled liquids and the glass transition. *Nature*, *410*(6825), 259–267. (Cit. on p. 8).

Debye, P. (1912). Zur Theorie der spezifischen Wärmen. *Annalen der Physik*, *344*(14), 789–839. (Cit. on p. 41).

Dove, M. T. (1993). *Introduction to lattice dynamics*. Cambridge University Press. (Cit. on pp. 43, 62).

Duwez, P. (1981). Metallic glasses-historical background. In H. J. Güntherodt & H. Beck (Eds.), *Glassy Metals I: Ionic Structure, Electronic Transport, and Crystallization* (pp. 19–23). Springer. (Cit. on p. 1).

Dyre, J. C. (2006). Colloquium: The glass transition and elastic models of glass-forming liquids. *Reviews of Modern Physics*, *78*(3), 953–972. (Cit. on p. 10).

Einstein, A. (1907). Planck's theory of radiation and the theory of specific heat. *Annalen der Physik*, *22*, 180–190. (Cit. on p. 40).

Español, P., & Warren, P. (1995). Statistical mechanics of dissipative particle dynamics. *EPL (Europhysics Letters)*, *30*(4), 191–196. (Cit. on p. 54).

Falk, M. L., & Langer, J. S. (1998). Dynamics of viscoplastic deformation in amorphous solids. *Physical Review E*, *57*(6), 7192–7205. (Cit. on p. 22).

Farago, O., & Kantor, Y. (2000). Fluctuation formalism for elastic constants in hard-spheres-and-tethers systems. *Physical Review E*, *61*(3), 2478–2489. (Cit. on p. 31).

Foret, M., Courtens, E., Vacher, R., & Suck, J. B. (1996). Scattering investigation of acoustic localization in fused silica. *Physical Review Letters*, *77*(18), 3831–3834. (Cit. on p. 44).

Frenkel, D., & Smit, B. (2001). *Understanding Molecular Simulation: From Algorithms to Applications* (2nd ed.). Elsevier Science. (Cit. on pp. 50–54, 58).

Fulcher, G. S. (1925). Analysis of recent measurements of the viscosity of glasses. *Journal of the American Ceramic Society*, *8*(6), 339–355. (Cit. on p. 11).

Ganguly, S., Sengupta, S., Sollich, P., & Rao, M. (2013). Nonaffine displacements in crystalline solids in the harmonic limit. *Physical Review E*, *87*(4), 042801. (Cit. on p. 22).

Golkia, M., Shrivastav, G. P., Chaudhuri, P., & Horbach, J. (2020). Flow heterogeneities in supercooled liquids and glasses under shear. arXiv: 2004.02868. (Cit. on pp. 19, 23, 52, 57, 87, 100)

Greer, A. L., Cheng, Y. Q., & Ma, E. (2013). Shear bands in metallic glasses. *Materials Science and Engineering: R: Reports*, *74*(4), 71–132. (Cit. on p. 27).

Grigera, T. S., & Parisi, G. (2001). Fast monte carlo algorithm for supercooled soft spheres. *Physical Review E*, *63*, 045102. (Cit. on p. 152).

Grigera, T. S., Martin-Mayor, V., Parisi, G., & Verrocchio, P. (2003). Phonon interpretation of the 'boson peak' in supercooled liquids. *Nature*, *422*(6929), 289–292. (Cit. on pp. 27, 44).

Gusev, A. A., Zehnder, M. M., & Suter, U. W. (1996). Fluctuation formula for elastic constants. *Physical Review B*, *54*(1), 1. (Cit. on p. 31).

Hansen, J. P., & McDonald, I. R. (2013). *Theory of simple liquids: With applications to soft matter*. Academic Press. (Cit. on pp. 13, 17, 45, 46, 57, 140).

Harp, G. D., & Berne, B. J. (1970). Time-correlation functions, memory functions, and molecular dynamics. *Physical Review A*, *2*(3), 975. (Cit. on p. 13).

Hayes, B. (2005). Why W? *American Scientist*, *93*, 104–108. (Cit. on p. 81).

Hays, C. C., Kim, C. P., & Johnson, W. L. (2000). Microstructure controlled shear band pattern formation and enhanced plasticity of bulk metallic glasses containing in situ formed ductile phase dendrite dispersions. *Physical Review Letters*, *84*, 2901–2904. (Cit. on p. 4).

Herschel, W. H., & Bulkley, R. (1926). Konsistenzmessungen von Gummi-Benzollösungen. *Kolloid-Zeitschrift*, *39*(4), 291–300. (Cit. on p. 24).

Hofmann, D. C., Suh, J.-Y., Wiest, A., Duan, G., Lind, M.-L., Demetriou, M. D., & Johnson, W. L. (2008). Designing metallic glass matrix composites with

high toughness and tensile ductility. *Nature*, *451*(7182), 1085–1089. (Cit. on pp. 4, 28).

Hoogerbrugge, P. J., & Koelman, J. M. V. A. (1992). Simulating microscopic hydrodynamic phenomena with dissipative particle dynamics. *EPL (Europhysics Letters)*, *19*(3), 155–160. (Cit. on p. 53).

Hooke, R. (2016). *Lectures de potentia restitutiva, or of spring explaining the power of springing bodies*. London : Printed for John Martyn. (Cit. on pp. 3, 31).

Hoover, W. G., Holt, A. C., & Squire, D. R. (1969). Adiabatic elastic constants for argon. Theory and Monte Carlo calculations. *Physica*, *44*(3), 437–443. (Cit. on p. 31).

Horbach, J., Kob, W., & Binder, K. (1999). Specific heat of amorphous silica within the harmonic approximation. *The Journal of Physical Chemistry B*, *103*(20), 4104–4108. (Cit. on pp. 26, 44).

Horbach, J., Kob, W., & Binder, K. (2001). High frequency sound and the boson peak in amorphous silica. *The European Physical Journal B-Condensed Matter and Complex Systems*, *19*(4), 531–543. (Cit. on pp. 27, 44).

Horbach, J., Kob, W., & Binder, K. (1999). The boson peak in amorphous silica: Results from molecular dynamics computer simulations. *AIP Conference Proceedings*, *479*(1), 136–141. (Cit. on p. 27).

Hu, S. Z., Zhou, Z. H., & Robertson, B. E. (2009). Consistent approaches to van der Waals radii for the metallic elements. *Zeitschrift für Kristallographie*, *224*(8), 375–383. (Cit. on p. 118).

Hubek, R., Seleznev, M., Binkowski, I., Peterlechner, M., Divinski, S. V., & Wilde, G. (2018). The impact of micro-alloying on relaxation dynamics in $Pd_{40}Ni_{40}P_{20}$ bulk metallic glass. *Journal of Applied Physics*, *124*(22), 225103. (Cit. on pp. 4, 28, 147, 151, 152).

Inoue, A., Wang, X. M., & Zhang, W. (2008). Developments and applications of bulk metallic glasses. *Reviews on Advanced Materials Science*, *18*(1), 1–9. (Cit. on p. 10).

Inoue, A. (2000). Stabilization of metallic supercooled liquid and bulk amorphous alloys. *Acta Materialia*, *48*(1), 279–306. (Cit. on p. 3).

Ioffe, A. F., & Regel, A. R. (1960). Non-crystalline, amorphous and liquid electronic semiconductors. *Progress in Semiconductors*, *4*(89), 237–291. (Cit. on p. 44).

Janssen, L. (2018). Mode-coupling theory of the glass transition: A primer. *Frontiers in Physics*, *6*, 97–115. (Cit. on p. 2).

Jiang, M. Q., Peterlechner, M., Wang, Y. J., Wang, W. H., Jiang, F., Dai, L. H., & Wilde, G. (2017). Universal structural softening in metallic glasses indicated by boson heat capacity peak. *Applied Physics Letters*, *111*(26), 261901. (Cit. on p. 44).

Kittel, C. (1968). *Introduction to solid state physics*. Wiley. (Cit. on pp. 16, 34).

Klement, W., Willens, R. H., & Duwez, P. (1960). Non-crystalline structure in solidified gold-silicon alloys. *Nature*, *187*(4740), 869–870. (Cit. on p. 1).

Kob, W., & Andersen, H. C. (1994). Scaling behavior in the β-relaxation regime of a supercooled Lennard-Jones mixture. *Physical Review Letters*, *73*(10), 1376–1379. (Cit. on pp. 2, 4, 13–15, 17, 18, 24, 28, 57–59, 63, 82, 147).

Kob, W., & Andersen, H. C. (1995a). Testing mode-coupling theory for a supercooled binary lennard-jones mixture I: The van hove correlation function. *Physical Review E*, *51*(5), 4626–4641. (Cit. on pp. 2, 57).

Kob, W., & Andersen, H. C. (1995b). Testing mode-coupling theory for a supercooled binary lennard-jones mixture. II. Intermediate scattering function and dynamic susceptibility. *Physical Review E*, *52*(4), 4134–4153. (Cit. on pp. 2, 57).

Landau, D. P., & Binder, K. (2014). *A guide to monte carlo simulations in statistical physics* (4th ed.). Cambridge University Press. (Cit. on p. 50).

Landau, L. D., Lifshitz, E. M., Kosevich, A. M., Sykes, J. B., Pitaevskii, L. P., & Reid, W. H. (1986). *Theory of elasticity: Volume 7*. Elsevier Science. (Cit. on p. 22).

Larson, R. G. (1999). *The structure and rheology of complex fluids*. Oxford University Press. (Cit. on pp. 3, 19, 22).

Ledbetter, H. M. (1981). Stainless-steel elastic constants at low temperatures. *Journal of Applied Physics*, *52*(3), 1587–1589. (Cit. on pp. 33–36).

Lees, A. W., & Edwards, S. F. (1972). The computer study of transport processes under extreme conditions. *Journal of Physics C: Solid State Physics*, *5*(15), 1921–1928. (Cit. on pp. 4, 55).

Lennard-Jones, J. E. (1924). On the determination of molecular fields. II. From the equation of state of gas. *Proceedings of the Royal Society A*, *106*, 463–477. (Cit. on pp. 2, 4, 57).

Leonforte, F., Boissiere, R., Tanguy, A., Wittmer, J. P., & Barrat, J. L. (2005). Continuum limit of amorphous elastic bodies. III. three-dimensional systems. *Physical Review B*, *72*(22), 224206. (Cit. on p. 27).

Leutheusser, E. (1984). Dynamical model of the liquid-glass transition. *Physical Review A*, *29*(5), 2765–2773. (Cit. on pp. 2, 15).

Li, Y., Yu, P., & Bai, H. Y. (2008). Study on the boson peak in bulk metallic glasses. *Journal of Applied Physics*, *104*(1), 013520. (Cit. on p. 44).

Liebermann, H., & Graham, C. (1976). Production of amorphous alloy ribbons and effects of apparatus parameters on ribbon dimensions. *IEEE Transactions on Magnetics*, *12*(6), 921–923. (Cit. on p. 2).

Louzguine-Luzgin, D. V., & Inoue, A. (2013). Bulk Metallic Glasses: Formation, Structure, Properties, and Applications. In *Handbook of magnetic materials* (Vol. 21, pp. 131–171). Elsevier Science. (Cit. on p. 10).

Lu, J., Ravichandran, G., & Johnson, W. L. (2003). Deformation behavior of the $Zr_{41.2}Ti_{13.8}Cu_{12.5}Ni_{10}Be_{22.5}$ bulk metallic glass over a wide range of strain-rates and temperatures. *Acta Materialia*, *51*(12), 3429–3443. (Cit. on p. 20).

Lutsko, J. (1989). Generalized expressions for the calculation of elastic constants by computer simulation. *Journal of Applied Physics*, *65*(8), 2991–2997. (Cit. on pp. 3, 31).

Maloney, C., & Lemaître, A. (2004). Universal breakdown of elasticity at the onset of material failure. *Physical Review Letters*, *93*(19), 195501. (Cit. on p. 30).

Maxwell, J. C. (1867). IV. On the dynamical theory of gases. *Philosophical Transactions of the Royal Society of London*, *157*, 49–88. (Cit. on p. 10).

McSkimin, H. J., & Andreatch Jr, P. (1972). Elastic moduli of diamond as a function of pressure and temperature. *Journal of Applied Physics*, *43*(7), 2944–2948. (Cit. on p. 33).

Mitrofanov, Y. P., Peterlechner, M., Divinski, S. V., & Wilde, G. (2014). Impact of plastic deformation and shear band formation on the boson heat capacity peak of a bulk metallic glass. *Physical Review Letters*, *112*(13), 135901. (Cit. on p. 44).

Morante, S., Rossi, G. C., & Testa, M. (2006). The stress tensor of a molecular system: An exercise in statistical mechanics. *The Journal of Chemical Physics*, *125*(3), 034101. (Cit. on p. 31).

Mullin, J. W. (2001). *Crystallization* (4th ed.). Elsevier Science. (Cit. on p. 8).

Newton, I. (1687). *Philosophiæ naturalis principia mathematica (Mathematical principles of natural philosophy)* (1st ed.). Jussu Societatis Regiæ ac Typis Joseph Streater. (Cit. on p. 50).

Nollmann, N., Binkowski, I., Schmidt, V., Rösner, H., & Wilde, G. (2016). Impact of micro-alloying on the plasticity of pd-based bulk metallic glasses. *Scripta Materialia*, *111*, 119–122. (Cit. on pp. 4, 28, 152).

O'hara, G. P. (1983). *Mechanical properties of silicone rubber in a closed volume*. Large Caliber Weapon Systems Laboratory, Army Armament Research and Development Center. Defense Technical Information Center. (Cit. on pp. 34–36).

Ogden, R. W. (1997). *Non-linear elastic deformations*. Dover Publications. (Cit. on p. 22).

Öttinger, H. C. (2006). Nonequilibrium thermodynamics of glasses. *Physical Review E*, *74*(1), 011113. (Cit. on pp. 3, 8).

Ozawa, M., Berthier, L., Biroli, G., Rosso, A., & Tarjus, G. (2018). Random critical point separates brittle and ductile yielding transitions in amorphous materials. *Proceedings of the National Academy of Sciences*, *115*(26), 6656–6661. (Cit. on p. 152).

Ozawa, M., Berthier, L., Biroli, G., & Tarjus, G. (2019). The role of fluctuations on the yielding transition of two-dimensional glasses. arXiv: 1912.06021. (Cit. on p. 152)

Pang, D. X., Wang, J. T., & Ding, B. Z. (1989). Amorphous-crystalline transformation and structure in selenium. *Journal of Non-Crystalline Solids*, *107*(2), 239–243. (Cit. on p. 9).

Papakonstantopoulos, G. J., Yoshimoto, K., Doxastakis, M., Nealey, P. F., & de Pablo, J. J. (2005). Local mechanical properties of polymeric nanocomposites. *Physical Review E*, *72*(3), 031801. (Cit. on p. 31).

Parrinello, M., & Rahman, A. (1982). Strain fluctuations and elastic constants. *The Journal of Chemical Physics*, *76*(5), 2662–2666. (Cit. on p. 31).

Pearson, K. (1905). Das Fehlergesetz und seine verallgemeinerungen durch Fechner und Pearson. *Biometrika*, *4*(1-2), 169–212. (Cit. on p. 77).

Peng, W. J., & Zhang, Y. (2011). Micro-alloying of yttrium in zr-based bulk metallic glasses. *Progress in Natural Science: Materials International*, *21*(1), 46–52. (Cit. on p. 151).

Petit, A. T., & Dulong, P. L. (1819). *Recherches sur quelques points importans de la theorie de la chaleur* (Doctoral dissertation, Académie des Sciences). (Cit. on p. 39).

Pfleiderer, P., Horbach, J., & Binder, K. (2006). Structure and transport properties of amorphous aluminium silicates: Computer simulation studies. *Chemical Geology*, *229*(1-3), 186–197. (Cit. on p. 143).

Pitre, L., Plimmer, M. D., Sparasci, F., & Himbert, M. E. (2019). Determinations of the boltzmann constant. *Comptes Rendus Physique*, *20*(1-2), 129–139. (Cit. on p. 118).

Plimpton, S. (1995). Fast parallel algorithms for short-range molecular dynamics. *Journal of Computational Physics*, *117*(1), 1–19. (Cit. on pp. 58, 60).

Press, W. H., Teukolsky, S. A., Vetterling, W. T., & Flannery, B. P. (2007). *Numerical recipes: The art of scientific computing* (3rd ed.). Cambridge University Press. (Cit. on p. 62).

Qiao, J., Yao, Y., Pelletier, J.-M., & Keer, L. M. (2016). Understanding of micro-alloying on plasticity in $Cu_{46}Zr_{47-x}Al_7Dy_x (0 \leqslant x \leqslant 8)$ bulk metallic glasses under compression: Based on mechanical relaxations and theoretical analysis. *International Journal of Plasticity*, *82*, 62–75. (Cit. on p. 151).

Rahman, A. (1964). Correlations in the motion of atoms in liquid argon. *Physical Review*, *136*(2A), A405–A411. (Cit. on pp. 4, 50).

Rapaport, D. C. (2004). *The art of molecular dynamics simulation*. Cambridge University Press. (Cit. on pp. 50, 58).

Ray, J. R., Moody, M. C., & Rahman, A. (1985). Molecular dynamics calculation of elastic constants for a crystalline system in equilibrium. *Physical Review B*, *32*(2), 733–735. (Cit. on p. 30).

Ray, J. R., & Rahman, A. (1987). Calculation of elastic constants using molecular dynamics. In *Condensed matter theories* (pp. 41–50). Springer. (Cit. on p. 31).

Reddy, V. S., Nath, P., Horbach, J., Sollich, P., & Sengupta, S. (2020). Nucleation theory for yielding of nearly defect-free crystals: Understanding rate dependent yield points. *Physical Review Letters*, *124*(2), 025503. (Cit. on p. 81).

Rodney, D., Tanguy, A., & Vandembroucq, D. (2011). Modeling the mechanics of amorphous solids at different length scale and time scale. *Modelling and Simulation in Materials Science and Engineering*, *19*(8), 083001. (Cit. on p. 60).

Ruben, S. (1985). *Handbook of the elements*. Open Court Publishing Company. (Cit. on p. 118).

Rumble, J. R. (2017). *CRC handbook of Chemistry and Physics, 98th Edition*. CRC Press LLC. (Cit. on p. 21).

Scheidler, P., Kob, W., Latz, A., Horbach, J., & Binder, K. (2001). Frequency-dependent specific heat of viscous silica. *Physical Review B*, *63*(10), 104204. (Cit. on p. 44).

Schnell, B., Meyer, H., Fond, C., Wittmer, J., & Baschnagel, J. (2011). Simulated glass-forming polymer melts: Glass transition temperature and elastic constants of the glassy state. *The European Physical Journal E*, *34*(9), 97–110. (Cit. on p. 31).

Schroers, J., Kumar, G., Hodges, T. M., Chan, S., & Kyriakides, T. R. (2009). Bulk metallic glasses for biomedical applications. *JOM*, *61*(9), 21–29. (Cit. on p. 3).

Schuh, C. A., Hufnagel, T. C., & Ramamurty, U. (2007). Mechanical behavior of amorphous alloys. *Acta Materialia*, *55*(12), 4067–4109. (Cit. on p. 27).

Schuh, C. A., Hufnagel, T. C., & Ramamurty, U. (2007). Mechanical behavior of amorphous alloys. *Acta Materialia*, *55*(12), 4067–4109. (Cit. on p. 3).

Schweidler, E. R. (1907). Studien über die Anomalien im Verhalten der Dielektrika. *Annalen der Physik*, *329*(14), 711–770. (Cit. on p. 15).

Scopigno, T., Suck, J. B., Angelini, R., Albergamo, F., & Ruocco, G. (2006). High-frequency dynamics in metallic glasses. *Physical Review Letters*, *96*(13), 135501. (Cit. on p. 47).

Sheng, H. W., Luo, W. K., Alamgir, F. M., Bai, J. M., & Ma, E. (2006). Atomic packing and short-to-medium-range order in metallic glasses. *Nature*, *439*(7075), 419–425. (Cit. on p. 18).

Shrivastav, G. P., Chaudhuri, P., & Horbach, J. (2016). Heterogeneous dynamics during yielding of glasses: Effect of aging. *Journal of Rheology*, *60*(5), 835–847. (Cit. on pp. 21, 23, 57, 82).

Shrivastav, G. P., Chaudhuri, P., & Horbach, J. (2016). Yielding of glass under shear: A directed percolation transition precedes shear-band formation. *Physical Review E*, *94*, 042605. (Cit. on pp. 23, 24, 27, 87).

Smit, B. (1992). Phase diagrams of Lennard-Jones fluids. *The Journal of Chemical Physics*, *96*(11), 8639–8640. (Cit. on p. 58).

Soddemann, T., Dünweg, B., & Kremer, K. (2003). Dissipative particle dynamics: A useful thermostat for equilibrium and nonequilibrium molecular dynamics simulations. *Physical Review E*, *68*(4), 046702. (Cit. on p. 53).

Sólyom, J. (2007). *Fundamentals of the Physics of Solids: Volume 1: Structure and Dynamics*. Springer Berlin Heidelberg. (Cit. on pp. 3, 16, 37, 39–41).

Spear, K. E., & Dismukes, J. P. (1994). *Synthetic diamond: Emerging cvd science and technology*. Wiley. (Cit. on pp. 35, 36).

Stanley, H. E. (1971). *Phase transitions and critical phenomena*. Clarendon Press, Oxford. (Cit. on p. 8).

Stephens, R. (1976). Relaxation effects in glassy selenium. *Journal of Non-Crystalline Solids*, *20*(1), 75–81. (Cit. on p. 9).

Stern, E. A. (1958). Theory of the anharmonic properties of solids. *Physical Review*, *111*(3), 786–797. (Cit. on p. 39).

Suck, J. B., Rudin, H., Güntherodt, H. J., & Beck, H. (1983). Experimental investigation of the dispersion of collective density fluctuations near Q_p in a metallic glass. *Physical Review Letters*, *50*(1), 49–52. (Cit. on p. 47).

Swope, W. C., Andersen, H. C., Berens, P. H., & Wilson, K. R. (1982). A computer simulation method for the calculation of equilibrium constants for the formation of physical clusters of molecules: Application to small water clusters. *The Journal of Chemical Physics*, *76*(1), 637–649. (Cit. on p. 51).

Tammann, G., & Hesse, W. (1926). Die Abhängigkeit der Viscosität von der Temperatur bei unterkühlten Flüssigkeiten. *Zeitschrift für anorganische und allgemeine Chemie*, *156*(1), 245–257. (Cit. on p. 11).

Tanguy, A. (2015). Vibration modes and characteristic length scales in amorphous materials. *JOM*, *67*(8), 1832–1839. (Cit. on p. 26).

Taraskin, S. N., & Elliott, S. R. (2000). Ioffe-Regel crossover for plane-wave vibrational excitations in vitreous silica. *Physical Review B*, *61*(18), 12031–12037. (Cit. on p. 44).

Tsai, D. H. (1979). The virial theorem and stress calculation in molecular dynamics. *The Journal of Chemical Physics*, *70*(3), 1375–1382. (Cit. on p. 31).

Tsamados, M., Tanguy, A., Goldenberg, C., & Barrat, J. L. (2009). Local elasticity map and plasticity in a model Lennard-Jones glass. *Physical Review E*, *80*(2), 026112. (Cit. on p. 30).

Tuckerman, M. (2010). *Statistical mechanics: Theory and molecular simulation*. Oxford University Press. (Cit. on p. 51).

Varnik, F. (2006). Structural relaxation and rheological response of a driven amorphous system. *The Journal of Chemical Physics*, *125*(16), 164514. (Cit. on p. 19).

Varnik, F., Bocquet, L., & Barrat, J. L. (2004). A study of the static yield stress in a binary Lennard-Jones glass. *The Journal of Chemical Physics*, *120*(6), 2788–2801. (Cit. on pp. 21, 24).

Varnik, F., & Henrich, O. (2006). Yield stress discontinuity in a simple glass. *Physical Review B*, *73*(17), 174209. (Cit. on p. 23).

Varnik, F., Bocquet, L., Barrat, J. L., & Berthier, L. (2003). Shear localization in a model glass. *Physical Review Letters*, *90*, 095702. (Cit. on pp. 4, 23).

Verlet, L. (1967). Computer "Experiments" on Classical Fluids. I. Thermodynamical Properties of Lennard-Jones Molecules. *Physical Review*, *159*(1), 98–103. (Cit. on p. 51).

Vogel, D. H. (1921). Das Temperaturabhaengigkeitsgesetz der Viskositaet von Flüssigkeiten. *Physikalische Zeitschrift*, (22), 645–646. (Cit. on p. 11).

Voigt, W. (1928). *Lehrbuch der Kristallphysik*. Teubner, Leipzig. (Cit. on p. 32).

Voyiatzis, E. (2013). Mechanical properties and elastic constants of atomistic systems through the stress-fluctuation formalism. *Computer Physics Communications*, *184*(1), 27–33. (Cit. on p. 31).

Wang, W. H. (2012a). The elastic properties, elastic models and elastic perspectives of metallic glasses. *Progress in Materials Science*, *57*(3), 487–656. (Cit. on p. 3).

Wang, W. H. (2012b). The elastic properties, elastic models and elastic perspectives of metallic glasses. *Progress in Materials Science*, *57*(3), 487–656. (Cit. on pp. 10, 33–36, 132).

Wang, W. H., Dong, C., & Shek, C. (2004). Bulk metallic glasses. *Materials Science and Engineering: R: Reports*, *44*(2-3), 45–89. (Cit. on p. 3).

Weber, T. A., & Stillinger, F. H. (1985). Local order and structural transitions in amorphous metal-metalloid alloys. *Physical Review B*, *31*(4), 1954–1963. (Cit. on p. 57).

Wen, J., Cheng, Y. Q., Wang, J. Q., & Ma, E. (2009). Distinguishing medium-range order in metallic glasses using fluctuation electron microscopy: A theoretical study using atomic models. *Journal of Applied Physics*, *105*(4), 043519. (Cit. on p. 18).

Winterling, G. (1975). Very-low-frequency Raman scattering in vitreous silica. *Physical Review B*, *12*(6), 2432–2440. (Cit. on p. 44).

Withers, P. (2007). Residual stress and its role in failure. *Reports on Progress in Physics*, *70*(12), 2211–2264. (Cit. on p. 26).

Wittmer, J. P., Xu, H., Polińska, P., Weysser, F., & Baschnagel, J. (2013). Shear modulus of simulated glass-forming model systems: Effects of boundary condition, temperature, and sampling time. *The Journal of Chemical Physics*, *138*(12), 12A533. (Cit. on pp. 30, 33).

Yanniotis, S., Skaltsi, S., & Karaburnioti, S. (2006). Effect of moisture content on the viscosity of honey at different temperatures. *Journal of Food Engineering*, *72*(4), 372–377. (Cit. on p. 21).

Yoshimoto, K., Jain, T. S., Van Workum, K., Nealey, P. F., & de Pablo, J. J. (2004). Mechanical heterogeneities in model polymer glasses at small length scales. *Physical Review Letters*, *93*(17), 175501. (Cit. on p. 31).

Yu, H.-B., Wang, W.-H., & Samwer, K. (2013). The β relaxation in metallic glasses: An overview. *Materials Today*, *16*(5), 183–191. (Cit. on p. 15).

Zallen, R. (2008). *The physics of amorphous solids*. Wiley. (Cit. on pp. 9, 12).

Zausch, J., & Horbach, J. (2009). The build-up and relaxation of stresses in a glass-forming soft-sphere mixture under shear: A computer simulation study. *EPL (Europhysics Letters)*, *88*(6), 60001. (Cit. on pp. 21, 76).

Zausch, J., Horbach, J., Laurati, M., Egelhaaf, S. U., Brader, J. M., Voigtmann, T., & Fuchs, M. (2008). From equilibrium to steady state: The transient dynamics of colloidal liquids under shear. *Journal of Physics: Condensed Matter*, *20*(40), 404210. (Cit. on p. 21).

Zberg, B., Uggowitzer, P. J., & Löffler, J. F. (2009). MgZnCa glasses without clinically observable hydrogen evolution for biodegradable implants. *Nature Materials*, *8*(11), 887–891. (Cit. on p. 3).

Zeller, R., & Pohl, R. (1971). Thermal conductivity and specific heat of noncrystalline solids. *Physical Review B*, *4*(6), 2029–2041. (Cit. on p. 44).

Ziman, J. M., & Ziman, P. J. M. (1979). *Models of Disorder: The Theoretical Physics of Homogeneously Disordered Systems*. Cambridge University Press. (Cit. on p. 17).

Eidesstattliche Versicherung

Ich versichere an Eides Statt, dass die Dissertation von mir selbständig und ohne unzulässige fremde Hilfe unter Beachtung der „Grundsätze zur Sicherung guter wissenschaftlicher Praxis an der Heinrich-Heine-Universität Düsseldorf“ erstellt worden ist.

Düsseldorf, den 30.04.2020 *Mehrdad Golkia*